INFORMATION TO USERS

This manuscript has been reproduced from the microfilm master. UMI films the text directly from the original or copy submitted. Thus, some thesis and dissertation copies are in typewriter face, while others may be from any type of computer printer.

The quality of this reproduction is dependent upon the quality of the copy submitted. Broken or indistinct print, colored or poor quality illustrations and photographs, print bleedthrough, substandard margins, and improper alignment can adversely affect reproduction.

In the unlikely event that the author did not send UMI a complete manuscript and there are missing pages, these will be noted. Also, if unauthorized copyright material had to be removed, a note will indicate the deletion.

Oversize materials (e.g., maps, drawings, charts) are reproduced by sectioning the original, beginning at the upper left-hand corner and continuing from left to right in equal sections with small overlaps.

Photographs included in the original manuscript have been reproduced xerographically in this copy. Higher quality 6" x 9" black and white photographic prints are available for any photographs or illustrations appearing in this copy for an additional charge. Contact UMI directly to order.

ProQuest Information and Learning
300 North Zeeb Road, Ann Arbor, MI 48106-1346 USA
800-521-0600

UMI®

DISSERTATION

SIMULATION AND PARAMETERIZATION OF VERTICALLY PROPAGATING CONVECTIVELY GENERATED GRAVITY WAVES

Submitted by
Zachary A. Eitzen
Department of Atmospheric Science

In partial fulfillment of the requirements
for the degree of Doctor of Philosophy
Colorado State University
Fort Collins, Colorado
Fall 2001

COLORADO STATE UNIVERSITY

SEPTEMBER 21, 2001

WE HEREBY RECOMMEND THAT THE DISSERTATION PREPARED UNDER OUR SUPERVISION BY ZACHARY ALAN EITZEN ENTITLED SIMULATION AND PARAMETERIZATION OF VERTICALLY PROPAGATING CONVECTIVELY GENERATED GRAVITY WAVES BE ACCEPTED AS FULFILLING IN PART REQUIREMENTS FOR THE DEGREE OF DOCTOR OF PHILOSOPHY.

Committee on Graduate Work

Richard H. Johnson

J. W. Thura

Wayne Schubert

Adviser

Department Head

ABSTRACT OF DISSERTATION

SIMULATION AND PARAMETERIZATION OF VERTICALLY PROPAGATING CONVECTIVELY GENERATED GRAVITY WAVES

In this work, we use a high-resolution, two-dimensional numerical model to simulate convection initiated with many different thermodynamic and wind profiles. The simulated convection produces gravity waves, some of which propagate vertically into the stratosphere. Several diagnoses are made of the convection. These include a gravity wave source diagnosis where source terms associated with heating and nonlinear advection are shown to be dominant. A diagnosis of the first and second moment equations is also performed, isolating the important terms in these equations in the troposphere and stratosphere. The empirical orthogonal functions of horizontal velocity, vertical velocity, and potential temperature are also calculated, yielding modes that represent convection and gravity waves. Moist updrafts and other convective phenomena are isolated using particle trajectory analysis and a conditional sampling analysis. Finally, the waves in the stratosphere were characterized using Fourier analysis. The waves generated by the simulated convection have characteristic wavelengths of 10-100 km, periods of 10-60 minutes, and phase speeds of -50 to 50 m s^{-1}. Each of these ranges is consistent with waves that have been observed above convection in the stratosphere, and simulated in previous modeling studies. In simulations with stratospheric shear layers, the simulated waves are absorbed near their critical levels.

A parameterization to represent the effects of convectively generated gravity waves in large-scale models is also proposed. The mechanism for the generation of the waves can be represented by transient topography. The effects of critical level absorption, wave breaking, and wave reflection are accounted for. The energy flux associated with the waves

is shown to represent a sink to the perturbation kinetic energy of the convection, and a method to calculate this effect is proposed.

Zachary A. Eitzen
Department of Atmospheric Science
Colorado State University
Fort Collins, CO 80523
Fall 2001

ACKNOWLEDGMENTS

I thank my advisor, Professor David Randall, for his patient guidance throughout my long career as a graduate student. He struck an excellent balance between giving advice when necessary and allowing me to work independently, and has always been dedicated to his students. I also thank the other members of my committee, Professors Richard Johnson, Wayne Schubert and Jim Thomas for agreeing to read my dissertation and for providing helpful comments throughout my doctoral program. I also thank all of the other professors that have helped expand my knowledge of atmospheric science, particularly Mike Montgomery and David Thompson. In addition, I wish to thank all of the other students, staff, and research associates at CSU that have helped me with this work, particularly Cindy Carrick, Erica Loechl, Matt Parker, and Stefan Tulich. Also, I thank the many colleagues outside of CSU that have helped me improve my research, particularly Joan Alexander, Brian Mapes, and Todd Lane.

I also thank the many friends I've had at CSU throughout the years, including Chris Golaz, Ken Knapp, Jim Kossin, David Mocko, Jason Nachamkin, and Lyle Pakula. I especially thank my mother and sister for their continued love and support.

This research was supported in part by a grant from the National Science Foundation (ATM-9812384), and by grants from the U.S. Department of Energy (DE-FG03-95ER62102 and DE-FG03-98ER62611).

TABLE OF CONTENTS

Chapter 1: Introduction

1.1. Overview of the problem

Waves are a ubiquitous feature of the atmosphere. From internal gravity waves with wavelengths of hundreds of meters to planetary waves with wavelengths of tens of thousands of kilometers, they cover a wide span of scales. Although some waves are not believed to have much influence on the general circulation (e.g., acoustic waves), many others are. One class of waves that is believed to have an important influence on the general circulation is gravity waves. Although general circulation models (GCMs) can simulate inertia-gravity waves that have wavelengths of at least two grid points (typically 200-500 km), they cannot simulate the shorter gravity waves that also exist in the real atmosphere.

One source of subgrid-scale gravity waves is orography. Orographic waves are stationary with respect to the earth, and can have a momentum flux amplitude of ~0.5 Pa (Palmer et al. 1986). These waves act as a drag on the mean flow, slowing it where they are absorbed. The parameterization of subgrid-scale orographically generated gravity wave drag has been examined for many years. These schemes were found to counteract a systematic westerly wind bias that existed in many GCMs (e.g., Palmer et al. 1986; McFarlane 1987).

Another source of short-wavelength gravity waves is moist convection. Convection can occur on many length and depth scales, from small cumuli that span a few hundred meters in the horizontal and vertical to superclusters in the tropics that extend thousands of kilometers in the horizontal and through the depth of the troposphere.

There are a number of reasons to study convectively generated gravity waves. Although this work will primarily focus on vertically propagating waves, horizontally propagating gravity waves generated by convection have also been identified as physically important, acting as triggers for the generation of new convection (Mapes 1993), and as a

mechanism for the organization of convection (Schmidt and Cotton 1990). Vertically propagating gravity waves carry a momentum flux that may alter the mean winds above the convection by well-known processes (Eliassen and Palm 1960). Convectively generated gravity waves may carry a momentum flux of similar magnitude to that of orographically generated waves (Fritts and Nastrom 1992), which have long been acknowledged as important to the flow for altitudes at and above the upper troposphere (Bretherton 1969). Researchers such as Dunkerton (1997) have identified vertically propagating convectively generated gravity waves as being important for the maintenance of the quasi-biennial oscillation (QBO; Baldwin et al. 2001). In addition, convectively generated gravity waves may play a role in the dessication of the lower stratosphere (Potter and Holton 1995), and the nucleation of stratospheric aerosols (Nilsson et al. 2000).

A parameterization of convectively generated gravity waves needs to include several elements to adequately represent the impact of these waves on the mean flow. One of these is a condition within a grid box under which the waves are generated. For orographic gravity wave parameterizations, the presence of land is obviously required, typically with some minimum amount of topographic variance. The most natural condition for convectively generated waves would seem to be the presence of convection, perhaps with a minimum strength. This is the path that Rind et al. (1988), Bossuet et al. (1998), Kershaw (1995), Roadnight (1999), and Chun and Baik (1998) have taken. There are other parameterizations (Hines 1997a,b; Warner and McIntyre 1999, 2001) that are meant to include the general effects of nonorographic gravity waves (including gravity waves produced by shear). These parameterizations do not include specific triggering mechanisms, but assume wave spectra that are isotropic at all grid points, or vary as a function of latitude.

Another element that the parameterization needs to include is a characterization of the waves, in terms of their strength, phase speed, and wavenumber. Many of the previous parameterizations (Kershaw 1995; Bossuet et al. 1998; Chun and Baik 1998; Roadnight 1999) assume that the waves produced by convection have a single phase speed. As we will see from the observations in Chapter 2, and the model results contained in Chapter 13 and Chapter 14, this is an unrealistic assumption. Other parameterizations (Rind et al. 1988; Alexander and Dunkerton 1999) do assume that convectively generated waves occur over a range of phase speeds.

Once the waves are launched within a grid cell, they can impart momentum to the mean flow via critical level absorption or saturation. Critical level absorption occurs when a wave's phase speed matches the mean flow speed of the atmosphere. Saturation occurs when a wave grows in amplitude until it distorts potential temperature surfaces to near the point of static instability, causing localized areas of Kelvin-Helmholtz instability and subsequent turbulence. Most existing parameterizations use variations on the linear theory proposed by Lindzen (1981) for wave absorption, although Hines (1997a) points out that wave-wave interactions may be important, and includes these effects. Another effect that may be important in some cases (Alexander and Dunkerton 1999) is that of wave reflection, which occurs when a vertically propagating wave encounters a region of the atmosphere with a Brunt-Väisälä frequency that is greater than the wave's frequency.

Finally, one effect that has not been accounted for in any existing parameterization is the effect of the waves on the energy budget of the convection. Taking this into account brings about a natural closure between the cumulus kinetic energy budget and the convective gravity wave parameterization that will be described in Chapter 15.

1.2. Basic properties of gravity waves

The fundamental properties of internal gravity waves are given in many texts, including Lighthill (1978), Gill (1982), Andrews et al. (1987), and Holton (1992). However, the importance of these properties to the rest of this work necessitates a brief review of the subject.

The linearized two-dimensional anelastic equations can be derived from the equations given in Bannon (1996) and are given by

$$\frac{\partial}{\partial x}(\rho_0 u') + \frac{\partial}{\partial z}(\rho_0 w') = 0, \tag{1.1}$$

$$\frac{\partial u'}{\partial t} + \bar{u}\frac{\partial u'}{\partial x} + w'\frac{d\bar{u}}{dz} = -\frac{\partial}{\partial x}\left(\frac{p'}{\rho_0}\right), \tag{1.2}$$

$$\frac{\partial w'}{\partial t} + \bar{u}\frac{\partial w'}{\partial x} = -\frac{\partial}{\partial z}\left(\frac{p'}{\rho_0}\right) + g\frac{\theta'}{\theta_0}, \tag{1.3}$$

$$\frac{\partial \theta'}{\partial t} + \bar{u}\frac{\partial \theta'}{\partial x} + w'\frac{d\bar{\theta}}{dz} = 0, \tag{1.4}$$

in the absence of heating. One way of summarizing the spectral characteristics of internal gravity waves is via the dispersion relation, which is given by Bannon (1996) as

$$(\omega - k\bar{u})^2 = \frac{k^2 N^2}{k^2 + m^2 + \frac{1}{4H^2}}, \tag{1.5}$$

for the linearized anelastic set in a two-dimensional, nonrotating, isothermal atmosphere. Here, H is a scale height, given by

$$H = \frac{RT_0}{g}, \tag{1.6}$$

where T_0 is the temperature of the atmosphere.Also, k and m are the horizontal and vertical wavenumbers, ω is the frequency, and N is the Brunt-Väisälä frequency. The scale height has a typical value of 7 km. Frequently, the $1/4H^2$ term can be neglected in (1.5), since the vertical wavelength $\lambda_z = 2\pi/m$ is usually shorter than 15 km, which is sufficient to satisfy $m^2 \gg 1/4H^2$ (Andrews et al. 1987). Marks and Eckermann (1995) and Alexander and Dunkerton (1999) note that the neglect of this term is not appropriate for waves with $\omega \sim N$.

The phase speed of a wave is a measure of how quickly the peak (or trough) of a wave moves in a given direction. Now, the horizontal and vertical phase speeds, denoted by c_{px} and c_{px} respectively, are given by

$$c_{px} = \frac{\omega}{k} = \bar{u} \pm \frac{N}{\left(k^2 + m^2 + \frac{1}{4H^2}\right)^{1/2}}, \tag{1.7}$$

$$c_{pz} = \frac{\omega}{m} = \frac{k\bar{u}}{m} \pm \frac{Nk}{m\left(k^2 + m^2 + \frac{1}{4H^2}\right)^{1/2}}. \tag{1.8}$$

The group velocity is a measure of how quickly wave energy propagates. For gravity waves that satisfy (1.5), the components of group velocity are given by

$$c_{gx} = \frac{\partial\omega}{\partial k} = \bar{u} \pm \frac{N(m^2 + 1/4H^2)}{\left(k^2 + m^2 + \frac{1}{4H^2}\right)^{3/2}}, \tag{1.9}$$

$$c_{gz} = \frac{\partial \omega}{\partial m} = \mp \frac{Nkm}{\left(k^2 + m^2 + \frac{1}{4H^2}\right)^{3/2}}. \tag{1.10}$$

Note that the dispersion relation (1.5) can be rewritten in terms of the vertical wavenumber as

$$m^2 = \frac{k^2 N^2}{(\omega - k\bar{u})^2} - \left(k^2 + \frac{1}{4H^2}\right). \tag{1.11}$$

From (1.11), we see that as a wave approaches a critical level where $c_{px} = \bar{u}$, or $\omega = k\bar{u}$, its vertical wavenumber approaches infinity. From (1.7)-(1.10), we see that this implies that the horizontal phase speed and group velocity approach $\bar{u}$, while the vertical phase speed and group velocity approach zero. This leads us to the following definition for a critical level: *A critical level is the level through which the energy and momentum associated with a vertically propagating wave cannot pass.* The wave gives up its energy to the mean flow, accelerating it according to

$$\frac{\partial}{\partial t}(\rho_0 \bar{u}) = -\frac{\partial}{\partial z}(\rho_0 \overline{u'w'}). \tag{1.12}$$

Following Saravanan (1990), Dunkerton (1997), and Alexander and Holton (1997), the behavior of the RHS of (1.12) as a wave with a given horizontal wavenumber and phase speed approaches a critical level can be understood according to

$$\rho_0 \overline{u'w'(z)} = \rho_0 \overline{u'w'(z_r)} \exp\left[-\int_{z_r}^{z} \frac{\alpha N}{k(c-\bar{u})^2} dz'\right]. \tag{1.13}$$

Here, z_r is the reference height at which the wave is launched, and α is the temporal damping rate. Note that the argument of the exponential in (1.13) gets large and negative as a critical level is approached, which causes the RHS of (1.13) to approach zero.

The phase behavior of one variable with respect to another is often called a polarization relationship. These relationships are particularly useful when trying to determine what the spatial mean of a second (or higher) moment quantity is. If we substitute wave solutions of the form

$$a' = \frac{\hat{a}}{\rho_0^{1/2}} \exp[i(kx + mz - \omega t)] \tag{1.14}$$

into (1.1)-(1.4) for u', w', θ' and p'/ρ_0, we obtain the following relationships:

$$\hat{u} = -\frac{1}{k}\left(m - \frac{i}{2\rho_0^{1/2}}\frac{d\rho_0}{dz}\right)\hat{w}, \tag{1.15}$$

$$(\omega - k\bar{u})\hat{u} + i\frac{d\bar{u}}{dz}\hat{w} = k\hat{p}, \tag{1.16}$$

$$(\omega - k\bar{u})\hat{w} = \left(m + \frac{i}{2\rho_0^{1/2}}\frac{d\rho_0}{dz}\right)\hat{p} + \frac{ig\hat{\theta}}{\theta_0}, \tag{1.17}$$

$$(\omega - k\bar{u})\hat{\theta} = -i\frac{d\theta_0}{dz}\hat{w}. \tag{1.18}$$

From the above, we see that the heat flux $\overline{w'\theta'}$, which can be expressed by

$$\frac{1}{2\rho_0}\mathrm{Re}(\hat{w}\hat{\theta}^*) = \frac{1}{2\rho_0}\mathrm{Re}\left[\frac{i(\omega - k\bar{u})}{d\theta_0/dz}\hat{\theta}\hat{\theta}^*\right] \tag{1.19}$$

following Andrews et al. (1987) is zero, provided that the frequency is real. In the case of wave transience, ω may be complex, and (1.19) may be nonzero, as noted by Roadnight (1999). Many other polarization relationships exist for gravity waves, and some will be derived in Chapter 8.

In this dissertation, we will study the generation of vertically propagating gravity waves produced by convection, and their interaction with the surrounding environment. To do this, we will use data generated by several numerical simulations of convection using ARPS (the Advanced Regional Prediction System), which is a model that is described in Xue et al. (2000; see also Xue et al. 1995), largely based upon the model of Klemp and Wilhelmson (1978). The results in this dissertation are from two types of simulations. Both are two-dimensional, and initialized with soundings associated with the formation of squall lines. Some of the simulations were based on an analytic mid-latitude sounding originally proposed by Weisman and Klemp (1982). The others were based on a tropical sounding described in Redelsperger et al. (2000) that was observed during the TOGA COARE (Tropical Ocean Global Atmosphere Coupled Ocean-Atmosphere Response Experiment) field experiment (Jorgensen et al. 1997).

Some of the questions that this research will attempt to answer are as follows:

- What do the gravity waves look like, and how separable are they from the convection that is responsible for their generation?
- What are the specific mechanisms through which gravity waves are generated by convection?
- How do the waves affect the mean flow above the convection?
- How do the waves affect the convection?
- What type of parameterization should large-scale models use to take this wave-mean flow interaction into account?

The organization of this dissertation is as follows. We will begin by examining prior research on observed and simulated convectively generated gravity waves. Following that, a brief review of squall lines is presented. Then, the source for the waves will be analyzed following the method of Lane et al. (2001). In addition, we will use the model output in diagnostic prediction equations for the wave momentum flux and other wave quantities to help understand which physical processes are most responsible for producing gravity waves. Then, we will study the theory of how these waves affect the mean flow, and examine previous efforts at parameterizing these effects in large-scale models. Afterwards, the simulations that were performed in this study will be summarized. To identify characteristic wave and convective motions, we will employ empirical orthogonal function (EOF) analysis. We will also use an analysis technique that tracks particles in the model based on the simulated winds, keeping track of scalar variables at the particles' positions in addition to calculating their trajectories. Following this, conditional sampling techniques will be applied to the model output, to diagnose the behavior of cloudy and dry air. A Fourier analysis scheme will then be used to determine the momentum flux spectra in terms of phase speed. Afterwards, the effects of the convectively generated waves on stratospheric shear layers will be quantified. Finally, we will use the model results to attempt to evaluate existing parameterizations of the momentum flux carried by vertically propagating convectively generated gravity waves, and suggest an improved parameterization.

Chapter 2: Gravity wave observations

There are limited measurements of gravity waves above the tropopause, due to the difficulty in flying planes or obtaining remote-sensing data at sufficiently high altitudes to detect these waves. Nevertheless, several researchers have detected such waves, using a variety of techniques.

One of the earliest observational studies of gravity waves occurred in connection with orographic waves that occurred above a downslope windstorm in Boulder, Colorado. This was carried out by Lilly (1978). In this study, supported by the modeling study of Klemp and Lilly (1978), turbulence observed in research aircraft was found to be associated with large-amplitude mountain waves, which had significant amounts (~5 Pa) of momentum flux. This was a rather extreme event, and not typical of orographic waves in general, but still serves to show their importance in the general circulation.

In the research described by Pfister et al. (1986), a U-2 (now known as an ER-2) aircraft equipped with temperature and ozone sensors was flown over Panama (approximately 9° N). The plane took data at altitudes from 17 to 21 km, detecting disturbances in the temperature and ozone fields with horizontal wavelengths between 5 and 25 km. Although vertical velocity was not directly measured, Pfister et al. (1986) combined the aircraft measurements with radiosonde measurements of potential temperature to estimate that the waves caused parcels to travel approximately 300 m in the vertical. In a similar aircraft-based observational study, Pfister et al. (1993) used data taken from flights above convection over Panama and Australia to detect gravity waves with wavelengths of approximately 100 km, and peak-to-trough variations of 300-400 m in the heights of isentropic surfaces.

In still another aircraft-based study, Alexander et al. (2000) noted that the largest magnitudes of momentum fluxes, defined as $\rho_0(|u'w'|^2 + |v'w'|^2)^{1/2}$, were generally associated with the lowest cloud-top brightness temperatures, which would indicate deep

convection. In this case, u', v', and w' represent differences from the mean zonal, meridional and vertical velocities measured along an aircraft leg, and the product is defined at each point along the leg, and is not averaged. Representative values of the momentum fluxes calculated by Alexander et al. (2000) from flights over northern Australia and Indonesia ranged up to 0.11 N m^{-2} (or Pascals) above the coldest cloud tops, while considerably smaller values of 0.016 N m^{-2} were measured above the coldest cloud tops from flights over the central Pacific. The 0.11 N m^{-2} value of momentum flux is comparable to those that have been measured in association with orographically generated gravity waves (Palmer et al. 1986). These fluxes were calculated for gravity waves with horizontal wavelengths between 5 and 150 km. Alexander et al. (2000) offered several hypotheses for the differences between the magnitudes of the momentum fluxes, including real differences in the strength of gravity wave momentum flux between the two experiments, and the fact that the Australia flights were designed to fly over deep, active convection, while the central Pacific flights were designed with a more general purpose of flying over the Intertropical Convergence Zone, with flights over convection being coincidental.

Sato (1992, 1993) and Sato et al. (1995) have used radar to detect gravity waves in the stratosphere. The radar used by Sato is a clear-air Doppler radar located in southern Japan with five beams that point in fixed directions (north, south, east, west and upward). The zenith angle for the off-vertical beams was 10°. The radar observations described in Sato (1992) were able to detect fluctuations in vertical velocity in both the troposphere and stratosphere with magnitudes of up to 1 m s^{-1}, and periods of 30-60 minutes. Due to the fact that the fluctuations had a higher amplitude during each afternoon, Sato associated the waves with the cumuli that were simultaneously present. In another paper, Sato (1993) used the same radar to observe gravity waves associated with a typhoon that passed near the radar site. Sato (1993) found significant momentum fluxes created by the typhoon's convection in both the troposphere and stratosphere. The values of $\rho_0 u'w'$ associated with gravity waves with periods of less than 60 minutes in this study covered a range from 0.01-0.04 N m^{-2}. The waves had periods that varied widely, ranging from tens of minutes for waves observed after the passage of the typhoon to several hours for an inertia-gravity wave observed about a day before the typhoon's passage.

Wu and Waters (1996a,b) and McLandress et al. (2000) used satellite observations from the Upper Atmosphere Research Satellite (UARS) Microwave Limb Sounder (MLS) to detect gravity waves at altitudes from 30 km to 80km. The MLS measured fluctuations in radiance, which Wu and Waters ascribe to atmospheric temperature variations. The strongest waves measured by Wu and Waters occurred at high altitudes (above 50 km), and were located at higher latitudes, being particularly pronounced above the polar stratospheric vortices in winter. Wu and Waters also measured enhanced areas of wave activity over areas of convection, primarily over the subtropics. This is despite the fact that equatorial areas contain the greatest amount of convection. Alexander (1998), McLandress et al. (2000), and Baldwin et al. (2001) note that the MLS can only detect waves with vertical wavelengths greater than approximately 10 km. These waves are more likely to be damped in areas with weak base-state winds, such as the tropics.

Dewan et al. (1998) also used satellite measurements to detect gravity waves, producing images similar to the idealized depiction of Fig. 2.1. The satellite images were taken in a region that was experiencing convection at the time. Since the stratosphere is dry, the rings in the image are exclusively due to variations in the temperature and density of that layer. The rings are associated with gravity waves propagating outward from the convection in concentric ellipses. The horizontal wavelength of the waves observed by Dewan et al. ranged from about 25-50 km.

Karoly et al. (1996) used radiosonde observations from the Tropical Ocean-Global Atmosphere Coupled Ocean-Atmosphere Response Experiment (TOGA COARE) to detect gravity waves. They defined a background wind profile by fitting two quadratic profiles to each of the soundings in the upper troposphere (defined as 10-17 km) and lower stratosphere (17-24 km). The deviations from these fitted curves were then interpreted as waves. It should be noted that these deviations could be quasi-horizontal features known as laminae (Danielson 1959; Newell et al. 1996, 1999), and identification of these features as gravity waves needs to be done with care. The vertical wavelengths could be directly measured, and were found to have typical values in the range of 2-4 km. The wave periods and horizontal wavelengths were estimated indirectly, and found to be 20-40 hours, and 1000-3000 km in the lower stratosphere, respectively. These values are more typical of inertia-gravity waves than the smaller-scale internal-gravity waves that most of the other

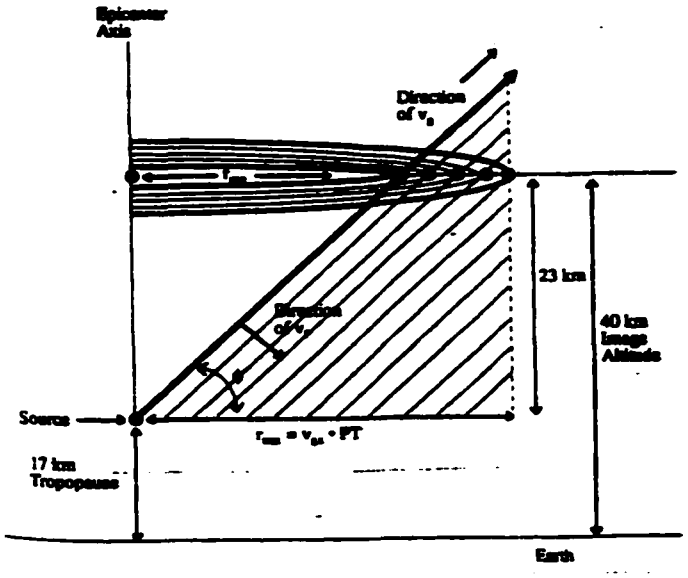

Fig. 2.1. Idealized representation of gravity waves generated by convection in the troposphere taken from Dewan et al. (1998). Wave packets propagate with group velocity v_g, while individual crests propagate with phase velocity v_p.

observational studies described above have focused upon. Vincent and Alexander (2000) also used radiosonde observations to detect gravity waves, in a similar manner to Karoly et al. The soundings used by Vincent and Alexander were taken at the Cocos Islands (12° S, 97° E), over a six-year period. The waves detected were found to have vertical wavelengths, periods, and horizontal wavelengths similar to those observed by Karoly et al. They observed maximum wave energy densities and momentum fluxes in the lower stratosphere at the times when the westerly winds were strongest in this region. In a companion paper, Alexander and Vincent (2000) used a modeling study to argue that while the tropospheric winds were westerly (which tended to happen while the stratospheric winds were westerly), waves were prevented from propagating into the stratosphere due to Richardson number instability (see Chapter 9), rather than critical level absorption.

Another study of convectively generated gravity waves by Clark and Morone (1981) focused on waves that reached the mesosphere. Using rocketsonde temperature data, Clark and Morone noticed that there was significant warming at mesospheric altitudes on dates when squall line convection existed in the area of the rocket launches. They hypothesized that this warming was due to the turbulent, viscous dissipation of breaking gravity waves that had grown large enough in amplitude to form localized areas with a Richardson num-

ber less than 0.25 (Lindzen 1981). Based on wave reflection considerations, the periods of the waves that could penetrate the mesosphere were 20-40 minutes, and horizontal wavelengths were >13 km.

Other researchers have used measurements of the vertical profiles of ozone and temperature obtained with ozonesondes to detect gravity wave activity. Pierce and Grant (1998) and Grant et al. (1998) have calculated correlations between perturbations in ozone and potential temperature to identify gravity and Rossby waves. Vertical profiles which contain a high positive correlation between perturbations in ozone and potential temperature were associated with gravity waves, while profiles in which the two perturbation quantities are uncorrelated were associated with Rossby waves. Chane-Ming et al. (2000) described the reason for these phase relationships. Ozone perturbations induced by gravity waves are expected to have the form

$$\frac{\mu'(z,t)}{\bar{\mu}(z)} = R(z)\frac{T'(z,t)}{\bar{T}(z)}, \tag{2.1}$$

where $\bar{\mu}$ and μ' represent the mean and perturbation ozone mixing ratio, T is temperature, and $R(z)$ depends on the background profile of ozone and potential temperature. The above relationship indicates that we expect perturbations in ozone and temperature to be in phase. For planetary waves, Chane-Ming et al. (2000) noted the following relationship

$$\frac{\partial \mu'}{\partial t} + \bar{u}\frac{\partial \mu'}{\partial x} \sim -DT' \tag{2.2}$$

for planetary waves, where $\bar{u}$ is the background mean wind, and D is a function that represents the dynamical response of ozone perturbations to temperature perturbations. From (2.2), we expect μ' and T' to be $\pi/2$ radians out of phase for planetary waves.

In this chapter, we have seen that researchers have used a variety of techniques to detect the presence of convectively generated gravity waves in the stratosphere including aircraft, radar, satellite, radiosonde and ozonesonde platforms. The gravity waves observed ranged widely in horizontal wavelength, period, and vertical wavelength. Momentum fluxes from many of the observed waves were sufficient to alter the mean flow at altitudes above the convection by processes that will be detailed in Chapter 8. The next

chapter summarizes the previous work that has been done by researchers to simulate these gravity waves.

Chapter 3: Previous simulations of convectively generated gravity waves

There have been several published simulations of vertically propagating, convectively generated waves. These simulations have largely focused on two-dimensional squall line convection. The primary distinction between these simulations and earlier two-dimensional simulations of squall lines (e.g. Weisman et al. 1988) is the use of a higher upper boundary, giving the waves a chance to propagate into the model stratosphere (and in some cases, mesosphere). Since the waves also propagate away from the convection in the horizontal direction, a large horizontal domain is typically needed.

The first simulations of vertically propagating, convectively generated waves were actually performed by Clark et al. (1986) in connection with boundary-layer convection. In their study, Clark et al. found that waves were forced in the overlying stable troposphere by convective eddies in the troposphere. Two physical mechanisms were offered for the forcing of these waves. The first of these, the "mechanical oscillator mechanism," is associated with the action of the thermals in forcing oscillatory displacements of the isentropic surfaces at the bottom of the stable layer, which excite gravity waves that propagate upward. The second is the "obstacle mechanism," which is associated with the excitation of gravity waves by the obstruction that a convective element poses to the mean flow, in a manner somewhat analogous to the forcing of gravity waves by orography.

Clark et al. found that the obstacle effect was dominant in their simulations, but as Fovell et al. (1992) note, it is not clear that this would necessarily be the case for deep moist convection. Fovell et al. used a two-dimensional, compressible, mesoscale model to simulate idealized squall-line convection. In their simulation, waves propagated upward and primarily rearward relative to the storm. The primary reason for the bias towards rearward propagation appears to be the rearward tilt of the leading line of the storm. In addition, the simulated convective updrafts tended to propagate to the rear of the storm as new updrafts were generated at the leading edge. Fovell et al. used a simple linear model of a

mechanical oscillator to show that their results were consistent with the mechanical oscillator hypothesis. The momentum flux convergence associated with the simulated waves in the stratosphere was found to be sufficiently large (approximately -0.2 Pa) to have a significant effect on the mean flow (-20 m s^{-1} day^{-1}) in the vicinity of the storm, if the flux decayed to zero in the layer between 16 km and 26 km.

Alexander et al. (1995) performed a similar simulation to that of Fovell et al. Alexander et al. noted that the spectrum of the simulated waves had a broad peak for wavelengths between 10 and 100 km, which includes waves shorter than those simulated by Fovell et al. because Fovell et al. used excessive computational diffusion, damping the shorter waves. The bias towards rearward wave propagation is also prevalent in the simulation of Alexander et al., with forward propagation of waves only occurring near the beginning of the simulation, before the storm's updraft has tilted. Alexander et al. used a plot of spectral power as a function of frequency and horizontal wavenumber to identify the 16 km vertical wavelength of the simulated storm's diabatic heating as an important source of the waves in their simulation, by processes similar to those studied by Nicholls et al. (1991) and Pandya et al. (1993). Alexander et al. also found the mechanical oscillator effect to be an important mechanism in their simulation.

To investigate the possible effects of convectively generated gravity waves on the QBO, Alexander and Holton (1997) simulated a West African squall line. The line produced vertically propagating gravity waves, similar to those simulated by Fovell et al. and Alexander et al. Alexander and Holton used two shear profiles in the stratosphere, corresponding to easterly and westerly phases of the QBO, to estimate how much effect the waves have on the mean flow. They found that the waves were absorbed, depositing their momentum as they encountered critical levels at which their phase speed matched the speed of the mean flow. The acceleration of zonal wind due to this momentum deposition was found to be a significant percentage of the acceleration needed to cause the QBO.

Holton and Alexander (1999) used a simulation similar to those of Fovell et al. and Alexander et al., except with an extremely high upper boundary (90 km) to estimate the effects of convectively generated gravity waves on the mesosphere. As the waves propagated to mesospheric heights, they increased in amplitude until breaking, in a process similar to that described by Lindzen (1981). The mean flow of the model mesosphere was

found to incur large accelerations due to these breaking waves, with the westerly flow strengthening east of the storm, and weakening west of the storm.

Pandya and Alexander (1999) compared the moist, fully nonlinear two-dimensional simulation of Alexander et al. to linear and "dry quasi-linear" simulations of the same phenomenon. The quasi-linear simulation was a dry simulation that was driven by the pattern of latent heating and cooling produced by the nonlinear simulation, and then dividing the amplitude of the heating by 1000 so that the amplitude of the resulting waves would be small, and behave in an approximately linear fashion. After the simulation, the vertical velocity field produced by the quasi-linear simulation was then multiplied by 1000 and compared to the nonlinear simulation. The spatial pattern of the normalized vertical velocity field produced by the quasi-linear simulation was similar to that of the nonlinear simulation, but the amplitude of the quasi-linear simulation's waves was considerably higher. The horizontal wavelength spectra of the vertical velocity fields produced by the nonlinear, quasi-linear, and linear runs were qualitatively similar, although the quasi-linear and linear spectral distributions were more strongly peaked at lower wavelengths. Pandya and Alexander also investigated the effects of adding a low-stability layer in the upper troposphere (as a proxy for the thunderstorm anvil) to the linear simulation, and found that it prevented many of the waves from propagating into the stratosphere.

Lane et al. (2001) used a three-dimensional mesoscale model to simulate "Hector" multicell convection over the Tiwi Islands of Australia. Plots of vertical velocity in the horizontal plane revealed concentric ring patterns similar to those observed in Dewan et al. (1998). The waves simulated by Lane et al. were found to be quite monochromatic, with a horizontal wavelength of about 17 km. Lane et al. derived a gravity wave source tensor (see Chapter 6) to analyze the physical cause of the waves. The momentum flux convergence associated with the waves in the Lane et al. simulation was quite small, causing accelerations on the order of 0.05 m s^{-1} day^{-1}. In their simulation, the mechanical oscillator effect appears to have been the most important cause for the waves, with shear and diabatic heating being unimportant to the generation of gravity waves.

Piani et al. (2000) also used a three-dimensional model to simulate Hector convection, but focused on the effects of convectively forced waves on the QBO, in a manner similar to Alexander and Holton (1997). As in the study of Alexander and Holton (1997), Piani et

al. found that the gravity waves triggered by squall lines may account for a significant percentage of the mean-flow forcing required to drive the QBO. They estimated the number of similar storms that exist in the tropics from an observational study (Mohr and Zipser 1996), and found that they may be responsible for accelerations of approximately -0.12 m s^{-1} day^{-1} for the westerly phase of the QBO, and 0.04 m s^{-1} day^{-1} for the easterly phase. These values would account for approximately 30% of the forcing required for the westerly phase, and 15% for the easterly phase.

In this chapter, we have examined previous simulations of convectively generated gravity waves. Although many of these simulations were made with similar models and initial conditions, the focus of each study was somewhat different. In the next chapter, we will give a brief review of the observed and simulated characteristics of squall lines.

Chapter 4: Squall lines

Although this chapter is not intended to be a detailed examination of squall-line simulations, some background on the general characteristics of squall lines is in order. Squall lines are a type of MCS (mesoscale convective system) that are defined by Bluestein (1993) as having radar echoes that are "at least 5 times long as wide, at least 5-10 km wide, and persist for hours." Squall lines can be distinguished from MCCs (mesoscale convective complexes) by the fact that MCCs are convective systems that are roughly circular.

Although the stratiform precipitation associated with squall lines can trail, lead, or be parallel to the convective precipitation with respect to the storm motion (Parker and Johnson 2000), the trailing stratiform case is the most widely studied and best understood in terms of its dynamics. Therefore, we will focus on this type of squall line.

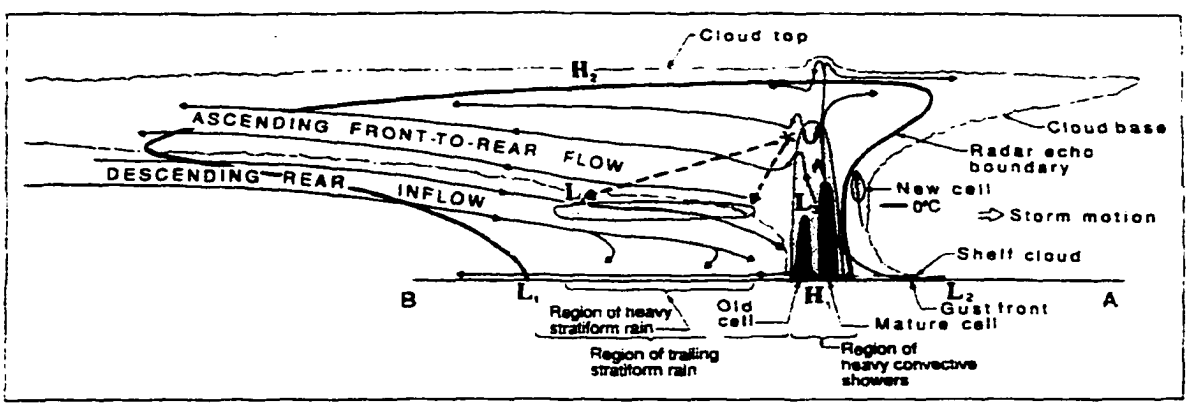

Fig. 4.1. Cross-section of a trailing stratiform squall line taken from Houze et al. (1989). See Fig. 4.2 for possible orientations of the cross-section.

Figure 1 shows a schematic diagram of a cross-section through such a squall line taken from Houze et al. (1989). The cross-section for Fig. 4.1 can be through either a symmetric or asymmetric squall line, as seen in Fig. 4.2, taken from Houze (1993). Near and slightly ahead of the gust front, air ascends rapidly. The convective towers at the front of the line

produce the most intense (often >25 mm/hr) precipitation in the line. Particularly strong updrafts can be associated with overshooting cumuliform cloud tops that are higher than the surrounding cirriform anvil. As the squall line progresses, new cells form near the front of the line as older cells progress rearward in the storm's frame of reference. A large (often on the order of 100 km) stratiform anvil trails behind this convective region. The precipitation in this area of the squall line is typically less intense than that of the convective region, but it can account for comparable amount of precipitation, since it covers a much larger area. The ascending front-to-rear flow is the source of the stratiform anvil and precipitation, and comes from the rearward advection of ice crystals from the convective towers. As Houze (1993) shows in Fig. 4.2, the descending rear inflow (also known as the "mesoscale downdraft") could be associated with a wind-shift line (in the case of a symmetric line), or with one branch of a mesoscale vortex (in the case of an asymmetric line).

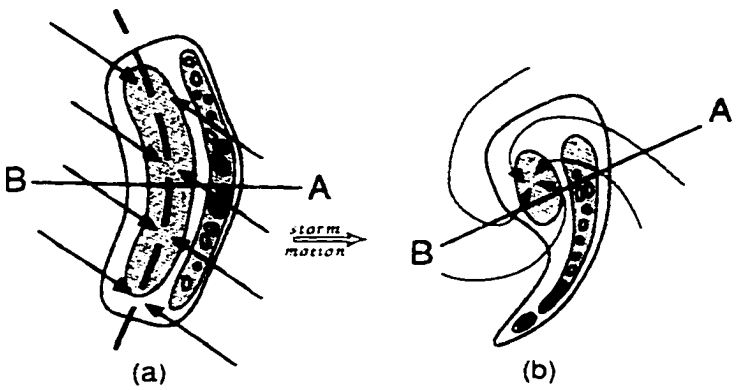

Fig. 4.2. Two possible cross-sections for Fig. 4.1: a) A symmetric system; b) An asymmetric system with a mid-level mesoscale vortex. Taken from Houze (1993).

One of the interesting aspects of squall lines is their persistence. While typical single-cell thunderstorms have lifetimes on the order of an hour or so, squall lines typically last for 6-12 hours. One explanation for this behavior is the formation of a "cold pool" by the evaporation of precipitation falling into unsaturated air. The layer of unsaturated air through which the precipitation falls through is larger in the trailing stratiform area. A schematic diagram of a cold pool is shown in Fig. 4.3. The cold pool spreads ahead of the precipitation itself, and the "head" of the cold pool is generally coincident with the gust front of a squall line. As the cold pool continues to propagate into a favorable environment (i.e., one with sufficient CAPE to support convection), new convective cells are triggered

at the front of the cold pool, and older cells propagate rearward, as seen in Fig. 4.1. It should be noted, however, that cold thunderstorm outflows are by no means unique to squall lines.

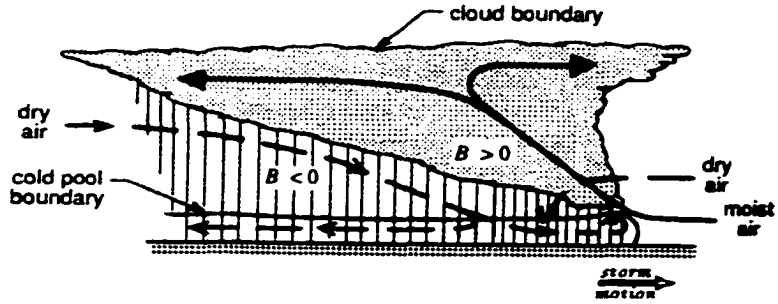

Fig. 4.3. Schematic diagram of a trailing-line squall line, featuring the cold pool and rear inflow jet. Taken from Houze (1993).

The rear-descending inflow is a mass source for the cold pool, and also maintains the area of unsaturated air behind the convective line by warming it adiabatically, as seen in Fig. 4.3. The formation of this descending air is due to the cooling caused by melting of frozen hydrometeors in the stratiform region.

A further explanation for the persistence of squall lines has been offered by Rotunno et al. (1988), or RKW, as well as Weisman (1992). The RKW theory involves the y-component of the two-dimensional (x, z) vorticity equation, given in Houze (1993) by

$$\frac{\partial \zeta}{\partial t} + u\frac{\partial \zeta}{\partial x} + w\frac{\partial \zeta}{\partial z} = -\frac{\partial B}{\partial x}. \tag{4.1}$$

Here the vorticity ζ is defined by

$$\zeta = \frac{\partial u}{\partial z} - \frac{\partial w}{\partial x}, \tag{4.2}$$

and B represents buoyancy, or

$$B = g\left[\frac{\theta_v'}{\theta_{v0}} - \frac{c_v}{c_p}\frac{p'}{p_0} - q_H\right], \tag{4.3}$$

where θ_v' and θ_{v0} represent the perturbation and base-state virtual potential temperature, and q_H represents the mixing ratio of all hydrometeors combined. An example of the vorticity generation in (4.1) can be visualized by picturing a "bubble" of warm dry air, neglecting pressure effects, as shown in Fig. 4.4.

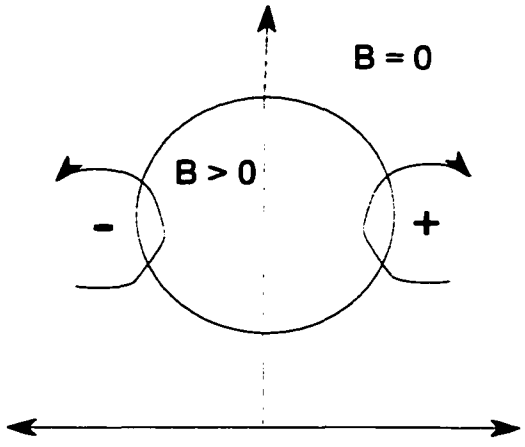

Fig. 4.4. A warm bubble of air is buoyant, causing negative and positive horizontal vortices to form on the left and right edges of the bubble, respec-

The amount of wind shear required to balance a cold pool was calculated by RKW by integrating (4.1) for a Boussinesq atmosphere over an area bounded by $x = L$ on the left, $x = R$ on the right, and from the ground to some level $z = d$. If the case where the cold air is stagnant relative to the edge of the cold pool, and restricted to a height H, with $H<d$, the integral reduces to

$$\Delta u = C, \tag{4.4}$$

where Δu is the difference in the horizontal velocity between $z = d$ and the ground, i.e.,

$$\Delta u = u_{R,d} - u_{R,0}, \tag{4.5}$$

and C^2 is the vertical integral of the negative buoyancy associated with the cold pool, defined by

$$C^2 = 2\int_0^H (-B_L)dz. \tag{4.6}$$

The essence of RKW theory is that long-lived squall lines are a result of favorable combinations of horizontal vorticity (due to both environmental and storm-induced shears) that result in vertically oriented updrafts, as seen in Fig. 5d. RKW call this state optimal, and it is typified by the creation of large-amplitude (as measured by maximum vertical velocity) new cells at the edge of the cold pool. However, Parker (1999) notes that many observed long-lived squall lines are not associated with the low-level shear necessary for these updrafts, and correspond more closely to Fig. 5b.

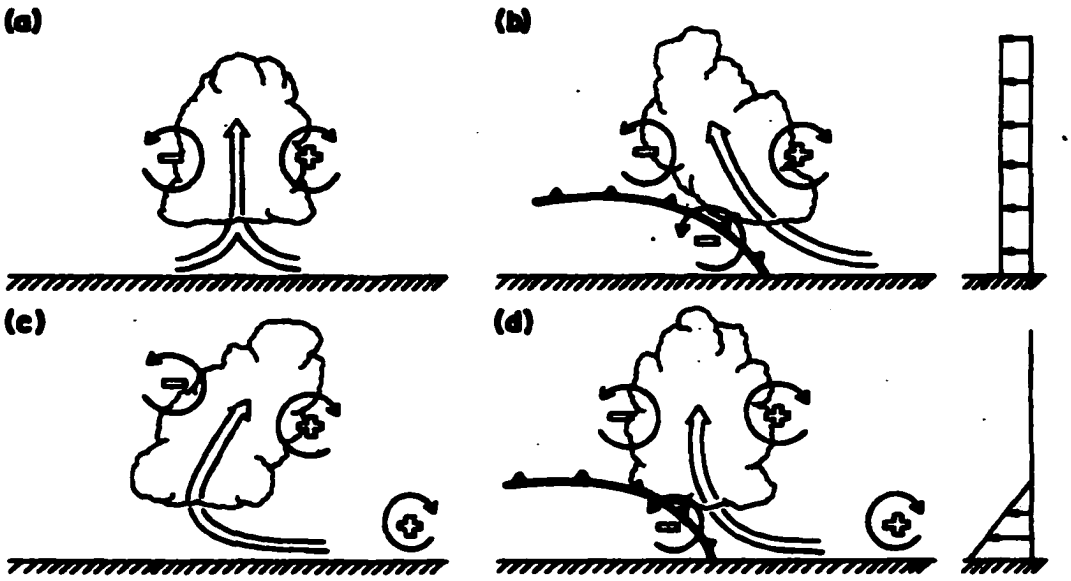

Fig. 4.5. Schematic diagram depicting the influence of ambient wind shear and/or a cold pool on a buoyant updraft. a) The lack of shear or a cold pool is associated with a vertical updraft. b) The presence of a cold pool causes the updraft to tilt upshear. c) The presence of ambient wind shear causes the updraft to tilt downshear. d) The presence of a cold pool that balances the ambient wind shear (see (4.4)) allows for long-lived convection. Taken from Rotunno et al. (1988).

Weisman (1992) found that numerically simulated squall lines tend to evolve through three of the states depicted in Fig. 4.5. The updrafts initially tilt upshear, in response to the ambient wind shear. This condition is equivalent to $\Delta u > C$, since there is no cold pool at the initial stage of convection. As precipitation begins to fall from the squall line, the cold pool strengthens, and its vorticity comes into balance with that of the ambient shear. As the cold pool continues to strengthen, $\Delta u < C$, and the updraft leans downshear. In an extension of RKW theory, Weisman (1992) found that environments with high CAPE and high environmental shear support rear-inflow jets that are located near the top of the cold pool at its head, maintaining the erect updrafts that characterize the optimal state for long periods of time. Environments with weak or moderate shear and CAPE are associated with rear-inflow jets that are located near the surface at the head of the cold pool, causing the cold pool to become shallower and the convection to tilt further upshear.

The ability of a two-dimensional model to realistically simulate squall-line convection is a subject of some debate. Clearly, in the case of asymmetric squall lines, a two-dimensional (2D) model will be inadequate, since the asymmetry takes place in the y-direction, which a 2D model does not recognize. Even in the case of symmetric squall lines, the con-

vection clearly does not extend to "infinity" in the y-direction, and a 2D model will be unable to resolve phenomena such as bow echoes. However, many of the gross characteristics of squall lines, such as those illustrated in Fig. 1 have been simulated well by 2D models (Nicholls 1987, Fovell and Ogura 1988, Nicholls et al. 1988, Lucas et al. 2000). The computational expense involved in realistically simulating a squall line (or any mesoscale phenomenon with explicitly simulated convection, for that matter) is quite large, particularly if one wishes to include stratospheric layers in the model, such as in this study. Therefore, we will use two dimensions, keeping in mind that convection is a three-dimensional process in nature, and that future research should focus on extending these results to three dimensions. In the following chapter, we will discuss the simulations that were performed for this work in more detail, and demonstrate that they possess similar characteristics to observed squall lines.

Chapter 5: Simulations

The simulations performed in this study have been designed in order to test the sensitivity of the waves generated by convection to changes in the tropospheric shear, convective available potential energy (CAPE) and type of initial sounding (tropical versus mid-latitude). In addition, two runs were performed to examine the effects of the generated waves on stratospheric shear layers. Also, the effects of microphysics were tested by performing one simulation without ice microphysics. Table 1 lists the run names, types, tropospheric and stratospheric shears and CAPE associated with each run that will be examined.

There are a myriad of possible sensitivity experiments that could have been performed in this work. The choices of the parameters that were adjusted among the experiments listed above are partially motivated by a desire to correlate the strength of the convection to the strength of the waves, which was addressed by adjusting the CAPE, and the type (tropical versus mid-latitude) of convection. Also, the amount of tropospheric shear has been shown to be important to the net momentum flux (Kershaw 1995) and the shape of the momentum flux spectrum (Pfister et al. 1993). The "WK calm" simulation was specifically chosen to illustrate that the net momentum flux (zero in this case) is not an appropriate measure of the ability of convectively generated waves to change the mean flow above the convection. In addition, ice microphysical processes can be important to the evolution of convective clouds (Emanuel 1994), so the "WK no ice" simulation provides a test of the importance of these processes in the generation of waves. The process of critical level absorption is illustrated by introducing shear layers into the stratosphere, which is similar to what Alexander and Holton (1997) and Piani et al. (2000) have done.

Table 1: Simulations performed

run name	moisture	trop. winds	strat. shear	CAPE
WK control	$q_{v0} = 15$	$U_S = 15$ m s^{-1}	None	2650 J kg^{-1}
WK no ice	$q_{v0} = 15$	$U_S = 15$ m s^{-1}	None	2650 J kg^{-1}
WK high CAPE	$q_{v0} = 16$	$U_S = 15$ m s^{-1}	None	3003 J kg^{-1}
WK low CAPE	$q_{v0} = 14$	$U_S = 15$ m s^{-1}	None	2085 J kg^{-1}
WK calm	$q_{v0} = 15$	$U_S = 0$ m s^{-1}	None	2650 J kg^{-1}
WK low trop. shear	$q_{v0} = 15$	$U_S = 10$ m s^{-1}	None	2650 J kg^{-1}
WK high trop. shear	$q_{v0} = 15$	$U_S = 20$ m s^{-1}	None	2650 J kg^{-1}
WK easterly strat. shear	$q_{v0} = 15$	$U_S = 15$ m s^{-1}	-30 m s^{-1} / 10 km	2650 J kg^{-1}
WK westerly strat. shear	$q_{v0} = 15$	$U_S = 15$ m s^{-1}	30 m s^{-1} / 10 km	2650 J kg^{-1}
TC control	observed	observed	None	2210 J kg^{-1}
TC no jet	observed	mod. observed	None	2210 J kg^{-1}

The runs denoted "WK" are based upon the thermodynamic and wind shear soundings prescribed in Weisman and Klemp (1982). The vertical profile of potential temperature in the WK sounding is given by

$$\theta_0(z) = \begin{cases} \theta_s + (\theta_{tr} - \theta_s)\left(\dfrac{z}{z_{tr}}\right)^{5/4}, & z \le z_{tr} \\ \theta_{tr}\exp\left[\dfrac{g}{c_p T_{tr}}(z - z_{tr})\right], & z > z_{tr} \end{cases} \quad (5.1)$$

where θ_s is the surface potential temperature, θ_{tr}, z_{tr}, and T_{tr} are the potential temperature, height and air temperature at the tropopause, respectively. Consistent with WK, we set θ_s to 300 K, θ_{tr} to 343 K, z_{tr} to 12 km, and T_{tr} to 213 K. The vertical profile of moisture in the WK sounding is specified in terms of relative humidity as

$$RH(z) = \begin{cases} 1 - \frac{3}{4}\left(\frac{z}{z_{tr}}\right)^{5/4}, & z \le z_{tr} \\ 0, & z > z_{tr} \end{cases} . \tag{5.2}$$

Note that Weisman and Klemp (1982) actually specify a relative humidity of 25% in the stratosphere, but the saturation water vapor ratio for $T = 213$ K is so small that this amount of moisture should have a negligible effect on the dynamics of the stratosphere. When the stratosphere is initialized as being completely dry, the detection of any moisture that does make its way into the stratosphere is straightforward.

The relative humidity specified by (5.2) implies that mixing ratios exist near the surface that would yield values of CAPE that are far too high (>5000 J kg^{-1}) to be realistic for all but the most severe convective events. Weisman and Klemp (1982) note that there is typically a mixed layer (caused by dry convection in the boundary layer) near the surface, and they assume a constant water vapor mixing ratio q_{v0} from the surface upwards to the point at which q_{v0} would be greater than the value given by (5.2). Above this point, the values from (5.2) are used. Weisman and Klemp do not modify the profile of θ_0 within the mixed layer, despite the fact that both θ_0 and q_v are normally well-mixed throughout the height of a convective boundary layer (Stull, 1988). In our simulations, we chose to use an average value of θ_0 for the mixed layer. The soundings associated with the WK runs are shown in Fig. 5.2, which is a skew T diagram taken from Weisman and Klemp (1982). The temperature, moisture and wind fields used in the TC control run are shown in Fig. 5.4

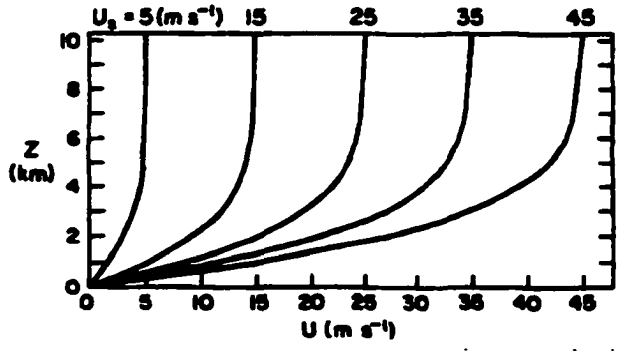

Fig. 5.1. Wind profiles defined in (5.3) for different values of U_S. Taken from Weisman and Klemp (1982).

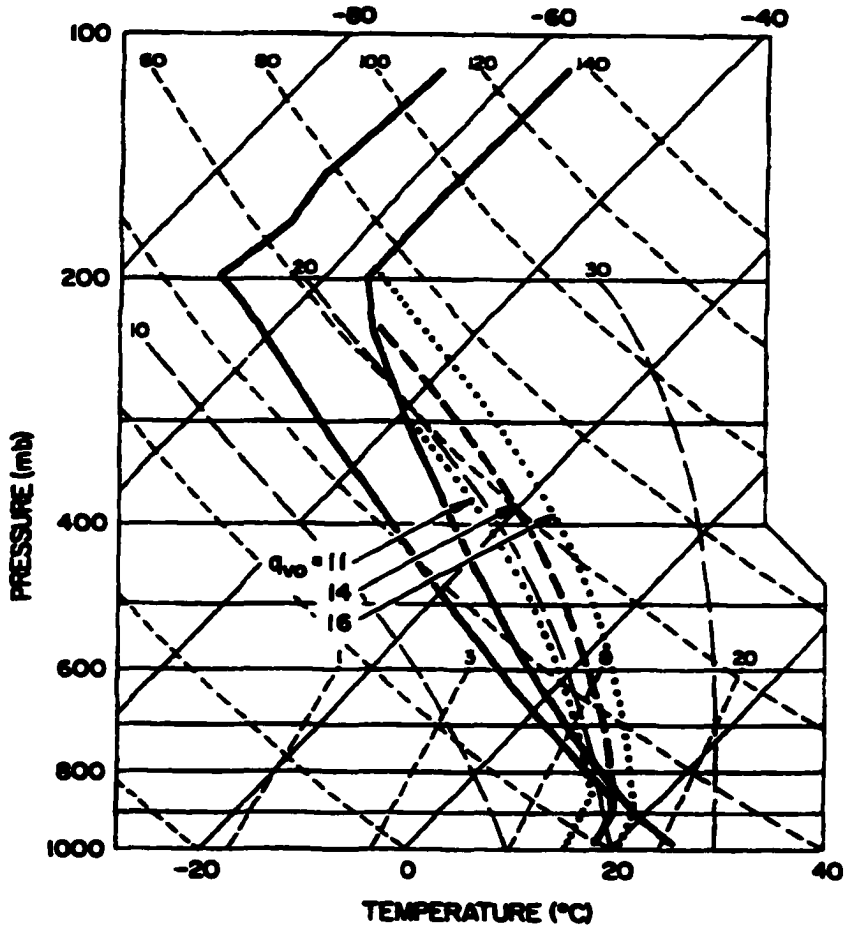

Fig. 5.2. Skew T diagram representing the temperature and moisture profiles used in the WK experiments in this study taken from Weisman and Klemp (1982). The thick solid lines represent the dewpoint temperature (left) and temperature (right profiles of the initial soundings, with the modifications listed in the text. The isotherms are tilted thin solid lines, short dashed lines are adiabats, and long dashed lines are moist adiabats. The thick dotted and dashed lines represent parcel ascents from the surface based on different values of q_{v0} (see text).

The tropospheric wind profiles used in the WK simulations were prescribed by an analytic function used by Weisman and Klemp (1982),

$$u_0(z) = U_S \tanh\left(\frac{z}{z_S}\right). \tag{5.3}$$

This profile exponentially approaches U_S with a characteristic scale of z_S. The values of U_S used are shown in Table 1, while the parameter z_S was set to 3 km. This caused most of the shear to be confined to the lowest 3 km of the atmosphere (see Fig. 5.1), which is consistent with the statement by Rotunno et al. (1988) that strong low-level shear is neces-

sary for long-lived squall lines. The winds associated with the TC control run are shown in Fig. 5.4, and correspond to a westerly jet, which is commonly observed with tropical squall lines (Jorgensen et al. 1997). The winds in the TC no jet run are identical up to the jet maximum, but remain constant above this level. This is comparable to a WK profile with $U_S = 12$ m s^{-1}.

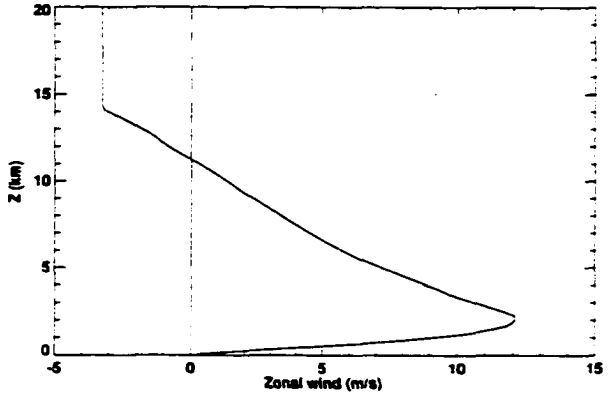

Fig. 5.3. Initial wind profile used in the TC control run.

The horizontal boundary conditions for all of the simulations in this study are periodic. This is equivalent to simulating a train of two-dimensional squall lines spaced at a distance corresponding to the width of the domain apart. This makes the domain width a "special" scale, without physical significance. However, it prevents non-physical wave reflections from the side boundaries from contaminating the results, and allows for straightforward interpretations of zonal-mean budget quantities.

The CAPE can be defined in a variety of ways, but the definition we will use is given by Emanuel (1994) as

$$CAPE = \int_{LFC}^{EL} R_d (T_\rho^{parcel} - T_\rho) d(\ln p). \tag{5.4}$$

Here, T_ρ is the density temperature, related to the conventional temperature T by

$$T_\rho = T\left(\frac{1 + q_v/\varepsilon}{1 + q_T}\right). \tag{5.5}$$

As Emanuel (1994) notes, T_ρ can be thought of as "the temperature that dry air would have to have to yield the same density as moist, cloudy air" at temperature T. Here, the

Z (m)	U ($m\ s^{-1}$)	V ($m\ s^{-1}$)	θ (K)	Q ($g\ g^{-1}$)	P (Pa)
35.5	−0.03	−6.50	299.413	0.199×10^{-1}	100202.7
110.3	0.75	−6.50	299.653	0.196×10^{-1}	99363.9
192.9	1.61	−6.50	299.917	0.193×10^{-1}	98439.7
285.7	2.57	−6.50	300.214	0.190×10^{-1}	97412.9
391.4	3.67	−6.50	300.552	0.186×10^{-1}	96268.3
512.2	4.93	−6.50	300.939	0.182×10^{-1}	94959.8
650.2	6.36	−6.50	301.381	0.177×10^{-1}	93464.5
807.4	7.77	−6.39	301.941	0.169×10^{-1}	91789.1
985.5	8.91	−6.03	302.689	0.156×10^{-1}	89945.3
1186.1	10.19	−5.63	303.531	0.142×10^{-1}	87869.3
1410.4	11.05	−5.12	304.377	0.132×10^{-1}	85622.1
1659.7	11.75	−4.52	305.275	0.125×10^{-1}	83158.5
1934.8	12.04	−4.00	306.450	0.118×10^{-1}	80524.1
2236.6	12.10	−3.52	307.839	0.111×10^{-1}	77680.3
2565.7	11.47	−3.18	309.668	0.104×10^{-1}	74724.6
2922.4	10.76	−2.86	311.700	0.962×10^{-2}	71604.6
3306.9	10.01	−2.58	313.941	0.880×10^{-2}	68354.7
3719.2	9.35	−2.41	316.415	0.806×10^{-2}	65020.9
4159.1	8.65	−2.24	318.727	0.718×10^{-2}	61630.5
4626.2	7.82	−2.05	321.081	0.640×10^{-2}	58188.1
5120.0	7.01	−1.78	323.772	0.561×10^{-2}	54723.0
5639.7	6.18	−1.39	326.370	0.489×10^{-2}	51262.2
6184.2	5.48	−1.13	329.158	0.419×10^{-2}	47829.4
6752.5	4.80	−0.80	332.113	0.340×10^{-2}	44448.8
7343.3	4.11	−0.44	335.148	0.269×10^{-2}	41166.0
7954.8	3.45	−0.04	337.919	0.202×10^{-2}	37975.3
8585.5	2.76	0.47	340.509	0.145×10^{-2}	34889.2
9233.4	2.02	0.89	343.037	0.101×10^{-2}	31920.6
9896.4	1.42	1.42	345.351	0.641×10^{-3}	29113.7
10572.2	0.74	1.83	346.909	0.403×10^{-3}	26444.8
11258.2	−0.01	2.20	348.215	0.228×10^{-3}	23917.0
11951.8	−0.80	2.48	349.504	0.477×10^{-4}	21569.9
12650.1	−1.42	2.84	350.900	0.100×10^{-4}	19373.1
13400.1	−2.25	3.39	352.040	0.100×10^{-5}	17209.5
14150.1	−3.24	4.08	352.680	0.100×10^{-5}	15226.0
14900.1	−3.24	4.08	354.960	0.100×10^{-5}	13421.1
15650.1	−3.24	4.08	358.180	0.100×10^{-5}	11783.7
16400.1	−3.24	4.08	363.341	0.100×10^{-5}	10312.2
17150.1	−3.24	4.08	377.021	0.100×10^{-5}	9006.9
17900.1	−3.24	4.08	386.421	0.100×10^{-5}	7860.9
18650.1	−3.24	4.08	400.521	0.100×10^{-5}	6850.3
19400.1	−3.24	4.08	414.621	0.100×10^{-5}	5968.3
20150.1	−3.24	4.08	428.721	0.100×10^{-5}	5194.1
20900.1	−3.24	4.08	442.821	0.100×10^{-5}	4517.6

Fig. 5.4. Initial sounding used in the TC control run. Note that only the u-component of wind was used, and an isothermal, dry stratosphere was assumed to exist above 19 km. Taken from Redelsperger et al. (2000).

quantity ε represents the ratio of the dry air and water vapor gas constants, $\varepsilon = R_d/R_v$. The total mixing ratio of water vapor and cloud condensate is given by q_T. The quantity T_ρ^{parcel} denotes the density temperature that a parcel would obtain if lifted dry-adiabatically to its lifted condensation level, and then moist-adiabatically to its level of free convection (LFC). The LFC is the point at which cloudy parcels are more buoyant than the surrounding environment, and continue to rise pseudoadiabatically until their equilibrium level (EL) is reached. The LFC and EL are the points at which the parcel ascents (indicated by thick dotted and dashed lines) in Fig. 5.2 intersect the temperature profile. Note that the CAPE values in Table 1 are based on parcels lifted from the surface. For the WK runs, a similar amount of CAPE is associated with parcels lifted from the lowest 1 km of the model domain, while the CAPE associated with the TC runs falls off more quickly with height, as shown in Fig. 5.5. Also shown is the reversible CAPE, which accounts for the effects of precipitation loading. Due to the more humid atmosphere associated with the TC runs, the reversible CAPE is smaller as a percentage of the pseudoadiabatic CAPE than in the WK runs.

The physical grid extended 32 km in the vertical in all of the simulations. The horizontal and vertical grid spacing in the simulations were set to constant values of 1000 m and 250 m, respectively for the WK runs, and the domain extended 900 km in the horizontal. The horizontal grid spacing in the TC runs was 500 m, following Nicholls et al. (1988), who found that very fine resolution in the horizontal was necessary to simulate tropical squall lines in 2-D. The horizontal grid extent of the domain in the TC runs was 600 km. A stretched grid in the vertical was used in the lowest 2500 m of the TC runs, which is consistent with the guidance of Redelsperger et al. (2000), who noted that the cold pool associated with this convective system is quite shallow. The grid spacing in the TC runs ranged from 71 m near the surface to a constant value of 258 m above 2500 m. A Rayleigh sponge layer with a depth of 16 km was placed above $z = 32$ km in order to suppress wave reflections from the model top. A depth of at least one vertical wavelength is necessary to prevent reflections from the sponge layer (Klemp and Lilly 1978). The Rayleigh damping coefficient was set to a maximum value of 0.0125 s^{-1}, which it approaches smoothly using a profile similar to that of Klemp and Lilly (1978). This value of viscosity is consistent

with small values of reflectivity from the sponge layer. Using Klemp and Lilly's linear analysis, less than 5% of wave energy will be reflected from a sponge layer with this value of viscosity for waves with a wavelength of approximately 30 km (typical for our experiments). Experiments with half and double this value showed the simulations to be insensitive to the value of this parameter.

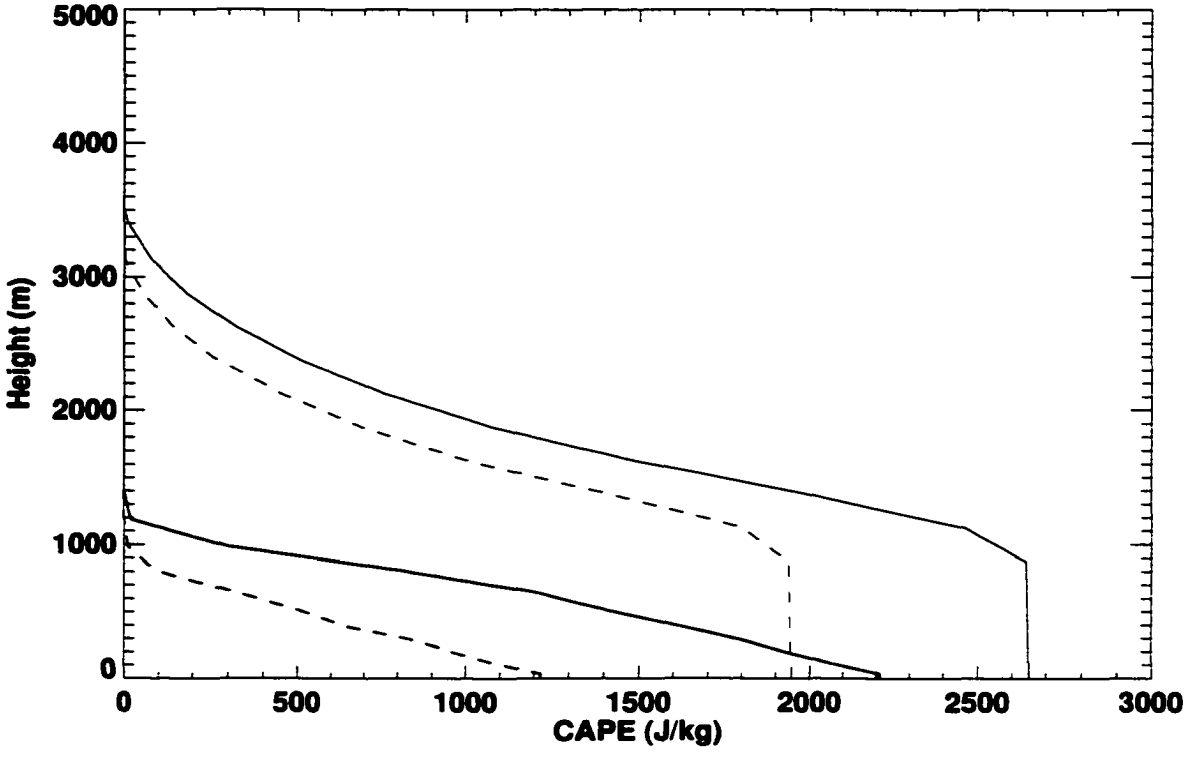

Fig. 5.5. Comparison of vertical profiles of pseudoadiabatic (solid) and reversible (dashed) CAPE, for the WK control (thin lines) and TC control (thick lines) runs. CAPE was calculated using code provided by K. Emanuel.

In addition to the large time step of 4 s over which most quantities were integrated, a smaller time step of 0.8 s was used for the acoustically active terms (pressure, momentum, and potential temperature). The sound waves were integrated implicitly in the vertical for the w and p equations. The temporal finite differencing was done using the second-order leapfrog scheme, with Robert-Asselin time filtering. The advection scheme used in all of the simulations is fourth-order accurate (Xue and Lin 2001) in space.

In nature and in numerical models, convection can be initiated in a number of ways. We will discuss two of the simpler methods to implement here. The first method is via a

buoyant "bubble" of warm air near the surface. The bubble ascends, carrying moist air from near the surface aloft with it, until condensation occurs. The second method is to place an area of anomalously cold air representing a preexisting cold pool or thunderstorm outflow near the surface. The cold, dense air associated with the cold pool will propagate horizontally, displacing warmer, lighter air that was next to the cold pool upwards. This has recently been illustrated in a simple model developed by Haertel et al. (2001), the results of which are shown in Fig. 5.6. If the air that has been forced upwards by the bubble or cold pool is buoyant enough, it will reach the level of free convection, and continue to rise pseudoadiabatically until its equilibrium level is reached.

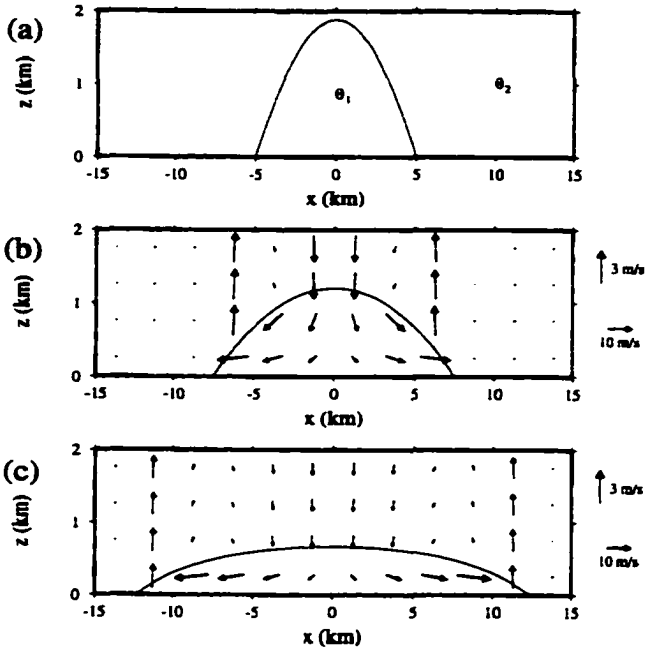

Fig. 5.6. Circulations associated with an idealized cold pool after a) 0 min, b) 5 min and c) 10 min. Taken from Haertel et al. (2001).

Between the two methods described above, the surface cold anomaly is probably more similar to how squall line convection is typically initiated in nature, although there are certainly many summertime "air mass" thunderstorms that erupt due to buoyant plumes, instead of along synoptic boundaries. All of the simulations listed in Table 1 used a surface cold anomaly to initiate convection, with the exception of the WK calm run, which required a bubble. Also, the TC runs were initiated using a cooling and drying tendency in the first 20 minutes of the simulation, as prescribed by Redelsperger et al. (2000).

To test the effects of the initiation mechanism on the evolution of the simulated convection, two experiments were performed with otherwise identical conditions. The first experiment initiated convection with a 2K elliptical, Gaussian (exponentially decaying away from the center) bubble that had a horizontal extent of 10 km and a vertical extent of 3 km. The bubble was centered at an altitude of 1.5 km. The second experiment used a -4K (constant value) half-ellipse of cold air, 40 km in horizontal extent and 1.5 km in height at the center of the ellipse.

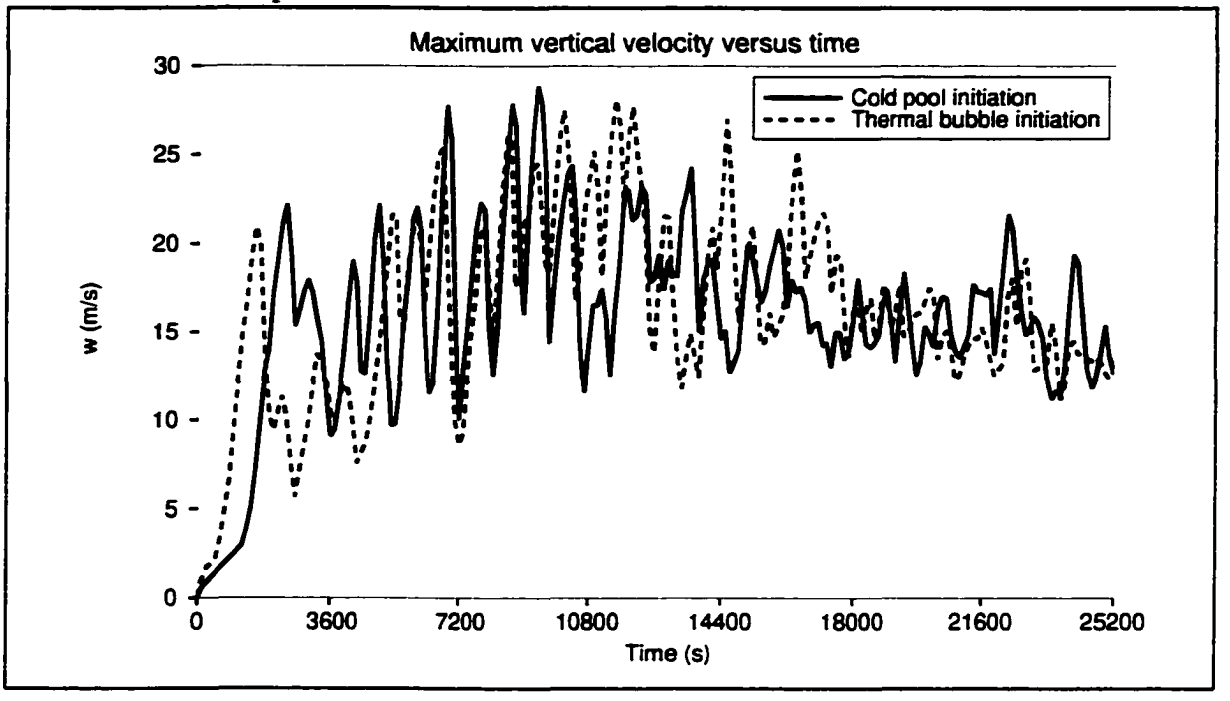

Fig. 5.7. Maximum vertical velocity (m s^{-1}) versus time for thermal bubble and cold pool initiations.

The behavior of the maximum vertical velocity with time for the two simulations is quite similar after the faster start of the bubble initiation, as shown below in Fig. 5.7. Both of these runs exhibit the large oscillations in maximum vertical velocity associated with new cell development, as described in Rotunno et al. (1988). The wave energy flux in the lower stratosphere also behaves similarly with time between the two simulations, as seen in Fig. 5.8. The cold pool run appears to produce a more constant value of wave energy flux after convection is initiated, but the values are similar between the two runs.

Another important factor in the simulation of convection is the microphysics scheme that is employed. For warm rain processes, ARPS uses a two-category (cloud liquid water (q_c) and rain (q_r)) scheme based on Kessler (1969). The implementation of this scheme

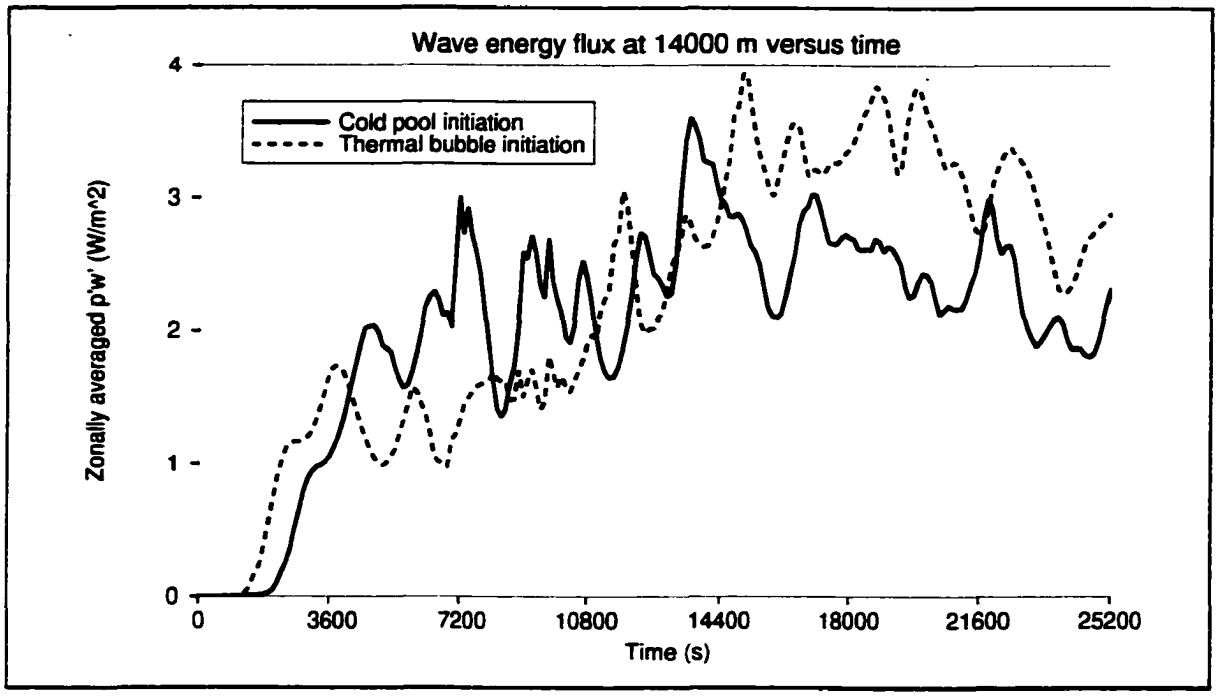

Fig. 5.8. Zonally averaged wave energy flux $\overline{p'w'}$ at 14000 m versus time for thermal bubble and cold pool initiations.

follows Klemp and Wilhelmson (1978) and Soong and Ogura (1973). ARPS uses a three-category (cloud ice (q_i), snow (q_s), and hail (q_h)) microphysics scheme for ice processes based on Lin et al. (1983). This scheme is implemented following Tao et al. (1989) and Tao and Simpson (1993). The source terms for the five species of condensate can be written as (Xue et al. 2001)

$$S_{q_c} = \rho(c - e_c) - T_{q_c}, \tag{5.6}$$

$$S_{q_r} = \rho(-e_c + m_s + m_h - f_s - f_h) - T_{q_r}, \tag{5.7}$$

$$S_{q_i} = \rho(d_i - s_i) - T_{q_i}, \tag{5.8}$$

$$S_{q_s} = \rho(d_s - s_s - m_s + f_s) - T_{q_s}, \tag{5.9}$$

$$S_{q_h} = \rho(d_h - s_h - m_h + f_h) - T_{q_h}. \tag{5.10}$$

The term denoted by c represents the rate of condensation of water vapor, which acts as a source for cloud liquid water. The rates of evaporation and sublimation are denoted by e, and s respectively, and act as sinks for the liquid and frozen species of cloud ice. Raindrops can be frozen into snow or hail, and these processes are represented by f. The

inverse process of hail and snow melting into raindrops is given by m. The rate of deposition of water vapor to ice is given by d. Finally, the transfer rates denoted by T represent processes such as collision-coalescence and are described by Lin et al. (1983).

Another important atmospheric process is radiation. However, radiation was not found to be important to the development of squall lines in the simulations featured in Redelsperger et al. (2000), perhaps due to the short lifetime and strong mesoscale forcing associated with such lines. Also, radiative damping is not believed to play a significant role in gravity wave damping for the waves simulated in these experiments, although it may have a significant effect for waves with short vertical wavelengths at altitudes greater than 50 km (Andrews et al. 1987). Radiation was not employed in this study.

The surface physics used in the model are described in Xue et al. (2001). For the WK experiments, we used constant drag coefficients for the parameterization of surface momentum and moisture fluxes. For the TC experiments, the drag coefficients were allowed to depend upon stability. This was employed due to the importance of accurately simulating the surface moisture flux in the tropical ocean environment of the observed TC storm.

As Alexander et al. (1995) noted, the amount of computational diffusion employed in a model can play a significant role in the gravity wave spectrum simulated by the model. Too much computational diffusion can lead to excessive damping of waves with wavelengths less than 20 km, as was observed in the Fovell et al. (1992) study. The computational diffusion used in all of the simulations of this study was a 4th-order derivative in the vertical and horizontal directions. The nondimensional 4th-order smoothing parameter S defined by

$$S = \frac{K\Delta t}{(\Delta x)^4} \tag{5.11}$$

was set to 0.015 by Fovell et al. (1992), while Alexander et al. used a value of $S = 0.005$ in their study. In this work, we use a value of $S = 0.001$, which should be sufficiently small for the effects of computational diffusion to be unimportant for all but the smallest-scale (i.e., $2\Delta x$, $2\Delta z$) waves. Pandya and Alexander (1999) note that the presence of clouds above the wave source causes most waves that have horizontal wavelengths of less

than 10 km to be trapped (see Chapter 13), so the resolution of these extremely short waves should be relatively unimportant.

Although the primary focus of this work will not be the cloud dynamics of the simulated storms themselves, we will examine a few fields of the WK control and TC control runs to verify that they have similar structures to observed squall lines (see Chapter 4). One quantity that is indicative of the vigor of convection is vertical velocity. In Fig. 5.9, the minimum and maximum vertical velocities for the WK control and TC control runs are shown. In this figure, we see that the WK control run experiences many large-amplitude new cells for a long period of the integration (until approximately $t = 7$ hours), corresponding to the optimal state discussed by Rotunno et al. (1988). However, the TC control run has an initial (first 1.5 hours) burst of a few large-amplitude new cells, followed by a long period of quasi-steady convection (until $t = 6.5$ hours), followed by more large-amplitude cells.

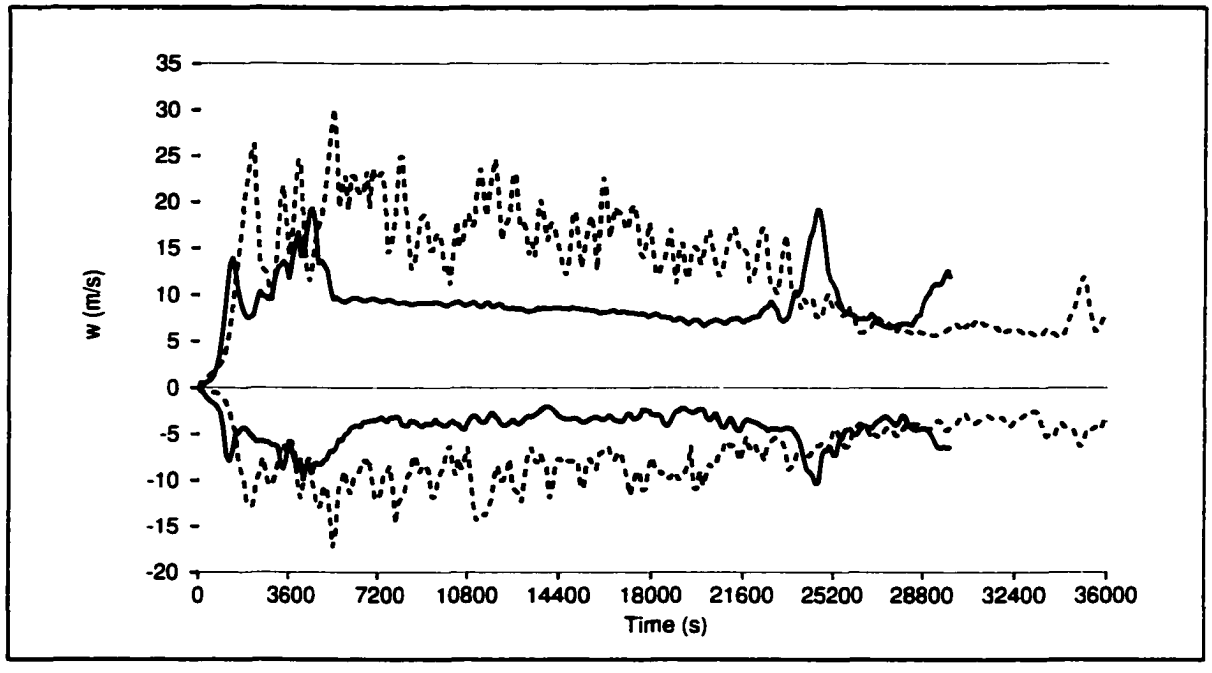

Fig. 5.9. Maximum and minimum vertical velocities in m s^{-1} as a function of time for the TC control (solid) and WK control (dashed) runs.

The vertical velocity fields near the most vigorous convection for the TC control and WK control runs are shown in Fig. 5.10 and Fig. 5.11, respectively. The simulated TC convection in Fig. 5.10a is quite shallow, only extending up to about 4 km at the leading edge. The convection is much deeper after the burst at $t = 7$ hours, as shown in Fig. 5.10b.

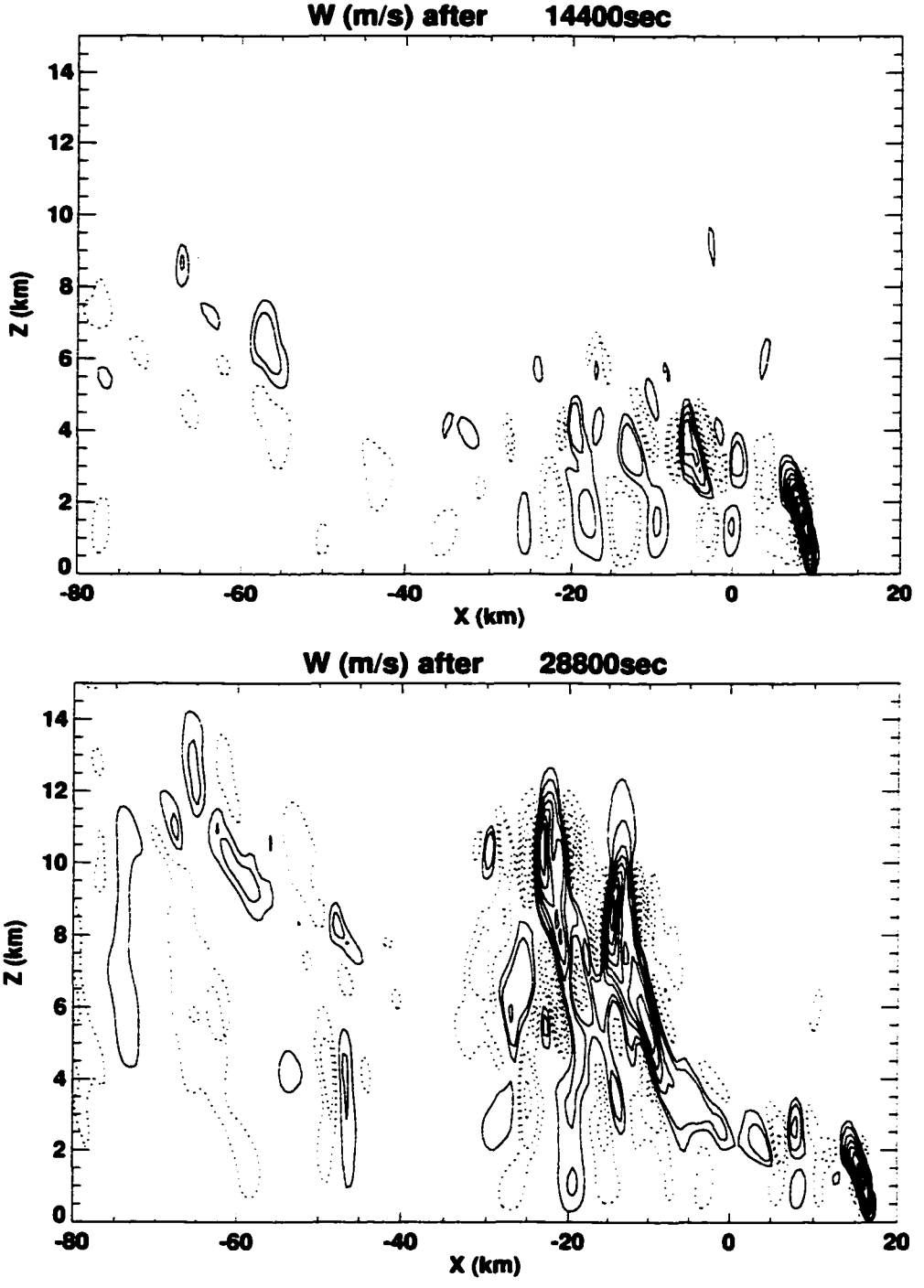

Fig. 5.10. Vertical velocity in the TC control run in the vicinity of the most active convection after a) four hours; b) eight hours.

This vertical velocity plot is qualitatively similar to that observed in Jorgensen et al. (1997) and simulated in Trier et al. (1996), with elevated vertical velocity maxima much

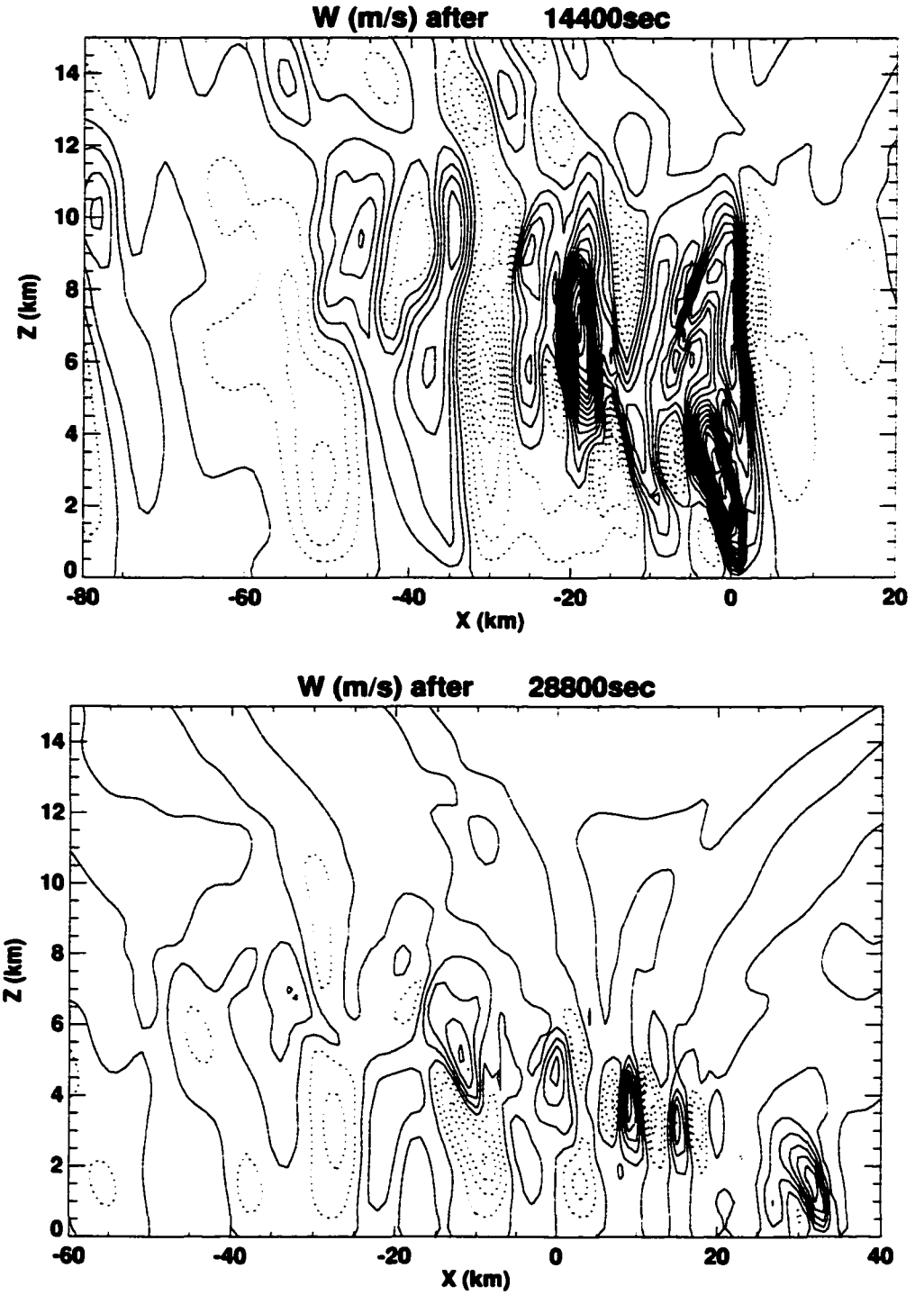

Fig. 5.11. Vertical velocity in the WK control run in the vicinity of the most active convection after a) four hours; b) eight hours.

higher and somewhat separated from the leading updraft, as shown in Fig. 5.12. The simulated WK convection in Fig. 5.11a is similar to the optimal state shown in Fig. 4.5d, with a

nearly vertical updraft. Note the rearward propagation of convective cells, similar to that shown in Fig. 4.1.

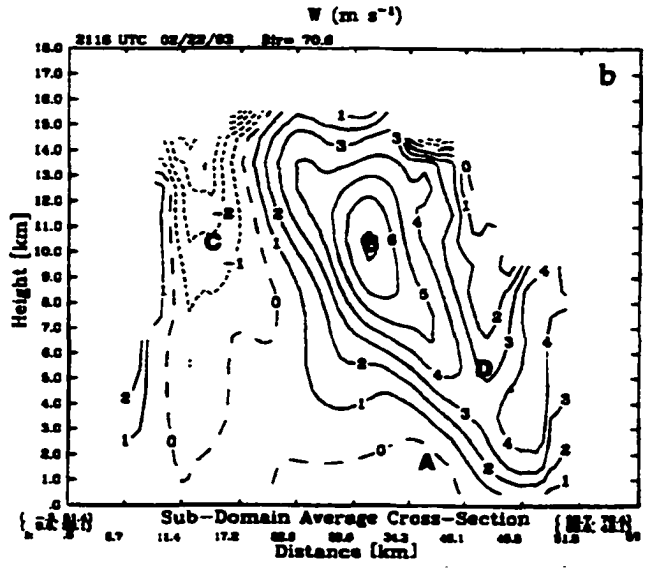

Fig. 5.12. Observed vertical velocity structure of the 22 Feb. TOGA-COARE squall line. Taken from Jorgensen et al. (1997). Horizontal distance is in the line-normal direction.

Another field that can be examined in association with mesoscale convective systems is diabatic heating. Houze (1982, 1989) noted the structure of heating in the convective region of tropical MCSs has roughly a half-wavelength sinusoidal shape in the vertical, which is associated with deep latent heating. The structure of heating in the stratiform region has a shape that is similar to a full-wavelength sine wave, corresponding to the effects of evaporative cooling beneath the trailing anvil, and latent heating in the anvil itself. In Fig. 5.13, we see that the WK control and TC control runs produced heating structures consistent with these observations. The convective region was defined as the region between x = -20 km and x = 20 km for the TC control run at t = 8 hours (see Fig. 5.10b), and between x = -20 km and x = 10 km for the WK run at t = 4 hours (see Fig. 5.11a). Similarly, the stratiform region in the TC control run was bounded by x = -50 km and x = -20 km for the WK run, and from x = -60 km to x = -20 km for the TC control run. These boundaries were chosen after examining the vertical velocity and cloud condensate fields, with the strongest vertical velocities and deepest clouds defined as convective regions, and the rearward anvil structures defined as stratiform regions. The stratiform

region actually extended further to the west in these simulations, but these boundaries are appropriate for the delineation between the two types of heating structure.

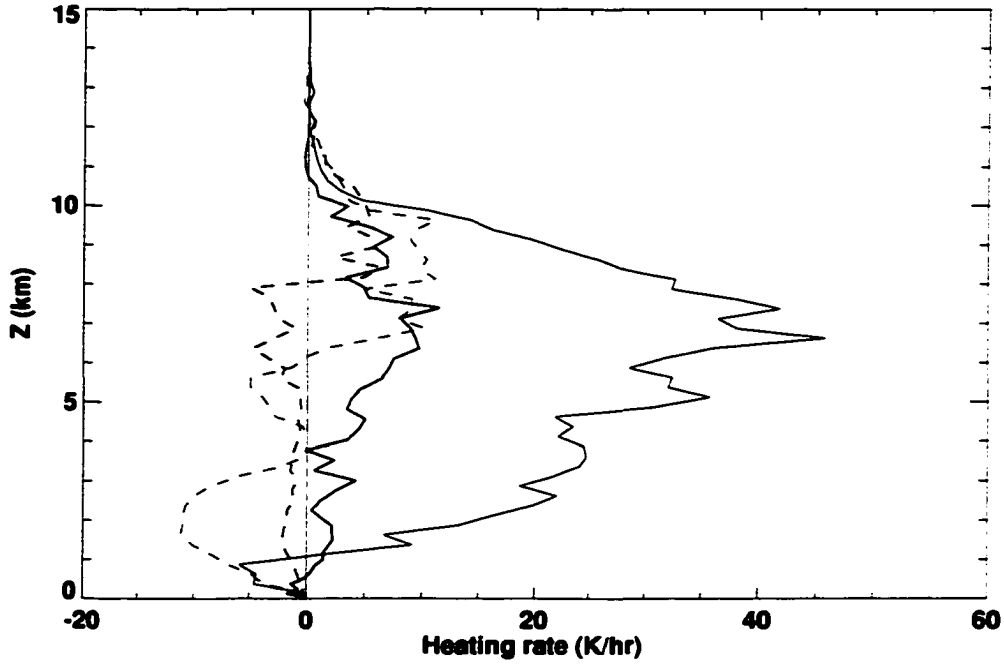

Fig. 5.13. Simulated vertical profiles of diabatic heating from the horizontal averages over the convective (solid lines) and stratiform (dashed lines) regions of the WK control (thin lines) and TC control (thick lines) runs after four and eight hours, respectively. See text for details.

In this chapter, we have examined the setup for the numerical experiments that were performed for this work, and confirmed that the simulated squall lines have similar characteristics to those found in nature. In the following chapters, we will use a variety of diagnostic techniques to examine what occurred in the troposphere and stratosphere of the simulations. This will begin with an examination of the gravity wave source defined by Lane et al. (2001).

Chapter 6: Gravity wave source

The purpose of this chapter is to summarize a derivation by Lane et al. (2001). The authors followed Lighthill's (1952) theory for the generation of sound and Ford's (1994) theory for the generation of shallow-water inertia-gravity waves. These theories grouped the linear terms that govern the motion of the waves of interest, and then considered the nonlinear terms as the sources of the waves. We start with the anelastic system of equations, neglecting Coriolis and viscous effects, and putting the linear terms on the left-hand side:

$$\frac{\partial u'}{\partial t} + u_0\frac{\partial u'}{\partial x} + v_0\frac{\partial u'}{\partial y} + w'\frac{du_0}{dz} + \frac{1}{\rho_0}\frac{\partial p'}{\partial x} = F_u, \tag{6.1}$$

$$\frac{\partial v'}{\partial t} + u_0\frac{\partial v'}{\partial x} + v_0\frac{\partial v'}{\partial y} + w'\frac{dv_0}{dz} + \frac{1}{\rho_0}\frac{\partial p'}{\partial y} = F_v, \tag{6.2}$$

$$\frac{\partial w'}{\partial t} + u_0\frac{\partial w'}{\partial x} + v_0\frac{\partial w'}{\partial y} + \frac{\partial}{\partial z}\left(\frac{p'}{\rho_0}\right) - b' = F_w, \tag{6.3}$$

$$\frac{\partial b'}{\partial t} + u_0\frac{\partial b'}{\partial x} + v_0\frac{\partial b'}{\partial y} + N^2 w' = \dot{b}' + F_b. \tag{6.4}$$

Here, we have separated the velocity into a vertically varying horizontal flow plus a perturbation,

$$\begin{aligned} u &= u_0(z) + u'(x, y, z, t) \quad , \\ v &= v_0(z) + v'(x, y, z, t) \quad , \\ w &= w'(x, y, z, t) \quad . \end{aligned} \tag{6.5}$$

In this dissertation, quantities that vary with height but not with time will have "0" subscripts, while quantities that are averaged, but allowed to vary in time (e.g., zonal means) will have an overbar. Note that the perturbation velocities are not necessarily small in amplitude compared to the base-state values. The dry buoyancy is defined by

$$b' = \frac{g\theta'}{\theta_0}, \tag{6.6}$$

and $\dot{b}'$ represents the change in dry buoyancy due to diabatic forcing. The right-hand sides of (6.1)-(6.4) are the nonlinear terms of the full anelastic equations, given by

$$F_u = -\left(u'\frac{\partial u'}{\partial x} + v'\frac{\partial u'}{\partial y} + w'\frac{\partial u'}{\partial z}\right), \tag{6.7}$$

$$F_v = -\left(u'\frac{\partial v'}{\partial x} + v'\frac{\partial v'}{\partial y} + w'\frac{\partial v'}{\partial z}\right), \tag{6.8}$$

$$F_w = -\left(u'\frac{\partial w'}{\partial x} + v'\frac{\partial w'}{\partial y} + w'\frac{\partial w'}{\partial z}\right), \tag{6.9}$$

$$F_b = -\left(u'\frac{\partial b'}{\partial x} + v'\frac{\partial b'}{\partial y} + w'\frac{\partial b'}{\partial z} + \frac{w'b'}{g}N^2\right). \tag{6.10}$$

The continuity equation is given by

$$\frac{\partial u'}{\partial x} + \frac{\partial v'}{\partial y} = -\frac{1}{\rho_0}\frac{\partial}{\partial z}(\rho_0 w') = -\frac{\partial w'}{\partial z} + \frac{1}{H_s}w', \tag{6.11}$$

where $H_s = -\rho_0(d\rho_0/dz)^{-1}$ is the scale height.

We want to combine (6.1)-(6.4) (6.12) and (6.11) into a single equation for w'. We begin by forming the divergence equation from (6.1) and (6.2):

$$\frac{D}{Dt}\left(\frac{\partial u'}{\partial x} + \frac{\partial v'}{\partial y}\right) + \frac{\partial w'}{\partial x}\frac{du_0}{dz} + \frac{\partial w'}{\partial y}\frac{dv_0}{dz} + \nabla_h^2\left(\frac{p'}{\rho_0}\right) = \frac{\partial F_u}{\partial x} + \frac{\partial F_v}{\partial y}. \tag{6.12}$$

Here, we use the definitions

$$\frac{D}{Dt} \equiv \frac{\partial}{\partial t} + u_0\frac{\partial}{\partial x} + v_0\frac{\partial}{\partial y}, \tag{6.13}$$

$$\nabla_h^2 \equiv \frac{\partial^2}{\partial x^2} + \frac{\partial^2}{\partial y^2}, \tag{6.14}$$

for the linear total derivative (excluding a contribution from vertical velocity) and horizontal Laplacian, respectively. Next, we substitute (6.11) into (6.12) to obtain

$$\frac{D}{Dt}\left(-\frac{\partial w'}{\partial z} + \frac{1}{H_s}w'\right) + \frac{\partial w'}{\partial x}\frac{du_0}{dz} + \frac{\partial w'}{\partial y}\frac{dv_0}{dz} + \frac{1}{\rho_0}\nabla_h^2 p' = \frac{\partial F_u}{\partial x} + \frac{\partial F_v}{\partial y}. \tag{6.15}$$

Now, we take $\partial/\partial z$ of (6.15) and the horizontal Laplacian of (6.3) and get

$$\frac{D}{Dt}\left[-\frac{\partial^2 w'}{\partial z^2} + \frac{\partial}{\partial z}\left(\frac{w'}{H_s}\right)\right] + \frac{du_0}{dz}\frac{\partial}{\partial x}\left(-\frac{\partial w'}{\partial z} + \frac{w'}{H_s}\right) + \frac{dv_0}{dz}\frac{\partial}{\partial y}\left(-\frac{\partial w'}{\partial z} + \frac{w'}{H_s}\right) + \frac{\partial^2 w'}{\partial x \partial z}\frac{du_0}{dz} + \frac{\partial w'}{\partial x}\frac{d^2 u_0}{dz^2}$$
$$+ \frac{\partial^2 w'}{\partial y \partial z}\frac{dv_0}{dz} + \frac{\partial w'}{\partial y}\frac{d^2 v_0}{dz^2} + \nabla_h^2\left[\frac{\partial}{\partial z}\left(\frac{p'}{\rho_0}\right)\right] = \frac{\partial^2 F_u}{\partial x \partial z} + \frac{\partial^2 F_v}{\partial y \partial z}, \tag{6.16}$$

$$\frac{D}{Dt}(\nabla_h^2 w') + \nabla_h^2\left[\frac{\partial}{\partial z}\left(\frac{p'}{\rho_0}\right)\right] - \nabla_h^2 b' = \nabla_h^2 F_w . \tag{6.17}$$

Subtracting (6.16) from (6.17) eliminates p', yielding

$$\frac{D}{Dt}\left[\nabla^2 w' - \frac{\partial}{\partial z}\left(\frac{w'}{H_s}\right)\right] - \frac{du_0}{dz}\frac{\partial}{\partial x}\left(\frac{w'}{H_s}\right) - \frac{\partial w'}{\partial x}\frac{d^2 u_0}{dz^2} - \frac{dv_0}{dz}\frac{\partial}{\partial y}\left(\frac{w'}{H_s}\right) - \frac{\partial w'}{\partial y}\frac{d^2 v_0}{dz^2} - \nabla_h^2 b' = \nabla_h^2 F_w - \frac{\partial^2 F_u}{\partial x \partial z} - \frac{\partial^2 F_v}{\partial y \partial z} \quad . \tag{6.18}$$

Now we take D/Dt of (6.18) and the horizontal Laplacian of (6.4) to obtain

$$\frac{D^2}{Dt^2}\left[\nabla^2 w' - \frac{\partial}{\partial z}\left(\frac{w'}{H_s}\right)\right] - \frac{D}{Dt}\left(\frac{du_0}{dz}\frac{\partial}{\partial x}\left(\frac{w'}{H_s}\right) + \frac{\partial w'}{\partial x}\frac{d^2 u_0}{dz^2} + \frac{dv_0}{dz}\frac{\partial}{\partial y}\left(\frac{w'}{H_s}\right) + \frac{\partial w'}{\partial y}\frac{d^2 v_0}{dz^2}\right) \tag{6.19}$$

$$-\nabla_h^2 \frac{Db'}{Dt} = \frac{D}{Dt}\left(\nabla_h^2 F_w - \frac{\partial^2 F_u}{\partial x \partial z} - \frac{\partial^2 F_v}{\partial y \partial z}\right) \quad ,$$

$$\nabla_h^2 \frac{Db'}{Dt} + N^2 \nabla_h^2 w' = \nabla_h^2 \dot{b}' + \nabla_h^2 F_b . \tag{6.20}$$

Finally we get what can be considered a single, forced, linear equation for w', if we regard the nonlinear terms on the right-hand side as forcing:

$$\frac{D^2}{Dt^2}\left[\nabla^2 w' - \frac{\partial}{\partial z}\left(\frac{w'}{H_s}\right)\right] - \frac{D}{Dt}\left(\frac{du_0}{dz}\frac{\partial}{\partial x}\left(\frac{w'}{H_s}\right) + \frac{\partial w'}{\partial x}\frac{d^2 u_0}{dz^2} + \frac{dv_0}{dz}\frac{\partial}{\partial y}\left(\frac{w'}{H_s}\right) + \frac{\partial w'}{\partial y}\frac{d^2 v_0}{dz^2}\right) +$$

$$N^2 \nabla_h^2 w' = \nabla_h^2 \frac{DF_w}{Dt} - \frac{\partial^2}{\partial x \partial z}\left(\frac{DF_u}{Dt}\right) - \frac{\partial^2}{\partial y \partial z}\left(\frac{DF_v}{Dt}\right) + \frac{\partial^2}{\partial x^2}\left(F_u \frac{du_0}{dz}\right) + \frac{\partial^2}{\partial x \partial y}\left(F_u \frac{dv_0}{dz}\right) \tag{6.21}$$

$$+ \frac{\partial^2}{\partial x \partial y}\left(F_v \frac{du_0}{dz}\right) + \frac{\partial^2}{\partial y^2}\left(F_v \frac{dv_0}{dz}\right) + \nabla_h^2 \dot{b}' + \nabla_h^2 F_b \equiv \Psi \quad .$$

Here, Ψ is the forcing, which can be written as

$$\Psi = \Psi_a + \Psi_s + \Psi_h , \tag{6.22}$$

where Ψ_a, Ψ_s, and Ψ_h represent the production of gravity waves by nonlinear advection, shear and heating, respectively. These terms are defined by

$$\Psi_a = \nabla_h^2 \frac{DF_w}{Dt} - \frac{\partial^2}{\partial y \partial z}\left(\frac{DF_v}{Dt}\right) - \frac{\partial^2}{\partial y \partial z}\left(\frac{DF_v}{Dt}\right) + \nabla_h^2 F_b , \tag{6.23}$$

$$\Psi_s = \frac{\partial^2}{\partial x^2}\left(F_u \frac{du_0}{dz}\right) + \frac{\partial^2}{\partial x \partial y}\left(F_u \frac{dv_0}{dz}\right) + \frac{\partial^2}{\partial x \partial y}\left(F_v \frac{du_0}{dz}\right) + \frac{\partial^2}{\partial y^2}\left(F_v \frac{dv_0}{dz}\right), \tag{6.24}$$

$$\Psi_h = \nabla_h^2 \dot{b}' . \tag{6.25}$$

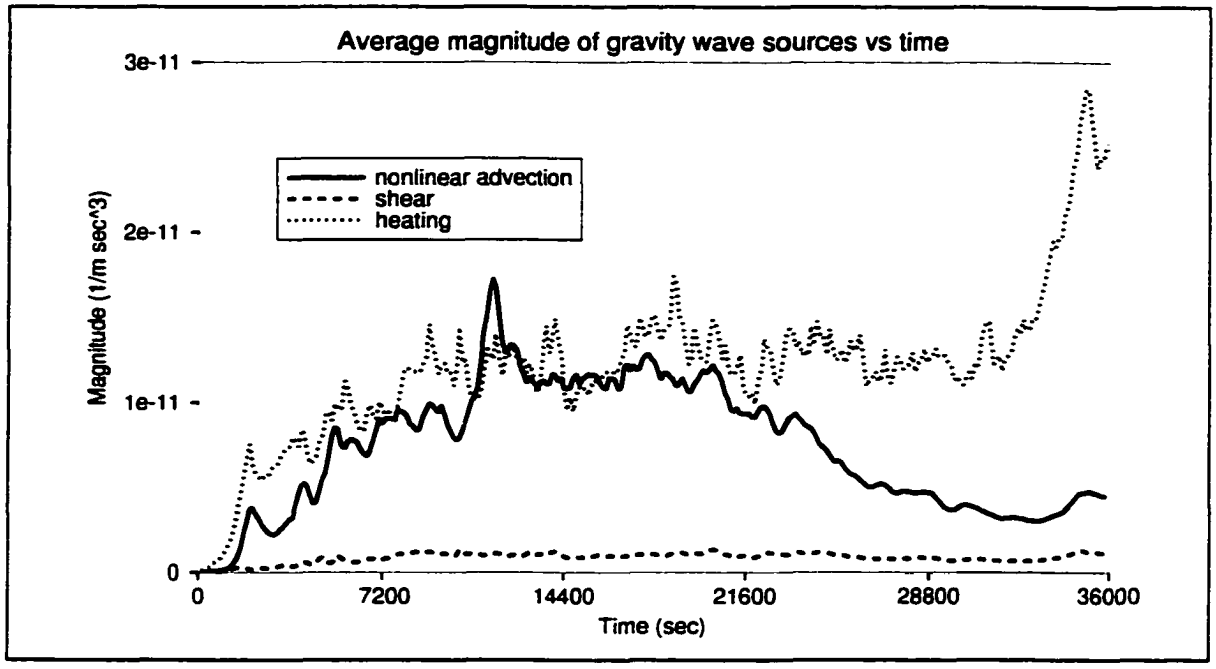

Fig. 6.1. Plot of the average magnitude of the three gravity wave source terms defined in (6.23)-(6.25) versus time for the control WK run. The terms were averaged over the troposphere of the domain.

The sources defined in (6.23)-(6.25) have been calculated versus time for the WK control run, as shown in Fig. 6.1. For this figure, the average magnitude (absolute value) of each term was calculated in the troposphere, as a measure of the importance of each source term. The maximum magnitude of each term was also calculated, and this is shown in Fig. 6.3. We see that by this measure, the heating term is at least as important as the buoyancy term throughout the simulation, with the shear term still playing a relatively unimportant role. The source terms were only large in the convection itself, reaching values of up to $\pm 8 \times 10^{-9}$ m^{-1} s^{-3}, but extended over a fairly large depth. These values are comparable (but somewhat smaller than) those calculated by Lane et al. Note that the magnitude of the heating source term is comparable to the nonlinear advection source term throughout most of the simulation, with the heating term becoming dominant after 21600 seconds. This is in contrast to Lane et al. (2001), who found that the nonlinear advection terms were dominant in their simulation. However, the source term associated with shear was quite small, which is similar to what Lane et al. found.

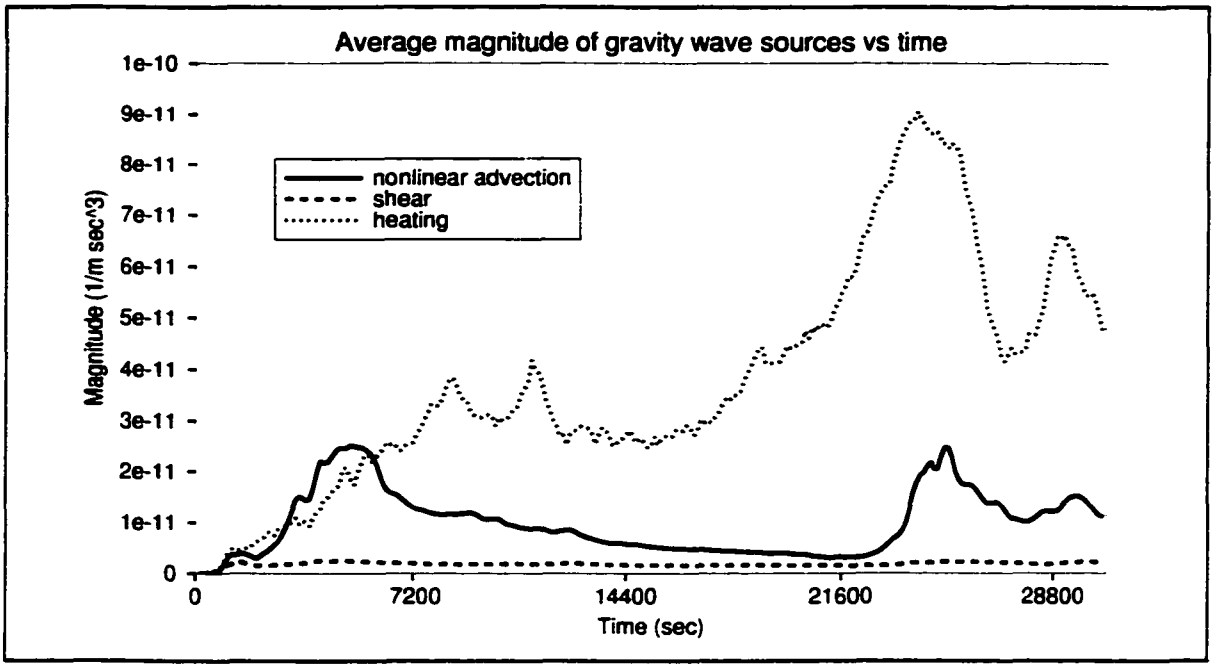

Fig. 6.2. Plot of the average magnitude of the three gravity wave source terms defined in (6.23)-(6.25) versus time for the control TC run. The terms were averaged over the troposphere of the domain.

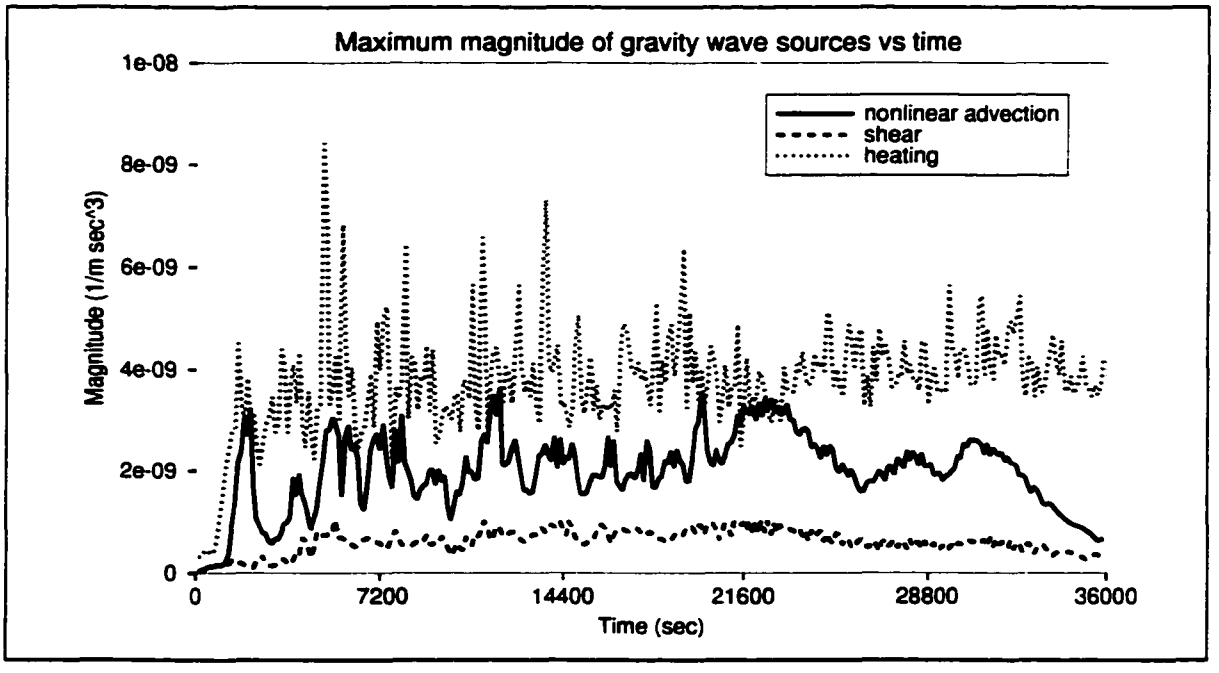

Fig. 6.3. Plot of the maximum magnitude of the three gravity wave source terms defined in (6.23)-(6.25) versus time for the control WK run.

The gravity wave source terms were also calculated for the control TC run, as shown in Fig. 6.2 and Fig. 6.4. The magnitude of the gravity wave sources in this simulation were significantly larger than those of the control WK run. This may be because of the finer hor-

izontal grid spacing (500 m versus 1000 m) in the control TC run. Features such as updrafts tend to become smaller in scale and stronger as grid resolution increases (Weisman et al. 1997). This would cause the terms involving horizontal derivatives to become larger. We see that this decidedly different simulation of convection still shows heating to be at least as important as nonlinear advection using the analysis method of Lane et al. throughout the simulation. However, Lane (personal communication) has indicated that the nonlinear advection in 3-D simulations plays more of a prominent role than in 2-D simulations such as this study. Shear still played a smaller role than heating and nonlinear advection.

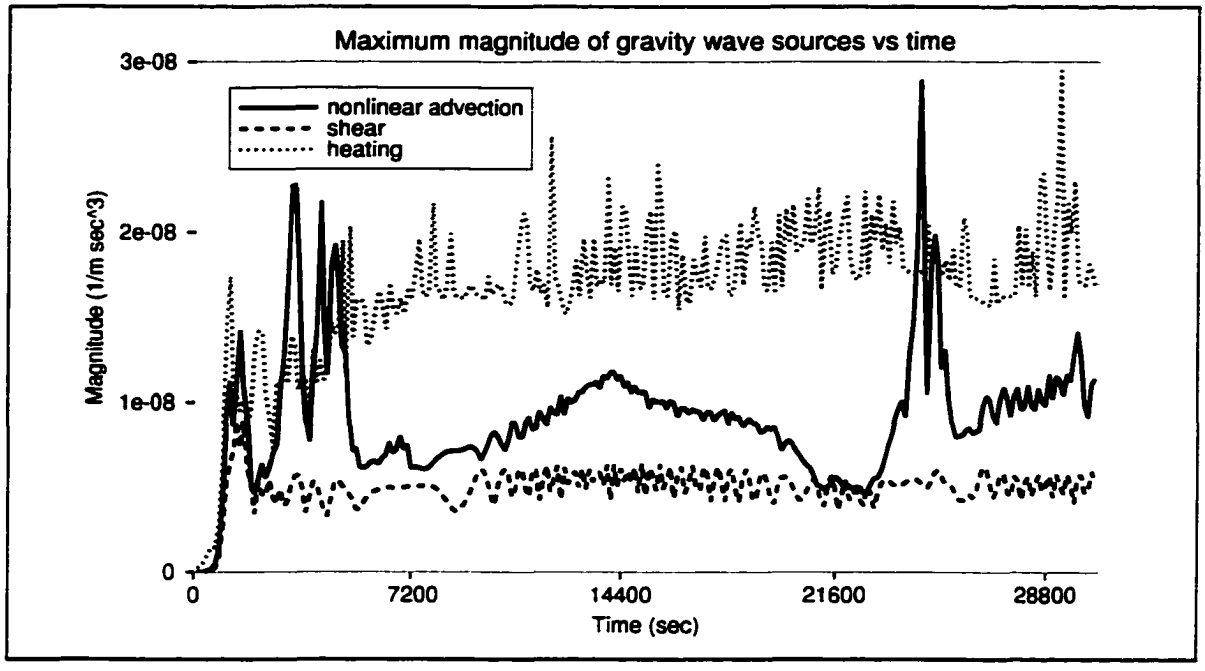

Fig. 6.4. Plot of the maximum magnitude of the three gravity wave source terms defined in (6.23)-(6.25) versus time for the control TC run.

In this chapter, we studied how perturbation equations can be combined to form a single equation describing gravity wave excitation. In the following chapter, we will examine another method in which waves and convection can be studied simultaneously. We will see how the anelastic momentum and thermodynamic equations can be combined to form prognostic equations for the second moments (variances and covariances) of these quantities.

Chapter 7: Prognostic equations for first and second moments

In this chapter, we will derive equations for mean and perturbation variables. The type of perturbations that the equations describe need not be specified, although most studies focus on one type of perturbation. Since we will study an environment in which waves and convection exist simultaneously, we will avoid specifying the type of perturbation that we are dealing with except to simplify illustrations of physical concepts. Later, we will apply the equations derived here to illustrate specific physical principles.

We begin with the anelastic (Bannon 1996) equation for momentum, neglecting Coriolis effects

$$\rho_0\left(\frac{\partial u_i}{\partial t} + u_j\frac{\partial u_i}{\partial x_j}\right) = -\rho_0\frac{\partial}{\partial x_i}\left(\frac{p}{\rho_0}\right) - \delta_{i3}\frac{\rho_0 g(\theta-\theta_0)}{\theta_0} + \rho_0 F_i, \tag{7.1}$$

where u_i represents the three components of velocity

$$(u_1, u_2, u_3) = (u, v, w), \tag{7.2}$$

p is pressure, θ_0 and ρ_0 are a vertically varying basic state potential temperature and density, g is gravity, and F_i is a term representing friction. When indices are repeated within a term, it means that the operation is summed over all three components, e.g.,

$$a_i b_i = a_1 b_1 + a_2 b_2 + a_3 b_3 = \vec{a} \bullet \vec{b}. \tag{7.3}$$

The term δ_{ij} is the Kronecker delta, and is equal to zero unless $i = j$. For more details on index notation, see Stull (1988).

We can form an equation for the perturbation of u_i if we take the mean of (7.1)

$$\rho_0\left(\frac{\partial \bar{u}_i}{\partial t} + \overline{u_j\frac{\partial u_i}{\partial x_j}}\right) = -\rho_0\frac{\partial}{\partial x_i}\left(\frac{\bar{p}}{\rho_0}\right) - \delta_{i3}\frac{\rho_0 g(\bar{\theta}-\theta_0)}{\theta_0} + \rho_0\overline{F_i}, \tag{7.4}$$

and subtract it from (7.1). Here, the averaging operator is not yet defined, except that it is

of the form

$$\bar{a} = \int_b^c a dx, \tag{7.5}$$

and can be separated into vertically varying mean and perturbation parts, i.e.,

$$a(x, z, t) = \bar{a}(z, t) + a'(x, z, t). \tag{7.6}$$

Also, the averaging operator commutes with vertical and temporal derivatives, and the average of a perturbation quantity is zero, i.e. $\overline{a'} = 0$. The averaging operator does not necessarily commute with the horizontal derivative. This is because the boundary conditions are not necessarily periodic. Subtracting (7.4) from (7.1), we obtain

$$\frac{\partial u_i'}{\partial t} + u_j \frac{\partial u_i}{\partial x_j} - \overline{u_j \frac{\partial u_i}{\partial x_j}} = -\frac{\partial}{\partial x_i}\left(\frac{p'}{\rho_0}\right) + \delta_{i3} g \frac{\theta'}{\theta_0} + F_i'. \tag{7.7}$$

Separating (7.7) into mean and fluctuating parts, we have

$$\frac{\partial u_i'}{\partial t} + (\bar{u}_j + u_j')\frac{\partial(\bar{u}_i + u_i')}{\partial x_j} - \overline{(\bar{u}_j + u_j')\frac{\partial(\bar{u}_i + u_i')}{\partial x_j}} = -\frac{\partial}{\partial x_i}\left(\frac{p'}{\rho_0}\right) + \delta_{i3} g \frac{\theta'}{\theta_0} + F_i', \tag{7.8}$$

which can be written as

$$\frac{\partial u_i'}{\partial t} + \bar{u}_j \frac{\partial u_i'}{\partial x_j} + u_j' \frac{\partial \bar{u}_i}{\partial x_j} + u_j' \frac{\partial u_i'}{\partial x_j} - \overline{u_j' \frac{\partial u_i'}{\partial x_j}} = -\frac{\partial}{\partial x_i}\left(\frac{p'}{\rho_0}\right) + \delta_{i3} g \frac{\theta'}{\theta_0} + F_i'. \tag{7.9}$$

There is a distinct contrast between the ways that the turbulence community and Eliassen and Palm (1960) have dealt with the above equations. The turbulence community has historically used the above equations to derive statements that predict future values of turbulence kinetic energy, momentum fluxes and heat fluxes. Eliassen and Palm (1960), on the other hand, used a steady, linearized version of the above equations to derive statements that relate the momentum flux to the wave energy flux for a steady state. As noted in the beginning of this chapter, these equations can apply to waves, turbulence or deep convection, providing a unified framework for the discussion.

Now, to form the equation for the covariance of u_i and u_k, we multiply (7.9) by u_k', and add it to a prognostic equation for u_k' that is identical to (7.9) except that u_k' replaces u_i'. After performing these operations, we obtain

$$\frac{\partial(u_i'u_k')}{\partial t} + \overline{u}_j\frac{\partial(u_i'u_k')}{\partial x_j} + u_j'u_i'\frac{\partial \overline{u}_k}{\partial x_j} + u_j'u_k'\frac{\partial \overline{u}_i}{\partial x_j} + u_j'\frac{\partial(u_i'u_k')}{\partial x_j} - u_k'\overline{u_j'\frac{\partial u_i'}{\partial x_j}}$$

$$-u_i'\overline{u_j'\frac{\partial u_k'}{\partial x_j}} = -u_k'\frac{\partial}{\partial x_i}\left(\frac{p'}{\rho_0}\right) - u_i'\frac{\partial}{\partial x_k}\left(\frac{p'}{\rho_0}\right) + \delta_{i3}g\frac{u_k'\theta'}{\theta_0} + \delta_{k3}g\frac{u_i'\theta'}{\theta_0} + u_k'F_i' + u_i'F_k' \quad . \tag{7.10}$$

If we add (7.10) to $u_i'u_k'$ times the anelastic continuity equation,

$$\frac{1}{\rho_0}\frac{\partial}{\partial x_j}(\rho_0 u_j') = 0, \tag{7.11}$$

the fourth term becomes a transport term, but another term representing the effects of density stratification is introduced:

$$\frac{\partial(u_i'u_k')}{\partial t} + \overline{u}_j\frac{\partial(u_i'u_k')}{\partial x_j} + u_j'u_k'\frac{\partial \overline{u}_i}{\partial x_j} + u_j'u_i'\frac{\partial \overline{u}_k}{\partial x_j} + \frac{\partial(u_j'u_i'u_k')}{\partial x_j} + \frac{u_i'u_k'w'}{\rho_0}\frac{d\rho_0}{dz}$$

$$-u_k'\overline{u_j'\frac{\partial u_i'}{\partial x_j}} + u_i'\overline{u_j'\frac{\partial u_k'}{\partial x_j}} = -u_k'\frac{\partial}{\partial x_i}\left(\frac{p'}{\rho_0}\right) - u_i'\frac{\partial}{\partial x_k}\left(\frac{p'}{\rho_0}\right) + \delta_{i3}g\frac{u_k'\theta'}{\theta_0} + \delta_{k3}g\frac{u_i'\theta'}{\theta_0} \tag{7.12}$$

$$u_k'F_i' + u_i'F_k' \quad .$$

Taking the mean of (7.12), we obtain

$$\frac{\partial(\overline{u_i'u_k'})}{\partial t} + \overline{u}_j\frac{\partial(\overline{u_i'u_k'})}{\partial x_j} = -\overline{u_j'u_i'}\frac{\partial \overline{u}_k}{\partial x_j} - \overline{u_j'u_k'}\frac{\partial \overline{u}_i}{\partial x_j} - \frac{\partial(\overline{u_j'u_i'u_k'})}{\partial x_j} - \frac{\overline{u_i'u_k'w'}}{\rho_0}\frac{d\rho_0}{dz} -$$

$$\frac{\partial}{\partial x_i}\left(\frac{\overline{p'u_k'}}{\rho_0}\right) - \frac{\partial}{\partial x_k}\left(\frac{\overline{p'u_i'}}{\rho_0}\right) + \overline{\frac{p'}{\rho_0}\left(\frac{\partial u_k'}{\partial x_i} + \frac{\partial u_i'}{\partial x_k}\right)} + \delta_{i3}g\frac{\overline{u_k'\theta'}}{\theta_0} + \delta_{k3}g\frac{\overline{u_i'\theta'}}{\theta_0} + \overline{u_k'F_i'} + \overline{u_i'F_k'} \quad . \tag{7.13}$$

Here, we have followed Stull (1988, p.134), and rewritten the terms involving pressure.

The physical interpretation of (7.13) is as follows, again following Stull. The first and second terms in the left-hand side represent the rate of change of $\overline{u_i'u_k'}$ due to the local tendency and advection by the mean wind, respectively. The first and second terms on the right-hand side (RHS) represents the production of $\overline{u_i'u_k'}$ by shears of the mean wind. The third and fourth RHS terms are triple-moment terms, and account for the transport of $\overline{u_i'u_k'}$ by turbulent motions. The fifth and sixth terms on the RHS represent transport by pressure correlations, while the next group of terms involving pressure are known in the turbulence community as "return-to-isotropy" terms. This label arises in the turbulence

kinetic energy equation because the terms only exchange energy between velocity components, taking energy from components that have large amounts of energy, and distributing it to components that have low amounts of energy. The ninth and tenth terms on the RHS arise from the production of $\overline{u_i'u_k'}$ by buoyancy. The final two terms on the RHS represent the effects of viscosity on $\overline{u_i'u_k'}$.

There are six unique prognostic equations described by (7.13). Three equations describe the evolution of variances ($\overline{u'u'}$, $\overline{v'v'}$, $\overline{w'w'}$), while three more describe the evolution of covariances ($\overline{u'w'}$, $\overline{u'v'}$, $\overline{v'w'}$). As an illustration, the upward wave momentum flux is prognosed by

$$\frac{\partial(\overline{u'w'})}{\partial t} + \bar{u}_j\frac{\partial(\overline{u'w'})}{\partial x_j} + \frac{\partial(\overline{u_j'u'w'})}{\partial x_j} + \frac{\overline{u'w'w'}}{\rho_0}\frac{d\rho_0}{dz} = -\frac{\partial}{\partial z}\left(\frac{\overline{p'u'}}{\rho_0}\right) - \frac{\partial}{\partial x}\left(\frac{\overline{p'w'}}{\rho_0}\right) + \overline{\frac{p'}{\rho_0}\left(\frac{\partial w'}{\partial x} + \frac{\partial u'}{\partial z}\right)} - \overline{u_j'w'}\frac{\partial \bar{u}}{\partial x_j} - \overline{u_j'u'}\frac{\partial \bar{w}}{\partial x_j} + g\frac{\overline{u'\theta'}}{\theta_0} + \overline{w'F_x'} + \overline{u'F_z'} \quad . \tag{7.14}$$

In a completely analogous manner, the evolution equation for the heat flux can be obtained by combining θ' times (7.9) and u_i' times the equation for potential temperature fluctuation, to obtain

$$\frac{\partial\theta'}{\partial t} + \bar{u}_j\frac{\partial\theta'}{\partial x_j} + u_j'\frac{\partial\bar{\theta}}{\partial x_j} + u_j'\frac{\partial\theta'}{\partial x_j} - \overline{u_j'\frac{\partial\theta'}{\partial x_j}} = \dot{\theta}' + F_\theta'. \tag{7.15}$$

The resulting equation for $\overline{u_i'\theta'}$ is

$$\frac{\partial(\overline{u_i'\theta'})}{\partial t} + \bar{u}_j\frac{\partial(\overline{u_i'\theta'})}{\partial x_j} = -\overline{u_j'\theta'}\frac{\partial\bar{u}_i}{\partial x_j} - \overline{u_i'u_j'}\frac{\partial\bar{\theta}}{\partial x_j} - \frac{\partial(\overline{u_j'u_i'\theta'})}{\partial x_j} - \frac{\overline{u_i'\theta'w'}}{\rho_0}\frac{d\rho_0}{dz} - \frac{\partial}{\partial x_i}\left(\frac{\overline{p'\theta'}}{\rho_0}\right) + \overline{\frac{p'}{\rho_0}\frac{\partial\theta'}{\partial x_i}} + \delta_{i3}g\frac{\overline{\theta'\theta'}}{\theta_0} + \overline{\theta'F_i'} + \overline{u_i'\dot{\theta}'} + \overline{u_i'F_\theta'} \quad . \tag{7.16}$$

The prognostic equations for the mean values of horizontal velocity and potential temperature are given by

$$\frac{\partial}{\partial t}(\rho_0\bar{\theta}) + \rho_0\bar{w}\frac{\partial\bar{\theta}}{\partial z} + \frac{\partial}{\partial z}(\rho_0\overline{w'\theta'}) = \rho_0\dot{\bar{\theta}}, \tag{7.17}$$

$$\frac{\partial}{\partial t}(\rho_0\bar{u}) + \rho_0\bar{w}\frac{\partial\bar{u}}{\partial z} + \frac{\partial}{\partial z}(\rho_0\overline{u'w'}) = \rho_0\overline{F_x}. \tag{7.18}$$

Although we can normally assume that $\bar{w} = 0$ in a domain with periodic boundary conditions, the compressibility of ARPS forced us to include the term involving the advection by the mean vertical velocity, particularly for the $\bar{\theta}$ equation (see Fig. 7.1b).

The set of prognostic second moment equations for velocity and potential temperature in a (x,z) horizontally periodic system based on the anelastic equations (with the additional condition that $\bar{w}$ is not necessarily zero) is given by

$$\frac{\partial}{\partial t}\left(\frac{\rho_0\overline{u'u'}}{2}\right) + \rho_0\bar{w}\frac{\partial}{\partial z}\left(\frac{\overline{u'u'}}{2}\right) + \rho_0\overline{u'w'}\frac{\partial\bar{u}}{\partial z} + \frac{\partial}{\partial z}\left(\frac{\rho_0\overline{u'u'w'}}{2}\right) = \overline{p'\frac{\partial u'}{\partial x}} + \rho_0\overline{u'F_x'}, \tag{7.19}$$

$$\begin{aligned}\frac{\partial}{\partial t}\left(\frac{\rho_0\overline{w'w'}}{2}\right) + \rho_0\bar{w}\frac{\partial}{\partial z}\left(\frac{\overline{w'w'}}{2}\right) + \rho_0\overline{w'w'}\frac{\partial\bar{w}}{\partial z} + \frac{\partial}{\partial z}\left(\frac{\rho_0\overline{w'w'w'}}{2}\right) = \\ \overline{p'\frac{\partial w'}{\partial z}} - \rho_0\frac{\partial}{\partial z}\left(\frac{\overline{p'w'}}{\rho_0}\right) + \rho_0 g\frac{\overline{w'\theta'}}{\theta_0} + \rho_0\overline{w'F_z'},\end{aligned} \tag{7.20}$$

$$\frac{\partial}{\partial t}\left(\frac{\rho_0\overline{\theta'\theta'}}{2}\right) + \rho_0\bar{w}\frac{\partial}{\partial z}\left(\frac{\overline{\theta'\theta'}}{2}\right) + \rho_0\overline{w'\theta'}\frac{\partial\bar{\theta}}{\partial z} + \frac{\partial}{\partial z}\left(\frac{\rho_0\overline{w'\theta'\theta'}}{2}\right) = \rho_0\overline{\dot{\theta}'\theta'}, \tag{7.21}$$

$$\begin{aligned}\frac{\partial}{\partial t}(\rho_0\overline{u'w'}) + \rho_0\bar{w}\frac{\partial}{\partial z}(\overline{u'w'}) + \rho_0\overline{w'w'}\frac{\partial\bar{u}}{\partial z} + \rho_0\overline{w'w'}\frac{\partial\bar{w}}{\partial z} + \frac{\partial}{\partial z}(\rho_0\overline{u'w'w'}) = \overline{p'\frac{\partial w'}{\partial x}} + \\ \overline{p'\frac{\partial u'}{\partial z}} - \rho_0\frac{\partial}{\partial z}\left(\frac{\overline{p'u'}}{\rho_0}\right) + \rho_0 g\frac{\overline{u'\theta'}}{\theta_0} + \rho_0\overline{u'F_z'} + \rho_0\overline{w'F_x'},\end{aligned} \tag{7.22}$$

$$\begin{aligned}\frac{\partial}{\partial t}(\rho_0\overline{u'\theta'}) + \rho_0\bar{w}\frac{\partial}{\partial z}(\overline{u'\theta'}) + \rho_0\overline{w'\theta'}\frac{\partial\bar{u}}{\partial z} + \rho_0\overline{u'w'}\frac{\partial\bar{\theta}}{\partial z} + \frac{\partial}{\partial z}(\rho_0\overline{u'w'\theta'}) = \\ \overline{p'\frac{\partial\theta'}{\partial x}} + \rho_0\overline{u'\dot{\theta}'} + \rho_0\overline{\theta'F_x'},\end{aligned} \tag{7.23}$$

$$\begin{aligned}\frac{\partial}{\partial t}(\rho_0\overline{w'\theta'}) + \rho_0\bar{w}\frac{\partial}{\partial z}(\overline{w'\theta'}) + \rho_0\overline{w'w'}\frac{\partial\bar{\theta}}{\partial z} + \rho_0\overline{w'\theta'}\frac{\partial\bar{w}}{\partial z} + \frac{\partial}{\partial z}(\rho_0\overline{w'w'\theta'}) = \\ \overline{p'\frac{\partial\theta'}{\partial z}} - \rho_0\frac{\partial}{\partial z}\left(\frac{\overline{p'\theta'}}{\rho_0}\right) + \rho_0 g\frac{\overline{\theta'\theta'}}{\theta_0} + \rho_0\overline{w'\dot{\theta}'} + \rho_0\overline{\theta'F_z'}.\end{aligned} \tag{7.24}$$

In the following figures, we will determine which terms are important in the budgets of (7.17)-(7.22), according to time-averaged (from $t = 4$ h to $t = 5$ h) zonal means that have been taken of the model output quantities for the WK control run (see Chapter 5). In these

figures, only the important terms are shown. The sign of each term is that which would be obtained by putting all of the terms other than the tendency terms on the RHS of (7.17)-(7.22). Sometimes, the tendency term is much smaller than some of the component terms, so it appears quite close to zero. Also, the model has both computational and turbulent mixing, the sum of which can be regarded as F_i' on the RHS of several of the budget equations. When one or more these terms are large enough to warrant inclusion, they are treated separately.

The budget for the zonal mean potential temperature is shown in Fig. 7.1. In the model troposphere (Fig. 7.1a), the tendency is mostly positive, and is largely balanced by diabatic heating. Within the lowest 2 km of the troposphere, several terms change rapidly with height, presumably because of the presence of the cold pool. In the model stratosphere (Fig. 7.1b), we do not expect the zonal mean potential temperature to change much, and indeed, the tendencies are much smaller than in the troposphere. The dominant term in the stratosphere is the divergence of the heat flux. This is somewhat surprising in the sense that we expect $\overline{w'\theta'}$ to be zero for steady, linear gravity waves, but as Roadnight (1999) showed, $\overline{w'\theta'}$ can be nonzero for transient waves. There is also a contribution to the $\bar{\theta}$ budget from the zonal mean vertical velocity. This is a product of the compressibility of the model (M. Xue, personal communication). This is because the continuity equation for the compressible system does not guarantee a zero value for $\bar{w}$, like the anelastic continuity equation does.

The prognostic budget for the zonal mean zonal wind is shown in Fig. 7.2. We see that $\bar{u}$ is accelerated in the lower troposphere, and decelerated in the upper troposphere and stratosphere. This is primarily due to the divergence of the vertical momentum flux, $\rho_0\overline{u'w'}$. This pattern of low-level divergence and upper-level convergence is consistent with what Weisman et al. (1997) obtained for a similar wind and thermodynamic profile. In a stratosphere without shear, we expect relatively little mean-flow acceleration, and this is illustrated in Fig. 7.2b, particularly above $z = 15$ km.

The prognostic horizontal kinetic energy budget is shown in Fig. 7.3. In the model troposphere, the pressure and turbulent transport terms are dominant, and the tendency is

generally a small difference between these terms that are large and opposite in sign. These terms are also dominant in the model stratosphere, with the pressure term being of primary importance in the vicinity of the tropopause.

The prognostic vertical kinetic energy budget is shown in Fig. 7.4. In this figure, we see that the tendency term is much smaller than several of the terms in the budget. Note that the pressure term is the first term on the RHS of (6.20), while the "pressure density" term is the second term on the RHS of (7.20). These two terms, the buoyant production term, and the turbulent transport term are dominant in the $\overline{w'w'}$ budget of the troposphere. The same terms are dominant in the stratosphere, with the exception of the turbulent transport term. The residual is occasionally quite large in this budget, particularly in the upper troposphere.

In Fig. 7.5, the prognostic potential temperature variance budget is shown. We see that the tendency is for the potential temperature variance to increase in the lower troposphere. The dominant contributors to the $\overline{\theta'\theta'}$ budget in the troposphere are the diabatic heating and gradient production terms. The signs of these terms (positive for diabatic heating, negative for gradient production) are consistent with the presence of moist convection, where we expect w' and θ' to be positively correlated, as well as θ' and $\dot{\theta}'$. The gradient production term is dominant in the stratosphere. This is similar to what we found in the $\bar{\theta}$ budget, except that now the heat flux term $\overline{w'\theta'}$ is multiplied by the stratification $\partial\bar{\theta}/\partial z$ rather than differentiated.

The prognostic momentum flux budget is shown in Fig. 7.6. In this figure, we see that the tendency is much smaller than the offsetting pressure terms, and the buoyant production term throughout the model atmosphere. The negative sign of the $\overline{u'\theta'}$ term in the lowest 2 km of the model domain can be understood as follows. The cold pool is associated with negative values of θ', and positive values of u', since it moves approximately at the same rate of the storm ($u \sim 15$ m s^{-1}), instead of the velocity of the base-state sounding ($u = 0$ m s^{-1} at the surface). The residual in this budget is generally smaller than the three major terms, but larger than the tendency.

a)

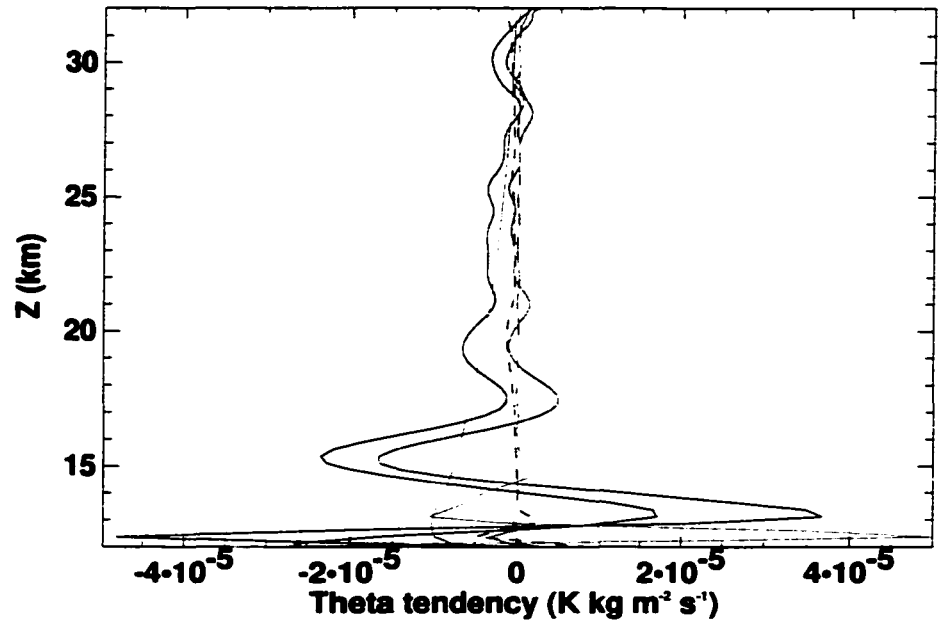

b)

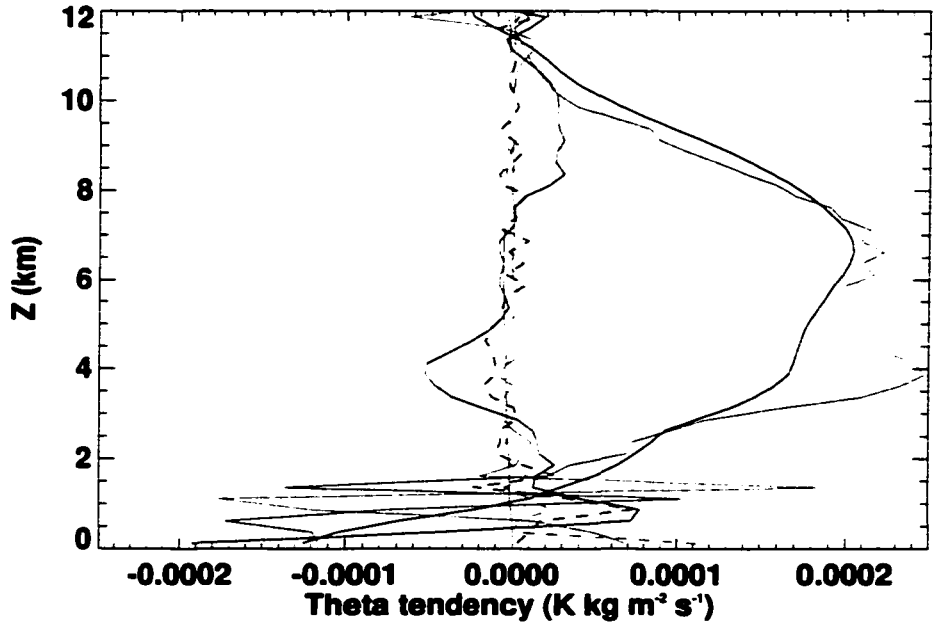

Fig. 7.1. Theta budget of (7.17) in a) the stratosphere and b) the troposphere from the WK control run averaged from t = 4 h to t = 5 h. The solid black line is the tendency, the blue line is the flux divergence, the dashed red line is turbulent mixing, the violet line is computational mixing, the red line is diabatic heating, the green line is mean vertical advection, and the dashed black line is the residual.

a)

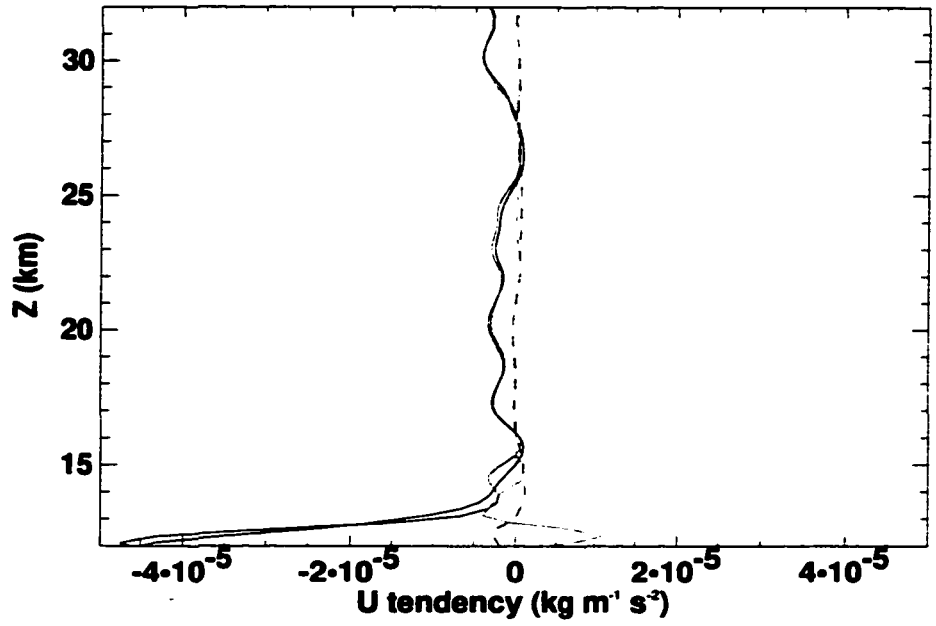

b)

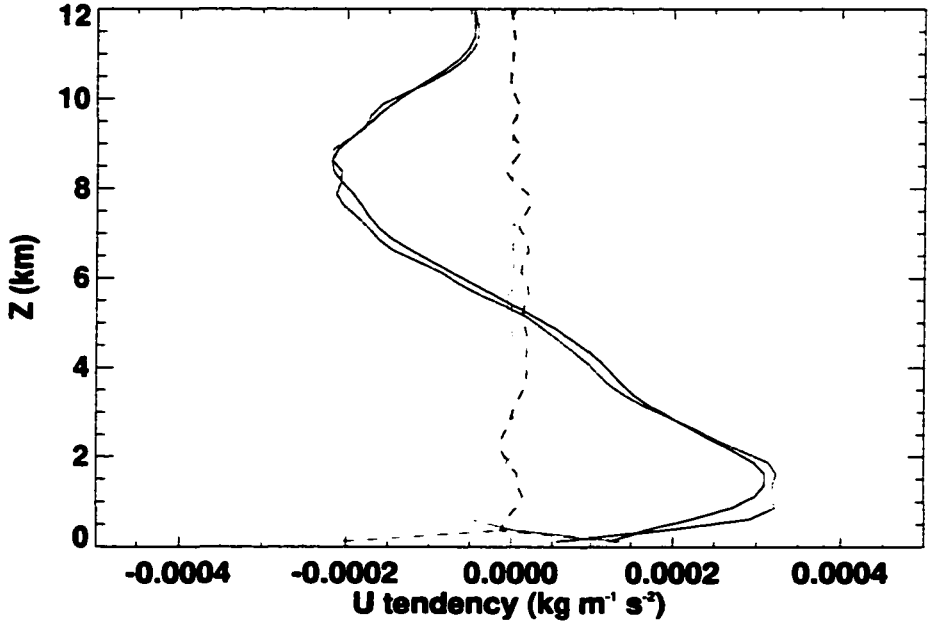

Fig. 7.2. Momentum budget of (7.18) in a) the stratosphere and b) the troposphere from the WK control run averaged from t = 4 h to t = 5 h. The solid black line is the tendency, the blue line is the flux divergence, the dashed red line is turbulent mixing, the violet line is computational mixing, and the dashed black line is the residual.

a)

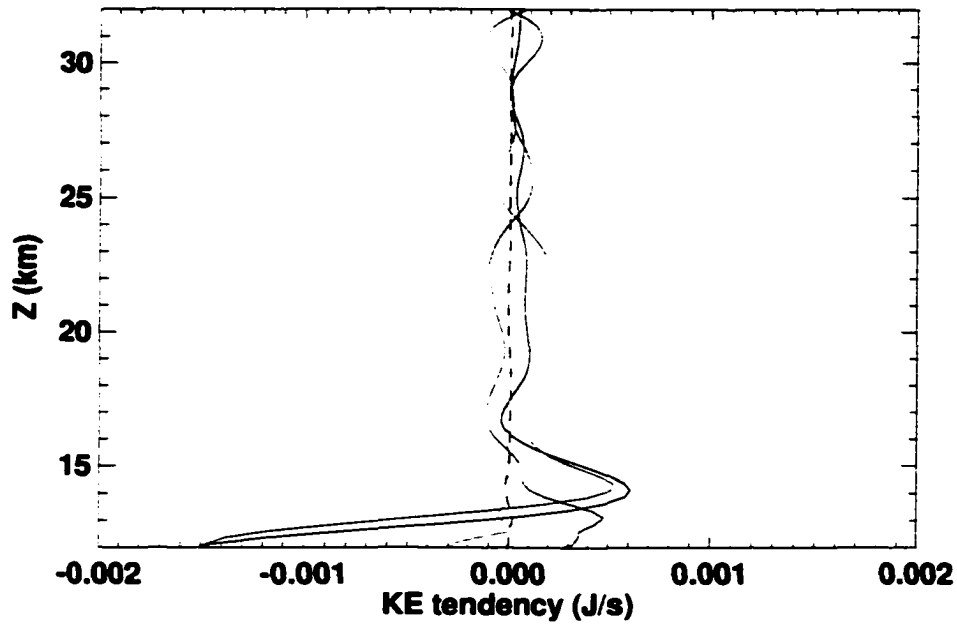

b)

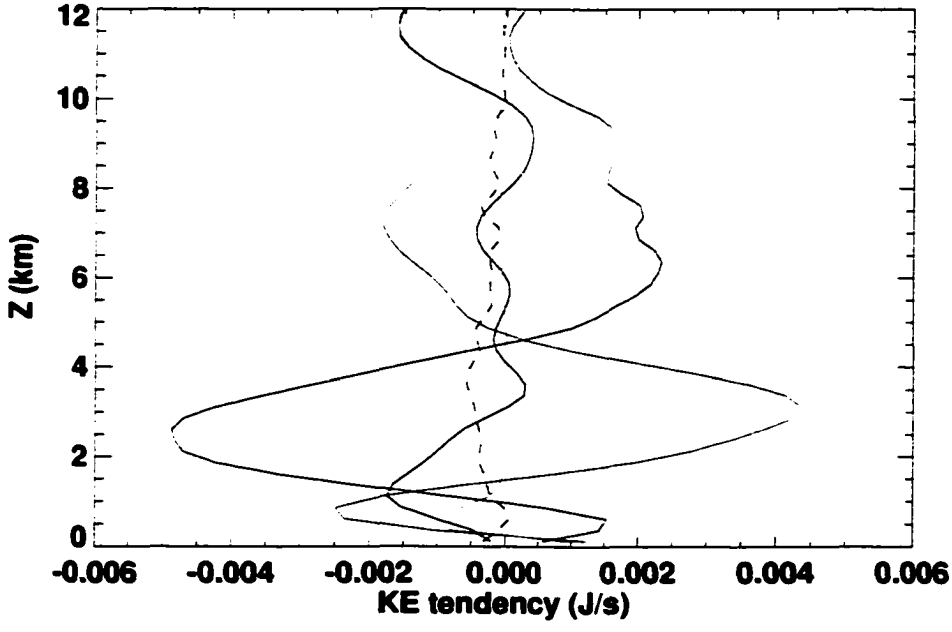

Fig. 7.3. Horizontal kinetic energy budget of (7.19) in a) the stratosphere and b) the troposphere from the WK control run averaged from t = 4 h to t = 5 h. The solid black line is the tendency, the blue line is turbulent transport, the green line is the pressure term, the violet line is computational mixing, and the dashed black line is the residual.

a)

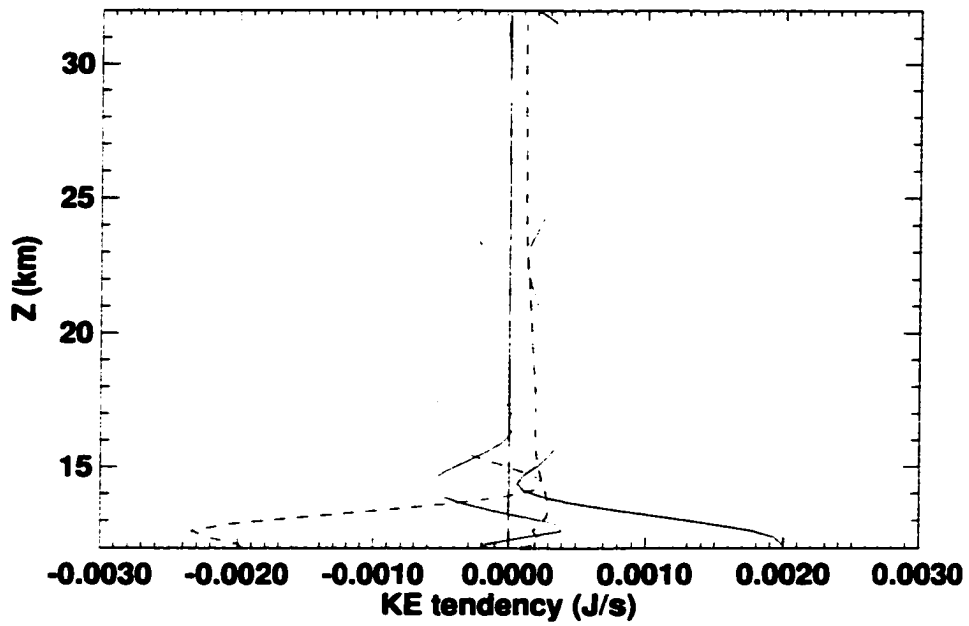

b)

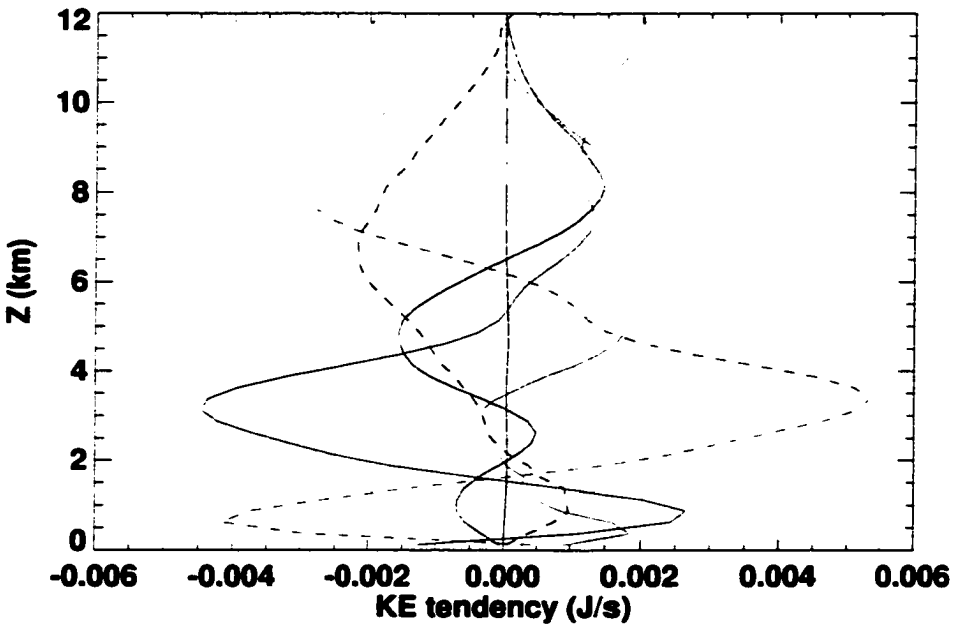

Fig. 7.4. Vertical kinetic energy budget of (7.20) in a) the stratosphere and b) the troposphere from the WK control run averaged from t = 4 h to t = 5 h. The solid black line is the tendency, the blue line is turbulent transport, the green line is the pressure term, the dashed green line is the pressure-density term, the red line is the buoyant production term, and the dashed black line is the residual.

a)

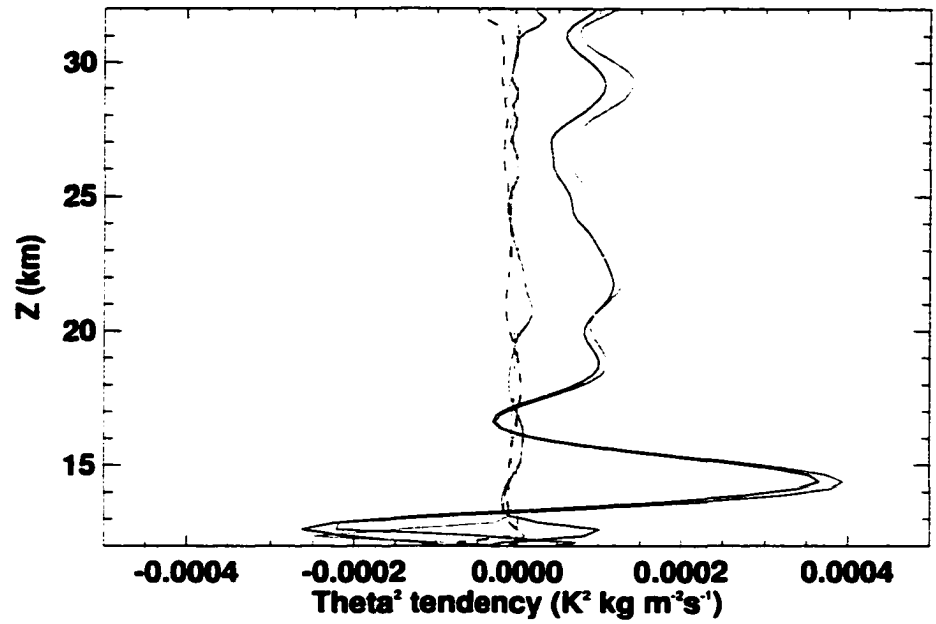

b)

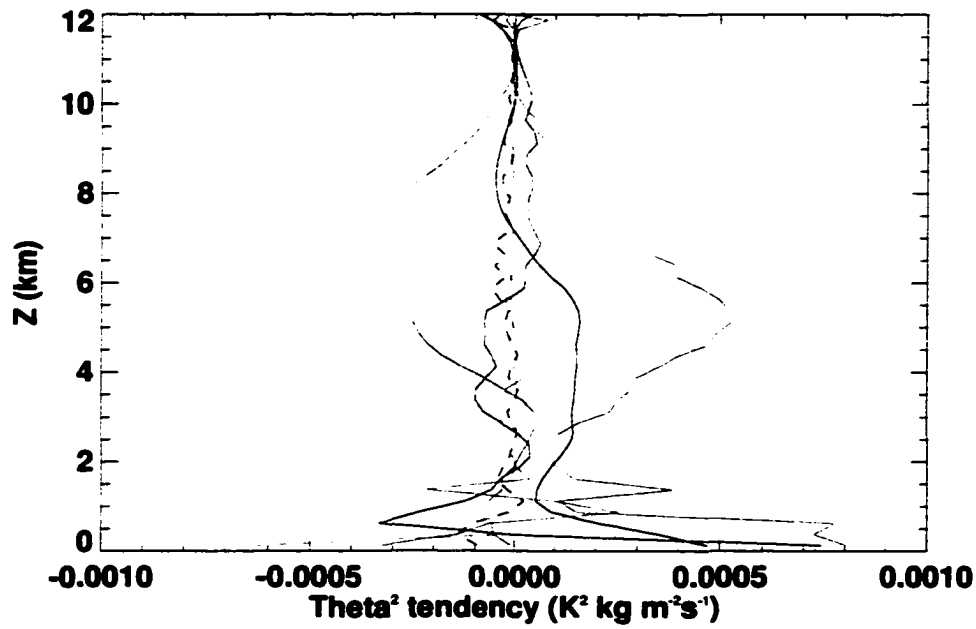

Fig. 7.5. Potential temperature variance budget of (7.21) in a) the troposphere and b) the stratosphere from the WK control run averaged from t = 4 h to t = 5 h. The solid black line is the tendency, the green line is gradient production, the blue line is turbulent transport, the red line is the diabatic heating term, the dashed red line is turbulent mixing, the violet line is computational mixing, and the dashed black line is the residual.

a)

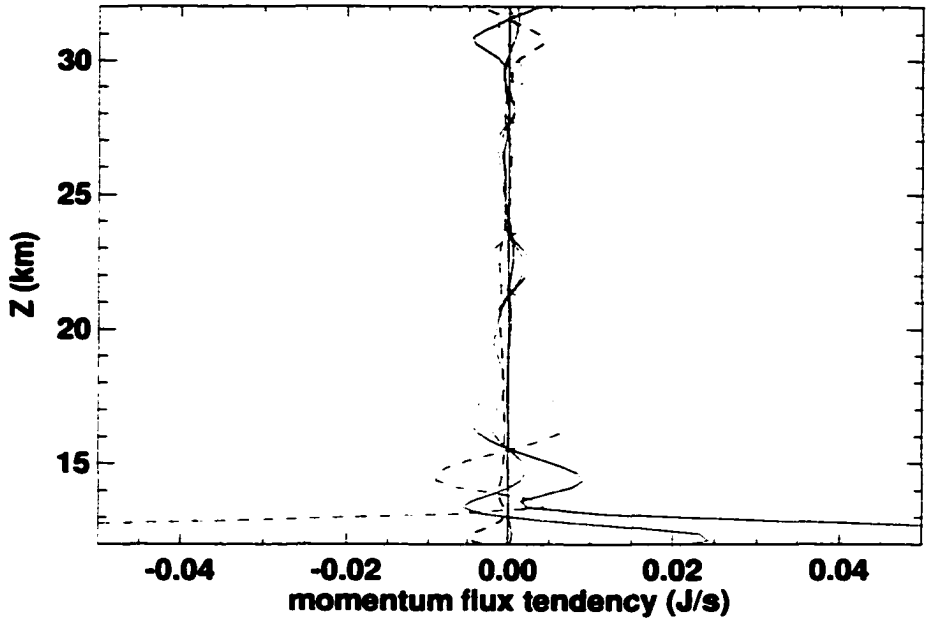

b)

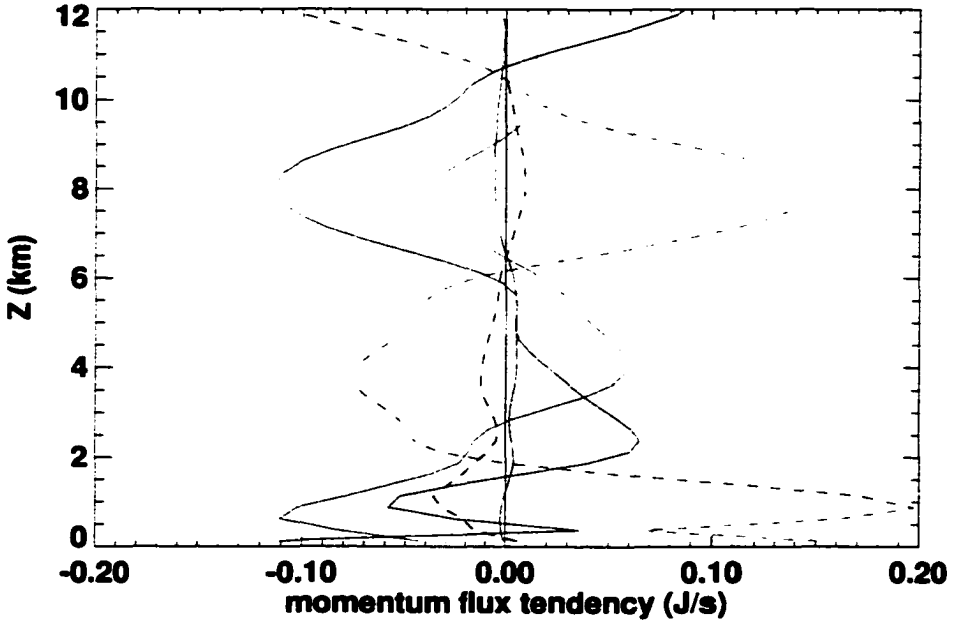

Fig. 7.6. Momentum flux budget of (7.21) in a) the troposphere and b) the stratosphere from the WK control run averaged from t = 4 h to t = 5 h. The solid black line is the tendency, the blue line is turbulent transport, the green line is the $p'u'$ pressure term, the dashed green line is the $p'u'$ pressure-density term, the red line is buoyant production, and the dashed black line is the residual.

The budgets for $\overline{u'\theta'}$ and $\overline{w'\theta'}$ have not been shown. These budgets were quite unbalanced, with the correlations between p' and θ' being the apparent culprits. The reason for this discrepancy remains uncertain, but may be due to sampling error.

In this chapter, we have diagnosed the sources of first and second moment quantities. For several of the budgets, we were able to diagnose which terms are most important within the budgets. The wave transience seen in this chapter, most easily diagnosed by examining $\overline{u'\theta'}$ and $\overline{w'\theta'}$, indicates that transient effects may be important, and this is a fertile ground for future parameterizations. To understand how the momentum flux interacts with the mean flow, the next chapter will review the work of Eliassen and Palm (1960), and some interesting extensions of their work.

Chapter 8: Wave-mean flow interactions

Wave-mean flow interactions are linked to sudden stratospheric warmings (Matsuno 1971), the QBO (Lindzen and Holton 1968), topographic wave drag (Bretherton 1969), hurricane intensification (Montgomery and Kallenbach 1997) and many other atmospheric phenomena. The deposition of wave momentum flux has sufficiently strong effects on the mean flow that researchers have found it necessary to parameterize the effects of topographically (Palmer et al. 1986) and convectively (Kershaw 1995) generated gravity waves in GCMs. This chapter begins with an examination of the results of Eliassen and Palm (1960, hereafter EP), proceeding to an extension of their results, and then concluding with an alternate derivation by Andrews et al. (1987, also see Andrews 1983).

8.2. Overview of the Eliassen-Palm Theorem

How do we connect the Eliassen and Palm (1960; hereafter EP) result to conventional turbulence equations? We will begin by recapitulating the results of EP from their section 2.

The symbol γ can be interpreted as a measure of compressibility and is defined by EP as

$$\gamma = \frac{d\rho}{dp}, \tag{8.1}$$

and is also given by $1/c_s^2$, where c_s is the speed of sound. The basic-state pressure and density fulfill the hydrostatic relation,

$$\frac{dp_0}{dz} = -\rho_0 g. \tag{8.2}$$

Note that the basic state variables are related to the total quantities here by

$$a(x, z, t) = a_0(z) + a'(x, z, t). \tag{8.3}$$

The stratification of the basic-state density can be characterized by what EP refer to as the "Bjerknes coefficient," defined by

$$\Gamma = \frac{d\rho_0}{dp_0}. \tag{8.4}$$

Equation (8.2) can be rewritten and combined with (8.4) to derive an expression for $d\rho_0/dz$:

$$\frac{d\rho_0}{dz} = \Gamma\frac{dp_0}{dz} = -\Gamma\rho_0 g. \tag{8.5}$$

The combination of equations (8.1)-(8.5) can produce an expression for the perturbation density:

$$\rho' = \frac{N^2}{g}\rho_0\eta' + \gamma p'. \tag{8.6}$$

Here N is the Brunt-Väisälä frequency, defined by

$$N^2 = (\Gamma - \gamma)g^2, \tag{8.7}$$

and η' is the vertical displacement, not specifically defined by EP, but if

$$\frac{N^2\eta'}{g} = \frac{1}{\theta_0}\frac{d\theta_0}{dz}\eta' = \frac{\theta'}{\theta_0}, \tag{8.8}$$

then (8.6) is consistent with the Boussinesq approximation, as shown by Holton (1992, p. 200). This comes from assuming a hydrostatic base state, as in (8.2), and then examining the departures from hydrostatic balance, i.e.

$$\frac{1}{\rho}\frac{\partial p}{\partial z} + g = \frac{1}{\rho_0 + \rho'}\left(\frac{dp_0}{dz} + \frac{\partial p'}{\partial z}\right) + g, \tag{8.9}$$

which becomes

$$\frac{1}{\rho_0}\frac{dp_0}{dz}\left(1 - \frac{\rho'}{\rho_0}\right) + \frac{1}{\rho_0}\frac{\partial p'}{\partial z} + g = \frac{1}{\rho_0}\frac{\partial p'}{\partial z} + \frac{\rho'}{\rho_0}g \tag{8.10}$$

after using a series approximation for $1/(\rho_0 + \rho')$ and the hydrostatic approximation. Now, potential temperature can be written in terms of pressure and density as

$$\theta = \frac{p}{\rho R}\left(\frac{p_s}{p}\right)^{\kappa}. \tag{8.11}$$

Taking the logarithm of the basic-state and full versions of the above, we have

$$\ln\theta_0 = \frac{c_v}{c_p}\ln p_0 - \ln\rho_0 + \text{const}, \tag{8.12}$$

$$\ln\left[\theta_0\left(1+\frac{\theta'}{\theta_0}\right)\right] = \frac{c_v}{c_p}\ln\left[p_0\left(1+\frac{p'}{p_0}\right)\right] - \ln\left[\rho_0\left(1+\frac{\rho'}{\rho_0}\right)\right] + \text{const}. \tag{8.13}$$

Combining the two, we have

$$\frac{\theta'}{\theta_0} = \frac{c_v}{c_p}\frac{p'}{p_0} - \frac{\rho'}{\rho_0}, \tag{8.14}$$

after using the approximation $\ln(1+\varepsilon) \cong \varepsilon$ if $\varepsilon \ll 1$.

Now, we list the 2-D, hydrostatic, adiabatic, linearized momentum, continuity, and thermodynamic equations for steady flow, neglecting Coriolis terms. Note that wave transience can be important, as we saw in Chapter 7, and these terms will be retained in the analysis of the next section.

$$\rho_0\bar{u}\frac{\partial u'}{\partial x} + \rho_0\frac{d\bar{u}}{dz}w' + \frac{\partial p'}{\partial x} = 0, \tag{8.15}$$

$$\rho_0\bar{u}\frac{\partial w'}{\partial x} + \frac{\partial p'}{\partial z} + \frac{dp_0}{dz} + (\rho_0+\rho')g = 0, \tag{8.16}$$

$$\bar{u}\frac{\partial \rho'}{\partial x} + w'\frac{d\rho_0}{dz} + \rho_0\left(\frac{\partial u'}{\partial x} + \frac{\partial w'}{\partial z}\right) = 0, \tag{8.17}$$

$$\bar{u}\frac{\partial \theta'}{\partial x} + w'\frac{d\theta_0}{dz} = 0. \tag{8.18}$$

Using (8.2) and (8.6) in (8.16), we obtain the following

$$\rho_0\bar{u}\frac{\partial w'}{\partial x} + \frac{\partial p'}{\partial z} + N^2\rho_0\eta' + \gamma g p' = 0, \tag{8.19}$$

which is identical to the equation that EP use. Application of (8.5) and (8.6) to (8.17) yields

$$\bar{u}\left(\frac{N^2}{g}\rho_0\frac{\partial \eta'}{\partial x} + \gamma\frac{\partial p'}{\partial x}\right) - \Gamma\rho_0 g w' + \rho_0\left(\frac{\partial u'}{\partial x} + \frac{\partial w'}{\partial z}\right) = 0. \tag{8.20}$$

The displacement is related to the vertical velocity by

$$w' = \bar{u}\frac{\partial \eta'}{\partial x}. \tag{8.21}$$

This relation is obtained from the thermodynamic equation, if we use (8.8) to write it as

$$\bar{u}\frac{\partial}{\partial x}\left(\eta'\frac{d\theta_0}{dz}\right) + w'\frac{d\theta_0}{dz} = 0. \tag{8.22}$$

When (8.21) and (8.7) are used in (8.20), we obtain

$$\frac{\partial u'}{\partial x} + \frac{\partial w'}{\partial z} - \gamma g w' + \frac{\gamma \bar{u}}{\rho_0}\frac{\partial p'}{\partial x} = 0. \tag{8.23}$$

From the above equations, EP derived two relationships between the wave energy flux $\overline{p'w'}$ and the wave momentum flux $\overline{u'w'}$. We will derive the first of these relationships by multiplying (8.15) by u', (8.19) by w', and (8.23) by p':

$$\rho_0\bar{u}\frac{\partial}{\partial x}\left(\frac{u'u'}{2}\right) + \rho_0\frac{d\bar{u}}{dz}u'w' + u'\frac{\partial p'}{\partial x} = 0 \tag{8.24}$$

$$\rho_0\bar{u}\frac{\partial}{\partial x}\left(\frac{w'w'}{2}\right) + w'\frac{\partial p'}{\partial z} + N^2\rho_0\bar{u}\frac{\partial}{\partial x}\left(\frac{\eta'\eta'}{2}\right) + \gamma g p'w' = 0 \tag{8.25}$$

$$p'\frac{\partial u'}{\partial x} + p'\frac{\partial w'}{\partial z} - \gamma g p'w' + \frac{\gamma\bar{u}}{\rho_0}\frac{\partial}{\partial x}\left(\frac{p'p'}{2}\right) = 0. \tag{8.26}$$

Adding (8.24)-(8.26) yields the wave energy equation,

$$\frac{\partial}{\partial x}\left[\frac{\rho_0\bar{u}}{2}\left(u'u' + w'w' + N^2\eta'\eta' + \frac{\gamma p'p'}{\rho_0^2}\right) + p'u'\right] + \frac{\partial}{\partial z}(p'w') = -\rho_0\frac{d\bar{u}}{dz}u'w'. \tag{8.27}$$

Now we take a horizontal average of (8.27), using one of two methods that will yield the same result. The first method is simply a horizontal average over a domain with cyclic boundaries (e.g., around a latitude circle). The second method, which is what EP used, is over an infinite domain, with the assumption that perturbations approach zero as $x \to \pm\infty$:

$$\overline{a'b'} = \int_{-\infty}^{\infty} a'b'dx. \tag{8.28}$$

Note that with either averaging method,

$$\overline{\frac{\partial}{\partial x}(a'b')} = 0. \tag{8.29}$$

Using this property, and taking the zonal average of (8.27), we have

$$\frac{d}{dz}\overline{p'w'} = -\rho_0\frac{d\bar{u}}{dz}\overline{u'w'}. \tag{8.30}$$

The second relationship between the wave momentum flux and wave energy flux is derived by multiplying (8.15) by $\rho_0\bar{u}u'$, and adding it to (8.15) multiplied by p'. Within a multiplicative factor, the result of the first operation is given by (8.24), a simplified form of the prediction equation for zonal wind variance that is frequently encountered in turbulence studies:

$$\rho_0^2\bar{u}^2\frac{\partial}{\partial x}\left(\frac{u'u'}{2}\right) + \rho_0^2\bar{u}\frac{d\bar{u}}{dz}u'w' + \rho_0\bar{u}u'\frac{\partial p'}{\partial x} = 0. \tag{8.31}$$

The second operation results in a "wave energy" equation that is not often remarked upon in turbulence literature:

$$\rho_0\bar{u}p'\frac{\partial u'}{\partial x} + \rho_0\frac{d\bar{u}}{dz}p'w' + \frac{\partial}{\partial x}\left(\frac{p'p'}{2}\right) = 0. \tag{8.32}$$

Adding these two equations yields

$$\frac{\partial}{\partial x}\left[\rho_0^2\bar{u}^2\left(\frac{u'u'}{2}\right) + \rho_0\bar{u}p'u' + \frac{p'p'}{2}\right] + \rho_0\frac{d\bar{u}}{dz}p'w' = -\rho_0^2\bar{u}\frac{d\bar{u}}{dz}u'w', \tag{8.33}$$

which becomes, after zonally averaging

$$\overline{p'w'} = -\rho_0\bar{u}\overline{u'w'}, \tag{8.34}$$

for $d\bar{u}/dz \neq 0$. Combining (8.30) and (8.34), we obtain

$$-\frac{d}{dz}(\rho_0\bar{u}\overline{u'w'}) = -\rho_0\frac{d\bar{u}}{dz}\overline{u'w'}, \tag{8.35}$$

or equivalently

$$-\bar{u}\frac{d}{dz}(\rho_0\overline{u'w'}) - \rho_0\frac{d\bar{u}}{dz}\overline{u'w'} = -\rho_0\frac{d\bar{u}}{dz}\overline{u'w'}, \tag{8.36}$$

which indicates that unless $\bar{u} = 0$,

$$\frac{d}{dz}(\rho_0\overline{u'w'}) = 0, \tag{8.37}$$

$$\rho_0\overline{u'w'} = \text{const}. \tag{8.38}$$

In other words, EP found that the vertical flux of momentum is constant with height, except at critical levels where $\bar{u} = 0$. At these critical levels, all of the wave momentum flux is deposited.

8.2. Application to the fully nonlinear equations

The previous discussion focused on a relatively restrictive set of equations. In this section, we will allow the effects of transience and nonlinearity to enter into the wave-mean flow interaction problem, and then see under which circumstances the results reduce to those of EP. Now, the fully nonlinear, anelastic (Bannon, 1996) turbulence equations, again neglecting Coriolis effects, are given by

$$\rho_0\left(\frac{\partial u'}{\partial t} + u'\frac{\partial \bar{u}}{\partial x} + \bar{u}\frac{\partial u'}{\partial x} + w'\frac{\partial \bar{u}}{\partial z} + u'\frac{\partial u'}{\partial x} + \bar{w}\frac{\partial u'}{\partial z} + w'\frac{\partial u'}{\partial z} - \overline{u'\frac{\partial u'}{\partial x}} - \overline{w'\frac{\partial u'}{\partial z}}\right) + \frac{\partial p'}{\partial x} = F_x' \quad , \tag{8.39}$$

$$\rho_0\left(\frac{\partial w'}{\partial t} + u'\frac{\partial \bar{w}}{\partial x} + \bar{u}\frac{\partial w'}{\partial x} + u'\frac{\partial w'}{\partial x} + \bar{w}\frac{\partial w'}{\partial z} + w'\frac{\partial \bar{w}}{\partial z} + w'\frac{\partial w'}{\partial z} - \overline{u'\frac{\partial w'}{\partial x}} - \overline{w'\frac{\partial w'}{\partial z}} - \frac{g\theta'}{\theta_0}\right) + \rho_0\frac{\partial}{\partial z}\left(\frac{p'}{\rho_0}\right) = F_z' \quad , \tag{8.40}$$

$$\rho_0\left(\frac{\partial \theta'}{\partial t} + u'\frac{\partial \bar{\theta}}{\partial x} + \bar{u}\frac{\partial \theta'}{\partial x} + w'\frac{\partial \bar{\theta}}{\partial z} + u'\frac{\partial \theta'}{\partial x} + \bar{w}\frac{\partial \theta'}{\partial z} + w'\frac{\partial \theta'}{\partial z} - \overline{u'\frac{\partial \theta'}{\partial x}} - \overline{w'\frac{\partial \theta'}{\partial z}}\right) = \rho_0\dot{\theta}' . \tag{8.41}$$

Here the frictional terms are given by F_x and F_z. Note that in this section, we are using overbars for quantities that are horizontally averaged. These quantities can vary in both time and height. This is to be distinguished from quantities with "0" subscripts, which indicate base-state quantities that are functions of height only. If we use an anelastic version of the continuity equation, we have

$$\rho_0\frac{\partial u'}{\partial x} + \rho_0\frac{\partial w'}{\partial z} + w'\frac{d\rho_0}{dz} = 0 . \tag{8.42}$$

This is identical to (8.17), which is the initial form of the continuity equation used by EP, except for the term involving $\partial\rho'/\partial x$, which should be negligible anyway. Using the same vertically varying base state as EP, (8.42) becomes

$$\frac{\partial u'}{\partial x} + \frac{\partial w'}{\partial z} - \Gamma g w' = 0. \tag{8.43}$$

If we derive the analog to (8.33) by multiplying (8.39) by u', (8.40) by w', and (8.41) by $g^2\theta'/N_0^2\theta_0^2$, we get:

$$\begin{aligned}\rho_0\left(\frac{\partial}{\partial t}\left(\frac{u'u'}{2}\right) + u'u'\frac{\partial \bar{u}}{\partial x} + \bar{u}\frac{\partial}{\partial x}\left(\frac{u'u'}{2}\right) + \frac{\partial \bar{u}}{\partial z}u'w' + \bar{w}\frac{\partial}{\partial z}\left(\frac{u'u'}{2}\right) + \frac{\partial}{\partial x}\left(\frac{u'u'u'}{3}\right)\right)\\ -\rho_0\left(u'\overline{u'\frac{\partial u'}{\partial x}} + u'\overline{w'\frac{\partial u'}{\partial z}} - w'\frac{\partial}{\partial z}\left(\frac{u'u'}{2}\right)\right) + u'\frac{\partial p'}{\partial x} = u'F_x' \quad ,\end{aligned} \tag{8.44}$$

$$\begin{aligned}\rho_0\left(\frac{\partial}{\partial t}\left(\frac{w'w'}{2}\right) + u'w'\frac{\partial \bar{w}}{\partial x} + \bar{u}\frac{\partial}{\partial x}\left(\frac{w'w'}{2}\right) + u'\frac{\partial}{\partial x}\left(\frac{w'w'}{2}\right) + \bar{w}\frac{\partial}{\partial z}\left(\frac{w'w'}{2}\right) + w'w'\frac{\partial \bar{w}}{\partial z} +\right.\\ \left. w'\frac{\partial}{\partial z}\left(\frac{w'w'}{2}\right) - w'\overline{u'\frac{\partial w'}{\partial x}} - w'\overline{w'\frac{\partial w'}{\partial z}} - \frac{gw'\theta'}{\theta_0}\right) + \rho_0 w'\frac{\partial}{\partial z}\left(\frac{p'}{\rho_0}\right) = w'F_z' \quad ,\end{aligned} \tag{8.45}$$

$$\begin{aligned}\frac{\rho_0 g^2}{N_0^2\theta_0^2}\left(\frac{\partial}{\partial t}\left(\frac{\theta'\theta'}{2}\right) + u'\theta'\frac{\partial \bar{\theta}}{\partial x} + \bar{u}\frac{\partial}{\partial x}\left(\frac{\theta'\theta'}{2}\right) + w'\theta'\frac{\partial \bar{\theta}}{\partial z} + u'\frac{\partial}{\partial x}\left(\frac{\theta'\theta'}{2}\right) + \bar{w}\frac{\partial}{\partial z}\left(\frac{\theta'\theta'}{2}\right)\right)\\ -\frac{\rho_0 g^2}{N_0^2\theta_0^2}\left(-w'\frac{\partial}{\partial z}\left(\frac{\theta'\theta'}{2}\right) + \theta'\overline{u'\frac{\partial \theta'}{\partial x}} + \theta'\overline{w'\frac{\partial \theta'}{\partial z}}\right) = \frac{\rho_0 g^2}{N_0^2\theta_0^2}\theta'\dot{\theta}' \quad .\end{aligned} \tag{8.46}$$

After adding these equations, we obtain

$$\begin{aligned}\rho_0\left\{\frac{\partial}{\partial t}\left(\frac{u'u'}{2}\right) + u'u'\frac{\partial \bar{u}}{\partial x} + \bar{u}\frac{\partial}{\partial x}\left(\frac{u'u'}{2}\right) + \frac{\partial \bar{u}}{\partial z}u'w' + \frac{\partial}{\partial x}\left(\frac{u'u'u'}{3}\right) + \bar{w}\frac{\partial}{\partial z}\left(\frac{u'u'}{2}\right) + w'\frac{\partial}{\partial z}\left(\frac{u'u'}{2}\right)\right.\\ - u'\overline{u'\frac{\partial u'}{\partial x}} - u'\overline{w'\frac{\partial u'}{\partial z}} + \frac{\partial}{\partial t}\left(\frac{w'w'}{2}\right) + u'w'\frac{\partial \bar{w}}{\partial x} + \bar{u}\frac{\partial}{\partial x}\left(\frac{w'w'}{2}\right) + u'\frac{\partial}{\partial x}\left(\frac{w'w'}{2}\right) + \bar{w}\frac{\partial}{\partial z}\left(\frac{w'w'}{2}\right)\\ \left. + w'w'\frac{\partial \bar{w}}{\partial z} + w'\frac{\partial}{\partial z}\left(\frac{w'w'}{2}\right) - w'\overline{u'\frac{\partial w'}{\partial x}} - w'\overline{w'\frac{\partial w'}{\partial z}} - \frac{gw'\theta'}{\bar{\theta}}\right\} +\\ \frac{\rho_0 g^2}{N_0^2\theta_0^2}\left\{\frac{\partial}{\partial t}\left(\frac{\theta'\theta'}{2}\right) + u'\theta'\frac{\partial \bar{\theta}}{\partial x} + \bar{u}\frac{\partial}{\partial x}\left(\frac{\theta'\theta'}{2}\right) + w'\theta'\frac{\partial \bar{\theta}}{\partial z}\right.\\ \left. + u'\frac{\partial}{\partial x}\left(\frac{\theta'\theta'}{2}\right) + \bar{w}\frac{\partial}{\partial z}\left(\frac{\theta'\theta'}{2}\right) + w'\frac{\partial}{\partial z}\left(\frac{\theta'\theta'}{2}\right) - \theta'\overline{u'\frac{\partial \theta'}{\partial x}} - \theta'\overline{w'\frac{\partial \theta'}{\partial z}}\right\}\\ + \rho_0 w'\frac{\partial}{\partial z}\left(\frac{p'}{\rho_0}\right) + u'\frac{\partial p'}{\partial x} = \frac{\rho_0 g^2}{N_0^2\theta_0^2}\theta'\dot{\theta}' + u'F_x' + w'F_z' \quad .\end{aligned} \tag{8.47}$$

Now, if we multiply (8.42) by

$$\frac{u'u'}{2}+\frac{w'w'}{2}+\frac{g^2}{N_0^2\theta_0^2}\left(\frac{\theta'\theta'}{2}\right)+\frac{p'}{\rho_0} \tag{8.48}$$

and add to (8.47), we have:

$$\begin{aligned}
&\rho_0\Bigg\{\frac{\partial}{\partial t}\left(\frac{u'u'}{2}\right)+u'u'\frac{\partial\bar{u}}{\partial x}+\bar{u}\frac{\partial}{\partial x}\left(\frac{u'u'}{2}\right)+\frac{\partial\bar{u}}{\partial z}u'w'+\bar{w}\frac{\partial}{\partial z}\left(\frac{u'u'}{2}\right)-\overline{u'u'\frac{\partial u'}{\partial x}}-\overline{u'w'\frac{\partial u'}{\partial z}}\\
&\quad+\frac{\partial}{\partial t}\left(\frac{w'w'}{2}\right)+u'w'\frac{\partial\bar{w}}{\partial x}+\bar{u}\frac{\partial}{\partial x}\left(\frac{w'w'}{2}\right)+\bar{w}\frac{\partial}{\partial z}\left(\frac{w'w'}{2}\right)+w'w'\frac{\partial\bar{w}}{\partial z}\\
&\quad-\overline{w'u'\frac{\partial w'}{\partial x}}-\overline{w'w'\frac{\partial w'}{\partial z}}-\frac{gw'\theta'}{\theta_0}\Bigg\}+\frac{\rho_0 g^2}{N_0^2\theta_0^2}\Bigg\{\frac{\partial}{\partial t}\left(\frac{\theta'\theta'}{2}\right)+u'\theta'\frac{\partial\bar{\theta}}{\partial x}+\bar{u}\frac{\partial}{\partial x}\left(\frac{\theta'\theta'}{2}\right)\\
&\quad+w'\theta'\frac{\partial\bar{\theta}}{\partial z}+\bar{w}\frac{\partial}{\partial z}\left(\frac{\theta'\theta'}{2}\right)-\overline{\theta'u'\frac{\partial\theta'}{\partial x}}-\overline{\theta'w'\frac{\partial\theta'}{\partial z}}\Bigg\}+\frac{\partial}{\partial x}\left(\frac{\rho_0 u'u'u'}{2}\right)+\frac{\partial}{\partial z}\left(\frac{\rho_0 u'u'w'}{2}\right)\\
&\quad+\frac{\partial}{\partial x}\left(\frac{\rho_0 u'w'w'}{2}\right)+\frac{\partial}{\partial z}\left(\frac{\rho_0 w'w'w'}{2}\right)+\frac{g^2}{N_0^2\theta_0^2}\left[\frac{\partial}{\partial x}\left(\frac{\rho_0 u'\theta'\theta'}{2}\right)+\frac{\partial}{\partial z}\left(\frac{\rho_0 w'\theta'\theta'}{2}\right)\right]\\
&\quad+\frac{\partial}{\partial x}(p'u')+\frac{\partial}{\partial z}(p'w')=\frac{\rho_0 g^2}{N_0^2\theta_0^2}\theta'\dot{\theta}'+u'F_x'+w'F_z' \quad .
\end{aligned} \tag{8.49}$$

If we take the average of (8.49), and use $\overline{a'\bar{b}}=0$, we are left with:

$$\begin{aligned}
&\rho_0\Bigg\{\frac{\partial}{\partial t}\left(\overline{\frac{u'u'}{2}}\right)+\overline{u'u'}\frac{\partial\bar{u}}{\partial x}+\bar{u}\frac{\partial}{\partial x}\left(\overline{\frac{u'u'}{2}}\right)+\frac{\partial\bar{u}}{\partial z}\overline{u'w'}+\bar{w}\frac{\partial}{\partial z}\left(\overline{\frac{u'u'}{2}}\right)+\frac{\partial}{\partial t}\left(\overline{\frac{w'w'}{2}}\right)+\overline{u'w'}\frac{\partial\bar{w}}{\partial x}\\
&\quad\bar{u}\frac{\partial}{\partial x}\left(\overline{\frac{w'w'}{2}}\right)+\bar{w}\frac{\partial}{\partial z}\left(\overline{\frac{w'w'}{2}}\right)+\overline{w'w'}\frac{\partial\bar{w}}{\partial z}-\frac{g\overline{w'\theta'}}{\theta_0}\Bigg\}+\frac{\rho_0 g^2}{N_0^2\theta_0^2}\Bigg\{\frac{\partial}{\partial t}\left(\overline{\frac{\theta'\theta'}{2}}\right)+\overline{u'\theta'}\frac{\partial\bar{\theta}}{\partial x}\\
&\quad+\bar{u}\frac{\partial}{\partial x}\left(\overline{\frac{\theta'\theta'}{2}}\right)+\overline{w'\theta'}\frac{\partial\bar{\theta}}{\partial z}+\bar{w}\frac{\partial}{\partial z}\left(\overline{\frac{\theta'\theta'}{2}}\right)\Bigg\}+\frac{\partial}{\partial x}\left(\overline{\frac{\rho_0 u'u'u'}{2}}\right)+\frac{\partial}{\partial z}\left(\overline{\frac{\rho_0 u'u'w'}{2}}\right)\\
&\quad+\frac{\partial}{\partial x}\left(\overline{\frac{\rho_0 u'w'w'}{2}}\right)+\frac{\partial}{\partial z}\left(\overline{\frac{\rho_0 w'w'w'}{2}}\right)+\frac{g^2}{N_0^2\theta_0^2}\left[\frac{\partial}{\partial x}\left(\overline{\frac{\rho_0 u'\theta'\theta'}{2}}\right)+\frac{\partial}{\partial z}\left(\overline{\frac{\rho_0 w'\theta'\theta'}{2}}\right)\right]\\
&\quad+\frac{\partial}{\partial x}(\overline{p'u'})+\frac{\partial}{\partial z}(\overline{p'w'})=\frac{\rho_0 g^2}{N_0^2\theta_0^2}\overline{\theta'\dot{\theta}'}+\overline{u'F_x'}+\overline{w'F_z'} \quad .
\end{aligned} \tag{8.50}$$

So far, we have made no assumptions about the boundary conditions for the horizontal averages. If we now use averages similar to EP, with

$$\overline{\frac{\partial}{\partial x}a'b'} = \frac{\partial}{\partial x}\overline{a'b'} = 0, \tag{8.51}$$

then many of the terms in (8.50) are zero:

$$\begin{aligned}\frac{\partial}{\partial z}(\overline{p'w'}) = &-\rho_0\frac{\partial\bar{u}}{\partial z}\overline{u'w'} - \rho_0\overline{w'w'}\frac{\partial\bar{w}}{\partial z} - \rho_0\frac{\partial}{\partial t}\left[\frac{\overline{u'u'}}{2} + \frac{\overline{w'w'}}{2} + \frac{g^2}{N_0^2\theta_0^2}\left(\frac{\overline{\theta'\theta'}}{2}\right)\right] \\ &-\rho_0\bar{w}\frac{\partial}{\partial z}\left[\frac{\overline{u'u'}}{2} + \frac{\overline{w'w'}}{2} + \frac{g^2}{N_0^2\theta_0^2}\left(\frac{\overline{\theta'\theta'}}{2}\right)\right] + \rho_0\overline{w'\theta'}\left(\frac{g}{\theta_0} - \frac{g^2}{N_0^2\theta_0^2}\frac{\partial\bar{\theta}}{\partial z}\right) \\ &-\left[\frac{\partial}{\partial z}\left(\frac{\rho_0\overline{u'u'w'}}{2}\right) + \frac{\partial}{\partial z}\left(\frac{\rho_0\overline{w'w'w'}}{2}\right) + \frac{g^2}{N_0^2\theta_0^2}\frac{\partial}{\partial z}\left(\frac{\rho_0\overline{w'\theta'\theta'}}{2}\right)\right] \\ &+\frac{\rho_0 g^2}{N_0^2\theta_0^2}\overline{\theta'\dot{\theta}'} + \overline{u'F_x'} + \overline{w'F_z'} \quad .\end{aligned} \tag{8.52}$$

When the anelastic equations are used, the divergence of the wave energy flux is apparently balanced by several additional terms that are neglected in the simple result (8.30) due to EP. The second term on the right hand side (RHS) is associated with the divergence of the mean vertical velocity. The next group of terms on the RHS indicates that a local increase in the zonal-mean perturbation energy will be associated with a convergence of the wave energy flux. The following group of terms are associated with the advection of wave energy by the mean vertical wind. The next term indicates that vertical heat flux can have either a positive or negative effect on the wave energy flux divergence, depending on the strength of the zonal-mean potential temperature stratification. We can see this by substituting for the square of the base-state Brunt-Väisälä frequency

$$N_0^2 = \frac{g}{\theta_0}\frac{d\theta_0}{dz}, \tag{8.53}$$

which leads to the result

$$\frac{g}{\theta_0} - \frac{g^2}{N_0^2\theta_0^2}\frac{\partial\bar{\theta}}{\partial z} = \frac{g}{\theta_0}\left[1 - \frac{(\partial\bar{\theta}/\partial z)}{(d\theta_0/dz)}\right]. \tag{8.54}$$

The following group of terms are due to the vertical transport of perturbation energy. The next term indicates that if diabatic heating and the potential temperature perturbation are positively correlated, they act as a source of wave energy flux divergence. Finally, the last two terms will be small if friction is negligible.

Note that for pure linear gravity-wave solutions, the triple-moment terms vanish if the horizontal average is over a wavelength such that

$$\lambda = \frac{2\pi n}{k}, \tag{8.55}$$

where n is an integer. We will show this by beginning with three wave fields of the form

$$a' = \hat{a}\exp(i\phi) + \hat{a}^*\exp(-i\phi) \tag{8.56}$$

where ϕ is defined by

$$\phi = kx + mz + \omega t, \tag{8.57}$$

and the star indicates complex conjugate. The amplitudes can be expanded as

$$\hat{a} = a_r + ia_i. \tag{8.58}$$

Applying a horizontal average to the wave fields, we have

$$\begin{aligned}\overline{a'b'c'} = \int_0^{2\pi/k} &[(a_r + ia_i)\exp(i\phi) + (a_r - ia_i)\exp(-i\phi)][(b_r + ib_i)\exp(i\phi) + \\ &(b_r - ib_i)\exp(-i\phi)][(c_r + ic_i)\exp(i\phi) + (c_r - ic_i)\exp(-i\phi)]dx \quad ,\end{aligned} \tag{8.59}$$

$$\begin{aligned}= \int_0^{2\pi/k} &[(a_r + ia_i)(b_r + ib_i)(c_r + ic_i)\exp(3i\phi) + (a_r + ia_i)(b_r + ib_i)(c_r - ic_i)\exp(i\phi) \\ &+ 2(a_rb_r + a_ib_i)(c_r + ic_i)\exp(i\phi) + 2(a_rb_r + a_ib_i)(c_r - ic_i)\exp(-i\phi) \\ &+ (a_r - ia_i)(b_r - ib_i)(c_r - ic_i)\exp(-i\phi) + (a_r - ia_i)(b_r - ib_i)(c_r - ic_i)\exp(-3i\phi)]dx \quad .\end{aligned} \tag{8.60}$$

Since the amplitudes, height, and time can be regarded as constants over the integration, we can evaluate the above integrals using

$$\begin{aligned}\int_0^{2\pi/k} \text{const}\exp(ni\phi)dx &= \text{const}\exp[in(mz - \omega t)] \int_0^{2\pi/k} \exp(inkx)dx \quad , \\ &= \text{const}\exp[in(mz - \omega t)]\left[\frac{\exp(inkx)}{ink}\right]_0^{2\pi/k} \quad , \\ &= \text{const}\exp[in(mz - \omega t)]\left[\frac{\exp(2\pi in) - 1}{ink}\right] \quad ,\end{aligned} \tag{8.61}$$

which is zero if n is an integer. Therefore,

$$\overline{a'b'c'} = 0 \tag{8.62}$$

for linear gravity wave solutions. This means that (8.52) reduces to

$$\frac{\partial}{\partial z}(\overline{p'w'}) = -\rho_0\frac{\partial\bar{u}}{\partial z}\overline{u'w'} - \rho_0\overline{w'w'}\frac{\partial\bar{w}}{\partial z} - \rho_0\frac{\partial}{\partial t}\left[\frac{\overline{u'u'}}{2} + \frac{\overline{w'w'}}{2} + \frac{g^2}{N_0^2\theta_0^2}\left(\frac{\overline{\theta'\theta'}}{2}\right)\right]$$
$$-\rho_0\bar{w}\frac{\partial}{\partial z}\left[\frac{\overline{u'u'}}{2} + \frac{\overline{w'w'}}{2} + \frac{g^2}{N_0^2\theta_0^2}\left(\frac{\overline{\theta'\theta'}}{2}\right)\right] \tag{8.63}$$

for linear gravity waves, in the absence of friction. Here we have used the fact that $\overline{w'\theta'}$ for linear gravity waves. If $\bar{w} = 0$ and the waves are steady, then (8.63) reduces to the Eliassen-Palm result of (8.30).

Now, we derive the analog of (8.34) by first multiplying (8.39) by $\rho_0\bar{u}u'$, and then multiplying (8.39) by p':

$$\rho_0^2\bar{u}\left[\frac{\partial}{\partial t}\left(\frac{u'u'}{2}\right) + u'u'\frac{\partial\bar{u}}{\partial x} + \bar{u}\frac{\partial}{\partial x}\left(\frac{u'u'}{2}\right) + u'w'\frac{\partial\bar{u}}{\partial z} + u'\frac{\partial}{\partial x}\left(\frac{u'u'}{2}\right) + \bar{w}\frac{\partial}{\partial z}\left(\frac{u'u'}{2}\right) + w'\frac{\partial}{\partial z}\left(\frac{u'u'}{2}\right)\right]$$
$$-\rho_0^2\bar{u}\left(u'u'\overline{\frac{\partial u'}{\partial x}} + u'w'\overline{\frac{\partial u'}{\partial z}}\right) + \rho_0\bar{u}u'\frac{\partial p'}{\partial x} = \rho_0\bar{u}u'F_x' \quad , \tag{8.64}$$

$$\rho_0\left(p'\frac{\partial u'}{\partial t} + p'u'\frac{\partial\bar{u}}{\partial x} + \bar{u}p'\frac{\partial u'}{\partial x} + \frac{\partial\bar{u}}{\partial z}p'w' + p'u'\frac{\partial u'}{\partial x} + \bar{w}p'\frac{\partial u'}{\partial z} + p'w'\frac{\partial u'}{\partial z}\right.$$
$$\left. - p'u'\overline{\frac{\partial u'}{\partial x}} - p'w'\overline{\frac{\partial u'}{\partial z}}\right) + \frac{\partial}{\partial x}\left(\frac{p'p'}{2}\right) = p'F_x' \quad . \tag{8.65}$$

Equation (8.64) is a version of a prediction equation for the variance of u' that is frequently encountered in turbulence studies. Equation (8.65) is not frequently encountered, however. Addition of these equations gives us

$$\rho_0\left\{\rho_0\bar{u}\frac{\partial}{\partial t}\left(\frac{u'u'}{2}\right) + \rho_0\bar{u}\frac{\partial\bar{u}}{\partial x}u'u' + \rho_0\bar{u}^2\frac{\partial}{\partial x}\left(\frac{u'u'}{2}\right) + \rho_0\bar{u}\frac{\partial\bar{u}}{\partial z}u'w' + \rho_0\bar{u}u'\frac{\partial}{\partial x}\left(\frac{u'u'}{2}\right)\right.$$
$$+ \rho_0\bar{u}w'\frac{\partial}{\partial z}\left(\frac{u'u'}{2}\right) + \rho_0\bar{u}\bar{w}\frac{\partial}{\partial z}\left(\frac{u'u'}{2}\right) + \frac{\partial\bar{u}}{\partial x}p'u' + \bar{u}p'\frac{\partial u'}{\partial x} + \frac{\partial\bar{u}}{\partial z}p'w' + p'u'\frac{\partial u'}{\partial x} +$$
$$\left. p'w'\frac{\partial u'}{\partial z} + p'\frac{\partial u'}{\partial t} - \rho_0\bar{u}u'u'\overline{\frac{\partial u'}{\partial x}} - \rho_0\bar{u}u'w'\overline{\frac{\partial u'}{\partial z}} - p'u'\overline{\frac{\partial u'}{\partial x}} - p'w'\overline{\frac{\partial u'}{\partial z}} + \bar{u}u'\frac{\partial p'}{\partial x}\right\} + \tag{8.66}$$

$$\frac{\partial}{\partial x}\left(\frac{p'p'}{2}\right) = \rho_0\bar{u}u'F_x' + p'F_x' \quad ,$$

which becomes

$$\rho_0\frac{\partial\bar{u}}{\partial z}\overline{p'w'} = -\rho_0^2\bar{u}\frac{\partial\bar{u}}{\partial z}\overline{u'w'} - \rho_0^2\bar{u}\frac{\partial}{\partial t}\left(\frac{\overline{u'u'}}{2}\right) - \rho_0\overline{p'\frac{\partial u'}{\partial t}} - \rho_0^2\bar{u}\overline{w'\frac{\partial}{\partial z}\left(\frac{u'u'}{2}\right)}$$
$$- \rho_0^2\bar{u}\bar{w}\frac{\partial}{\partial z}\left(\frac{\overline{u'u'}}{2}\right) - \rho_0\overline{p'u'\frac{\partial u'}{\partial x}} - \rho_0\overline{p'w'\frac{\partial u'}{\partial z}} + \rho_0\bar{u}\overline{u'F_x'} + \overline{p'F_x'} \tag{8.67}$$

after averaging. Note that for steady, linear, gravity waves (8.67) reduces to the EP result of (8.34), in the absence of friction and a mean vertical velocity.

Unlike the results of EP that were derived from (8.30) and (8.34), (8.52) and (8.67) cannot be combined into a simple non-interaction theorem such as (8.37). If we neglect friction and assume steady, adiabatic flow with $\bar{w} = 0$, then (8.52) and (8.67) become

$$\frac{\partial}{\partial z}(\overline{p'w'}) = -\rho_0\overline{u'w'}\frac{\partial\bar{u}}{\partial z} - \frac{\partial}{\partial z}\left(\rho_0\frac{\overline{u'u'w'}}{2}\right) - \frac{\partial}{\partial z}\left(\rho_0\frac{\overline{w'w'w'}}{2}\right) - \frac{g^2}{N_0^2\theta_0^2}\frac{\partial}{\partial z}\left(\frac{\rho_0\overline{w'\theta'\theta'}}{2}\right)$$
$$+ \rho_0\overline{w'\theta'}\left(\frac{g}{\theta_0} - \frac{g^2}{N_0^2\theta_0^2}\frac{\partial\bar{\theta}}{\partial z}\right) \tag{8.68}$$

and

$$\frac{\partial\bar{u}}{\partial z}\overline{p'w'} = -\rho_0\bar{u}\frac{\partial\bar{u}}{\partial z}\overline{u'w'} - \rho_0\bar{u}\overline{w'\frac{\partial}{\partial z}\left(\frac{u'u'}{2}\right)} - \overline{p'u'\frac{\partial u'}{\partial x}} - \overline{p'w'\frac{\partial u'}{\partial z}}. \tag{8.69}$$

These results were derived from the u' equation, (8.39). It seems natural to wonder if by applying the steps (8.64)-(8.67) to the w' equation, (8.40), we can obtain more physical information about the system. Multiplying the steady version of (8.40) by p', we obtain

$$\rho_0\left(p'u'\frac{\partial\bar{w}}{\partial x} + \bar{u}p'\frac{\partial w'}{\partial x} + p'u'\frac{\partial w'}{\partial x} + \bar{w}p'\frac{\partial w'}{\partial z} + p'w'\frac{\partial\bar{w}}{\partial z} + p'w'\frac{\partial w'}{\partial z}\right.$$
$$\left. - p'\overline{u'\frac{\partial w'}{\partial x}} - p'\overline{w'\frac{\partial w'}{\partial z}}\right) - \frac{\rho_0 g p'\theta'}{\theta_0} + \rho_0 p'\frac{\partial}{\partial z}\left(\frac{p'}{\rho_0}\right) = p'F_z' \quad . \tag{8.70}$$

If we multiply (8.40) by $\rho_0\bar{w}w'$, we get

$$\rho_0^2\bar{w}\left(u'w'\frac{\partial\bar{w}}{\partial x} + \bar{u}\frac{\partial}{\partial x}\left(\frac{w'w'}{2}\right) + u'\frac{\partial}{\partial x}\left(\frac{w'w'}{2}\right) + \bar{w}\frac{\partial}{\partial z}\left(\frac{w'w'}{2}\right) + w'w'\frac{\partial\bar{w}}{\partial z} + \frac{\partial}{\partial z}\left(\frac{w'w'w'}{3}\right)\right.$$
$$\left. - w'\overline{u'\frac{\partial w'}{\partial x}} - w'\overline{w'\frac{\partial w'}{\partial z}} - \frac{gw'\theta'}{\theta_0}\right) + \rho_0^2\bar{w}w'\frac{\partial}{\partial z}\left(\frac{p'}{\rho_0}\right) = \rho_0\bar{w}w'F_z' \quad . \tag{8.71}$$

Adding the two yields

$$\rho_0\Big\{ p'u'\frac{\partial \bar{w}}{\partial x} + \bar{u}p'\frac{\partial w'}{\partial x} + p'u'\frac{\partial w'}{\partial x} + \bar{w}p'\frac{\partial w'}{\partial z} + p'w'\frac{\partial \bar{w}}{\partial z} + p'w'\frac{\partial w'}{\partial z} - \overline{p'u'\frac{\partial w'}{\partial x}} - \overline{p'w'\frac{\partial w'}{\partial z}}$$

$$- \frac{gp'\theta'}{\bar{\theta}} + p'\frac{\partial}{\partial z}\left(\frac{p'}{\rho_0}\right) + \rho_0\bar{w}\frac{\partial \bar{w}}{\partial x}u'w' + \rho_0\bar{u}\bar{w}\frac{\partial}{\partial x}\left(\frac{w'w'}{2}\right) + \rho_0\bar{w}u'\frac{\partial}{\partial x}\left(\frac{w'w'}{2}\right) + \tag{8.72}$$

$$\rho_0\bar{w}^2\frac{\partial}{\partial z}\left(\frac{w'w'}{2}\right) + \rho_0\bar{w}\frac{\partial \bar{w}}{\partial z}w'w' + \rho_0\bar{w}\frac{\partial}{\partial z}\left(\frac{w'w'w'}{3}\right) - \rho_0\bar{w}\overline{u'\frac{\partial w'}{\partial x}}w'$$

$$- \rho_0\bar{w}\overline{w'\frac{\partial w'}{\partial z}}w' - \rho_0 g\bar{w}\frac{w'\theta'}{\theta_0}\Big\} + \rho_0^2\bar{w}w'\frac{\partial}{\partial z}\left(\frac{p'}{\rho_0}\right) = (\rho_0\bar{w}w' + p')F_z' \quad .$$

After averaging, we obtain

$$\rho_0\Big\{ \bar{u}\overline{p'\frac{\partial w'}{\partial x}} + \overline{p'u'\frac{\partial w'}{\partial x}} + \bar{w}\overline{p'\frac{\partial w'}{\partial z}} + \overline{p'w'}\frac{\partial \bar{w}}{\partial z} + \overline{p'w'\frac{\partial w'}{\partial z}} - \frac{g\overline{p'\theta'}}{\bar{\theta}} + \rho_0\bar{w}\overline{u'\frac{\partial}{\partial x}\left(\frac{w'w'}{2}\right)}$$

$$+ \rho_0\bar{w}^2\frac{\partial}{\partial z}\left(\overline{\frac{w'w'}{2}}\right) + \rho_0\bar{w}\frac{\partial \bar{w}}{\partial z}\overline{w'w'} + \rho_0\bar{w}\frac{\partial}{\partial z}\left(\overline{\frac{w'w'w'}{3}}\right) - \rho_0 g\bar{w}\frac{\overline{w'\theta'}}{\theta_0}\Big\} \tag{8.73}$$

$$+ \frac{\partial}{\partial z}\left(\overline{\frac{p'p'}{2}}\right) + \Gamma g\overline{p'p'} - \Gamma g\rho_0\bar{w}\overline{p'w'} + \rho_0\bar{w}\overline{w'\frac{\partial p'}{\partial z}} = \rho_0\bar{w}\overline{w'F_z'} + \overline{p'F_z'} \quad .$$

If we neglect friction and the mean vertical velocity $\bar{w}$, then the above expression simplifies to

$$\rho_0\Big\{ \bar{u}\overline{p'\frac{\partial w'}{\partial x}} + \overline{p'u'\frac{\partial w'}{\partial x}} + \overline{p'w'\frac{\partial w'}{\partial z}} - \frac{g\overline{p'\theta'}}{\theta_0}\Big\} + \frac{\partial}{\partial z}\left(\overline{\frac{p'p'}{2}}\right) + \Gamma g\overline{p'p'} = 0. \tag{8.74}$$

Now, as shown in (8.55)-(8.62), triple-moment terms should vanish for linear waves. Also, since the linear wave solutions for p', u', and w' are each either in phase or π radians out of phase, covariances between these perturbation fields are nonzero in general. However, the linear wave solution for θ' is $\pi/2$ radians out of phase with those of p', u', and w', so covariances between these fields and θ' are zero. Taking this into account, (8.74) reduces to a single equation in the variance of the perturbation pressure $\overline{p'p'}$:

$$\frac{\partial}{\partial z}\left(\overline{\frac{p'p'}{2}}\right) = -\Gamma g\overline{p'p'}. \tag{8.75}$$

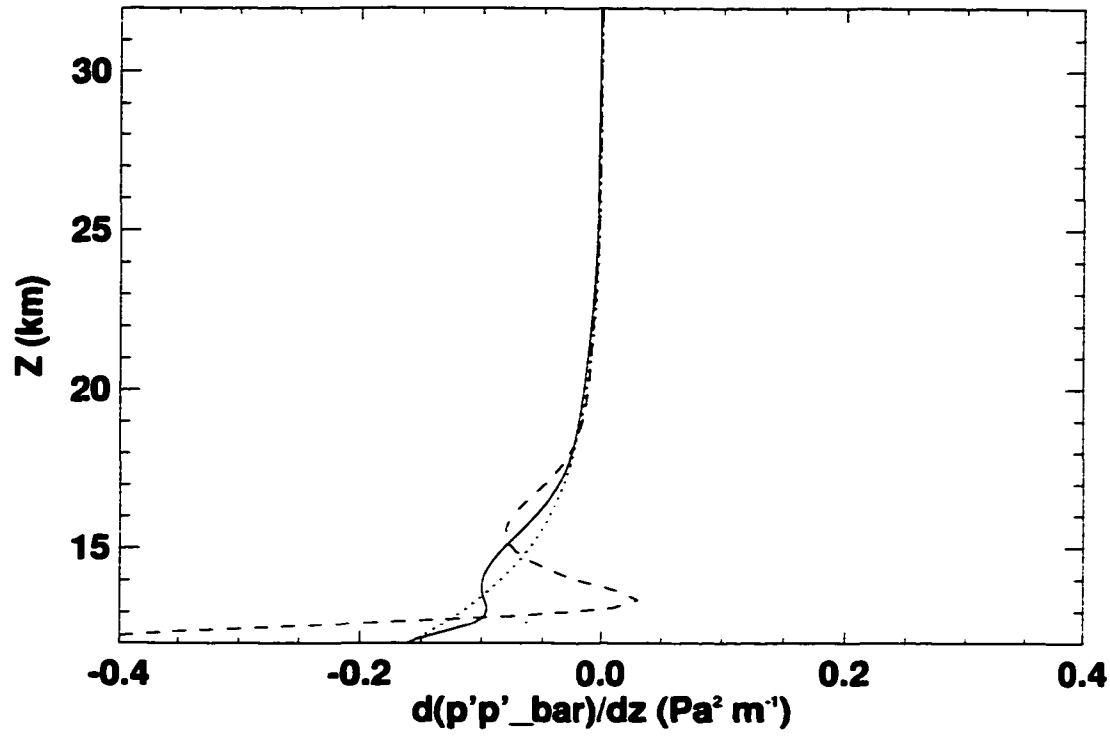

Fig. 8.1. Comparison of the RHS (solid line) and LHS (dashed line) of (8.75) in the model stratosphere of the WK control run averaged from 2-4 h, along with a simple exponential function based on the value of $\overline{p'p'}$ at z = 12.125 km.

Provided that Γ is a constant, (8.75) indicates that $\overline{p'p'}$ decreases exponentially with height, with an *e*-folding distance of

$$\frac{1}{2\Gamma g}. \tag{8.76}$$

For an isothermal, hydrostatic atmosphere (which is a good approximation to the lower stratosphere), we have

$$\frac{1}{2\Gamma g} = \frac{R\bar{T}}{2g}, \tag{8.77}$$

which corresponds to a distance of approximately 3 km, using typical values for the lower stratosphere. The RHS and LHS of (8.75) are compared to one another in Fig. 8.1, based on time-averaged (t = 2-4 hours) data in the model stratosphere of the WK control run. Also plotted is an exponential function that uses the value of $\overline{p'p'}$ at the tropopause, and then decays at a rate given by (8.77). The three curves agree fairly well with one another, although there is some disagreement in the lowermost stratosphere, where the influences

of wave transience and penetrative convection may play a role. Similar results were found for other periods of time in the WK control run.

8.2.. Derivation of E-P Theorem in Isentropic Coordinates

Following Andrews et al. (1987, p. 142), we begin with the flux form of the zonal momentum equation with an isentropic (i.e. constant θ surfaces) vertical coordinate, neglecting body forces:

$$\frac{\partial}{\partial t}(\sigma u)+\frac{1}{a\cos\phi}\left[\frac{\partial}{\partial\lambda}(\sigma uu)+\frac{\partial}{\partial\phi}(\sigma uv\cos\phi)\right]-\sigma v\left(f+\frac{u\tan\phi}{a}\right)+\frac{1}{a\cos\phi}\sigma\frac{\partial M}{\partial\lambda}= -\frac{\partial}{\partial\theta}(\sigma u\dot{\theta}) \quad . \tag{8.78}$$

Here, λ represents longitude, ϕ represents latitude, and M is the Montgomery potential, which is defined by

$$M = gz + c_p T . \tag{8.79}$$

Now we adjust the last term on the LHS of (8.78), by first using the definition of the mass-like variable σ

$$\sigma = -\frac{1}{g}\frac{\partial p}{\partial\theta}, \tag{8.80}$$

$$\sigma\frac{\partial M}{\partial\lambda} = -\frac{1}{g}\frac{\partial p}{\partial\theta}\frac{\partial M}{\partial\lambda} = -\frac{1}{g}\frac{\partial}{\partial\theta}\left(p\frac{\partial M}{\partial\lambda}\right)+\frac{1}{g}p\frac{\partial}{\partial\lambda}\left(\frac{\partial M}{\partial\theta}\right). \tag{8.81}$$

Now, the hydrostatic equation is given by

$$\frac{\partial M}{\partial\theta} = \Pi(p)\equiv c_p\left(\frac{p}{p_s}\right)^{R/c_p}. \tag{8.82}$$

Substituting (8.82) into (8.81), we obtain

$$\sigma\frac{\partial M}{\partial\lambda} = -\frac{1}{g}\frac{\partial}{\partial\theta}\left(p\frac{\partial M}{\partial\lambda}\right)+\frac{1}{g}p\frac{\partial p}{\partial\lambda}\frac{d\Pi}{dp}. \tag{8.83}$$

The above expression is identical to that of the second line of Eqn. (3.9.2) in Andrews et al. (1987). The following analysis produces a slightly different expression from the third line of the same equation (see below), although this will be a moot point once the zonal mean is taken of the relevant terms. In any case, the quantity given by

$$\frac{\partial}{\partial\lambda}\left[\frac{1}{g}\int_{p_s}^{p} p'\frac{d\Pi(p')}{dp'}dp'\right] \tag{8.84}$$

becomes

$$\frac{1}{g}p\frac{\partial p d\Pi}{\partial\lambda dp}+\frac{1}{g}\int_{p_s}^{p}\frac{\partial}{\partial\lambda}\left[p'\frac{d\Pi(p')}{dp'}\right]dp' \tag{8.85}$$

after using Leibniz's rule.

So, we can substitute the difference of two integrals for the second term on the RHS of (8.83):

$$\sigma\frac{\partial M}{\partial\lambda} = -\frac{1}{g}\frac{\partial}{\partial\theta}\left(p\frac{\partial M}{\partial\lambda}\right)+\frac{\partial}{\partial\lambda}\left[\frac{1}{g}\int_{p_s}^{p} p'\frac{d\Pi(p')}{dp'}dp'\right]-\frac{1}{g}\int_{p_s}^{p}\frac{\partial}{\partial\lambda}\left[p'\frac{d\Pi(p')}{dp'}\right]dp' . \tag{8.86}$$

The third line of Eqn. (3.9.2) in Andrews et al. (1987) does not contain the third term on the RHS of (8.86). Substituting into (8.78), we have the expression,

$$\begin{aligned}&\frac{\partial}{\partial t}(\sigma u)+\frac{1}{a\cos\phi}\left[\frac{\partial}{\partial\lambda}(\sigma uu)+\frac{\partial}{\partial\phi}(\sigma uv\cos\phi)\right]-\sigma v\left(f+\frac{u\tan\phi}{a}\right)\\ &+\frac{1}{a\cos\phi}\left\{-\frac{1}{g}\frac{\partial}{\partial\theta}\left(p\frac{\partial M}{\partial\lambda}\right)+\frac{\partial}{\partial\lambda}\left[\frac{1}{g}\int_{p_s}^{p} p'\frac{d\Pi(p')}{dp'}dp'\right]-\frac{1}{g}\int_{p_s}^{p}\frac{\partial}{\partial\lambda}\left[p'\frac{d\Pi(p')}{dp'}\right]dp'\right\}\\ &\qquad = -\frac{\partial}{\partial\theta}(\sigma u\dot{\theta}) \quad .\end{aligned} \tag{8.87}$$

When we take the zonal mean of (8.87), defined by

$$\overline{A}(\phi,\theta,t) = \frac{1}{2\pi}\int_{0}^{2\pi} A(\lambda,\phi,\theta,t)d\lambda , \tag{8.88}$$

we eliminate the $\partial/\partial\lambda$ terms:

$$\begin{aligned}&\frac{\partial}{\partial t}(\overline{\sigma u})+\frac{1}{a\cos\phi}\frac{\partial}{\partial\phi}(\overline{\sigma uv}\cos\phi)-f\overline{\sigma v}-\frac{\overline{\sigma uv}\tan\phi}{a}-\frac{1}{ag\cos\phi}\frac{\partial}{\partial\theta}\left(p\overline{\frac{\partial M}{\partial\lambda}}\right)\\ &\qquad = -\frac{\partial}{\partial\theta}(\overline{\sigma u\dot{\theta}}) \quad .\end{aligned} \tag{8.89}$$

Note that since we are taking averages on isentropic surfaces, extended definitions are required when isentropes intersect the earth's surface. The above expression can be simplified slightly by combining the second and fourth terms,

$$\frac{\partial}{\partial t}(\overline{\sigma u}) + \frac{1}{a\cos^2\phi}\frac{\partial}{\partial\phi}(\overline{\sigma uv}\cos^2\phi) - f\overline{\sigma v} - \frac{1}{ag\cos\phi}\frac{\partial}{\partial\theta}\left(\overline{p\frac{\partial M}{\partial\lambda}}\right) = \frac{\partial}{\partial\theta}(\overline{\sigma u\dot{\theta}}). \quad (8.90)$$

Now, we take the zonal mean of the continuity equation

$$\frac{\partial\sigma}{\partial t} + \frac{1}{a\cos\phi}\left[\frac{\partial}{\partial\lambda}(\sigma u) + \frac{\partial}{\partial\phi}(\sigma v\cos\phi)\right] = \frac{\partial}{\partial\theta}(\sigma\dot{\theta}), \quad (8.91)$$

to obtain

$$\frac{\partial\overline{\sigma}}{\partial t} + \frac{1}{a\cos\phi}\frac{\partial}{\partial\phi}(\overline{\sigma v}\cos\phi) = \frac{\partial}{\partial\theta}(\overline{\sigma\dot{\theta}}). \quad (8.92)$$

The dependent variables σ, u, p, M, and $\dot{\theta}$ can be split into mean and fluctuating parts:

$$A(\lambda, \phi, \theta, t) = \bar{A}(\phi, \theta, t) + A'(\lambda, \phi, \theta, t). \quad (8.93)$$

Since

$$\overline{\bar{A}B'} = 0 \quad (8.94)$$

in general, we have

$$\overline{AB} = \bar{A}\bar{B} + \overline{A'B'}. \quad (8.95)$$

Andrews et al. (1987) define a "mass-weighted zonal mean" by

$$\bar{A}^* = \frac{\overline{\sigma A}}{\bar{\sigma}}. \quad (8.96)$$

Note that using the definition (8.96), we can rewrite products of two and three variables that involve σ as

$$\sigma A = \overline{\sigma A} + (\sigma A)' = \bar{\sigma}\bar{A}^* + (\sigma A)', \quad (8.97)$$

$$\overline{\sigma AB} = \bar{\sigma}\bar{A}^*\bar{B} + \overline{(\sigma A)'B'}, \quad (8.98)$$

respectively.

If we use (8.95) in (8.90), we get

$$\frac{\partial}{\partial t}(\bar{\sigma}\bar{u} + \overline{\sigma' u'}) + \frac{1}{a\cos\phi}\frac{\partial}{\partial\phi}(\overline{\sigma uv}\cos\phi) - f\overline{\sigma v} - \frac{\overline{\sigma uv}\tan\phi}{a} - \frac{1}{ag\cos\phi}\frac{\partial}{\partial\theta}\left(\overline{p'\frac{\partial M'}{\partial\lambda}}\right) = \frac{\partial}{\partial\theta}(\overline{\sigma u\dot{\theta}}) \quad . \quad (8.99)$$

Now, we subtract $\bar{u}$ times (8.92) from (8.99):

$$\bar{\sigma}\frac{\partial\bar{u}}{\partial t}+\frac{\partial}{\partial t}(\overline{\sigma' u'})+\frac{1}{a\cos^2\phi}\frac{\partial}{\partial\phi}(\overline{\sigma uv}\cos^2\phi)-f\overline{\sigma v}-\frac{1}{ag\cos\phi}\frac{\partial}{\partial\theta}\left(\overline{p'\frac{\partial M'}{\partial\lambda}}\right)$$
$$-\frac{\bar{u}}{a\cos\phi}\frac{\partial}{\partial\phi}(\overline{\sigma v}\cos\phi)=\bar{u}\frac{\partial}{\partial\theta}(\overline{\sigma\dot{\theta}})-\frac{\partial}{\partial\theta}(\overline{\sigma u\dot{\theta}}) \quad . \tag{8.100}$$

Using the operations defined in (8.97) and (8.98), we obtain

$$\bar{\sigma}\frac{\partial\bar{u}}{\partial t}+\frac{\partial}{\partial t}(\overline{\sigma' u'})+\frac{1}{a\cos\phi}\frac{\partial}{\partial\phi}[(\bar{\sigma}\bar{v}^*\bar{u}+\overline{(\sigma v)' u'})\cos\phi]-f(\bar{\sigma}\bar{v}^*)$$
$$-\frac{1}{ag\cos\phi}\frac{\partial}{\partial\theta}\left(\overline{p'\frac{\partial M'}{\partial\lambda}}\right)-\frac{\bar{u}}{a\cos\phi}\frac{\partial}{\partial\phi}(\bar{\sigma}\bar{v}^*\cos\phi)=\bar{u}\frac{\partial}{\partial\theta}(\bar{\sigma}\dot{\bar{\theta}}^*)-\frac{\partial}{\partial\theta}(\bar{\sigma}\dot{\bar{\theta}}^*\bar{u}+\overline{(\sigma\dot{\theta})' u'}) \quad . \tag{8.101}$$

Dividing by $\bar{\sigma}$ and rearranging terms, we are left with

$$\frac{\partial\bar{u}}{\partial t}+\left[\frac{1}{a\cos\phi}\frac{\partial}{\partial\phi}(\bar{u}\cos\phi)-f\right]\bar{v}^*+\dot{\bar{\theta}}^*\frac{\partial\bar{u}}{\partial\theta}=-\frac{1}{\bar{\sigma}}\frac{\partial}{\partial t}(\overline{\sigma' u'})+\frac{1}{\bar{\sigma}ag\cos\phi}\frac{\partial}{\partial\theta}\left(\overline{p'\frac{\partial M'}{\partial\lambda}}\right)$$
$$-\frac{1}{\bar{\sigma}a\cos\phi}\frac{\partial}{\partial\phi}[\overline{(\sigma v)' u'}\cos\phi]-\frac{1}{\bar{\sigma}}\frac{\partial}{\partial\theta}[\overline{(\sigma\dot{\theta})' u'}] \quad . \tag{8.102}$$

If we define the isentropic Eliassen-Palm flux as

$$\vec{F}=(0,F_\phi,F_\theta) \quad ,$$
$$F_\phi=-a\cos\phi\overline{(\sigma v)' u'} \quad , \tag{8.103}$$
$$F_\theta=\frac{1}{g}\overline{p'\frac{\partial M'}{\partial\lambda}}-a\cos\phi[\overline{(\sigma\dot{\theta})' u'}] \quad ,$$

and its isentropic divergence as

$$\nabla\cdot\vec{F}=\frac{1}{a\cos\phi}\frac{\partial}{\partial\phi}(F_\phi\cos\phi)+\frac{\partial F_\theta}{\partial\theta}, \tag{8.104}$$

then (8.102) can be written as

$$\frac{\partial\bar{u}}{\partial t}+\left[\frac{1}{a\cos\phi}\frac{\partial}{\partial\phi}(\bar{u}\cos\phi)-f\right]\bar{v}^*+\dot{\bar{\theta}}^*\frac{\partial\bar{u}}{\partial\theta}=-\frac{1}{\bar{\sigma}}\frac{\partial}{\partial t}(\overline{\sigma' u'})+\frac{1}{\bar{\sigma}a\cos\phi}\nabla\cdot\vec{F}. \tag{8.105}$$

If we examine conditions with steady flow, no heating, and no wave transience, we have

$$\overline{\sigma v}\cos\phi=0, \tag{8.106}$$

since (8.92) reduces to

$$\frac{\partial}{\partial\phi}(\overline{\sigma v}\cos\phi)=0 \tag{8.107}$$

under these conditions, and $\overline{\sigma v}\cos\phi$ must vanish at the poles. Multiplying (8.106) by $\bar{\sigma}\cos\phi$ and using (8.96), we are left with

$$\nabla\bullet\vec{F} = \frac{-1}{\cos\phi}\frac{\partial}{\partial\phi}[\overline{(\sigma v)'u'}\cos^2\phi] + \frac{1}{g}\frac{\partial}{\partial\theta}\left(\overline{p'\frac{\partial M'}{\partial\lambda}}\right) = 0. \qquad (8.108)$$

In other words, the divergence of the meridional momentum flux is balanced by the vertical derivative of the form drag (the amount of pressure force exerted on an isentropic surface by the fluid above that surface, see p. 136 of Andrews et al., 1987). Note that the last term in (8.108) can be written as

$$\frac{1}{g}\frac{\partial}{\partial\theta}\left(\overline{p'\frac{\partial M'}{\partial\lambda}}\right) = \frac{\partial}{\partial\theta}\left(\overline{p'\frac{\partial z'}{\partial\lambda}}\right), \qquad (8.109)$$

using (8.79).

In this chapter, we have reviewed how waves can interact with the mean flow. In the following chapter, we will examine how other researchers have parameterized this effect for large-scale models.

Chapter 9: Existing gravity wave parameterizations

As we saw in Chapter 1, there have been several parameterizations of convectively generated gravity waves developed in the past. Each of these parameterizations is at least somewhat different from the other. Many have somewhat similar forms for the triggering mechanism of the waves (i.e., the presence of convection), and how the waves are dissipated (generally similar to the theory of Lindzen (1981). Expressions for the amplitude, phase speed and wavenumbers of the gravity waves differ widely, as we will see.

The first attempt to parameterize the effects of convectively generated gravity wave drag was made by Rind et al. (1988) in their global climate-middle atmosphere model. The form of this scheme is given by

$$\vec{F_c} = \frac{A\rho_t k(MF)^2 N_t \vec{u}}{|\vec{u}|}. \tag{9.1}$$

Here, $\vec{F_c}$ is the momentum flux, A is a constant, ρ_t is the density at the top of the convection, k is the horizontal wavenumber, MF is the vertically integrated convective mass flux, N_t is the Brunt-Väisälä frequency at the top of the convection, and $\vec{u}$ is the wind velocity averaged over the layers with convection. The value of k used depends on latitude, and varies between 80 and 270 km at polar and tropical latitudes, respectively. The phase speed used for convectively generated waves is $c_c = |\vec{u}| \pm 10$ m s^{-1} for shallow convection, and additional speeds of $c_c = |\vec{u}| \pm 20$ m s^{-1} and $c_c = |\vec{u}| \pm 40$ m s^{-1} are used for deep convection, defined by Rind et al. as convection that penetrates the 400 mb surface. The values of these phase speeds were chosen because they fall within observed values of gravity waves within the mesosphere. The form of (9.1) comes from the form of the equation that Rind et al. (also see Lindzen 1984) used to parameterize orographically generated gravity wave drag,

$$\overrightarrow{F_m} = \frac{\rho_0 k h^2 N_0 \overrightarrow{u_0}}{2\left(1 + \frac{l^2}{k^2}\right)^{1/2}}. \tag{9.2}$$

Here, several symbols have the same meaning as in (9.1), except with a 0 subscript denoting values taken near the surface. In addition, h^2 represents the variance of the topography within a grid cell, and l represents the wavenumber of a cosine bell that is perpendicular to k. Rind et al. also used a similar form to (9.1) and (9.2) to parameterize gravity waves generated by shear, for a total of three gravity wave drag parameterizations.

The parameterized orographic, shear, and convective waves in the model used by Rind et al. interact with the background wind when their combined momentum flux is greater than the saturated value defined by

$$\overrightarrow{F_{sat}} = \frac{\rho k (\vec{e_i} \bullet \vec{u} - c)^3}{2N\left(1 + \frac{l^2}{k^2}\right)^{3/2}}, \tag{9.3}$$

obtained by Lindzen (1984). Here, $\vec{e_i}$ is the unit vector $(\hat{i}, \hat{j}, \hat{k})$, and c is the phase speed of the wave. Consistent with the results of Eliassen and Palm (1960), the waves totally dissipate in the case of a critical level where $\vec{e_i} \bullet \vec{u} - c = 0$. Orographic waves were allowed to affect the flow above ~600mb, while the shear and convective waves were ignored within the troposphere.

When (9.1) was added to their GCM, Rind et al. found that the convectively generated gravity wave drag parameterization significantly affected the simulated winds in the tropics, causing easterlies in the tropical mesosphere to be significantly slowed, and bringing these winds closer to those observed at similar altitudes and latitudes.

The development of the Rind et al. parameterization seems to have been made with reasonable guesses of which terms should be important to the forcing of waves, but with no real attempt to physically justify the functional dependence. However, the waves in the Rind et al. parameterization are nonstationary, which is more consistent with observational and modeling studies than the assumption that the waves move with a single phase speed.

As we will see, other authors have used significantly different expressions for the parameterization of momentum flux, some with more physical justification.

Bossuet et al. (1998) also proposed a parameterization for convectively generated gravity waves. Their parameterization has the form

$$\vec{F}_c = \frac{-CP_c\vec{u}_t}{\left|\vec{u}_t\right|}. \tag{9.4}$$

Here, C is an "empirical constant", P_c is the convective precipitation rate, and the velocity is measured at the top of the cloud. The saturation condition that Bossuet et al. used is taken from Lindzen (1981), and given by

$$\Gamma(\rho, N, U) = \frac{\rho}{\rho_t}\frac{N_t}{N}\left(\frac{U}{U_t}\right)^3 \leq 1. \tag{9.5}$$

This expression comes from Lindzen's (1981) derivation of the value of momentum flux at the breaking level. A wave breaking event is judged to occur when the temperature perturbation associated with the vertically propagating wave causes the local lapse rate to become unstable. Here, U is defined by

$$U = \frac{(\vec{u} - \vec{c}) \bullet \vec{u}_t}{\left|\vec{u}_t\right|}. \tag{9.6}$$

The momentum flux at each level is given by the value of Γ at that level multiplied by $\vec{F}_c$ taken from (9.4). Bossuet et al. assume that the parameterized vertically propagating waves are exactly saturated at the top of the cloud (since $\Gamma = 1$ by definition there), and that Γ remains constant above this level until a critical level is encountered. Above the critical level, Γ decreases according to

$$\Gamma_l = \min(\Gamma_l(\rho_l, N_l, U_l), \Gamma_{l+1}(\rho_{l+1}, N_{l+1}, U_{l+1})), \tag{9.7}$$

with the number of the model level denoted by l, and $l = 0$ at the top of the model.

Bossuet et al. also assume that $\vec{F}_c$ decreases linearly from the cloud top to the cloud base, where it is set to zero. In addition, the phase speed is set to a value of the wind at cloud base. The convergence of momentum flux within the cloud is associated with a slowing of

the winds in the cloud layer. This momentum flux within the cloud is associated solely with gravity waves, although the transport of momentum by the convection itself has been shown to be important in both observational (Gallus and Johnson 1992) and numerical (Gao et al. 1990) studies.

The parameterization developed by Bossuet et al. seems to lack much physical justification. The connection between cumulus precipitation and momentum flux is probably too indirect to base a parameterization upon. Also, the empirical constant used by Bossuet et al. appears to have been tuned for the best effect on zonal winds ("realistic simulation is obtained with a coefficient C equal to 1000"), despite the authors' claims to the contrary ("no attempt has been made to obtain improvements in the zonal wind by excessive tuning of C.") Finally, the Bossuet et al. parameterization assumes that the convection generates a single phase speed that is stationary with respect to the wind at cloud-top. As the observational results of Dewan et al. (1998) and modeling results of Alexander and Holton (1997), Piani et al. (2000), Lane et al. (2001) and this work (see Chapter 13) have shown, this is not an accurate characterization of the gravity waves.

Chun and Baik (1998, 2001) analytically derived the perturbations caused by thermal forcing to the flow of a linear, Boussinesq, steady-state atmosphere with a uniform zonal basic-state wind in the xz-plane. The formula for zonal momentum flux above the top of the heating (interpreted as the latent heating from a convective tower) was derived as,

$$F_c = \frac{-\rho \bar{u}^3 c_1 c_2^2 \mu^2}{N \Delta x}. \tag{9.8}$$

Here, Δx is the size of the grid cell in the zonal direction, and $\bar{u}$ is the zonal basic-state wind. The parameter c_1 is related to a_1 and a_2, which are length scales of the thermal forcing Q, which is given by

$$Q(x,z) = Q_0 \left(\frac{a_1^2}{x^2 + a_1^2} - \frac{a_1 a_2}{x^2 + a_2^2} \right) \tag{9.9}$$

within the heating layer $z_b \le z \le z_t$ and zero below and above the heating. The parameter c_2 is related to the magnitude of the basic-state wind and stability. The nonlinear effects of the heating on the flow are given by

$$\mu = \frac{gQ_0 a_1}{c_p T_0 N \bar{u}^2}, \tag{9.10}$$

where T_0 is the basic-state temperature. This factor is defined in Lin and Chun (1991), where the authors derived prognostic equations for buoyancy and vorticity in a two-dimensional, hydrostatic, Boussinesq, nonrotating system, given in nondimensional form as

$$\frac{\partial b}{\partial t} + \bar{u}\frac{\partial b}{\partial x} - \frac{\partial \zeta}{\partial x} - \mu J(\zeta, b) = Q, \tag{9.11}$$

$$\frac{\partial^3 \zeta}{\partial z^2 \partial t} + \bar{u}\frac{\partial^3 \zeta}{\partial z^2 \partial x} + \frac{\partial b}{\partial x} - \mu J\left(\zeta, \frac{\partial^2 \zeta}{\partial z^2}\right) = 0, \tag{9.12}$$

where the Jacobian operator J represents the operation

$$J(A, B) = \frac{\partial A}{\partial x}\frac{\partial B}{\partial z} - \frac{\partial A}{\partial z}\frac{\partial B}{\partial x}. \tag{9.13}$$

To implement the parameterization, Chun and Baik apply a wave saturation hypothesis, similar to that of Lindzen (1981). The Richardson number, Ri, is a measure of buoyancy divided by shear, given by

$$\mathrm{Ri} = \frac{\frac{g}{\bar{\theta}}\frac{d\bar{\theta}}{dz}}{\left(\frac{\partial \bar{u}}{\partial z}\right)^2 + \left(\frac{\partial \bar{v}}{\partial z}\right)^2}. \tag{9.14}$$

The value of Ri can change at a given level as potential temperature surfaces are distorted by vertically propagating waves, changing $d\bar{\theta}/dz$. If the minimum value of Ri, denoted by $\mathrm{Ri}_{\min}$, is less than 1/4, then the shear causes overturning, and turbulence results. The saturation hypothesis states that the amplitude of the wave momentum flux above the turbulent layer is decreased, since a portion of the wave's energy has been given up to the turbulence itself. To determine the value of the wave momentum flux above the turbulence, Chun and Baik derived an expression for $\mathrm{Ri}_{\min}$:

$$\mathrm{Ri}_{min} = \frac{\mathrm{Ri}(1 - \mu|c_2|)}{(1 + \mu \mathrm{Ri}^{1/2}|c_2|)^2}. \tag{9.15}$$

The momentum flux is calculated at the cumulus cloud top, and is kept constant through each layer above if $\mathrm{Ri}_{\min}$ is greater than 1/4. When the value of $\mathrm{Ri}_{\min}$ is less than 1/4, a value of 1/4 is substituted into (9.15) and then the saturation value of the nonlinearity factor μ_s is calculated. The saturation momentum flux is then given by

$$F_{cs} = \frac{-\rho \bar{u}^3 c_1 c_2^2 \mu_s^2}{N\Delta x}. \tag{9.16}$$

The parameterization developed by Chun and Baik certainly has a stronger physical basis than that of Bossuet et al. However, it does not take shear into account, which is found to be an important consideration by Kershaw (1995, see below). Chun and Baik also point out the difficulty in characterizing the size and heating parameters for the various depths of convection that take place within a GCM grid cell.

Kershaw (1995) used linear wave theory to produce another parameterization for convectively forced gravity wave drag. He assumed that the waves are monochromatic and propagating in the xz-plane with constant zonal wind $\bar{u}$ and constant static stability N^2. Under these assumptions, Kershaw derived the expression,

$$F_c = -\frac{1}{2}\rho \mathrm{Fr}(1-\mathrm{Fr}^2)^{1/2} N^2 \hat{h}^2. \tag{9.17}$$

Here, Fr is the Froude number, a measure of the importance of inertia divided by buoyancy

$$\mathrm{Fr} \equiv \frac{(\bar{u}-c_x)k}{N}, \tag{9.18}$$

where c_x is the horizontal phase speed of the waves. Also, $\hat{h}$ is the displacement amplitude of the waves. To relate this displacement to some measure of convective activity, Kershaw assumes that

$$\alpha \frac{1}{2}\rho_c \overline{w_{max}^2} = \frac{1}{2}\rho N^2 \hat{h}^2. \tag{9.19}$$

In other words, some proportion α of the vertical component of convective energy $\rho_c \overline{w_{max}^2}/2$ is converted to wave energy $\rho N^2 \hat{h}^2/2$. Here, $\overline{w_{max}^2}$ is the maximum value of the variance of vertical velocity, and ρ_c is the density at that level. Using (9.19) and the fact that $\mathrm{Fr}(1-\mathrm{Fr}^2)^{1/2} \cong \mathrm{Fr}$ for $\mathrm{Fr} \ll 1$, (9.17) can be written as

$$F_c = \frac{-\alpha \rho_c u_{rel} k \overline{w_{max}^2}}{2N}. \tag{9.20}$$

The quantity u_{rel} is a measure of shear that has been substituted for $\bar{u} - c_x$. Here, Kershaw assumes that the phase speed c_x is equal to the zonal wind at the same level as $\overline{w_{max}^2}$, and $\bar{u}$ is taken to be the zonal wind at cloud top.

To check the validity of (9.20), Kershaw performed numerical experiments with a cloud-resolving model. This was done because of the difficulty in obtaining high-resolution observations of many of the quantities in (9.20). Kershaw found linear correlations between F_c and three of the variables from (9.20) (u_{rel}, $\overline{w_{max}^2}$, and $1/N$), consistent with the parameterization.

The parameterization developed by Kershaw seems to be based far more on physical considerations than that of Bossuet et al. The numerical experiments of Kershaw also helped establish the credibility of his parameterization. However, these experiments all simulated conditions corresponding to a mid-latitude cold-air outbreak, which is not necessarily the best example of "standard" convection. Also, Kershaw acknowledges that "estimation of the wavelength of the waves is likely to prove one of the main uncertainties in applying the parameterization."

The Kershaw parameterization was further refined by Roadnight (1999). In Roadnight's study, it was found that the assumption Fr « 1 is not necessarily valid for typical values of u_{rel}, k, and N. Also, the efficiency α was found to have a non-constant value when it was calculated for a variety of simulations of convection.

Roadnight noted that the assumption that waves are monochromatic (used to derive (9.17)) is not valid for a nonlinear numerical simulation. However, after performing a Fourier transform upon the fields, the validity of the parameterization could be examined for individual wave components. The efficiency α was found to depend strongly on wavelength, with the shortest wavelength examined (12.5 km) having a value of approximately 0.03, and the longest wavelength (50 km) having a value of approximately 0.3.

Another problem that Roadnight found with the Kershaw parameterization was the characterization of the convective kinetic energy by $\overline{w_{max}^2}$. Roadnight noted that this may be accurate in conditions of very weak shear where vertical motions are dominant within the convection, but is not generally accurate for conditions of stronger shear. Roadnight defined γ as the quantity that represents the proportion of the total convective kinetic energy that results from the variance of vertical velocity,

$$\frac{1}{2}\rho_c \overline{w_{max}^2} = \gamma \frac{\rho}{2}(\overline{u^2} + \overline{v^2} + \overline{w^2}). \tag{9.21}$$

This quantity is similar to one defined in Eqn. (25) of Pan and Randall (1998; also see Arakawa and Xu 1990). The quantity γ was found to have a strong dependence on shear, and that

$$\frac{u_{rel}}{2}\rho_c \overline{w_{max}^2} \tag{9.22}$$

is a better approximation to the total convective kinetic energy. Substituting (9.22) into (9.20) without the Fr « 1 assumption and non-dimensionalizing, Roadnight obtained

$$F_c = -\frac{\alpha}{2}\rho_c \mathrm{Fr}^* \mathrm{Fr}(1-\mathrm{Fr}^2)^{1/2}\overline{w_{max}^2}. \tag{9.23}$$

Here, Fr* is another Froude number, defined by

$$\mathrm{Fr}^* = \frac{u_{rel}}{H_c N}, \tag{9.24}$$

with H_c representing the depth of the unstable layer. The inclusion of an additional shear factor into (9.24) changes the numerical value of α, which is still observed to depend on wavelength.

The work done by Roadnight in improving Kershaw's parameterization appears to have been productive, with further success at obtaining a parameterization that is usable across a wide range of shear, stability and wavelength values. However, Roadnight notes that for the short wavelengths of her simulations, Fr reaches values over 1, rendering (9.23) invalid since it would produce imaginary values of momentum flux. This is tem-

pered by the fact that short wavelengths contributed very little to the overall momentum flux in Roadnight's simulations.

Another parameterization that specifically addresses convectively generated gravity waves has been developed by Alexander and Dunkerton (1999; hereafter AD99). This is to be distinguished from other characterizations of nonstationary gravity waves such as those of Hines (1997a), and Warner and McIntyre (1999) that do not specify the causes of the wave spectrum. In AD99, the momentum flux is launched from a height z_0 equal to 15 km (in the vicinity of the tropopause), and is assumed to have a spectrum B_0 that has a functional form given by

$$B_0(\bar{u}-c) = B_m\left(\frac{\bar{u}-c}{c_p}\right)\exp\left(1-\left|\frac{\bar{u}-c}{c_p}\right|\right). \tag{9.25}$$

The quantity B_m is an amplitude, specified as 1.2 m^2 s^{-2}, and c_p is the location of the maximum in the forcing, specified as 25 m s^{-1}, which roughly matches the results of Alexander and Holton (1997). The spectrum in (9.25) is designed to characterize *local* wave events, and to be constrained by observations on the mesoscale (e.g., flights over an area of active convection). The total momentum flux is specified with a separate parameter F_{S0}, which is meant to represent a long-term average of the momentum flux at z_0. The amplitude of F_{S0} indicated by AD99 for convectively generated waves has a time-averaged value of 0.004 Pa. As AD99 point out, the implied average intermittency ε is then given by

$$\varepsilon = \frac{F_{S0}\Delta c}{\rho_0 \sum_c |B_0(c)|\Delta c}. \tag{9.26}$$

This intermittency can be defined as a measure of the frequency of the occurrence of the waves. The intermittency given by the summation of (9.25) over the range of -150 to 150 m s^{-1}, with a phase speed interval Δc equal to 1 m s^{-1} is then approximately 0.000125, assuming a density at 15 km of 0.2 kg m^{-3}. Note that this number of phase speed intervals may not be practical for use in a GCM, and that a compromise between resolution and computational cost must be made for spectral parameterizations of this type. The implied

total westward and eastward momentum fluxes according to the denominator of (9.26) have a magnitude of 16 Pa each, which is far too high. Using a value of B_m equal to 0.0012 m^2 s^{-2} yields magnitudes of 0.016 Pa, which is closer to the values obtained by Alexander and Holton (1997; see their Fig. 7), the work that (9.25) is loosely based upon, according to AD99.

After the source spectrum is specified, each of the waves in the spectrum is allowed to be absorbed by the mean flow or reflected. Reflection occurs when the magnitude of the intrinsic frequency of the wave ω_i is greater than or equal to the reflection frequency, i.e., when

$$|\omega_i| \equiv k|\bar{u} - c| \geq \left(\frac{N^2 k^2}{k^2 + \frac{1}{4H^2}} \right)^{1/2}. \tag{9.27}$$

Waves that are reflected are removed from the spectrum. A stability condition similar to that of Lindzen (1981) is then applied, with the quantity

$$Q_n(c) = \frac{\rho_0}{\rho(z_n)} \frac{2N(z_n)B_0(c)}{k[c - \bar{u}(z_n)]^3}. \tag{9.28}$$

When $Q_n \geq 1$, all of the waves' momentum is deposited between z_n and z_{n-1}, as in Lindzen and Holton (1968). Note that this is to be distinguished from the condition used by Lindzen (1981), who assumed that only the excess momentum flux beyond the stability criteria is absorbed by the mean flow. This has the advantage of allowing the modeler to remove absorbed waves from the spectrum as the spectrum travels upward in a simple manner, and produces results that are qualitatively similar to those with the saturation condition intact (see AD99).

In this chapter, we have reviewed the previous efforts at the parameterization of momentum flux due to gravity waves. Several of the parameterizations listed above (Bossuet et al. 1998; Chun and Baik 1998; Kershaw 1995; Roadnight 1999) assume that the convectively generated waves carry a single phase speed that is stationary relative to some point within the convection, and attempt to parameterize the net momentum flux. As we will see in Chapter 13, this is probably not a very accurate assumption. The Rind et al. (1988) approach does allow for multiple phase speeds, but in their parameterization, the

waves are not allowed to affect the troposphere. Also, the Rind et al. parameterization is only very loosely tied to observations. The Alexander and Dunkerton (1999) parameterization contains more dependence on observations and model results, but contains significant amounts of wave momentum flux at high phase speeds, which implies larger amounts of wave energy flux than are probably realistic, as we will see in Chapter 15. In addition, none of the parameterizations account for the effect of the wave energy flux drain on the convection itself.

The previous chapters have focused on previous work that has been done in the detection, simulation and parameterization of convectively generated gravity waves. The next several chapters will focus on new methods that can also be applied to understand these waves.

Chapter 10: Empirical orthogonal functions

The empirical orthogonal function, or EOF, was developed by Lorenz (1956) to develop a statistical method of weather prediction. Although this implementation of EOFs was never used widely, EOFs have been used to extract physically important modes of temporal variation from large data sets. Most of these studies have focused on finding the predominant modes for the fluctuations of fields on planetary and synoptic scales (e.g., Kutzbach, 1967; Barnett, 1983). However, Wilson (1996) and Wilson and Wyngaard (1996) have recently used EOFs to examine flow structures in the boundary layer simulated by a large-eddy simulation. In these studies, the authors found that some EOFs corresponded to gravity wave structures, while others had the form of horizontal roll vortices. In this section, we will examine what flow structures are uncovered when the EOF technique is applied to convection simulated by a mesoscale model.

The following outline of the EOF technique is similar to that of Kutzbach (1967). Let $\vec{f}_n$ represent a vector of observations at M different spatial locations taken at the nth time. If we are examining N times at which observations are taken, then F is an M by N matrix, with the nth column corresponding to $\vec{f}_n$. We are looking for the vector $\vec{e}$ that is most similar to all of the $\vec{f}_n$ simultaneously. The way that Kutzbach (1967) measures similarity is by taking the normalized, squared inner product between $\vec{e}$ and F:

$$\frac{\left(\vec{e}^T \bullet F\right)^2}{N\left(\vec{e}^T \bullet \vec{e}\right)}. \tag{10.1}$$

Note that the T superscript denotes the transpose of a vector or matrix. If we impose the condition

$$\vec{e}^{T} \bullet \vec{e} = 1, \tag{10.2}$$

then maximizing (10.1) is equivalent to maximizing

$$\vec{e}^{T} \bullet R \bullet \vec{e}, \tag{10.3}$$

where R is an M by M symmetric matrix with elements that are defined by

$$\begin{aligned} R &= \frac{1}{N}(FF^{T}) \quad , \\ R_{ij} &= \frac{1}{N}\sum_{n=1}^{N} f_{in}f_{jn} \quad . \end{aligned} \tag{10.4}$$

Now, if we maximize (10.3) subject to the condition (10.2), the problem reduces to an eigenvalue problem of the form,

$$R\vec{e} = \vec{e}\lambda, \tag{10.5}$$

where λ represents an eigenvalue.

There are in fact M eigenvalues that correspond to solutions of (10.5), each with a corresponding eigenvector. Therefore, we can rewrite (10.5) as

$$RE = EL, \tag{10.6}$$

where E is an M by M matrix comprised of the eigenvectors $\vec{e}_1, \vec{e}_2, \ldots, \vec{e}_M$, and L is an M by M diagonal matrix comprised of eigenvalues $\lambda_1, \lambda_2, \ldots, \lambda_M$. Typically, the eigenvalues are placed in decreasing order, so that the eigenvector with the most resemblance to all of the observations is denoted as the first EOF, the next most similar eigenvector is the second EOF, and so on. As an extension of (10.2), we have

$$E^{T}E = I. \tag{10.7}$$

Combining (10.4), (10.6), and (10.7), we have

$$E^{T}FF^{T}E = LN. \tag{10.8}$$

If we define C as an M by N matrix that satisfies

$$C = E^{T}F, \tag{10.9}$$

then we also have

$$F = EC. \tag{10.10}$$

To express (10.10) in another way, each observation vector $\vec{f}_n$ can be expanded as a sum of eigenvectors given by

$$\vec{f}_n = \sum_{i=1}^{M} c_{in}\vec{e}_i. \tag{10.11}$$

Each element c_{in} corresponds to the coefficient associated with the *i*th eigenvector for the *n*th observation. As Kutzbach (1967) points out, "the coefficients c_{in} play the same role in (10.11) as the coefficients in ... a Fourier series."

As with any statistical technique, with a higher amount of samples over which the EOFs are calculated, the conclusions that can be drawn from the statistics are more robust. North et al. (1982) derived the following criterion for determining whether two eigenvalues are sufficiently separated for their associated EOFs to be distinguishable from one another,

$$\lambda_i - \lambda_i\left(\frac{2}{N}\right)^{1/2} > \lambda_{i+1} + \lambda_{i+1}\left(\frac{2}{N}\right)^{1/2}. \tag{10.12}$$

In other words, if the "error bars" due to sampling error that surround a particular eigenvalue λ_i and its neighbor λ_{i+1} overlap, the EOFs associated with λ_i and λ_{i+1} can be said to be degenerate. In this case, each of the overlapping EOFs produced by the analysis will be a combination of the two or more "true" EOFs that would be calculated given a sufficiently large number of samples.

However, a pair of degenerate EOFs can sometimes represent a propagating disturbance rather than a mixture of two physical phenomena. In Marcus et al. (1996), the authors found that an extratropical 40-day oscillation simulated by a GCM was represented by two EOFs that exhibited similar spatial and temporal structure, but were separated by a lag of six days.

The EOF technique described above can be applied to model output as well as observations. Each grid point can be regarded as an "observing station", and the output that is saved can be regarded as a set of observations. The application of the technique to a single field of interest (e.g., vertical velocity) is therefore relatively straightforward. Using EOFs with multiple fields simultaneously can also be illuminating, since one may wish to exam-

ine the variations in both vertical velocity and potential temperature, and how they are associated with one another. Note that calculating the first EOF separately for two fields and then combining them will not produce the same picture as calculating the first EOF for both fields simultaneously, in general. When calculating multiple fields simultaneously, they must be scaled so that the units are appropriate, and that the variations of each field are comparable in magnitude to one another.

The solution of the matrix equation (10.6) becomes increasingly taxing on computer resources as the number of observing stations M increases. For a mesoscale simulation with a significant (say 10000 or more) number of points, it becomes impossible to calculate eigenvectors for all of the grid points, particularly if the EOFs of multiple meteorological fields are simultaneously calculated.

We will perform the EOF analysis on the output from a two-dimensional mesoscale simulation of convection. The EOFs of vertical velocity, horizontal velocity perturbation and potential temperature perturbation were calculated simultaneously, with the potential temperature scaled by

$$\theta_{vel} = \frac{g\tau\theta'}{\theta_0}. \tag{10.13}$$

Here, θ_{vel} represents a "velocity" associated with potential temperature, g is the acceleration of gravity, τ is a timescale of 100 seconds, which is on the order of the inverse of the Brunt-Väisälä frequency, θ' is the perturbation (from the initial horizontally homogenous state) potential temperature, and θ_0 is the vertically varying average potential temperature.

The storm-averaged perturbations are shown in Fig. 10.1. The velocity field has many of the characteristic features of observed (Houze et al. 1989) and previously simulated (Weisman 1992) squall lines in the mature stage, including an ascending front-to-rear flow, a descending rear inflow and a strong, updraft that is tilted against the shear of the storm. Also, there is an area of cool θ near the surface, which is associated with the cold pool of the storm.

The first EOF is shown in Fig. 10.2, and its velocity field has some similarities to that of the storm average. The variation of the first five EOFs with time are shown in Fig. 10.3.

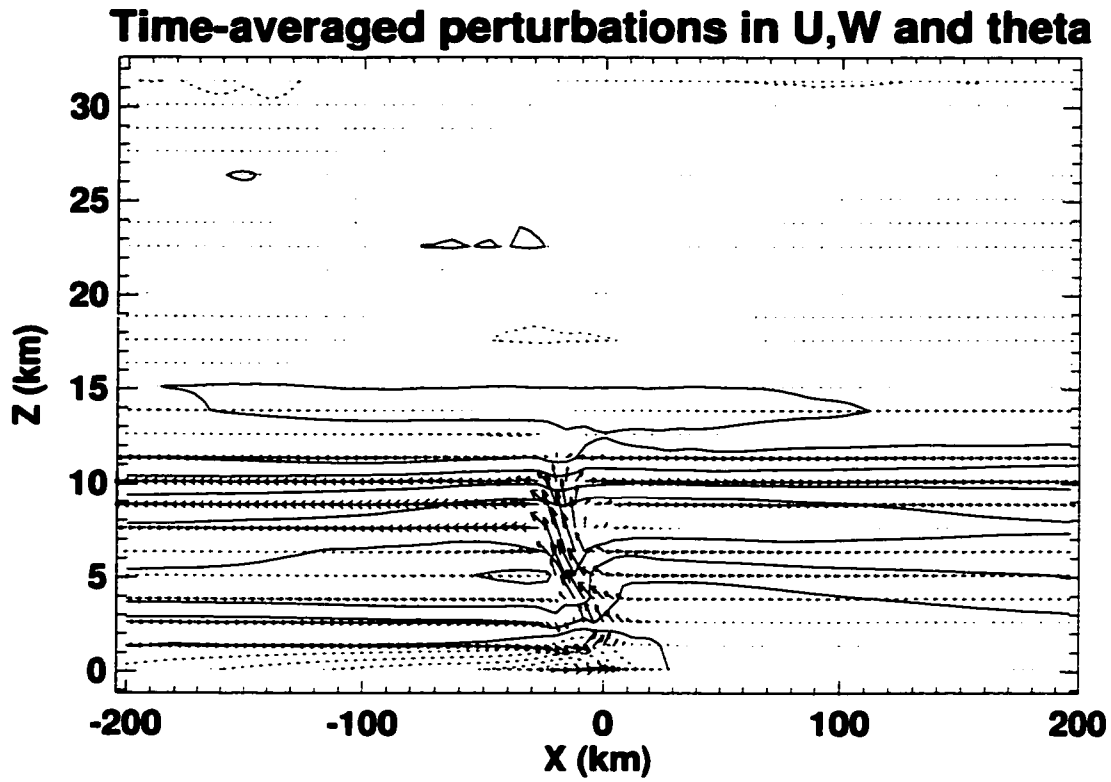

Fig. 10.1. Time-averaged values of perturbation potential temperature and velocity. The maximum perturbations in θ are approximately 8 K near the surface, and the largest velocity is approximately 16 m s^{-1}

The first EOF has an area of strong upward vertical motion in the troposphere centered near the center of the domain. The updraft associated with the first EOF is more upright than that of the storm average updraft. With this structure, and since the first EOF decreases from a large positive value at t=3600 sec, it appears to be associated with the increase of the tilt of the storm from the initial state of developing convection. The potential temperature perturbations near the surface are positive, which indicates that the cold pool strengthens with time, since the coefficient first EOF decreases with time.

The second and third EOFs are shown in Fig. 10.4, respectively. These EOFs also appear to be primarily associated with the convective development of the storm. There are horizontal vortices identifiable in these structures, somewhat similar to those seen in Rotunno et al. (1988). There appears to be a standing-wave pattern in the stratospheric potential temperature field of each of the first three EOFs. The physical significance of

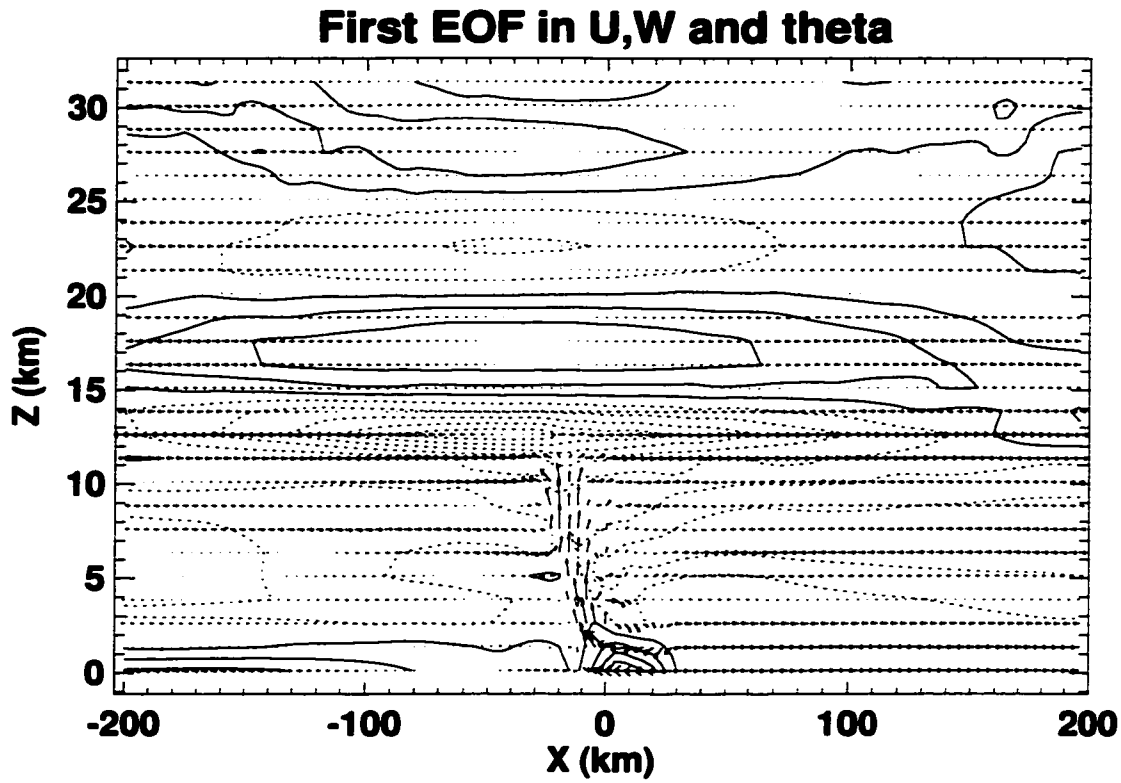

Fig. 10.2. Structure of first EOF in potential temperature and velocity from the WK run. Contours are of potential temperature, and vectors indicate velocity. The magnitudes of the contours only make sense when multiplied by the time-varying coefficients. For a coefficient of 200, the maximum perturbations in θ are approximately 3 K near the surface, and the largest velocity is approximately 9 m s^{-1}.

these standing waves is not immediately apparent, although they may be signatures of low-wavenumber, low-frequency gravity waves.

When a separate EOF calculation was performed upon only the stratospheric portion of the model domain, very similar low-wavenumber, low-frequency structures were observed. In addition, an EOF calculation involving only the tropospheric portion of the domain revealed that the first two EOFs had very similar patterns to the tropospheric portions of the first two EOFs calculated for the entire atmosphere. These analyses show that the EOFs presented here are probably robust.

The fourth and fifth EOFs (not shown) also appeared to be primarily associated with convective circulations in the troposphere.

The sixth and seventh EOFs are shown in Fig. 10.5. The behavior of their coefficients with time is shown in Fig. 10.6. The spatial and temporal structure of these two modes is

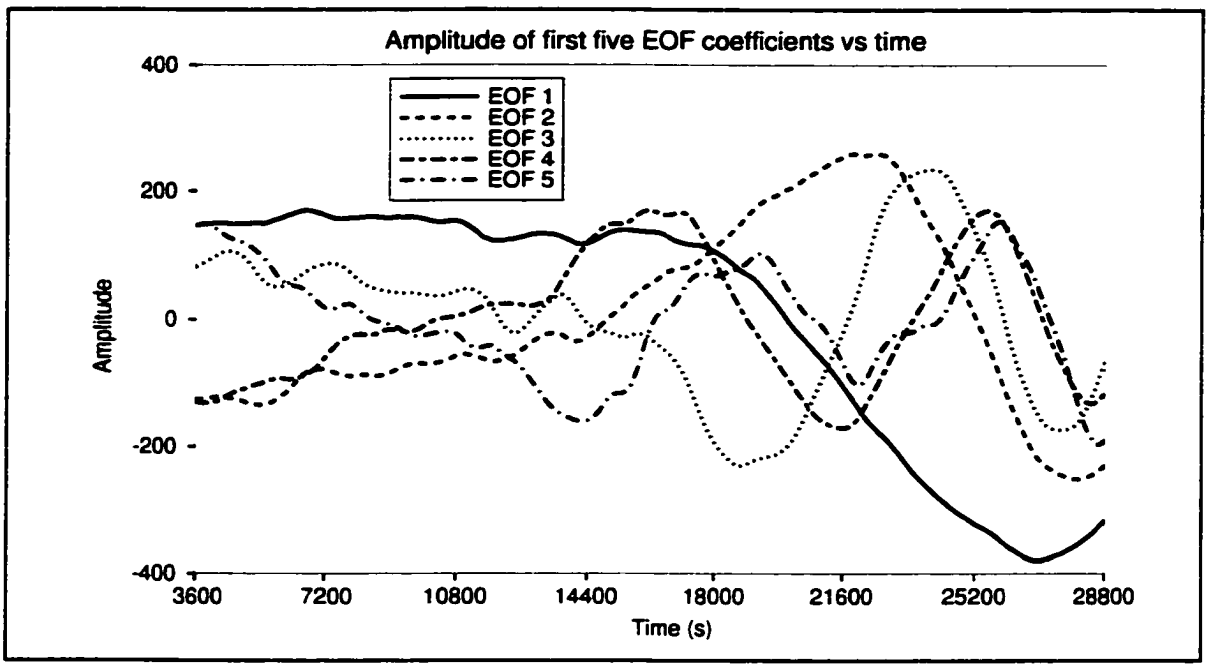

Fig. 10.3. Variation of coefficients versus time for the first five EOFs.

very similar, with most of the amplitude of the modes appearing as gravity wave structures in the stratosphere. The identification of these structures as gravity waves is due to the fact that the vertical velocity and potential temperature are a quarter-wavelength out of phase with one another, which is consistent with gravity waves. The waves in EOFs 6 and 7 are mostly to the rear of the storm center, which is consistent with what is observed in the simulation in the mature stage of the squall line. These waves have a period of approximately 23 minutes, and a horizontal wavelength of roughly 30-50 km. The horizontal phase speed of these waves is therefore approximately 20-35 m s^{-1}. These values of wavelength, period, and phase speed are comparable to what have been simulated and observed by other authors (e.g., Pfister et al., 1986; Alexander et al., 1995).

The direction that these waves are propagating can be ascertained by examining the relative phase of vertical velocity and potential temperature. A simplified depiction of one of these waves is shown in Fig. 10.7. On the left side of this wave, the upward motion causes the air to cool, while the downward motion on the right side of the wave is associated with warming. Since the coldest and warmest air is to the left of the peak cooling and warming, respectively, the wave propagates to the right. If the velocity vectors in Fig. 10.7 had the opposite direction, then the above analysis is simply reversed, and the wave propa-

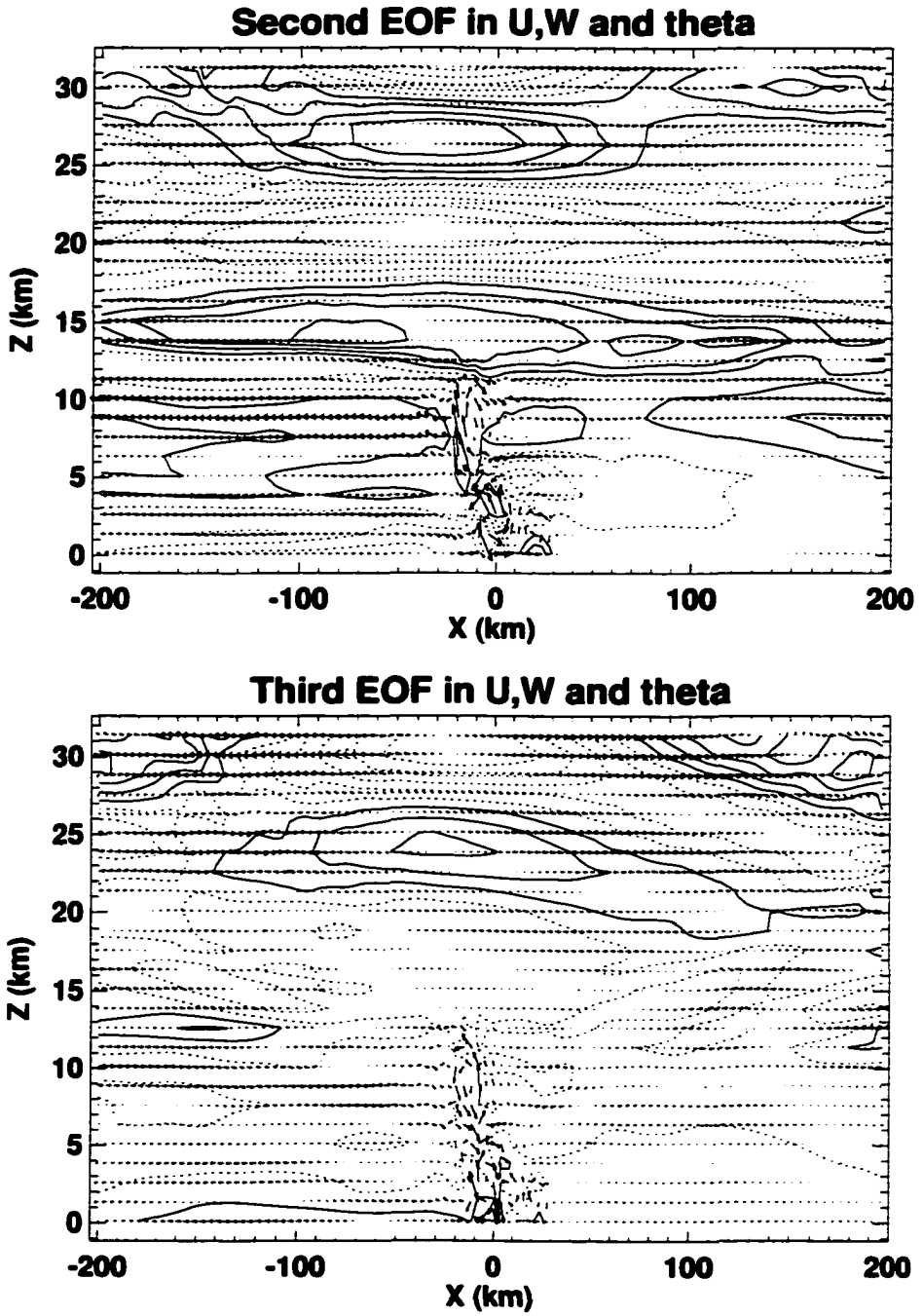

Fig. 10.4. Structure of potential temperature and velocity for the second and third EOFs. For a coefficient of 200, the largest velocity is approximately 7 m s^{-1}.

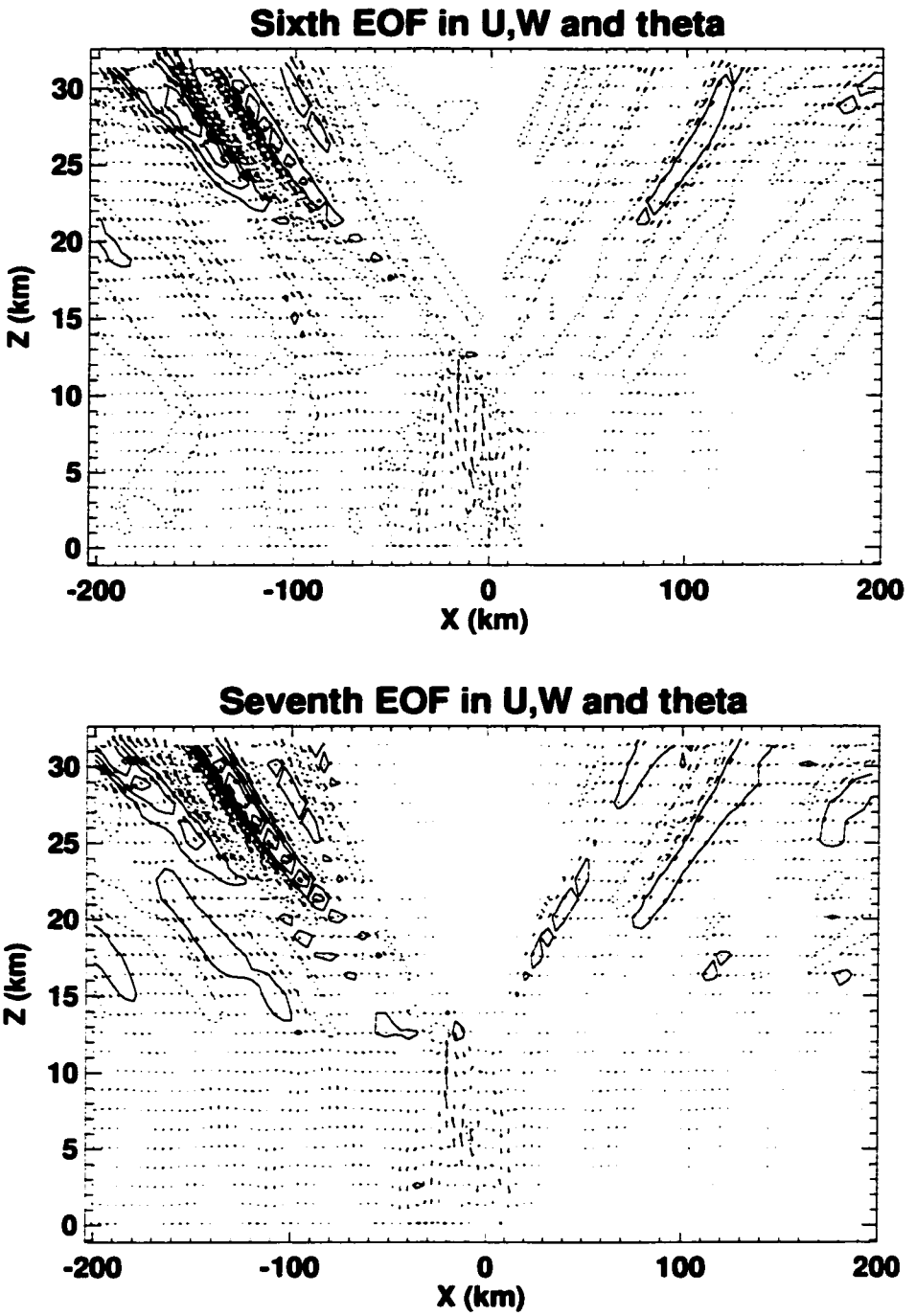

Fig. 10.5. Structure of potential temperature and velocity for the sixth and seventh EOFs. For a coefficient of 200, the maximum perturbations in θ are approximately 15 K at an altitude of 25 km, and the largest velocity is approximately 14 m s^{-1}.

gates to the left. Note that if the signs of *both* the velocity vectors and potential temperature anomalies are reversed (which will be the case for a negative coefficient of an EOF with this structure), that the wave will propagate to the right. Applying this analysis to the

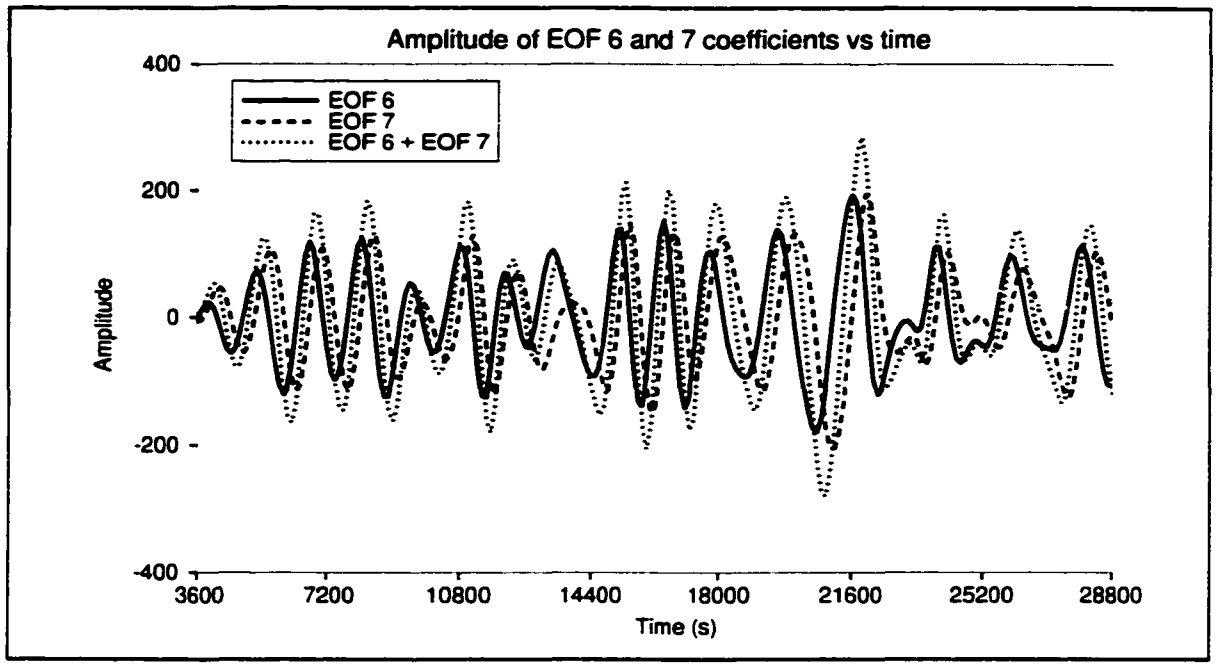

Fig. 10.6. Variation of coefficients versus time for the sixth and seventh EOFs, and their sum.

fourth and fifth EOFs, we see that the stratospheric gravity waves are propagating outward from an axis around near the center of the domain, which is the average position of the maximum intensity of convection in the troposphere, as seen in Fig. 10.1. This strongly indicates a convective origin for the gravity waves.

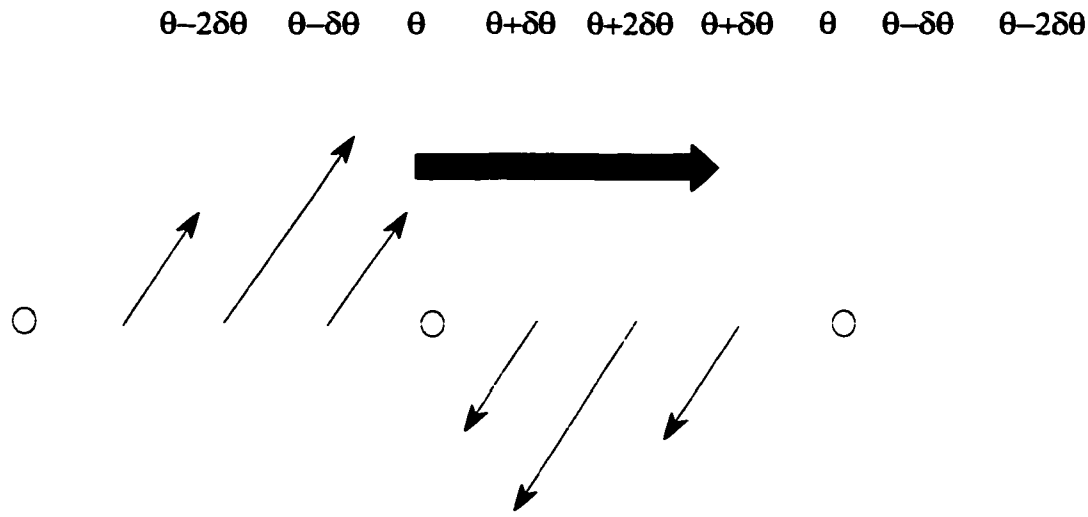

Fig. 10.7. Idealized depiction of an internal gravity wave, similar to those seen in the stratosphere of Fig. 10.5. The colored lines correspond to potential temperature contours (labeled at the top), and the thin arrows correspond to velocity vectors, with circles representing nodes. The thick arrow represents the direction of wave propagation.

The normalized eigenvalues of the first 20 EOFs and the confidence interval associated with them (calculated from (10.12)) are shown in Fig. 10.8. The first four EOFs appear to be robust, and EOFs 5, 6 and 7 form a degenerate triplet according to this criterion. However, the amount of coherence in the time variation of the coefficients of EOFs 6 and 7 indicates that these two modes are primarily only linked with one another.

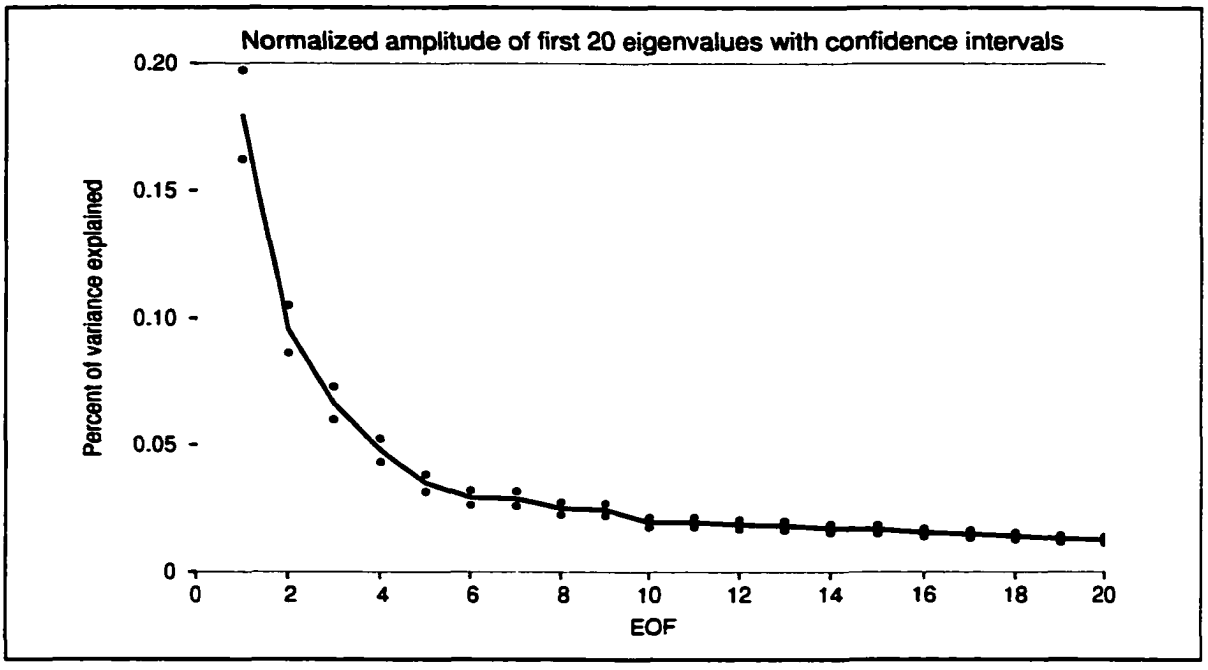

Fig. 10.8. Normalized eigenvalues of the first 20 EOFs. Dots above and below the line outline the confidence interval calculated from (10.12).

In this chapter, we have seen that convective motions in the stratosphere and wave motions in the troposphere are associated with separate EOFs in the control WK run. EOF analyses of other simulations do not show such a strong separation between convective and wave modes, and exhibit degeneracy among the first few EOFs. So, the EOF method described in this chapter is not useful as a diagnostic tool for all simulations of convection. In the next chapter, we will use a particle tracking method to separate convective and non-convective motions within the troposphere.

Chapter 11: Particle Trajectories

In this chapter, we will examine the use of particle trajectories to examine the behavior of air parcels in a numerical simulation of convection. First, the method of advection and interpolation will be described, then some results will be shown, along with possible methods for separating convective and non-convective motions from one another.

The velocity fields simulated by ARPS are stored at three time levels, spanning an interval of twice the large time step (which was 4 seconds for all of the simulations presented in this study). These velocities were used to construct the background winds for the particles. The method used to advect the particles is the fourth-order Runge-Kutta scheme, similar to that used by Krueger et al. (1995). The Runge-Kutta scheme is one example of a finite-difference approximation to

$$\frac{dx}{dt} = u[x(t), t]. \tag{11.1}$$

Although (11.1) is written with one spatial dimension, the following discussion generalizes to two or three dimensions in a straightforward manner. In the case of the Runge-Kutta scheme, the solution to (11.1) is obtained iteratively, as follows:

$$\frac{x^{(n+1)} - x^{(n)}}{\Delta t} = \frac{1}{6}(k_1 + 2k_2 + 2k_3 + k_4), \tag{11.2}$$

$$k_1 = u(x^{(n)}, n\Delta t), \tag{11.3}$$

$$k_2 = u\left[x^{(n)} + \frac{k_1 \Delta t}{2}, \left(n + \frac{1}{2}\right)\Delta t\right], \tag{11.4}$$

$$k_3 = u\left[x^{(n)} + \frac{k_2 \Delta t}{2}, \left(n + \frac{1}{2}\right)\Delta t\right], \tag{11.5}$$

$$k_4 = u[x^{(n)} + k_3 \Delta t, (n+1)\Delta t]. \tag{11.6}$$

To advect a particle forward in time, we need to have u defined at integral increments of $n\Delta t$ as well as at $(n + 1/2)\Delta t$. If we take Δt to be 8 seconds, then the finite difference method defined by (11.2)-(11.6) can be applied at the three time levels for which the velocities are stored.

To calculate particle trajectories, we also need to have a value of u at the particle's location. This was accomplished by performing a linear interpolation to the position of the particle from surrounding gridpoints where u is defined

$$u_T = \left(\frac{x_T - x_1}{\Delta x}\right)u_2 + \left(\frac{x_2 - x_T}{\Delta x}\right)u_1 . \tag{11.7}$$

The variables in (11.7) are defined in Fig. 11.1 Note that as the position x_T of the particle

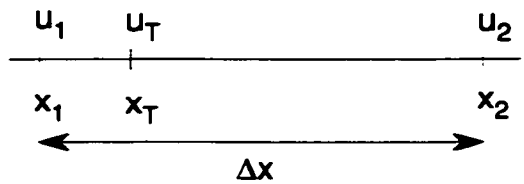

Fig. 11.1. Simple illustration of the parameters defined in (11.7). Note that analogous interpolations can be constructed in two and three dimensions.

gets close to x_1 and x_2, its speed u_T approaches u_1 and u_2, respectively. Also, if x_T is at $x_1 + \Delta x/2$, its speed is $(u_1 + u_2)/2$, corresponding to a simple arithmetic mean, as expected.

In addition to calculating the position and speed of the particles, we can also interpolate the values of other scalar variables to the particles' positions. Once the trajectories are obtained, statistics can be calculated for the particles, some of which can be combined in an attempt to separate convective motions from non-convective motions (including gravity waves). One such statistic is a normalized mean vertical velocity given by

$$\hat{w} = \frac{\bar{w}}{(\overline{w^2})^{1/2}} . \tag{11.8}$$

Note that the overbar in this case denotes a time average along the particle's path. This quantity will be 1 for a particle that experiences upward vertical velocity that is constant in time, -1 for a particle that experiences downward vertical velocity that is constant in time,

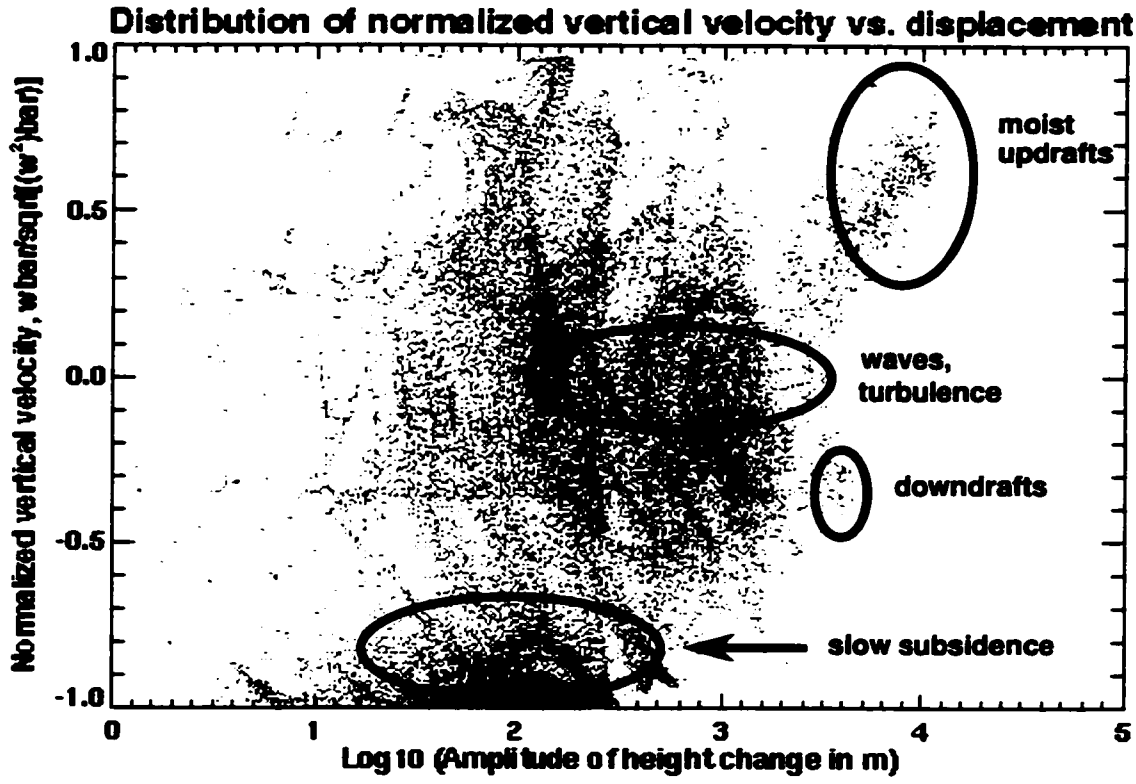

Fig. 11.2. Plot of convection factor defined in (11.8) versus the $\log_{10}$ of displacement for particles that have been advected for 30 minutes in the WK control run, starting at t = 3 hours. The red "dry" particles have $\overline{q_c} < 10^{-2}$ g/kg , while the blue "wet" particles have $\overline{q_c} > 10^{-2}$ g/kg .

and 0 for particles with oscillatory or no vertical motion. The magnitude of a particle's displacement over the time period of the trajectory integration can be determined by calculating

$$\delta z = z_{max} - z_{min} . \tag{11.9}$$

Finally, we will also calculate the average cloud condensate (liquid water plus ice) $\overline{q_c}$ along each particle's path.

An example of these three variables plotted for many particles released in the WK control run at t = 3 hours is shown in Fig. 11.2.The particles shown in this figure were initially placed at all of the points at which scalar particles are defined throughout the lowest 12 km of the model atmosphere, and then advected for 30 minutes. This duration of time was chosen as long enough for particles to travel great vertical distances, but short enough so that not too many particles experience both convective and non-convective motions, which

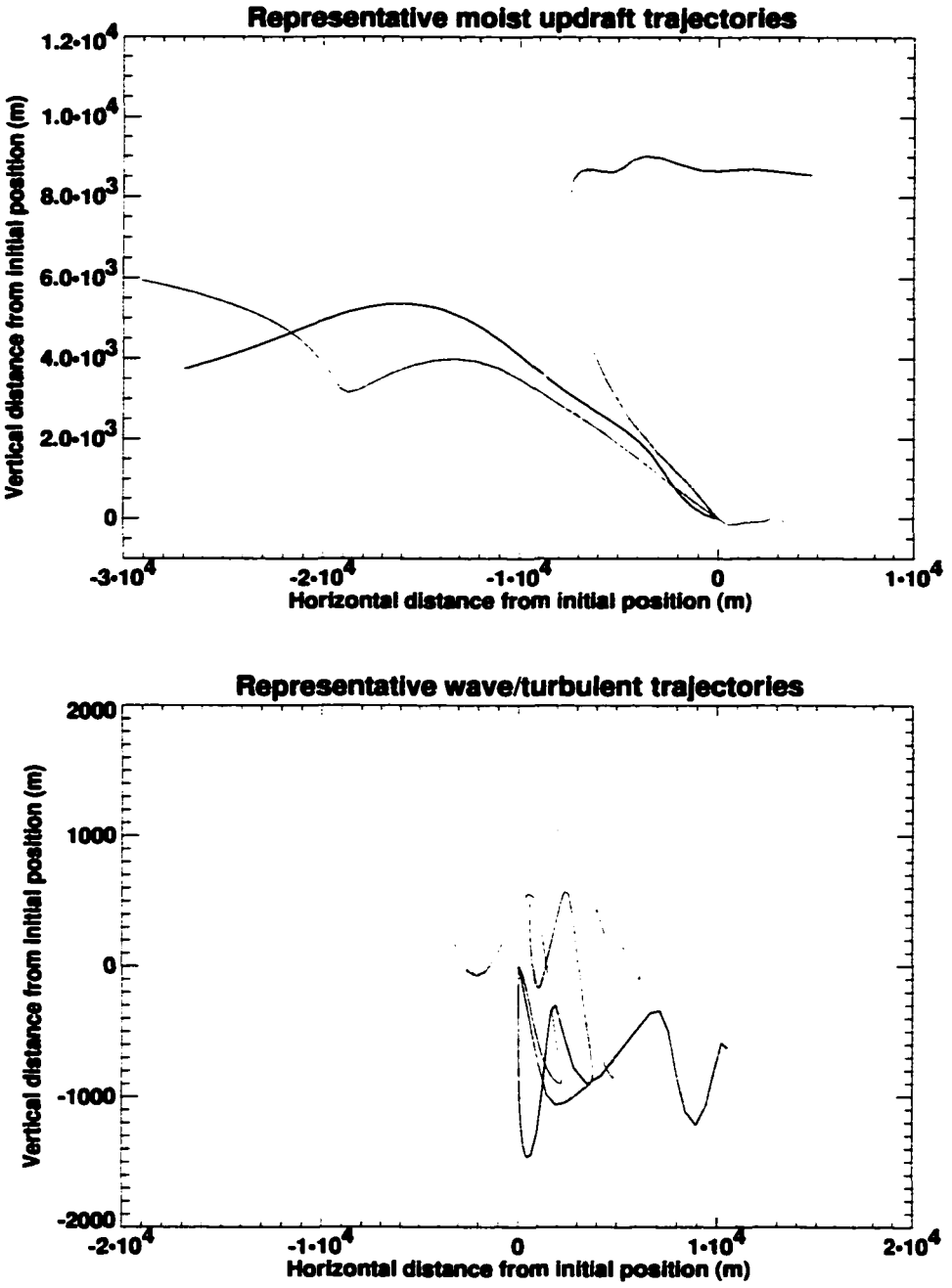

Fig. 11.3. a) Plot of particle displacement for five trajectories classified as experiencing wave and turbulent motions in Fig. 11.2. b) Plot of particle displacement for five trajectories classified as moist updrafts in Fig. 11.2 (bottom). The displacements are normalized so that the initial positions are all at (0,0), and particle paths can be followed outward from that point.

would hamper separation. Physical interpretations can be made of several of the regions in the plot. The trajectories with the highest displacements also move up on average, and are

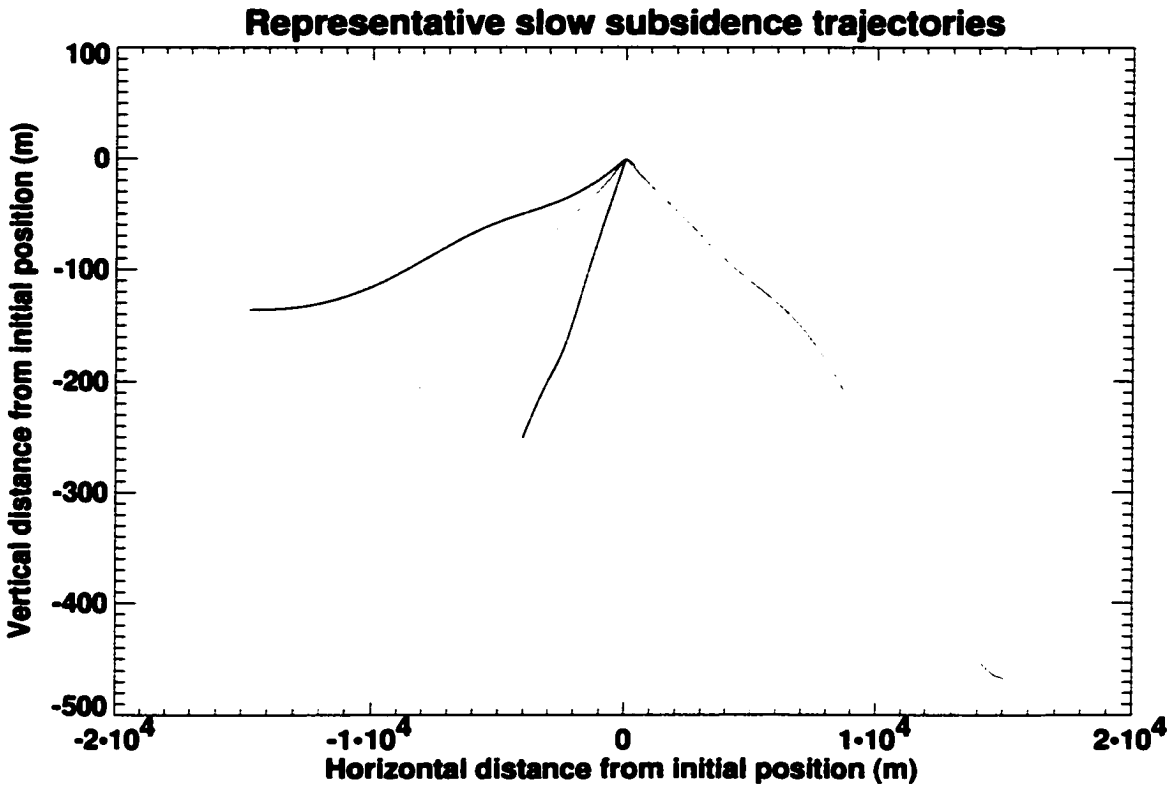

Fig. 11.4. Plot of particle displacement for five trajectories classified as experiencing slow subsidence in Fig. 11.2. The displacements are normalized so that the initial positions are all at (0,0), and particle paths can be followed outward from that point.

cloudy as well, indicating that these particles can be associated with moist convective updrafts. The many particles that have displacements of 50 - 500 m and a normalized vertical velocity near -1 are affected by the slow subsidence outside of the storm. The particles with significant displacements and a convective factor near zero are undergoing wave or turbulent motions, oscillating about their initial position. Note that nearly all of the particles with large-amplitude displacements also have $\hat{w} > 0$ and $\overline{q_c} > 10^{-2}$ g/kg. In fact, most of the particles in the "moist updrafts" category have $\overline{q_c} > 10^{-1}$ g/kg, whereas the few "downdraft" particles have 10^{-1} g/kg $\geq \overline{q_c} > 10^{-2}$ g/kg. The reason that there are few convective downdrafts in this simulation, may be because it was performed in two dimensions (Haertel and Johnson, 2000).

A few of the different classes of trajectories are shown in Fig. 11.3a, Fig. 11.3b, and Fig. 11.4 for the "moist updraft", "waves and turbulence" and "slow subsidence" catego-

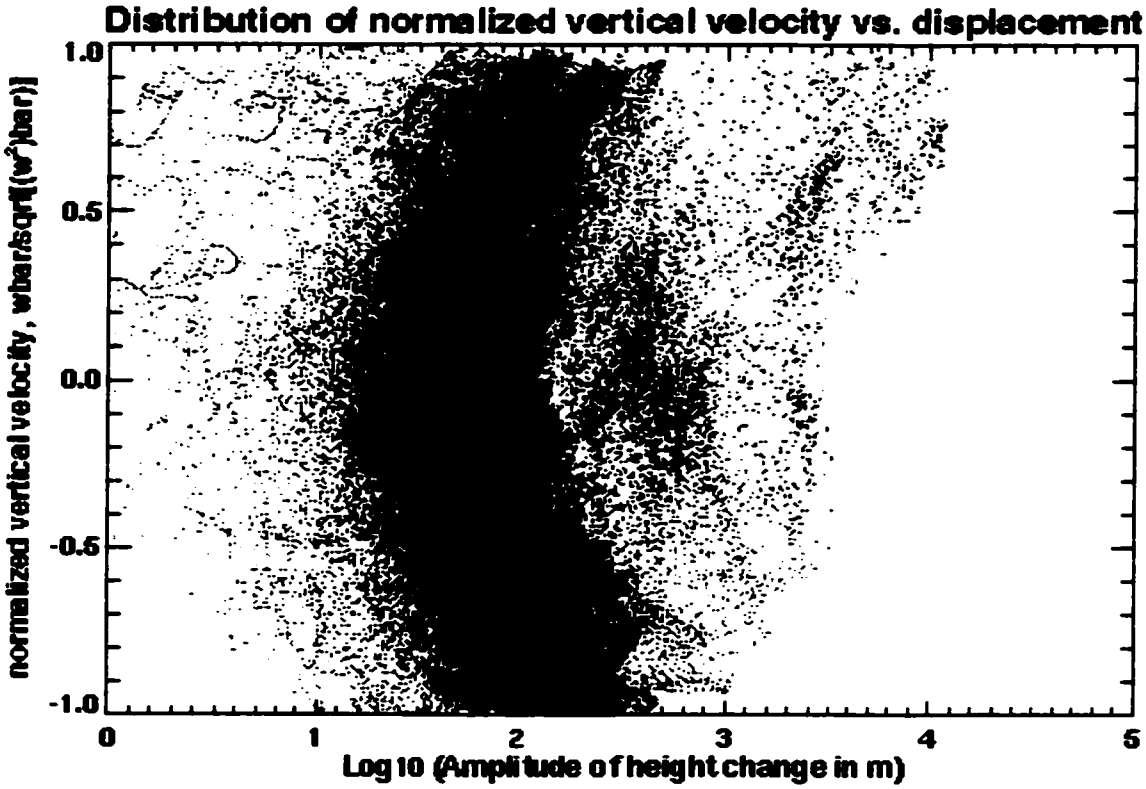

Fig. 11.5. Plot of convection factor defined in (11.8) versus the $\log_{10}$ of displacement for particles that have been advected for 30 minutes in the TC control run, starting at t = 6.5 hours. The red "dry" particles have $\overline{q_c} < 10^{-2}$ g/kg , while the blue "wet" particles have $\overline{q_c} > 10^{-2}$ g/kg .

ries of Fig. 11.2, respectively. We see that the moist updraft trajectories generally move in a slanted path, as we would expect from the orientation of the storm itself. It is interesting to note that some air (represented by the blue trajectory in Fig. 11.3a) moves eastward after undergoing its ascent. In Fig. 11.3b, we see that the particles classified as undergoing wave and turbulent motions run the gamut from those experiencing violent motions (the red trajectory) to relatively smooth, orbit-like trajectories (the green trajectory). Finally, the slow subsidence trajectories shown in Fig. 11.4 show that these particles underwent steady, downward motion to the west and east.

The above tropospheric particle advection experiment was repeated for the TC control run, with a start time of 6.5 hours (approximately when the second strong convective event of the simulation occurred). The results of this particle integration are shown in Fig. 11.5. Many of the same qualitative features of Fig. 11.2 are apparent in this figure, despite the fact that the simulated storms are quite different from one another. There are apparently more particles that experience slow, steady upward motion (i.e. low-amplitude height

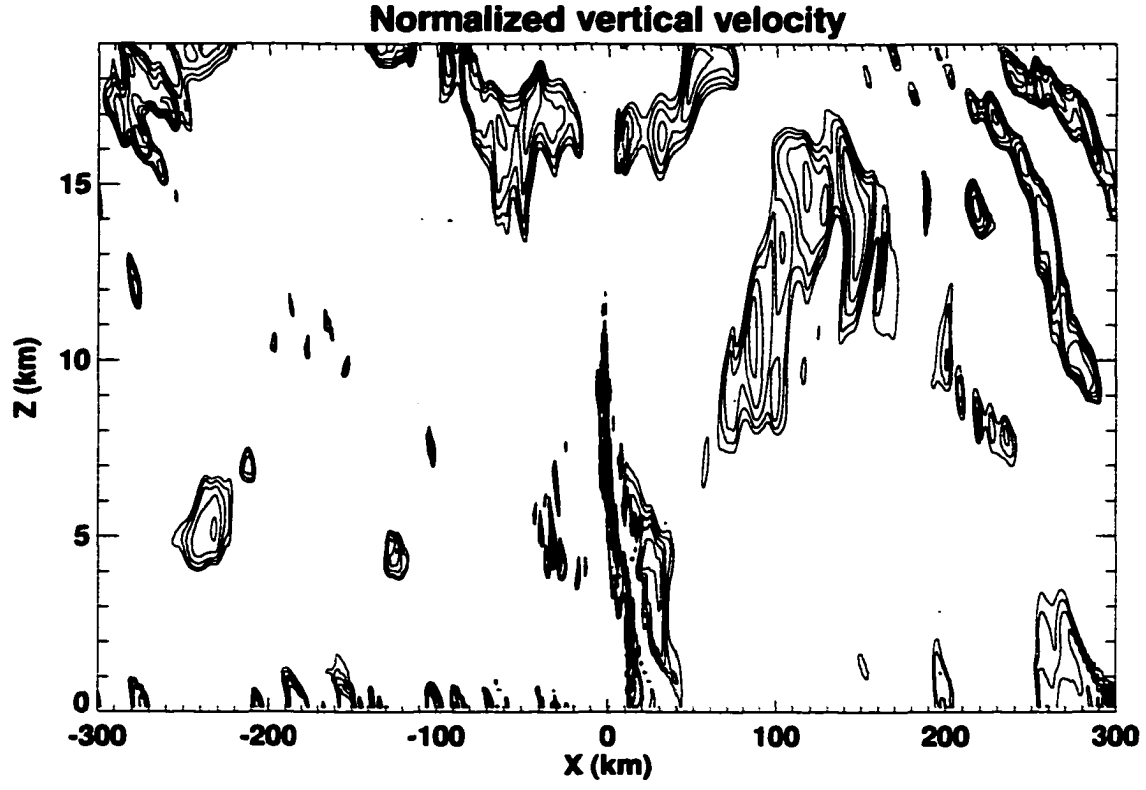

Fig. 11.6. Locations of upward vertical motion in the troposphere of the TC control run. Contours are of normalized vertical velocity greater than 0.5. The locations correspond to the initial locations of the particles.

change with $\hat{w} > 0.5$). This may be because the troposphere is much deeper in this simulation (19 km), and the convection never reaches the tropopause. The points with slow, steady upward motion may be associated with deep gravity waves that are within the troposphere, as seen in Fig. 11.6. Aside from the vertical motion associated with the convection itself, there are also areas with $\hat{w} > 0.5$ in the boundary layer, and in the troposphere, propagating away from the convection.

In addition to examining the behavior of particles in the model troposphere, we can use the particle analysis to examine what happens in the model stratosphere. In this case, we allowed the particles to be advected for two hours, since we expect the motion in the stratosphere to be dominated by gravity waves. Since the model stratosphere is dominated by wave motion, we expect particles that undergo wave motions with periods that are short in comparison to the integration time of the trajectories to have $|\hat{w}| \ll 1$, while particles that undergo long-period wave motion could have $|\hat{w}| \sim 1$. In Fig. 11.7, we see that most

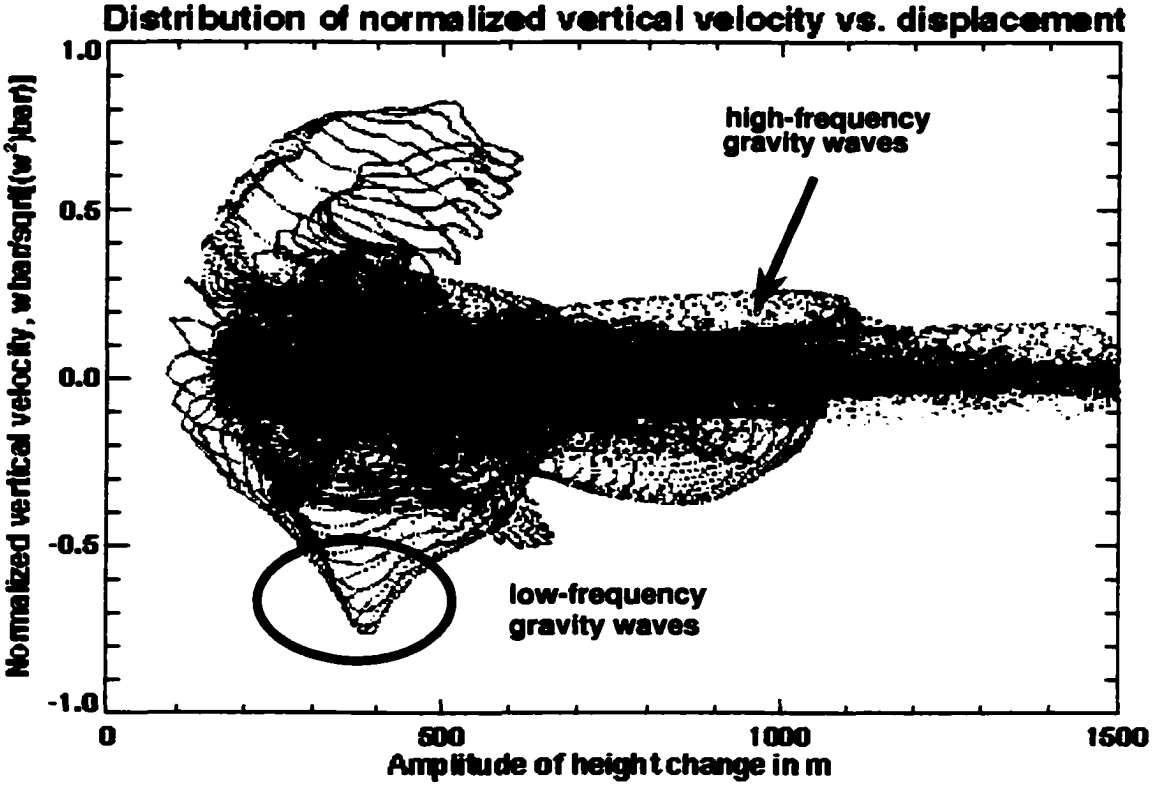

Fig. 11.7. Plot of normalized vertical velocity defined in (11.8) versus displacement in m for particles that have been advected for two hours in model stratosphere of the WK control run.

of the particles released in the WK control run starting at t = 3 hours apparently underwent wave motion in the stratosphere with a period less than 2 hours. This is not an unexpected result, since a Fourier analysis of the motions in the stratosphere (see Chapter 13) shows that most of the waves in the stratosphere had periods of 10-60 minutes.

As pointed out by Andrews et al. (1987), a particle will remain on an isentropic surface in the absence of heating or friction. Therefore, one way to test how well the trajectory model is doing in the stratosphere is to see whether θ remains roughly constant along a particle's path. The values of θ were calculated for several particles initialized at the z = 20 km level, in a region of strong gravity wave activity, approximately 50-100 km to the west of the center of the domain. The results of this calculation are shown in Fig. 11.9. We see that despite the fact that potential temperature varied widely at z = 20 km, each particle initialized at that level maintained a nearly constant value of θ.

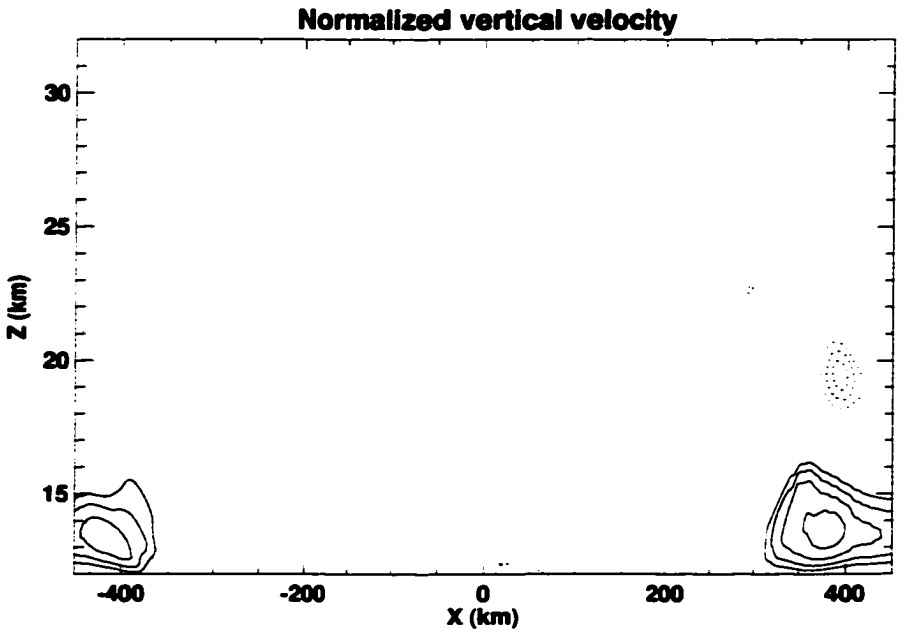

Fig. 11.8. Locations of the low-frequency gravity waves. Contours are of normalized vertical velocity greater than 0.5 (solid) and less than -0.5 (dashed). The locations correspond to the initial locations of the particles.

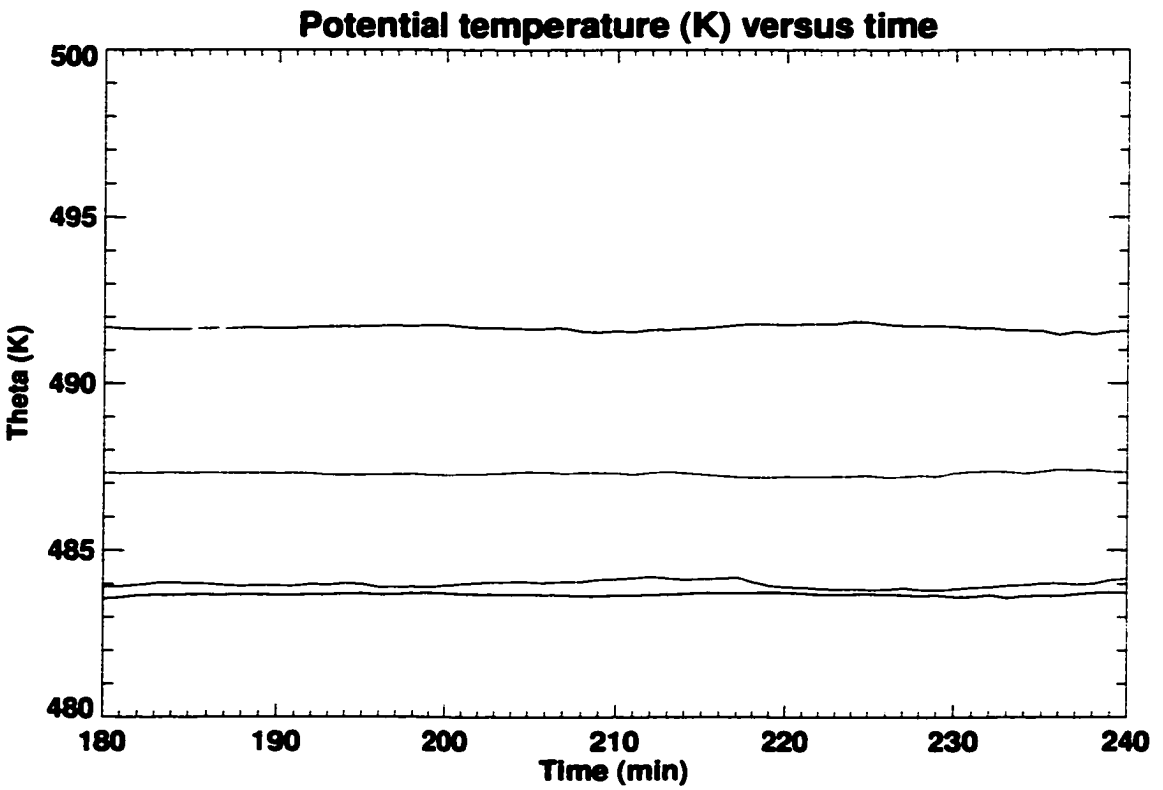

Fig. 11.9. Plot of potential temperature versus time for five particles released at z=20 km in a region of strong gravity wave activity.

The stratospheric trajectory experiment was also carried out for the TC control run. In Fig. 11.10, we see that the particles in this simulation were clustered around $|\hat{w}| \sim 0$, like those of the WK control run. However, the particles advected in the TC control run underwent much smaller vertical displacements, with most of the displacements clustered around 200-400 m. It should be noted that this is quite similar to the magnitude of isentropic displacements measured over a tropical MCS by Pfister et al. (1993).

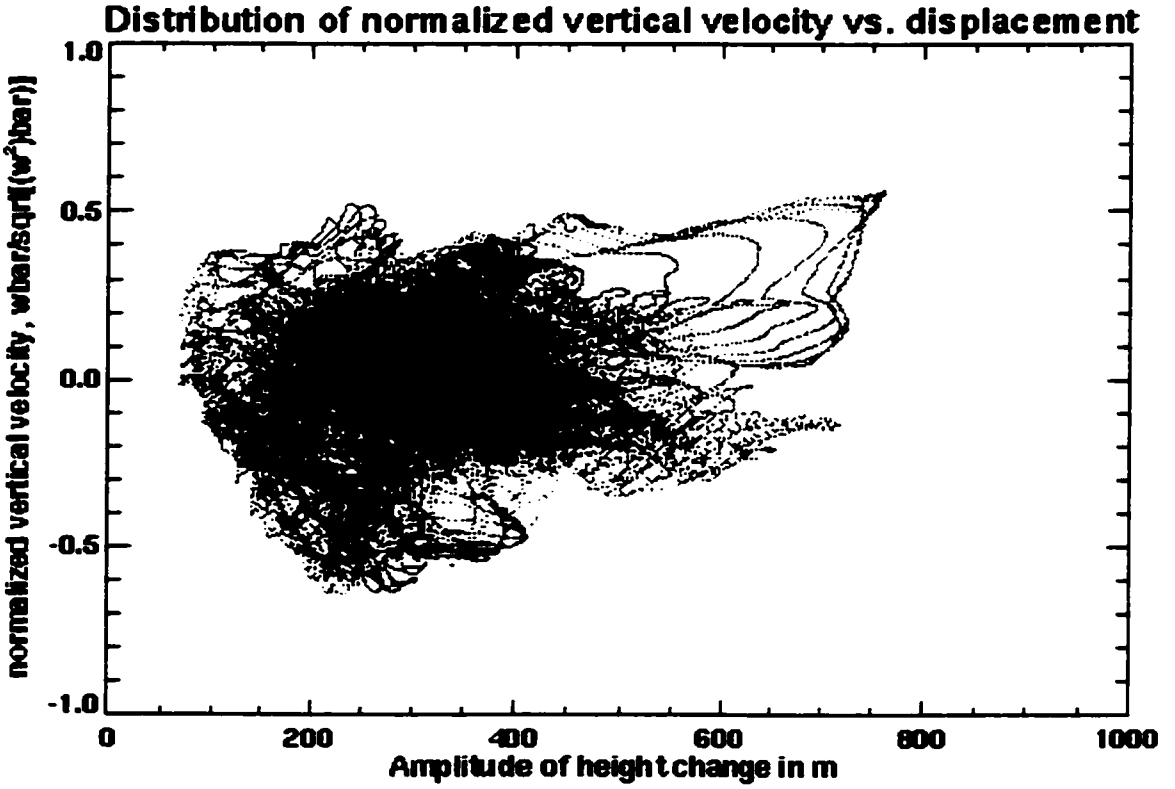

Fig. 11.10. Plot of normalized vertical velocity defined in (11.8) versus displacement in m for particles that have been advected for two hours in model stratosphere of the TC control run.

In this chapter, we have calculated trajectories for massless particles that were advected by the wind calculated from two numerical simulations of squall-line convection. From what has been shown here, it appears that moist updrafts can be isolated by using the following criteria:

$$\begin{aligned} \hat{w} &> 0 \quad , \\ \delta z &> 2000 \text{ m} \quad , \\ \overline{q_c} &> 10^{-1} \text{ g/kg} \quad . \end{aligned} \tag{11.10}$$

The qualitative behavior of the particles in the troposphere was quite similar between the two runs, and several different regimes for the particles can be described by constructing scatter plots of $\hat{w}$ versus δz. The motion of the particles in the stratosphere was consistent with what one would expect with high-frequency gravity waves. In the following chapter, we will use criteria consistent with (11.10) to separate the behavior of clear, cloudy and updraft air.

Chapter 12: Conditional sampling

In addition to particle trajectory diagnosis, another technique for identifying cloudy and updraft particles is to apply criteria to the individual snapshots of the storm evolution. If the location of a data point has sufficient condensate ($\overline{q_c} > 10^{-1}$ g/kg) to be a cloudy particle, then that location is assigned a "cloud mask" value of 1. Otherwise, the cloud mask has a value of 0. The contribution of cloudy grid points to the covariances or variance of a quantity can then be calculated at each vertical level according to the sum,

$$(\overline{a'b'})_{\text{clouds}} = \frac{1}{nx}\sum_{i=1}^{nx} \text{CM}_i a_i' b_i' . \tag{12.1}$$

Here, CM_i is the value of the cloud mask at the ith location, a' and b' are the departures of the variables a and b from the horizontal mean. When (12.1) is a variance calculation, $a = b$. The criteria for updraft mask (UM) includes the condensate concentration, but also includes a vertical velocity threshold, i.e.,

$$\text{UM}_i = \begin{cases} 1 & \text{if } \overline{q_c} > 10^{-1} \text{ g/kg and } w > 1 \text{ m s}^{-1} ; \\ 0 & \text{otherwise.} \end{cases} \tag{12.2}$$

Note that updraft points are a subset of cloudy points according to the above criteria. In addition, these points have similar values of cloud water and vertical velocity the moist updraft trajectories described in Chapter 11.

The time-averaged number of points that are cloudy points, updraft points, and downdraft points are shown as a function of height in Fig. 12.1a and Fig. 12.1b, for the WK control and TC control runs, respectively. The downdraft points were calculated using a mask similar to that of (12.2), except with $w < -1$ m s^{-1}. In both plots, the number of downdraft points is significantly smaller than that of the updraft points, which is consistent with the results from the trajectory analysis of Chapter 11. Note that the width of each

point in the WK control run (1000 m) is twice that of the TC control run. Each of these classes of points are most prevalent in the upper troposphere for the WK control run, while there is a lower tropospheric maximum in the TC control run. There is also a secondary maximum in the lower troposphere in the WK control run. In the WK control run, all of the fields approach zero around 13500 m, which is well above the 12000 m model tropopause. This indicates that the convection overshoots the tropopause in this simulation. On the other hand, the convection does not overshoot the higher 19000 m model tropopause in the TC control run.

When the perturbation kinetic energy, defined by

$$\frac{1}{2}\rho_0(\overline{u'u'} + \overline{w'w'}), \tag{12.3}$$

is vertically integrated throughout the troposphere, a measure of the amount of the average perturbation kinetic energy contained in a troposphere-deep 1 m^2 column is obtained. This quantity can be interpreted as a measure of the cumulus kinetic energy. The vertically integrated perturbation kinetic energy as a function of time with the cloud and updraft masks is shown in Fig. 12.2a and Fig. 12.2b. The perturbation kinetic energy due to cloudy and updraft points is only a small fraction of the overall perturbation kinetic energy for both simulations. The updraft points comprise the majority of this fraction, however.

The component of perturbation kinetic energy due to vertical motion, $\frac{1}{2}\rho_0\overline{w'w'}$, for all points, cloudy points, and is shown in Fig. 12.3. The cloudy and updraft points are responsible for a significant portion of the overall vertical perturbation kinetic energy, and are highly correlated to the overall vertical perturbation kinetic energy. The updraft points comprise the vast majority of the amount of $\overline{w'w'}$ due to cloudy points overall. This is in spite of the fact that there are significantly higher amounts of cloudy points than updraft points, on average, as we saw in Fig. 12.1.

As one might guess from a comparison of Fig. 12.2 to Fig. 12.3, the horizontal portion of the overall perturbation kinetic energy field (not shown) is dominant for the entire domain for both simulations. This is consistent with the results of Xu et al. (1992).

The strength of the updrafts can be measured by calculating an average value of the vertical velocity within the updraft points. In Fig. 12.4a and Fig. 12.4b, this quantity is

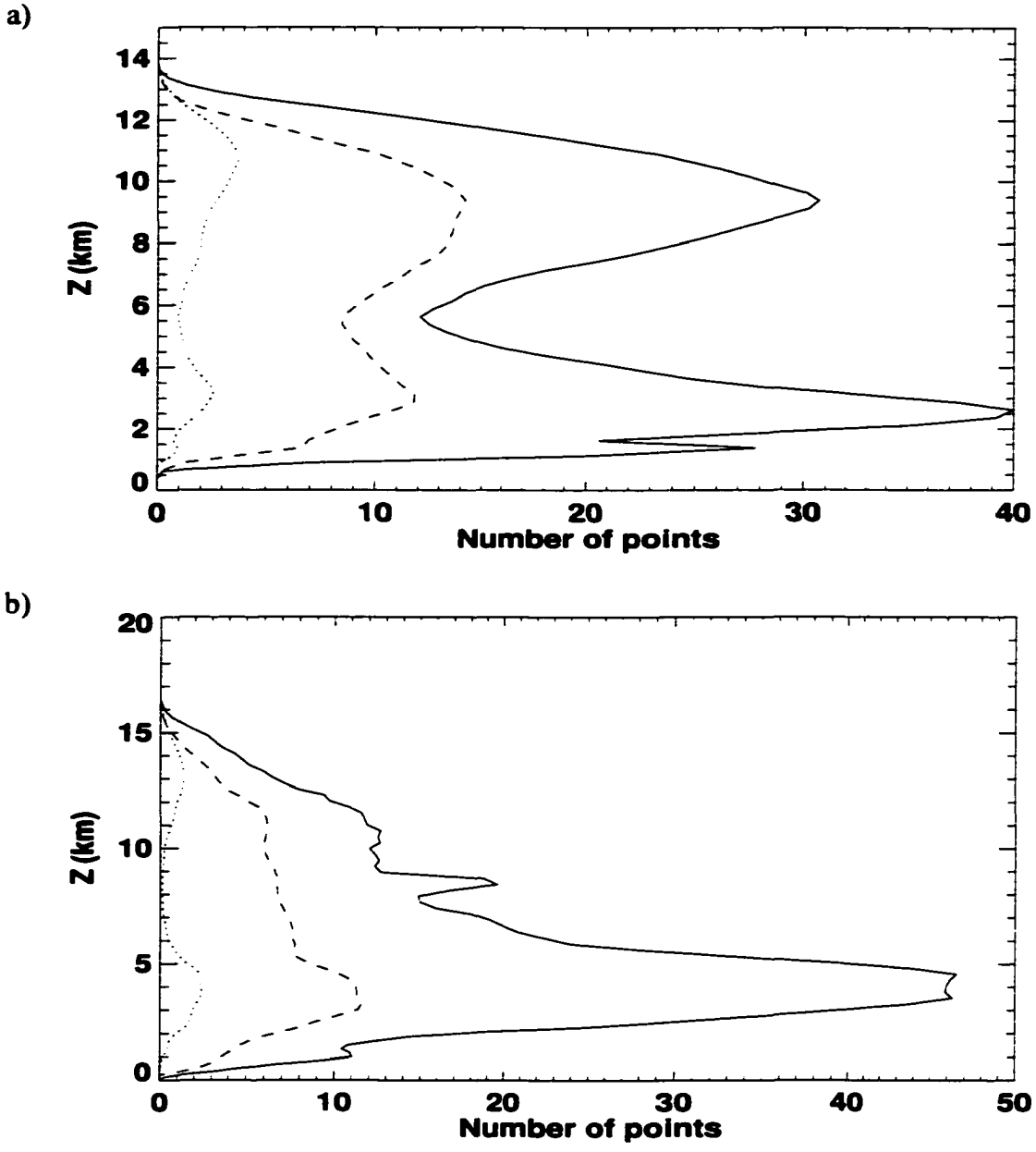

Fig. 12.1. Plot of the time-averaged number of cloudy points (solid line), updraft points (dashed line), and downdraft points (dotted line) at each vertical level for the a) WK control run, and b) TC control run.

shown as a function of time for the WK control and TC control runs, respectively. This is a bulk measure of the strength of the updrafts, as opposed to the maximum vertical velocity shown in Fig. 5.9. In this figure, we see that the WK control run has considerably stronger updrafts than those of the TC control run, which is consistent with the differences in $\frac{1}{2}\rho_0 \overline{w'w'}$ we saw in Fig. 12.3.

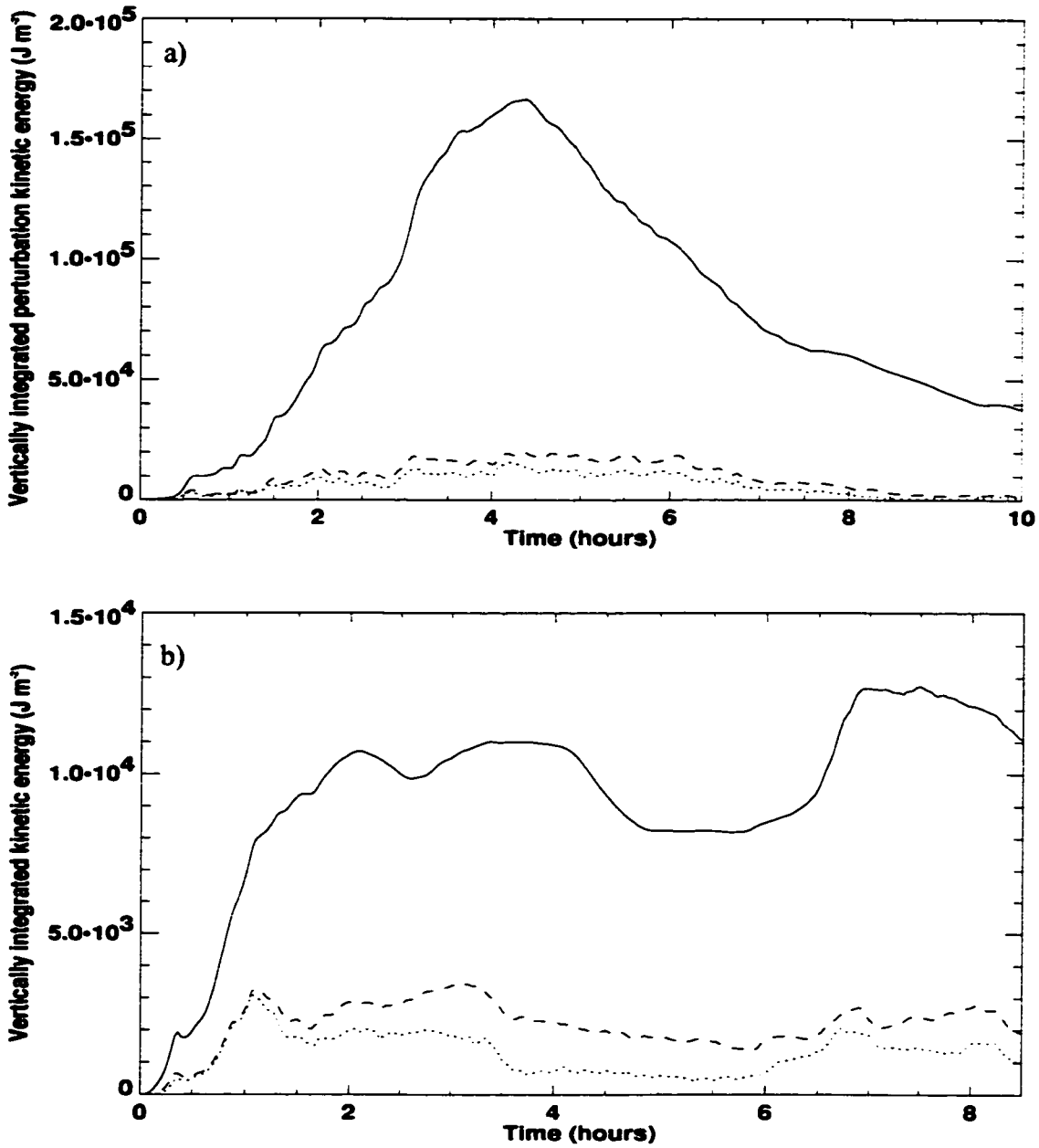

Fig. 12.2. Vertically integrated perturbation kinetic energy of the troposphere versus time for all points (solid line), cloudy points (dashed line), and updraft points (dotted line) for the a) WK control run, and b) TC control run.

Another quantity that is of interest is the extent to which the moist convective updrafts represent an obstacle to the mean flow. Such an obstacle can be considered a "transient mountain" poking into a mean flow, as shown by Pfister et al. (1993). This concept will be discussed in more detail in Chapter 15. One way to measure the amount of "obstacle" the convection poses to the mean flow is to calculate the difference between u at each updraft

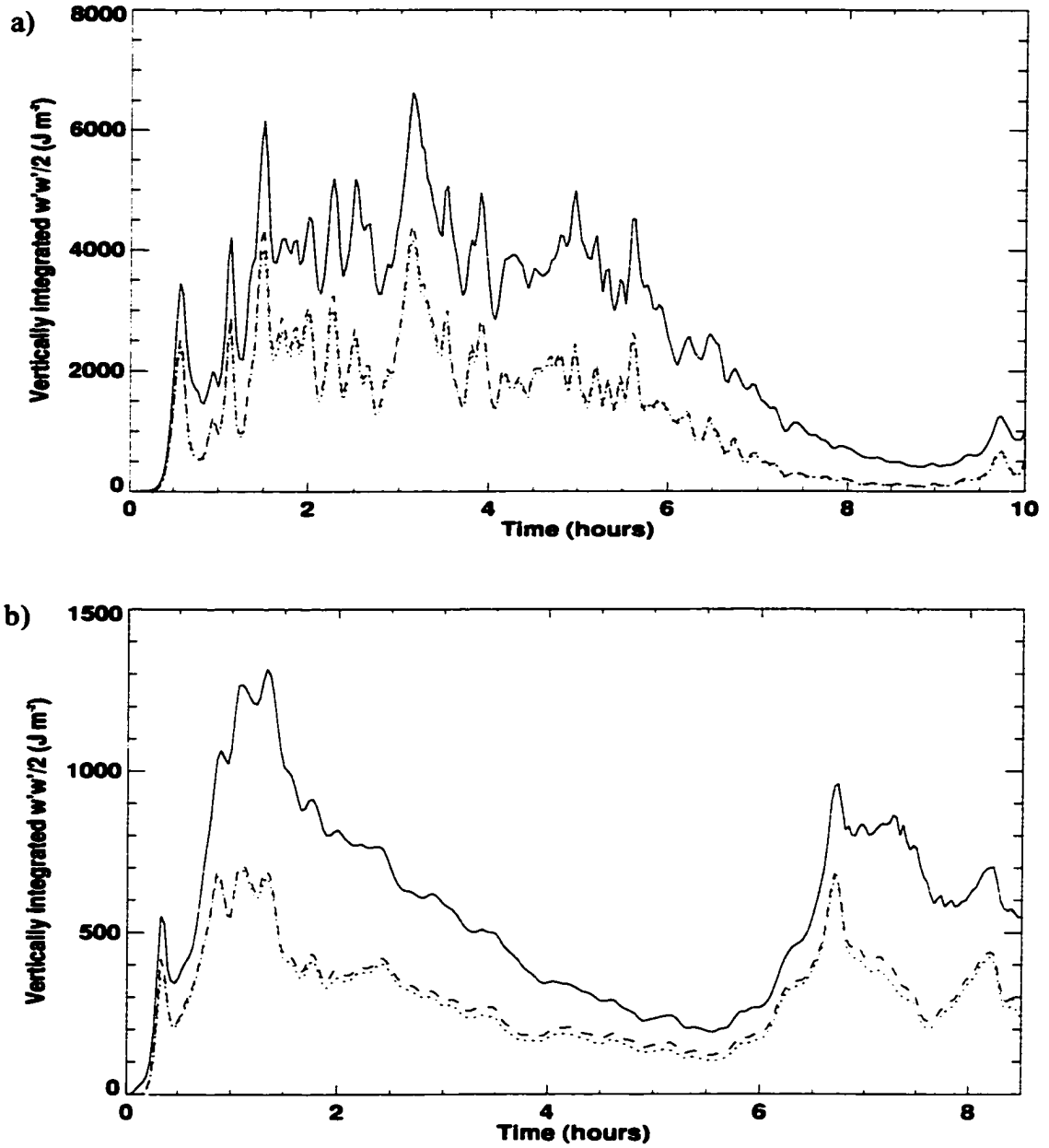

Fig. 12.3. Vertically integrated perturbation kinetic energy of the troposphere due to vertical motions versus time for all points (solid line), cloudy points (dashed line), and updraft points (dotted line). for the a) WK control run, b) TC control run.

point and $\bar{u}$ at that particle's vertical level, and then average over the updraft particles. In Fig. 12.5, we see that the WK low-shear, control, and high-shear runs share some similarities in terms of the behavior of this quantity. The control and high-shear runs begin with the updrafts having winds that are more westerly than those of the surrounding atmosphere, and then becoming more easterly with time. This is consistent with observations of

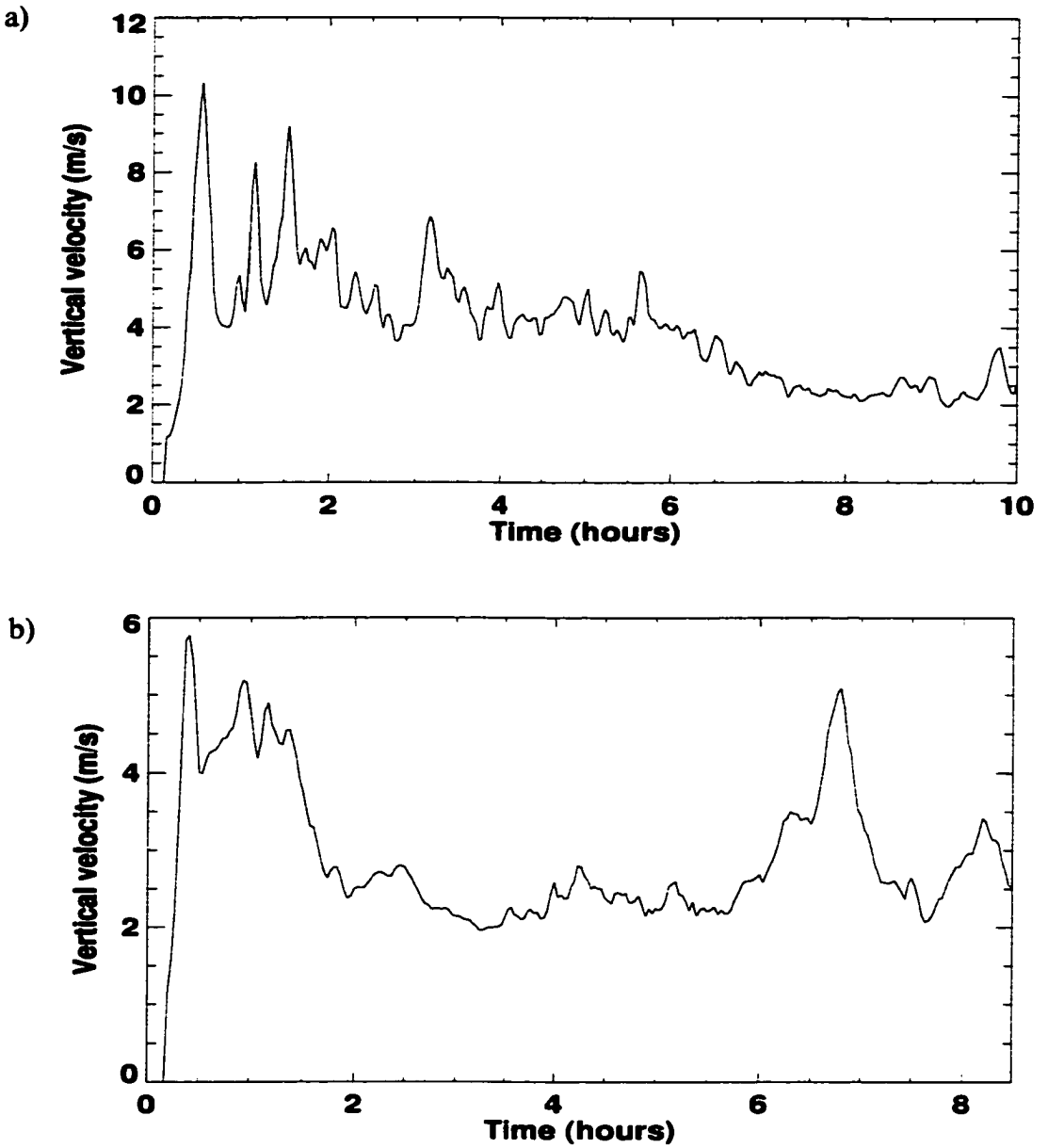

Fig. 12.4. Average vertical velocity of updraft points versus time for a) the WK control run and b) the TC control run.

an initial downshear tilt to the convection, followed by an upshear tilt, and is also consistent with the production of more eastward-propagating waves earlier in the WK control simulation, evident in Fig. 14.2. These processes are also evident in the WK low-shear run, although it does not have westerlies for nearly as long as the control or high-shear

simulations. Similar diagnoses that attempted to isolate the effects of the high-altitude updrafts revealed that these points had similar values of u_{up}' to those of all simulations.

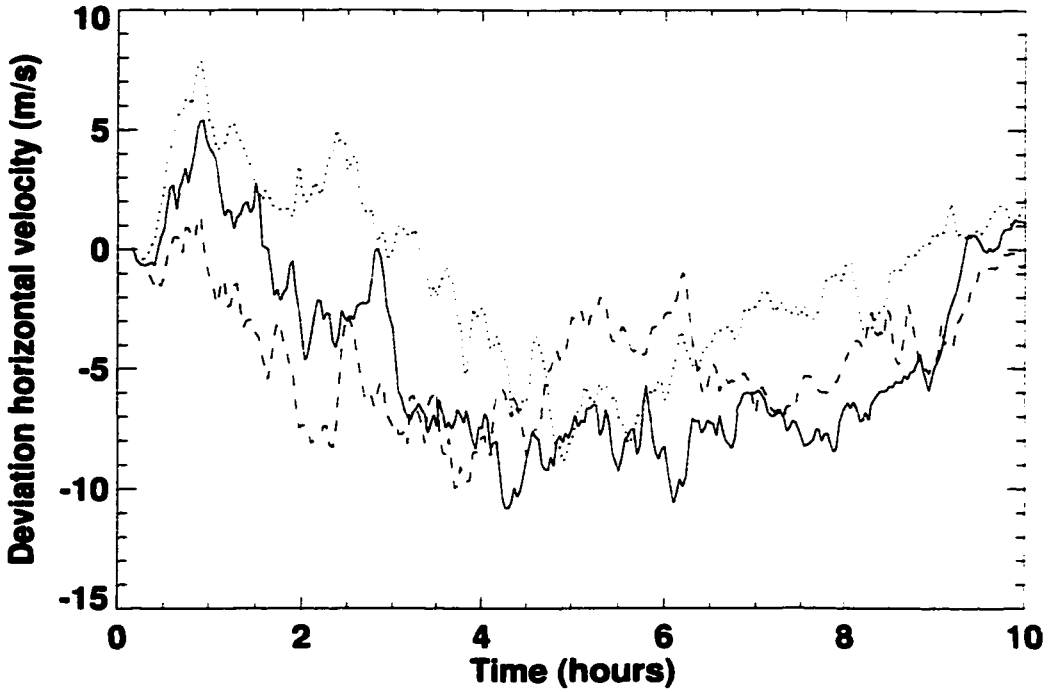

Fig. 12.5. Comparison of the average difference between the horizontal velocity of the updraft-masked points and those of the mean flow for the WK control (solid line), WK low-shear (dashed line), and WK high-shear (dotted line) runs.

The difference between the u of the updrafts and $\bar{u}$ was also tested between the TC control and TC no jet runs, as shown in Fig. 12.6. This figure shows that there are significant differences in how u_{up}' evolves with time for these simulations. In the TC control run, we see that after a short period with $u_{up}' > 0$, the sign of this quantity is consistently negative, as we would expect from a rearward-tilting squall line, illustrated in Fig. 4.5b. The TC no jet run, on the other hand, experiences a fairly long period with $u_{up}' > 0$, which is associated with a structure similar to that of Fig. 4.5c. As we will see in Chapter 13 and Chapter 15, this forward tilt is consistent with the production of more eastward-propagating waves than the TC control run.

In this chapter, we have described a method to diagnose cloudy, updraft, and downdraft points within simulations of convection. The results of this diagnosis have shown

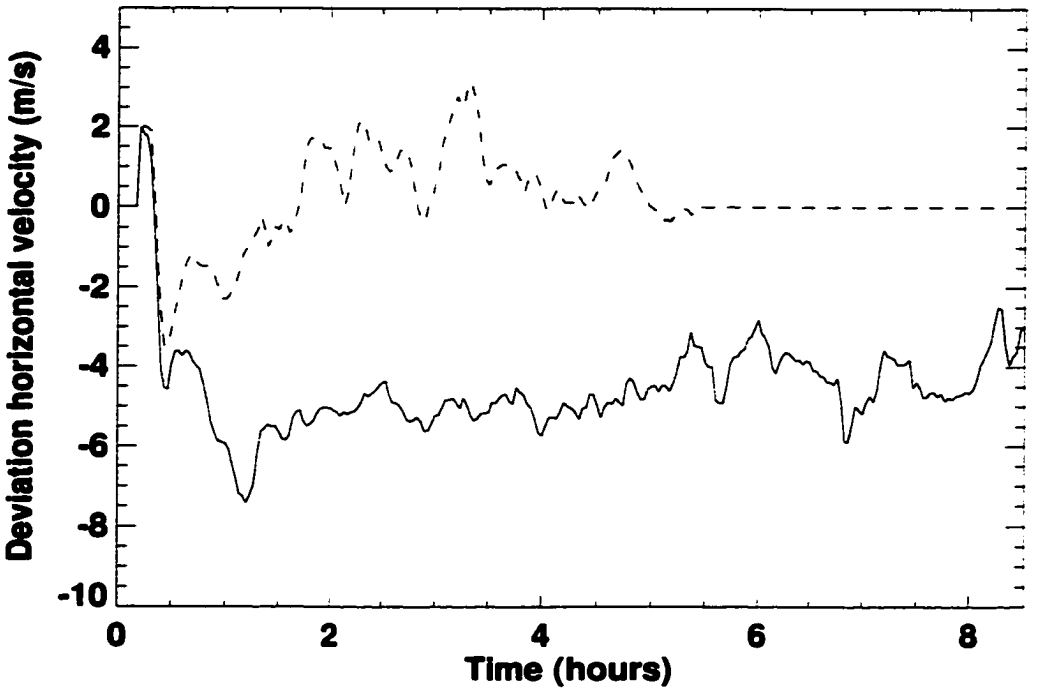

Fig. 12.6. Comparison of the average difference between the horizontal velocity of the updraft-masked points and those of the mean flow for the TC control (solid line) and TC no jet (dashed line) runs.

that the points in these classes take up a small portion of the overall domain. It should be noted that the use of a smaller threshold of cloudiness would result in more points, but the overall results would be similar. The perturbation kinetic energy of the troposphere has been shown to be dominated by horizontal motions, which is consistent with the results of Xu et al. (1992). In addition, we have seen that the moist updrafts accounted for a disproportionate amount of the vertical component of the perturbation kinetic energy, while the vast majority of the horizontal component of the perturbation kinetic energy occurred outside of the cloudy air. We also diagnosed the horizontal velocity within the updrafts. When this quantity was subtracted from the zonal mean, a measure of the amount of blocking that the updrafts have on the mean flow was obtained. In the following chapter, we will examine the spectral properties of the waves produced by the simulated convection, and then we will attempt to couple the properties of the convection to those of the waves it generates in Chapter 15, using a modified version of the theory offered by Pfister et al. (1993).

Chapter 13: Fourier Analysis

Fourier analysis has been used in a multitude of applications throughout the sciences. Fourier analysis techniques are generally used to determine the characteristic spatial and/or temporal scales of variation for a given dataset. This chapter will briefly outline the theory behind one- and two-dimensional Fourier transforms, and then present results from the application of these transforms to the velocity fields from the WK and TC control runs.

13.1. Background

A Fourier transform pair of a continuous periodic function $f(t)$ can be expressed as a sum of sines and cosines (Hamming 1988; Hartmann 1999)

$$f(t) = \sum_{\omega=0}^{\infty} A_\omega \cos(\omega t) + B_\omega \sin(\omega t), \tag{13.1}$$

where the coefficients of the cosines and sines are given by

$$A_\omega = \frac{1}{\pi}\int_0^{2\pi} f(t)\cos(\omega t)dt, \tag{13.2}$$

$$B_\omega = \frac{1}{\pi}\int_0^{2\pi} f(t)\sin(\omega t)dt, \tag{13.3}$$

respectively. It should be noted that there are equivalent transforms that can be defined using the complex form of the periodic functions (Percival and Walden 1993).

Actual data sets, of course, cover a finite length of time and are sampled at discrete intervals. Thus, if we have some quantity f that is sampled at N times, each denoted by t_i, that are spaced with a constant interval of Δt, we can define a discrete Fourier transform given by

$$f(t_i) = \sum_{\omega=0}^{N/2} A_\omega \cos(\omega t_i) + B_\omega \sin(\omega t_i), \tag{13.4}$$

where the coefficients are now given by

$$A_\omega = \begin{cases} \frac{1}{N}\sum_{i=1}^{N} f(t_i) & ,\omega = 0; \\ \frac{2}{N}\sum_{i=1}^{N} f(t_i)\cos(\omega t_i), & 0 < \omega < \frac{N}{2}; \\ \frac{1}{N}\sum_{i=1}^{N} f(t_i)\cos(\omega t_i), & \omega = \frac{N}{2}, \end{cases} \tag{13.5}$$

$$B_\omega = \frac{2}{N}\sum_{i=1}^{N} f(t_i)\cos(\omega t_i). \tag{13.6}$$

The variance spectrum (or power spectral density) associated with f is a real-valued quantity given by

$$\Gamma_\omega = \frac{A_\omega^2 + B_\omega^2}{2}. \tag{13.7}$$

The dataset represented by f is not normally periodic with respect to its endpoints. This can cause aliasing, as the discontinuity between f_0 and f_{N-1} is treated as spectral power at high frequencies. One solution to this problem is the implementation of a taper, such as the $p \times 100\,\%$ cosine filter defined below (Percival and Walden 1993):

$$h_t = \begin{cases} \frac{C}{2}\left[1 - \cos\left(\frac{2\pi t}{pN+1}\right)\right] & , \quad 1 \le t \le \frac{pN}{2}; \\ C & , \frac{pN}{2} < t \le N + 1 - \frac{pN}{2}; \\ \frac{C}{2}\left[1 - \cos\left(\frac{2\pi(N+1-t)}{pN+1}\right)\right], & N + 1 - \frac{pN}{2} < t \le N. \end{cases} \tag{13.8}$$

Here, C is a normalization constant chosen such that

$$\sum_{t=1}^{N} h_t^2 = 1. \tag{13.9}$$

In this work, we are interested in the behavior of quantities such as the momentum flux $\overline{u'w'}$ in both wavenumber and frequency space. Obtaining the cospectrum between the zonal and vertical components of velocity at each wavenumber and frequency allows us to

integrate the amount of momentum flux at a given phase speed, since the phase speed is simply ω/k. This procedure is similar to what Alexander and Holton (1997) used.

The calculation of the 2-D space-time Fourier spectrum is outlined below, following Hartmann (1999) and Hamming (1988). We will again use the real forms of the Fourier series, to parallel the manner in which the actual computer code was constructed. First, we perform a zonal Fourier transform on some function $f(x, t)$, which is defined at NX points in the horizontal, and NT times:

$$f(x,t) = \sum_{k=0}^{NX/2} C_k(t)\cos kx + S_k(t)\sin kx. \tag{13.10}$$

We can then perform a Fourier transform on the time-varying coefficients $C_k(t)$ and $S_k(t)$ into frequency space,

$$C_k(t) = \sum_{\omega=0}^{NT/2} A_{k,\omega}\cos\omega t + B_{k,\omega}\sin\omega t, \tag{13.11}$$

$$S_k(t) = \sum_{\omega=0}^{NT/2} a_{k,\omega}\cos\omega t + b_{k,\omega}\sin\omega t. \tag{13.12}$$

Substitution of (13.11) and (13.12) into (13.10) yields an expression in terms of the spectral coefficients

$$f(x,t) = \sum_{k=0}^{NX/2}\sum_{\omega=0}^{NT/2} [(A_{k,\omega}\cos\omega t + B_{k,\omega}\sin\omega t)\cos kx + (a_{k,\omega}\cos\omega t + b_{k,\omega}\sin\omega t)\sin kx] \quad . \tag{13.13}$$

The above expression can then be converted into one that splits between waves that propagate westward ($\omega > 0$) and eastward ($\omega < 0$), by using the complex forms of the cosine and sine functions:

$$\cos a = \frac{e^{ia} + e^{-ia}}{2}, \tag{13.14}$$

$$\sin a = \frac{e^{ia} - e^{-ia}}{2i}. \tag{13.15}$$

Note that we will actually use the opposite convention to that defined above in the analysis of the model data, so that eastward-propagating waves can be associated with positive phase speeds. Using (13.14) and (13.15) into (13.13), we obtain

$$f(x,t) = \frac{1}{2}\sum_{k=0}^{NX/2}\sum_{\omega=0}^{NT/2}\left[(A_{k,\omega}-b_{k,\omega})\frac{e^{i(kx+\omega t)}+e^{-i(kx+\omega t)}}{2}+\right.$$
$$(B_{k,\omega}+a_{k,\omega})\frac{e^{i(kx+\omega t)}-e^{-i(kx+\omega t)}}{2i}+(A_{k,\omega}+b_{k,\omega})\frac{e^{i(kx-\omega t)}+e^{-i(kx-\omega t)}}{2}+ \qquad (13.16)$$
$$\left.(-B_{k,\omega}+a_{k,\omega})\frac{e^{i(kx-\omega t)}-e^{-i(kx-\omega t)}}{2i}\right] .$$

which becomes

$$f(x,t) = \frac{1}{2}\sum_{k=0}^{NX/2}\sum_{\omega=0}^{NT/2}\left[(A_{k,\omega}-b_{k,\omega})\cos(kx+\omega t)+(B_{k,\omega}+a_{k,\omega})\sin(kx+\omega t)+\right. \qquad (13.17)$$
$$\left.(A_{k,\omega}+b_{k,\omega})\cos(kx-\omega t)+(-B_{k,\omega}+a_{k,\omega})\sin(kx-\omega t)\right] .$$

If we examine the above series, we can use the following definitions to convert it to phase form (see Hamming 1988):

$$T_{k,\pm\omega} = \frac{(A_{k,\omega}\mp b_{k,\omega})}{2}, \qquad (13.18)$$

$$U_{k,\pm\omega} = \frac{(\pm B_{k,\omega}+a_{k,\omega})}{2}, \qquad (13.19)$$

$$W_{k,\pm\omega} = \sqrt{T_{k,\pm\omega}^2+U_{k,\pm\omega}^2}. \qquad (13.20)$$

Applying (13.18)-(13.20) to (13.17), we have

$$\sum_{k=0}^{NX/2}\sum_{\omega=0}^{NT/2}W_{k,\pm\omega}\left[\frac{T_{k,\pm\omega}}{W_{k,\pm\omega}}\cos(kx\pm\omega t)+\frac{U_{k,\pm\omega}}{W_{k,\pm\omega}}\sin(kx\pm\omega t)\right]. \qquad (13.21)$$

Since the cosine of two angles added together can be written as

$$\cos(a+b) = \cos(a)\cos(b)-\sin(a)\sin(b), \qquad (13.22)$$

we can express (13.21) as

$$\sum_{k=0}^{NX/2}\sum_{\omega=0}^{NT/2}W_{k,\pm\omega}\cos(kx\pm\omega t+\Phi_{k,\pm\omega}) \qquad (13.23)$$

if the phase angle $\Phi_{k,\pm\omega}$ satisfies

$$\cos\Phi_{k,\pm\omega} = \frac{T_{k,\pm\omega}}{W_{k,\pm\omega}}, \tag{13.24}$$

$$\sin\Phi_{k,\pm\omega} = \frac{-U_{k,\pm\omega}}{W_{k,\pm\omega}}. \tag{13.25}$$

As Hamming (1988) notes, care needs to be taken when inverting either of the above expressions, since the ranges of the inverse trigonometric functions are periodic.

The variance spectrum associated with (13.23) for some dataset f can be written as

$$\Gamma_{k,\pm\omega}(f) = \frac{1}{2}[W_{k,\pm\omega}(f)]^2, \tag{13.26}$$

while the cospectrum and quadrature spectrum between f and g are given by

$$C_{k,\pm\omega}(f,g) = \frac{1}{2}[W_{k,\pm\omega}(f)][W_{k,\pm\omega}(g)]\cos[\Phi_{k,\pm\omega}(g) - \Phi_{k,\pm\omega}(f)], \tag{13.27}$$

$$Q_{k,\pm\omega}(f,g) = \frac{1}{2}[W_{k,\pm\omega}(f)][W_{k,\pm\omega}(g)]\sin[\Phi_{k,\pm\omega}(g) - \Phi_{k,\pm\omega}(f)], \tag{13.28}$$

respectively. The cospectrum has a high magnitude when $\Phi_{k,\pm\omega}(g)$ and $\Phi_{k,\pm\omega}(f)$ are separated by 0 or π radians. We expect the cospectrum to be high for quantities such as the momentum flux $u'w'$, if the waves obey polarization relationships similar to those of linear gravity waves. The quadrature spectrum has a high magnitude when $\Phi_{k,\pm\omega}(g)$ and $\Phi_{k,\pm\omega}(f)$ are separated by $\pi/2$ radians, so we would expect the quadrature spectrum to be high for quantities such as the vertical heat flux $w'\theta'$ for gravity waves.

13.2. WK control run

The fields that we will apply the above analyses to are the perturbation zonal and vertical velocities. Here, we define a perturbation as a departure from the zonal mean at each time. For the one-dimensional power spectra in time, we calculated the power spectrum of the time series in horizontal or vertical velocity at each point, and then averaged the spectra at each vertical level. Thus, there were 900 samples of each power spectrum in time at each vertical level for the WK control run. The power spectrum versus frequency is shown in Fig. 13.1. Here, we are using cycles per second to facilitate comparisons with previous studies (Alexander et al. 1995; Pandya and Alexander, 1999). A broad peak is seen at fre-

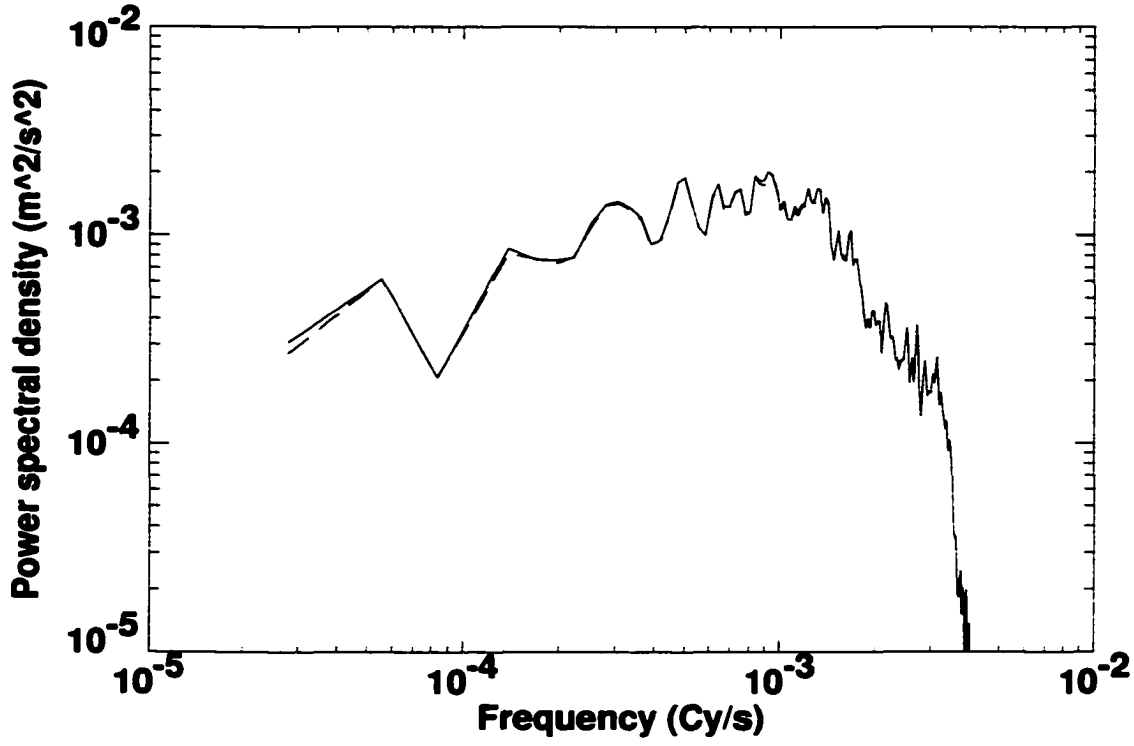

Fig. 13.1. Log-log plot of the power spectrum of vertical velocity at 14125 m as a function of frequency. The solid line represents the spectrum calculated from the unaltered time series, while the dashed line represents the spectrum calculated from the time series after a 20% cosine taper defined in (13.8) was applied.

quencies between 0.00025 Cy s^{-1} and 0.0015 Cy s^{-1}, which corresponds to periods between 10 and 60 minutes. The highest amplitude peak corresponds to a periodicity of 18 minutes, which is fairly close to the 23 minute periodicity of EOFs 6 and 7, which were the modes associated with stratospheric gravity waves in Chapter 10. The overall spectrum is similar in shape to that calculated by Pandya and Alexander (1999), although the highest peak in their frequency spectrum is more prominent than that of Fig. 13.1. The application of a taper function such as (13.8) on the time series seems to have had very little effect on the spectrum, as shown in Fig. 13.1. We will refrain from using a taper for the remainder of this chapter.

As noted in Andrews et al. (1987), vertically propagating gravity waves increase in amplitude with height in proportion to the inverse square root of density. Therefore, in the absence of all other factors, we would expect the variance spectrum of Fig. 13.1 to be replicated at higher altitudes when the spectrum is multiplied by a factor of

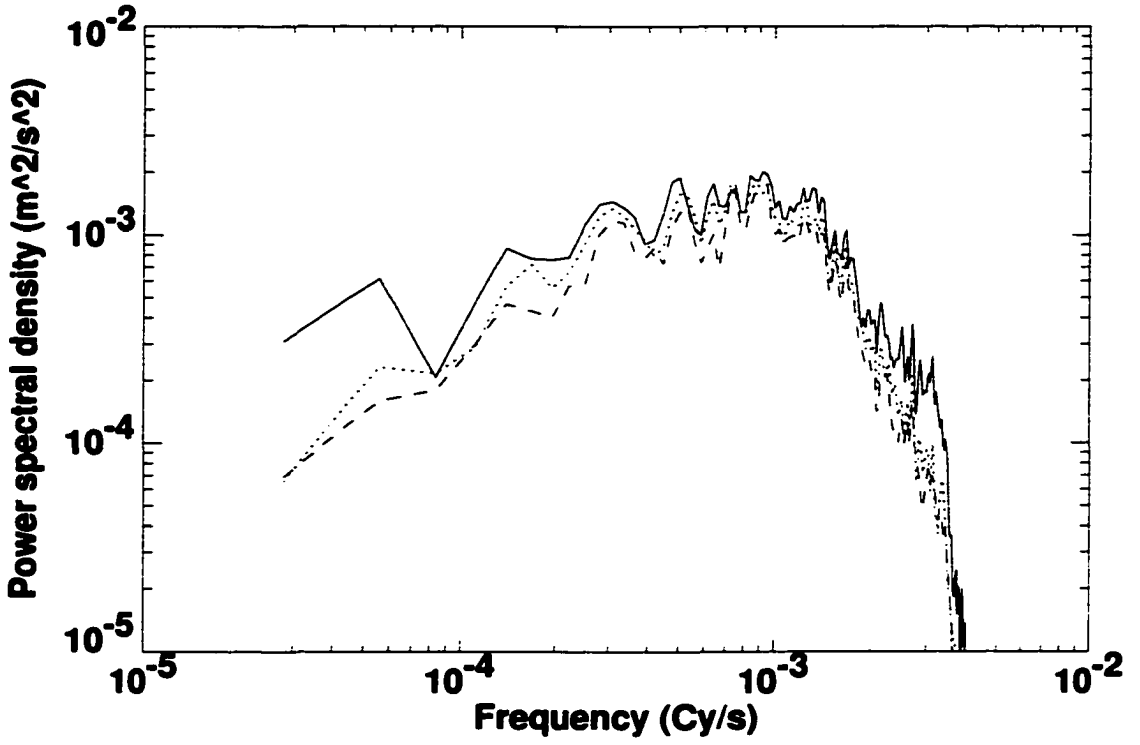

Fig. 13.2. Log-log plot of the normalized power spectra of vertical velocity at 14125 m (solid), 21125 (dotted) and 28125 m (dashed) as a function of frequency.

$\rho_0(z)/\rho_0(14125\text{m})$. A comparison between the normalized power spectra at 14125, 21125 and 28125 m is shown in Fig. 13.2. We see that the locations of many of the frequency peaks are maintained with height. However, there is a slight decrease in the (normalized) amplitude of the spectra with height. There are two possible reasons for this decrease. One is the amount of time for the waves to reach the upper stratosphere. In other words, the model atmosphere at 14125 m experiences wave motions prior to (and for a longer duration) than the model atmosphere at higher altitudes. Another explanation is due to diffusive damping, which would explain the significant decrease in spectral power at the highest frequencies. In any case, Fig. 13.2 shows that the stratosphere of the WK control run oscillated over a range of frequencies between 10 and 60 minutes throughout its depth.

The normalized variance spectrum of horizontal velocity versus frequency at 14125 m, 21125 m and 28125 m is shown in Fig. 13.3. This frequency spectrum has some significant differences from that calculated from vertical velocity, the most obvious being the overall higher power at each frequency. In addition, there is much more power at low fre-

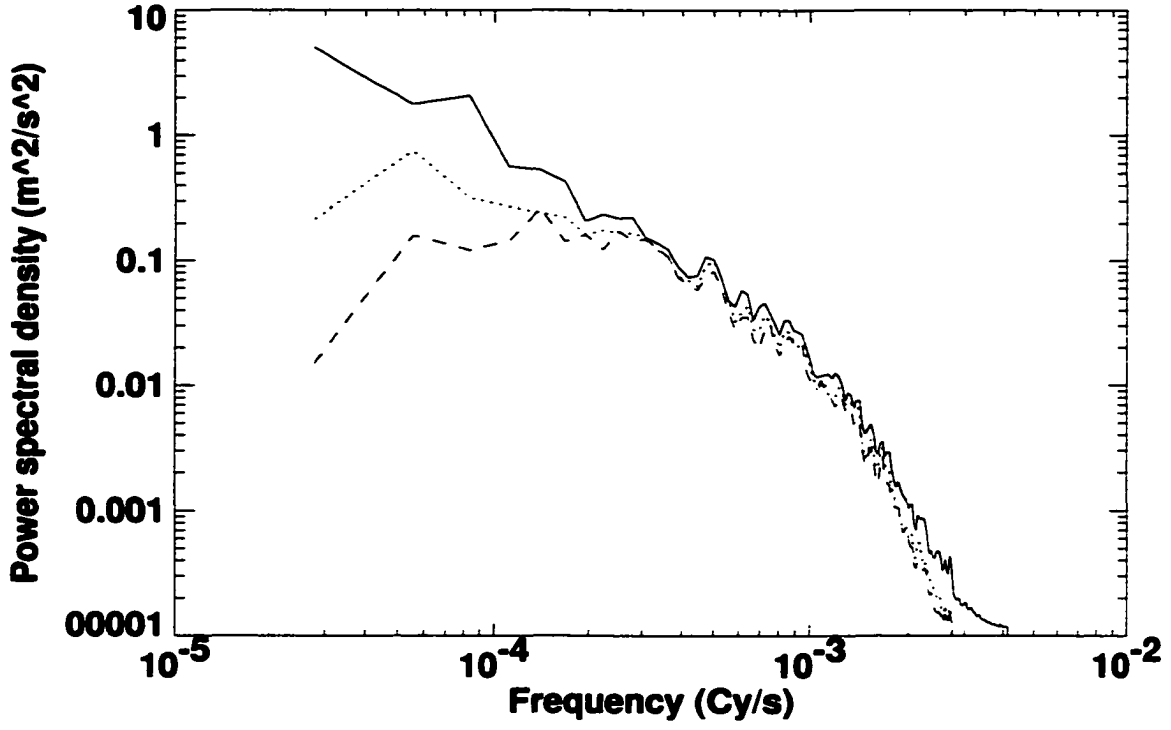

Fig. 13.3. Log-log plot of the normalized power spectra of horizontal velocity at 14125 m (solid), 21125 (dotted) and 28125 m (dashed) as a function of frequency.

quencies in the power spectrum of horizontal velocity, particularly at lower altitudes in the stratosphere. There are still prominent peaks in the frequency range of 10-60 minutes, as we saw in the vertical velocity spectrum.

The normalized power spectrum of vertical velocity versus horizontal wavenumber is shown in Fig. 13.4. There is a broad peak from wavenumbers of 10^{-4} Cy m^{-1} to 10^{-5} Cy m^{-1}, corresponding to wavelengths of 10-100 km. This is consistent with the results of Pandya and Alexander (1999). It is interesting to note that the most prominent peak in Fig. 13.4 is at a wavelength of about 30 km, which is similar to the waves seen in EOFs 6 and 7. The variance falls off quite rapidly for wave shorter than 10 km, which is similar to what Pandya and Alexander (1999) observed in their study.

Another quantity that is interesting to examine is the vertical wavenumber. Although this can be calculated directly via FFTs, we have used the linear phase relationship given in (1.11) to calculate $m(\omega, k)$ for each frequency and horizontal wavenumber, and then

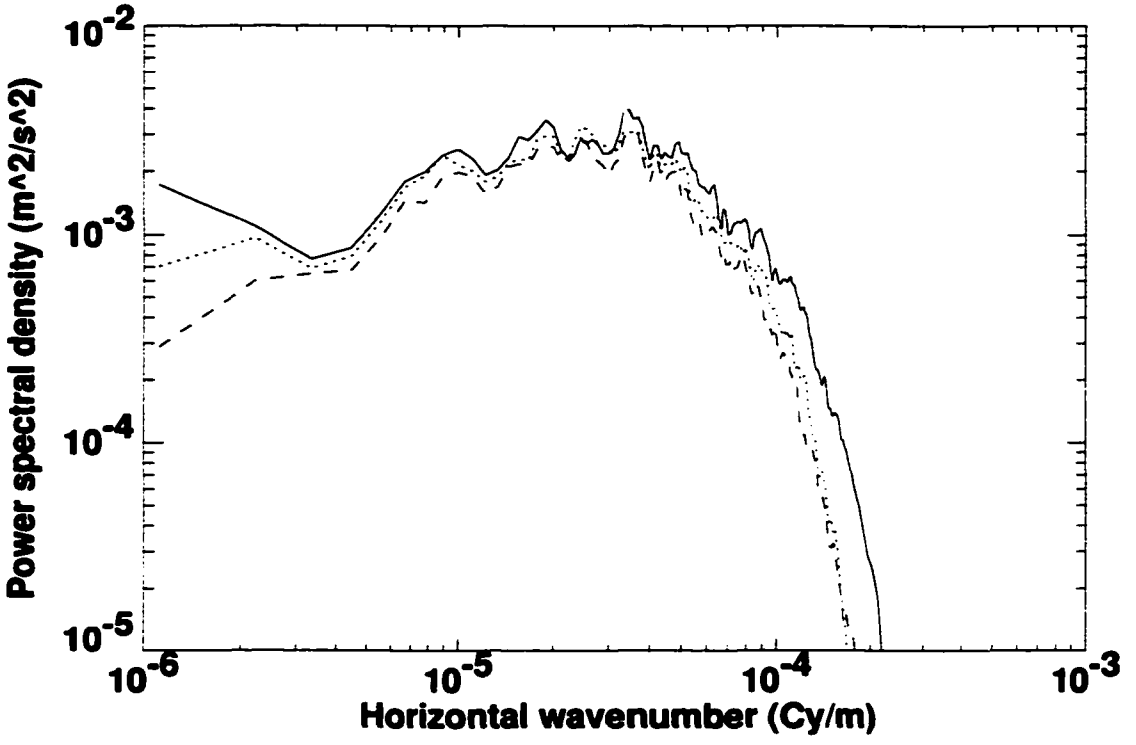

Fig. 13.4. Log-log plot of the normalized power spectra of vertical velocity at 14125 m (solid), 21125 (dotted) and 28125 m (dashed) as a function of horizontal wavenumber.

added up the spectral power of the vertical velocity within several vertical wavenumber bins. The results of this calculation are shown in Fig. 13.5, in terms of the vertical wavelength. In this figure, we see that there is a peak near $\lambda_z = 8$ km, which is similar to the results of Alexander et al. (1995) and Pandya and Alexander (1999) for similar simulations, as well as Piani et al. (2000) for a somewhat different simulation. These authors attributed the vertical wavelength of the waves to the depth of the convective heating, consistent with the theoretical results of Salby and Garcia (1987), Nicholls et al. (1991), and Pandya et al. (1993). Since the Brunt-Väisälä frequency roughly doubles between the troposphere and stratosphere, the half-wavelength heating depth of ~8 km (see Fig. 5.13) becomes a full-wavelength wave in the stratosphere, according to (1.11). The fairly sharp peak in Fig. 13.5 is may be due to the fact that the convection in the WK control run has a fairly consistent structure throughout the simulation.

The vertical group velocity spectrum can also be obtained, following a similar procedure to the one we used to get the vertical wavenumber spectrum. In Fig. 13.6, we see that

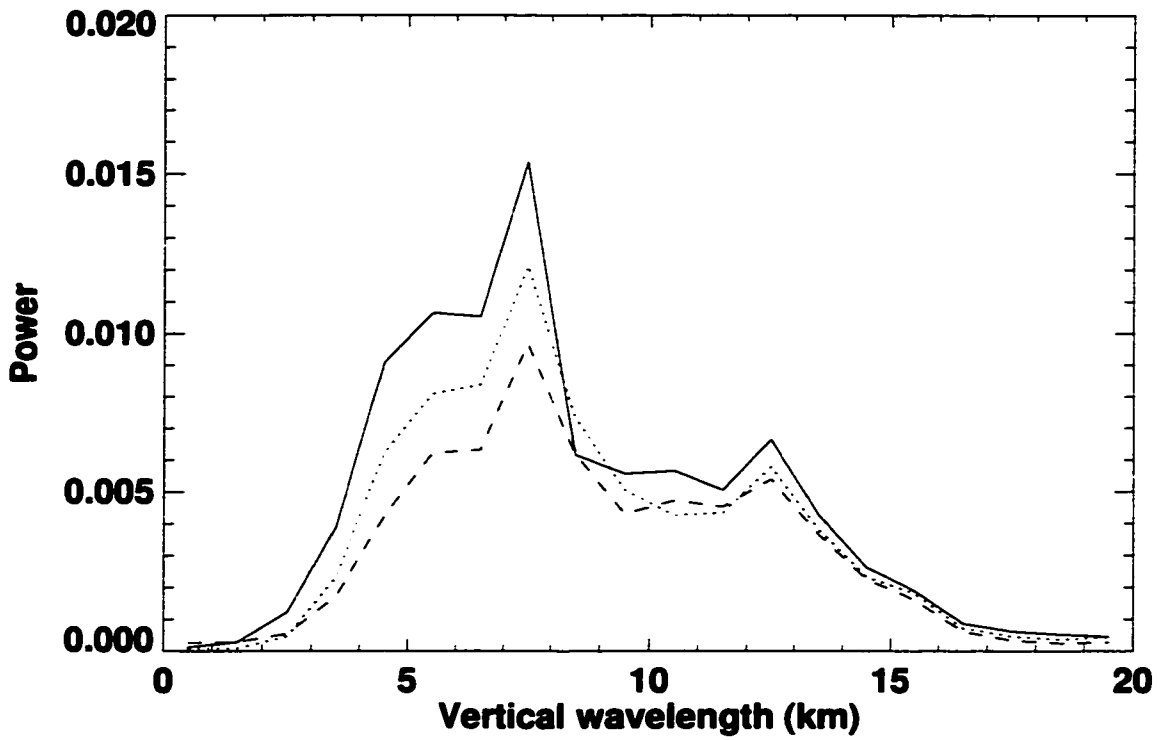

Fig. 13.5. Plot of the normalized power spectra of vertical velocity at 14125 m (solid), 21125 (dotted) and 28125 m (dashed) as a function of vertical wavenumber.

the power spectrum of vertical velocity is distributed across a fairly broad range of c_{gz}, with a peak around 5 m s^{-1}. The energy associated with waves that have a vertical group velocity of 5 m s^{-1} take a little over an hour to traverse the 20 km model stratosphere. It is interesting to note that the waves with lower group velocities have are damped more than those with higher group velocities. This makes sense, since these waves have a longer period of time over which damping processes can affect them.

The cospectrum defined in (13.27) was calculated between the perturbation zonal and vertical velocities at each vertical level. We expect the integral of such a cospectrum over all frequencies and wavenumbers to be equivalent to the Eulerian mean momentum flux at the same vertical level averaged over time. A plot of the cospectrum in wavenumber and frequency space is shown in Fig. 13.7. In this plot, we see negative values of momentum flux associated with westward-propagating waves, and positive values of momentum flux associated with eastward-propagating waves, as we would expect. Also, the highest magnitudes of momentum flux are clustered along two lines of constant ω/k in both the neg-

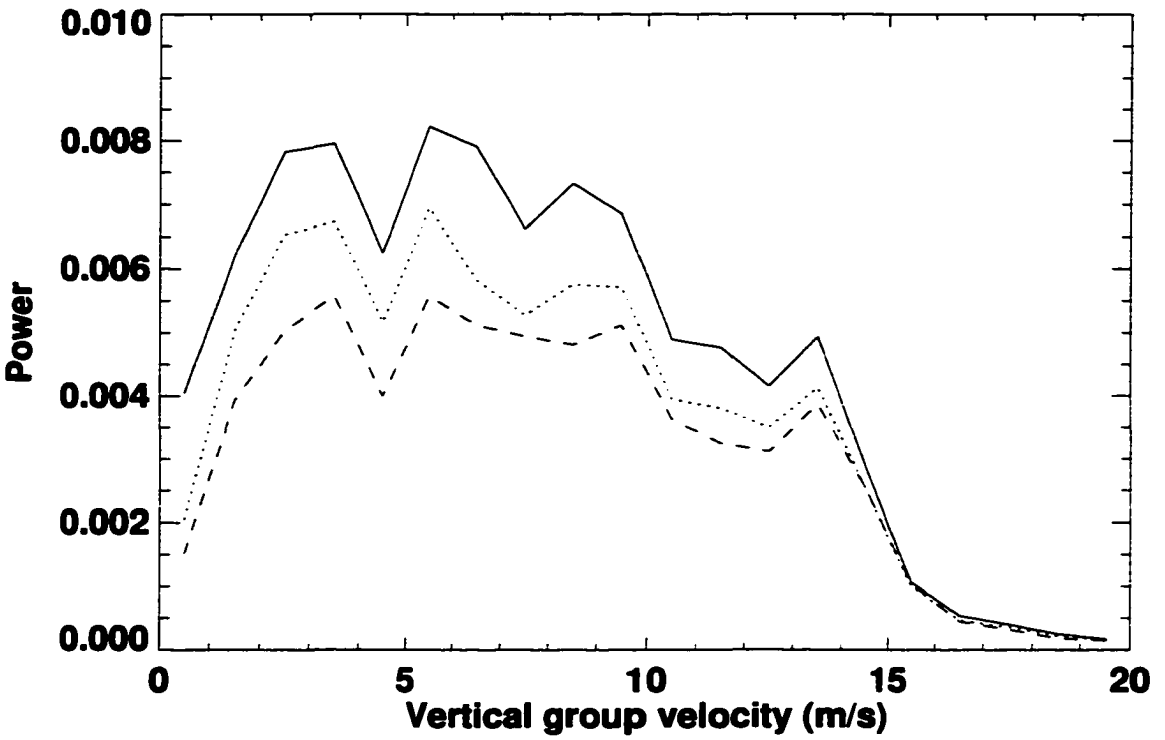

Fig. 13.6. Plot of the normalized power spectra of vertical velocity at 14125 m (solid), 21125 (dotted) and 28125 m (dashed) as a function of vertical group velocity.

ative and positive frequency ranges. We would therefore expect the waves in the model atmosphere to have two peaks at positive and negative phase speed.

We can actually calculate the amount of momentum flux associated with a "bin" of phase speed between $c_n - \Delta c$ and $c_n + \Delta c$ by following the procedure of Alexander and Holton (1997). We begin by adding up the amount of momentum flux from each point in (ω, k) space that falls within a given interval of phase speed. The choice of Δc is immaterial to the amount of momentum flux that is associated with positive and negative phase speeds, but the character of the phase speed spectrum will become more spiky with smaller Δc.

The results of such a calculation for the WK control run, with Δc set to 1 m s^{-1}, are shown in Fig. 13.8. We see that the most prominent peak is associated with phase speeds between -10 and -30 m s^{-1}. This is consistent with the phase speed estimate of 20-35 m s^{-1} for EOFs 6 and 7, which were primarily associated with westward-propagating waves.

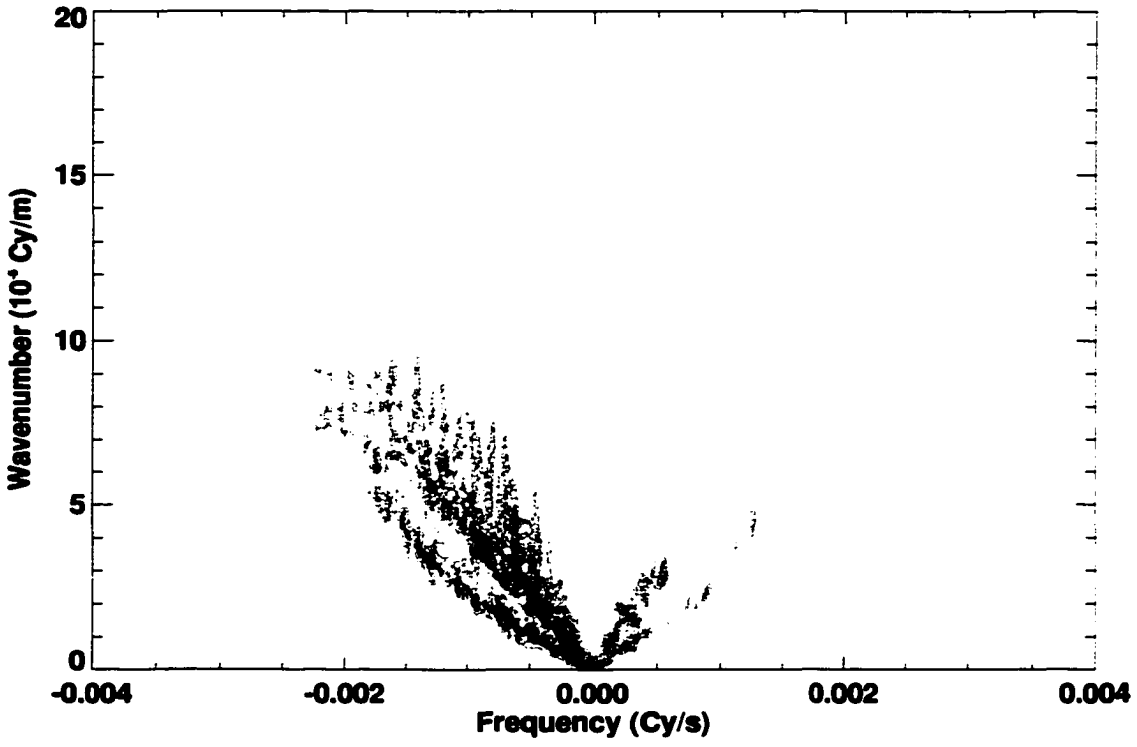

Fig. 13.7. Contour plot of the cospectra of horizontal and vertical velocity at 14125 m as a function of horizontal wavenumber and frequency for the WK control run. The red contours (0.00001, 0.0001, 0.001, 0.01 $m^2 s^{-2}$) correspond to positive values of $\overline{u'w'}$, while the blue contours (-0.00001, -0.0001, -0.001, -0.01 $m^2 s^{-2}$) correspond to negative values of $\overline{u'w'}$. The zero contour is omitted.

There are also peaks at other negative (-50 m s^{-1}) and positive (15 m s^{-1}, 25 m s^{-1}) phase speeds, which is the four-peaked spectrum that we expected from Fig. 13.7. There is very little momentum flux associated with waves with phase speeds greater than ±50 m s^{-1}, or less than ±10 m s^{-1}. The flat area in the spectrum at low phase speeds (also observed in Alexander and Holton 1997 and Piani et al. 2000) can be understood in a number of ways. One of these is that waves that are close to an intrinsic phase speed of zero are preferentially damped, as we saw in Chapter 1. Also, Saravanan (1990) used the 1-D model of Plumb (1977) to simulate the forcing of the QBO by a spectrum of waves in the presence of the upwelling Brewer-Dobson circulation (Brewer 1949; Dobson 1956). Saravanan found that waves with low phase speeds were damped after passing through an area of upwelling. Within this area of upwelling, a "buffer zone" was created where the mean flow

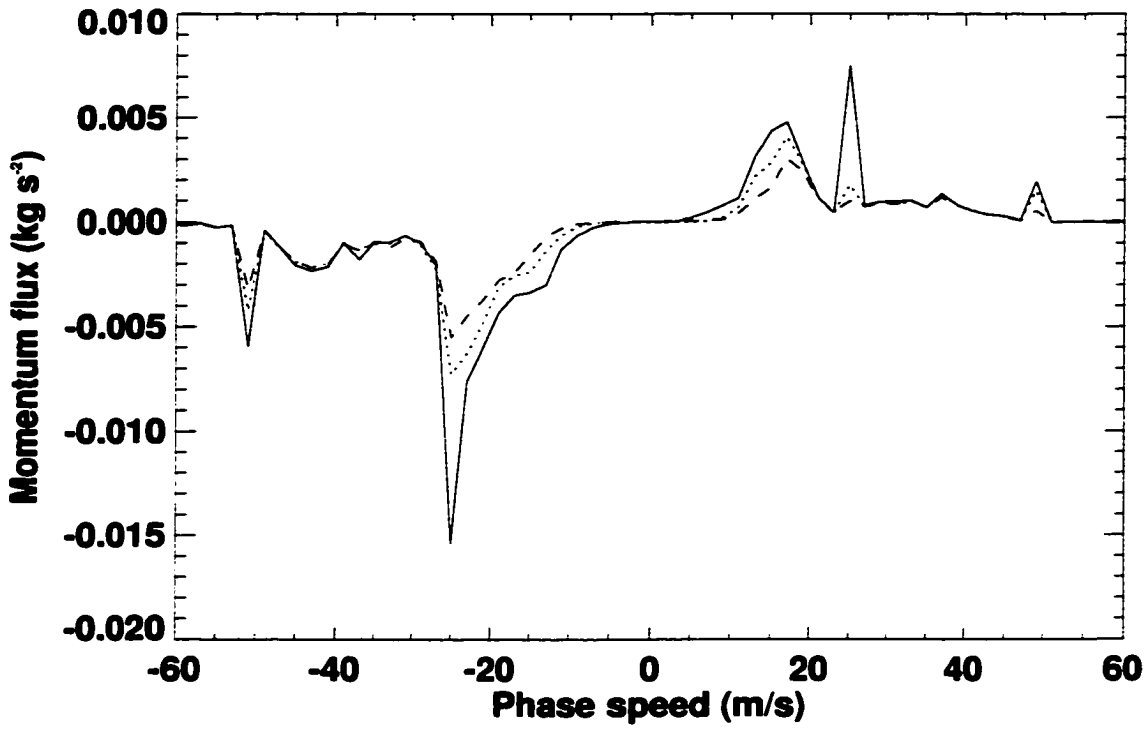

Fig. 13.8. Plot of the momentum flux $\rho_0 \overline{u'w'}$ at 14125 m (solid), 21125 m (dotted) and 28125 m (dashed) as a function of horizontal phase speed for the WK control run.

speed remained relatively close to zero, due to the homogenizing effects of vertical advection,

$$\frac{\partial \bar{u}}{\partial t} \sim -\bar{w}(0)\exp\left(-\frac{z}{H_w}\right)\frac{\partial \bar{u}}{\partial z}. \tag{13.29}$$

Here, $\bar{w}(0)$ is the vertical velocity at the bottom of Saravanan's model (located at 200 mb), and H_w is the scale over which the upwelling persists. We see from (13.29) that strong wind shears will tend to be damped in the presence of vertical advection in Saravanan's model. By the time the waves reach the top of the buffer zone, those with slow horizontal phase speeds have been damped due to a damping term of the form (1.13). Since the waves are generated within an area of upward motion (the interior of a convective cloud), they might be expected to exhibit similar behavior.

The peaks in the spectrum depicted in Fig. 13.8 at ±25 m s^{-1} are partially associated with a mode that is an artifact of our use of periodic lateral boundary conditions. This

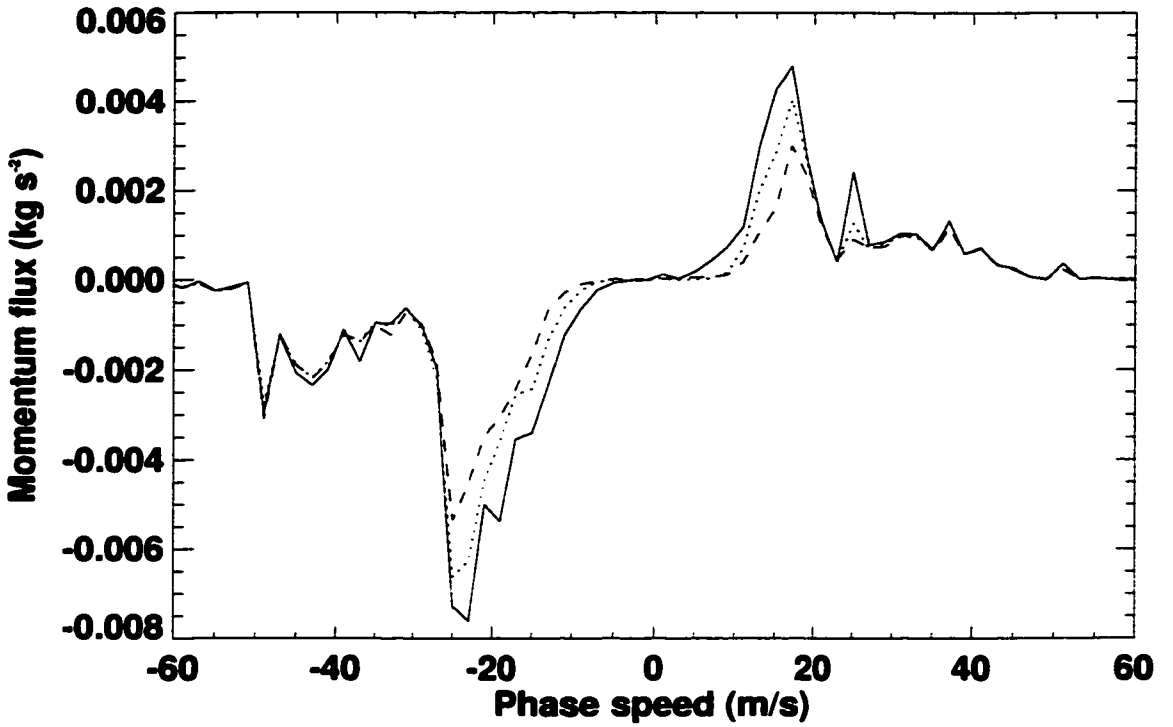

Fig. 13.9. Plot of the momentum flux $\rho_0\overline{u'w'}$ at 14125 m (solid), 21125 m (dotted) and 28125 m (dashed) as a function of horizontal phase speed for the WK control run with the k = 1, $\omega = \pm 1$ mode removed.

"transient standing wave" mode has a wavenumber 1 (associated with the antisymmetry in the sign of momentum flux in the domain), and a frequency of ± 1 (associated with the commencement of convection). Since the sizes of the space and time domains in our simulation are 900000 m and 36000 s, respectively, the transient standing wave mode shows up as a peak at ± 25 m s^{-1}. When the Fourier analysis is performed over shorter time periods (e.g., from 2-10 hours), the peaks move to higher phase speeds, since the time domain has been reduced, while the rest of the spectrum remains relatively constant. Since we believe this mode to be a peculiarity of the specific domain size, analysis interval, and lateral boundary conditions of our simulation, the mode will be filtered in all subsequent presentations of the momentum flux spectra. The spectrum with this mode removed is shown in Fig. 13.9. The transient standing wave mode is a contributor to the total eastward and westward momentum flux of the experiments, however, so the calculations of these quan-

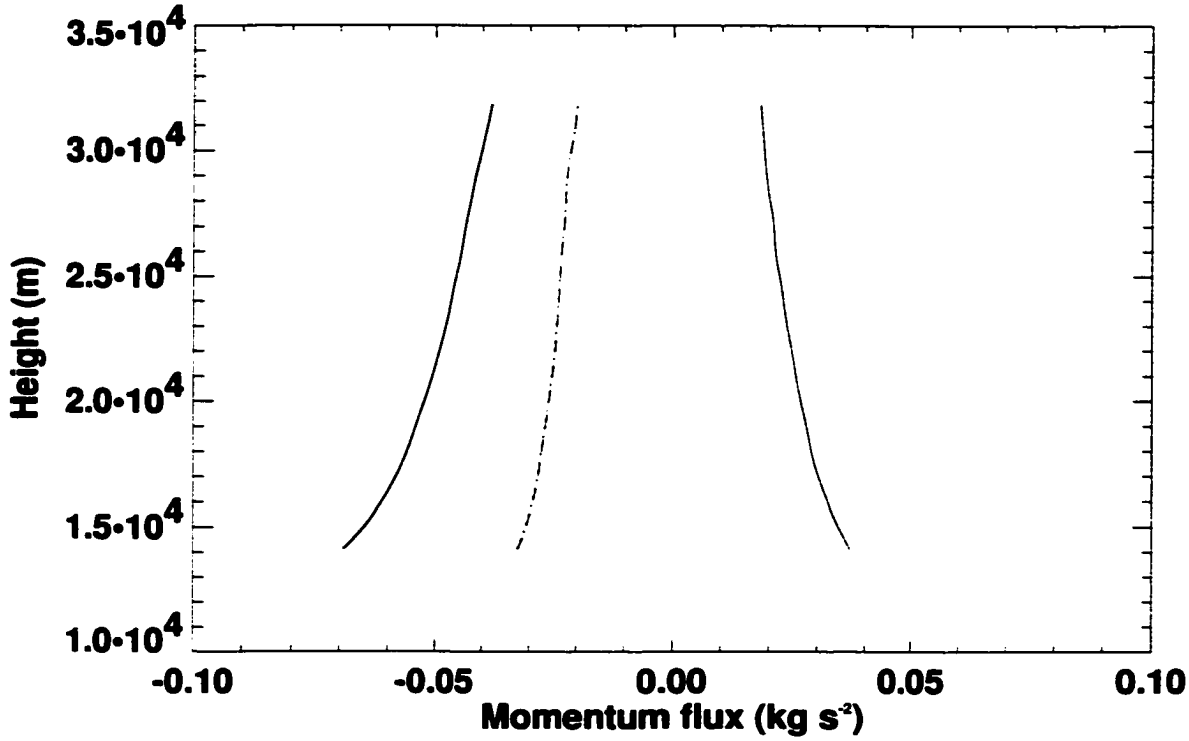

Fig. 13.10. Plot of the momentum flux $\rho_0\overline{u'w'}$ as a function of height due to westward-propagating (thick solid line) and eastward-propagating (thin solid line) waves in the WK control run. Their sum is represented by the dashed line, while the time-averaged momentum flux calculated from taking the standard Eulerian mean is represented by the dotted line.

tities will contain the mode. Experiments where higher wavenumbers were removed revealed little additional differences in the momentum flux spectra.

We can get an idea of how much momentum flux is associated with westward- and eastward-propagating waves by adding up the contributions from negative and positive phase speeds. The total momentum flux was summed for (westward-propagating) waves with $-100 \text{ m/s} \le c < 0 \text{ m/s}$, and for (eastward-propagating) waves with $0 \text{ m/s} \le c < 100 \text{ m/s}$. In Fig. 13.10, we see that the westward-propagating waves are dominant at all heights. Note that the sum of the positive and negative fluxes calculated using spectral methods agrees extremely well with the momentum flux calculated by using the gridpoint values of u' and w'. The waves are apparently being diffused somewhat as they propagate upward. The implied easterly acceleration of the lower portion of the model stratosphere would be under 1 m s^{-1} day^{-1}, which is somewhat consistent with the results

of Alexander and Holton (1997; see their Fig. 8), although the upper portion of the model stratosphere has an implied easterly acceleration of up to 3 m s^{-1} day^{-1}.

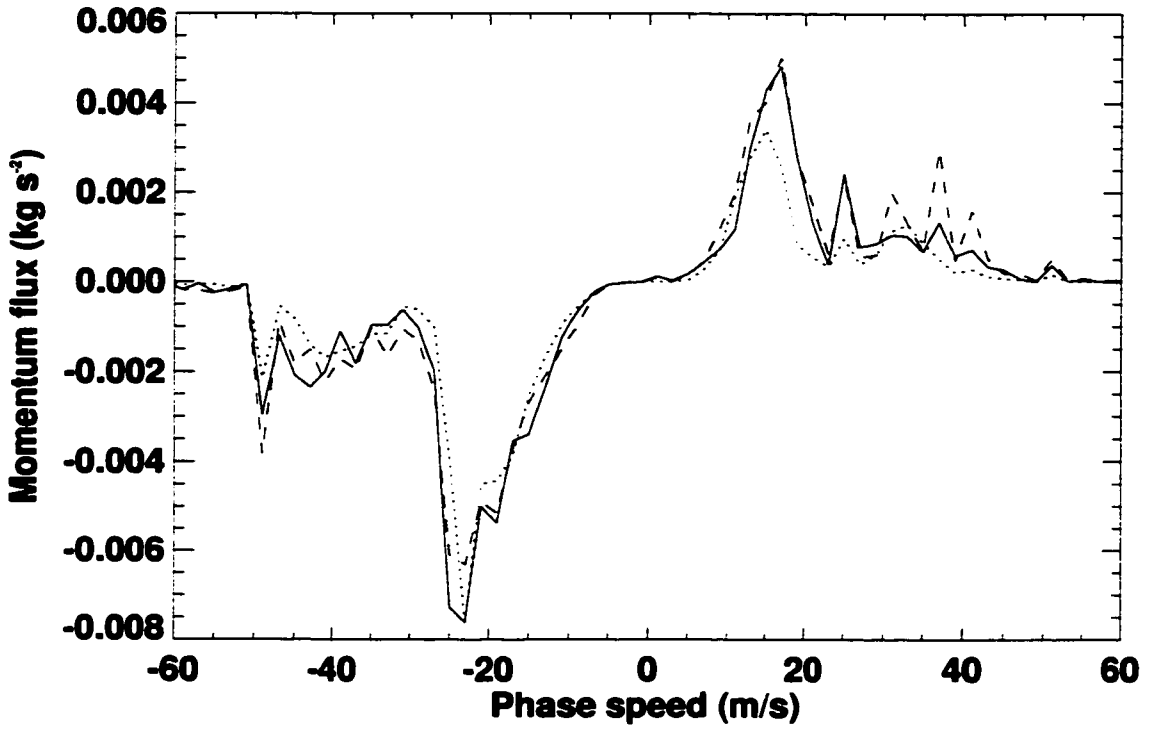

Fig. 13.11. Plot of the momentum flux $\rho_0\overline{u'w'}$ at 14125 m for the WK control run (solid), low-CAPE run (dotted) and high-CAPE run (dashed) as a function of horizontal phase speed.

13.3. Impact of variations in CAPE

As we noted in Chapter 4 and Chapter 5, variations in CAPE are generally expected to produce variations in the strength of the convection, and perhaps corresponding variations in the amount of wave momentum flux caused by the convection, as well. The behavior of the simulated wave spectrum for the WK control run, the low-CAPE WK run, and the high-CAPE WK run is examined in Fig. 13.11 and Fig. 13.12. The spectra of momentum flux versus phase speed among these runs are strikingly similar, with the high-CAPE and control runs producing a relatively similar amount of momentum flux at 14125 m, and the low-CAPE run considerably less at all altitudes. In Fig. 13.12, we see that the total momentum flux associated with the eastward-propagating waves increases with increasing CAPE, as one might expect. However, the momentum flux associated with the west-

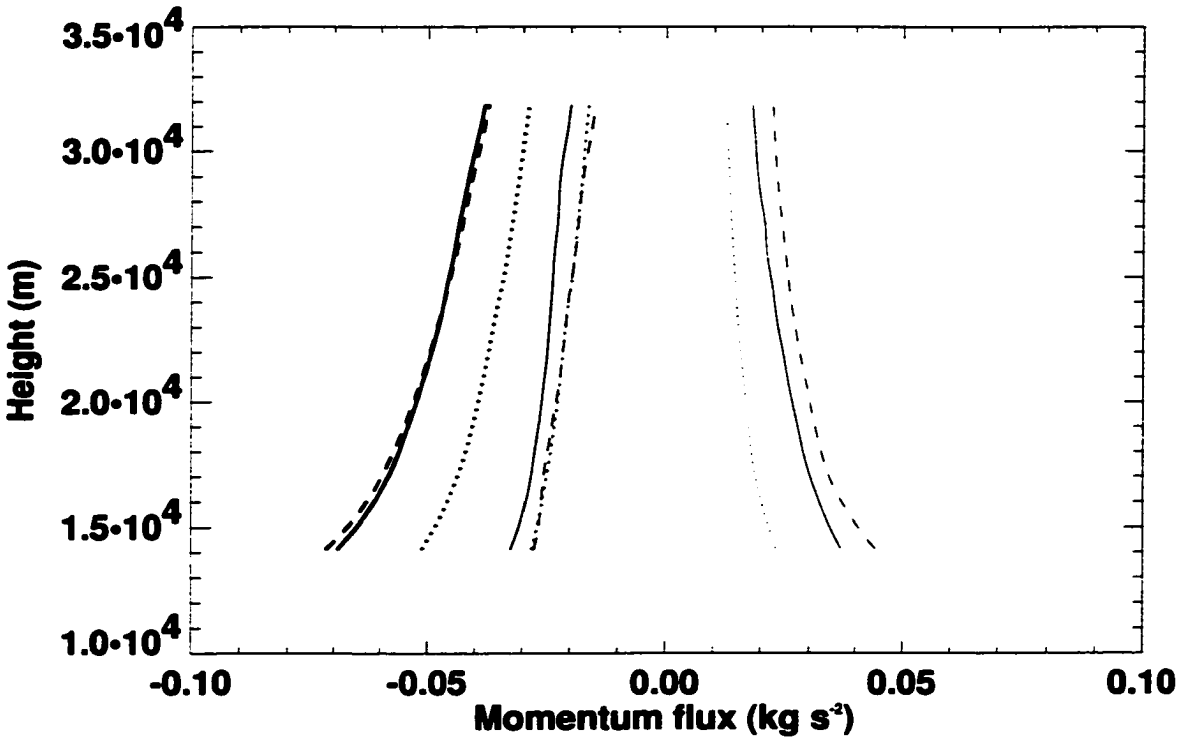

Fig. 13.12. Plot of the momentum flux $\rho_0 \overline{u'w'}$ as a function of height due to westward-propagating (thickest lines) and eastward-propagating (thinnest lines) waves. Their sum is represented by the lines of medium thickness. The WK control run, low-CAPE run and high-CAPE run are denoted by solid, dotted, and dashed lines, respectively.

ward-propagating waves is very similar between the high-CAPE and control runs. This may be because the simulated updraft in the high-CAPE run was upright for a longer period of time, causing more eastward-propagating waves to be produced than in the control run.

It is important to note that although the net momentum flux in the low-CAPE, control and high-CAPE runs are all similar, the amount of acceleration that the atmosphere would experience in a shear layer would be quite a bit different between the simulations. In an atmosphere with winds that become more westerly with height, the absorption of all of the waves with positive phase speeds over a layer 5 km deep centered at 20 km would lead to an acceleration of approximately 3.1 m s^{-1} day^{-1} for the low-CAPE run, and 5.6 m s^{-1} day^{-1} in the high-CAPE run. In the case of a similar shear layer with winds that become more easterly with height, the acceleration would be approximately -7.5 m s^{-1} day^{-1} for

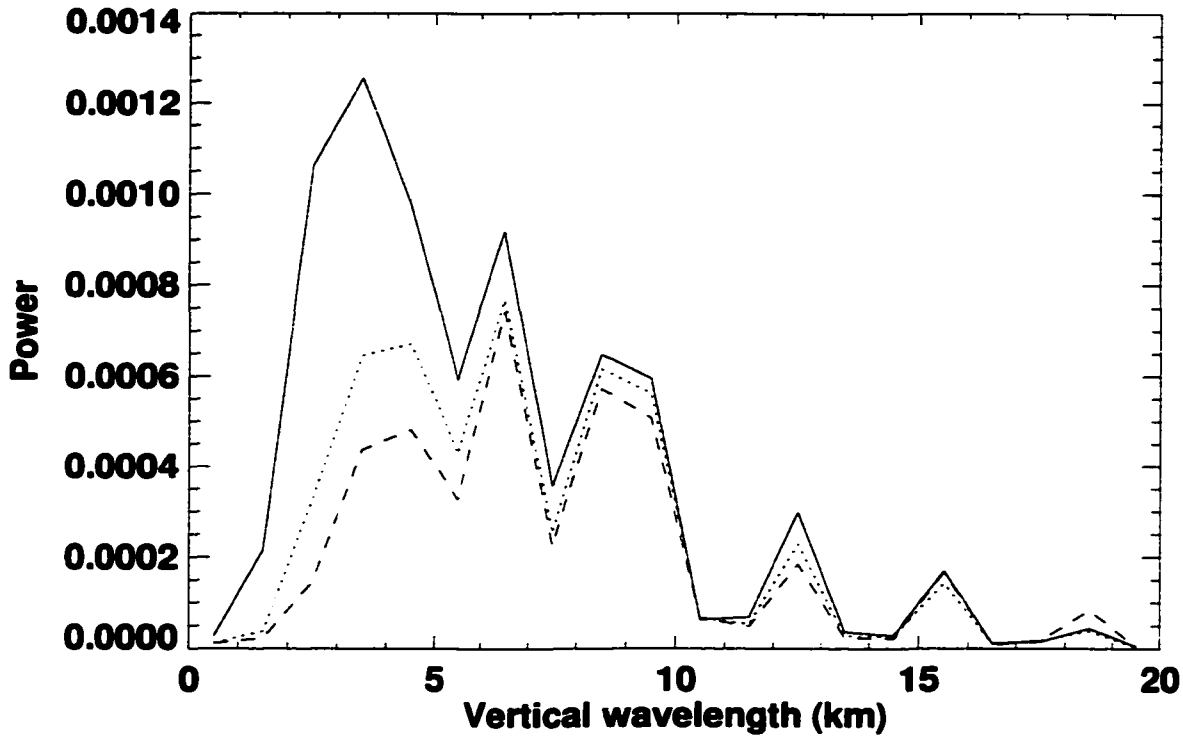

Fig. 13.13. Plot of the normalized spectra of vertical velocity at 19255 m (solid), 24927 m (dotted) and 29825 m (dashed) as a function of vertical wavelength for the TC control run.

the low-CAPE run, and -10.3 m s^{-1} day^{-1} for the high-CAPE run. The source for these differences appears to be the strength of the convection, which in turn produces a larger wave energy flux in the lower stratosphere for the high-CAPE run.

13.4. TC runs

As mentioned in Chapter 5, the convection in the TC control run was weaker and more intermittent than that of the WK control run. In Fig. 13.13, we see a considerably broader spectrum of vertical wavelengths than we saw in Fig. 13.5. In particular, there is significant power for vertical wavelengths of approximately 3 km. This may be due to the fact that the convection had a similar depth for a significant portion of the simulation, as we saw in Fig. 5.10a. Alexander and Holton (1997) reported a similar broad spectrum of vertical wavelengths in their simulations of a West African squall line.

We expect the shallow waves in Fig. 13.13 to have small vertical group velocities. This is because the equation for group velocity, given in Chapter 1 as

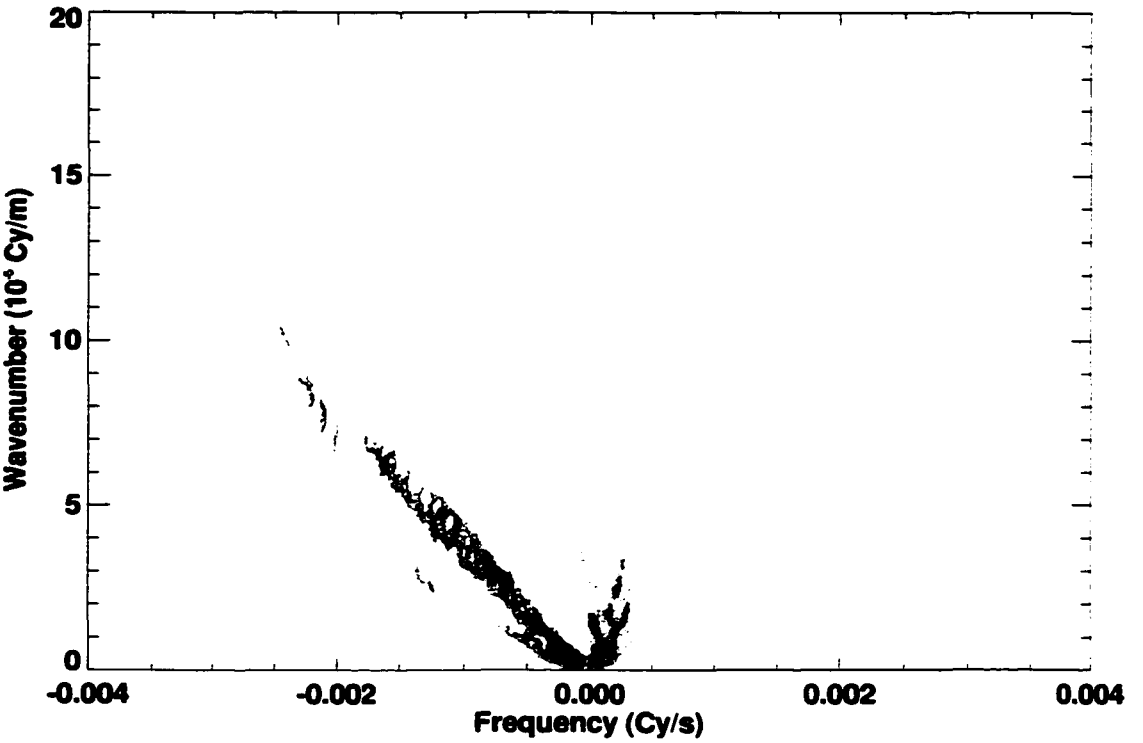

Fig. 13.14. Contour plot of the cospectra of horizontal and vertical velocity at 14125 m as a function of horizontal wavenumber and frequency for the TC control run. The red contours (0.00001, 0.0001, 0.001, 0.01 $m^2 s^{-2}$) correspond to positive values of $\overline{u'w'}$, while the blue contours (-0.00001, -0.0001, -0.001, -0.01 $m^2 s^{-2}$) correspond to negative values of $\overline{u'w'}$. The zero contour is omitted.

$$c_{gz} = \frac{\partial \omega}{\partial m} = \mp \frac{Nkm}{\left(k^2 + m^2 + \frac{1}{4H^2}\right)^{3/2}}, \tag{13.30}$$

indicates that c_{gz} is approximately proportional to the square of the vertical wavelength. As we see in Fig. 13.17, the waves in the TC control run do indeed propagate more slowly in the vertical than those of the WK control run. As with the WK control run, we see the strongest dissipation among the waves with the slowest vertical group velocities.

A plot of the cospectrum of momentum flux at 19255 m from the TC control run is shown in Fig. 13.14. Although the model tropopause in this simulation was at 19000 m, the convection did not penetrate to this level, unlike the WK control run. While this figure does share some characteristics with Fig. 13.7, there are also significant differences. We see that the magnitude of momentum flux produced by the TC control run is smaller than that of the WK control run. In addition, there are apparently positive momentum fluxes

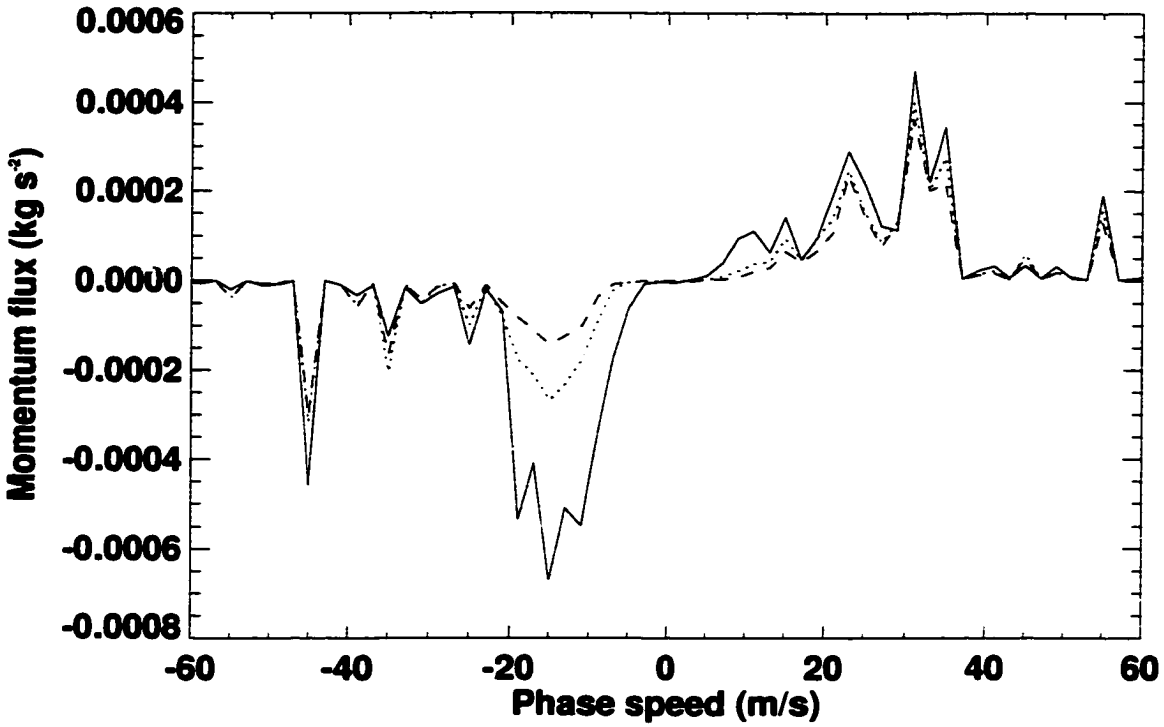

Fig. 13.15. Plot of the momentum flux $\rho_0\overline{u'w'}$ at 19255 m (solid), 24927 m (dotted) and 29825 m (dashed) as a function of horizontal phase speed for the TC control run.

associated with some of the waves that travel to the west. This is only an apparent effect, and can be explained due to the Doppler shifting of frequencies. We are calculating the absolute frequencies relative to the moving domain. The intrinsic frequency of the waves relative to the moving air is then given by

$$\omega_{int} = \omega - k\bar{u}, \tag{13.31}$$

where $\bar{u}$ is measured relative to the moving domain.

Thus, the apparent negative phase speeds that Fig. 13.14 implies can be corrected for if one simply adds $\bar{u}$ to them as has been done in Fig. 13.15. Here, we have used the time-averaged $\bar{u}$, which is very close to the initial value of $\bar{u}$ within the model stratosphere, in any case. In the case of the WK control run, Doppler shifting had very little effect on the intrinsic frequencies of the waves in the model stratosphere, since the stratospheric wind was only -1 m s^{-1} relative to the moving domain. The momentum flux spectrum produced by the TC control run has some interesting differences from that of the WK

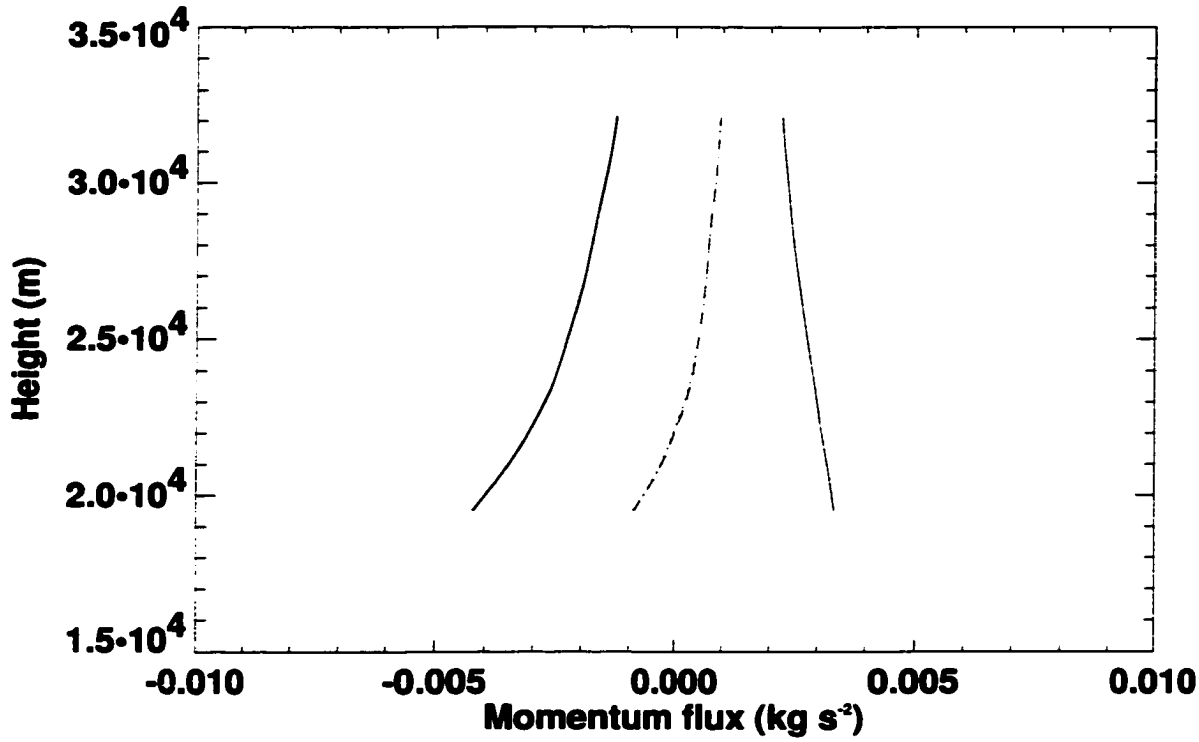

Fig. 13.16. Plot of the momentum flux $\rho_0 \overline{u'w'}$ as a function of height due to westward-propagating (thick solid line) and eastward-propagating (thin solid line) waves for the TC control run. Their sum is represented by the dashed line, while the time-averaged momentum flux calculated from taking the standard Eulerian mean is represented by the dotted line.

control run, besides having a much smaller amplitude. Note that the peak in momentum flux near -15 m s^{-1} is damped quite a bit more than most of the other peaks in the spectrum. This leads to a change in sign of the net momentum flux with height, as is seen in Fig. 13.16. One possible reason for the asymmetry in damping for the eastward- and westward-propagating waves is that westward-propagating waves will encounter more cloudy air through their path, due to the westward tilt of the convection. The waves that propagate through this cloudy air will tend to be partially reflected, due to the low Brunt-Väisälä frequency (Pandya and Alexander 1999). Also, the vertical group velocity in an area with low Brunt-Väisälä frequency will tend to be slower, giving dissipation more time to affect the waves. The agreement between the sum of the momentum flux contributions from all phase speeds with the time-averaged Eulerian mean is again quite good. The implied forcing of the mean wind is everywhere negative, but is less than 0.5 m s^{-1} day^{-1}, which is consistent with the results of Alexander and Holton (1997). The likely reason for the stronger

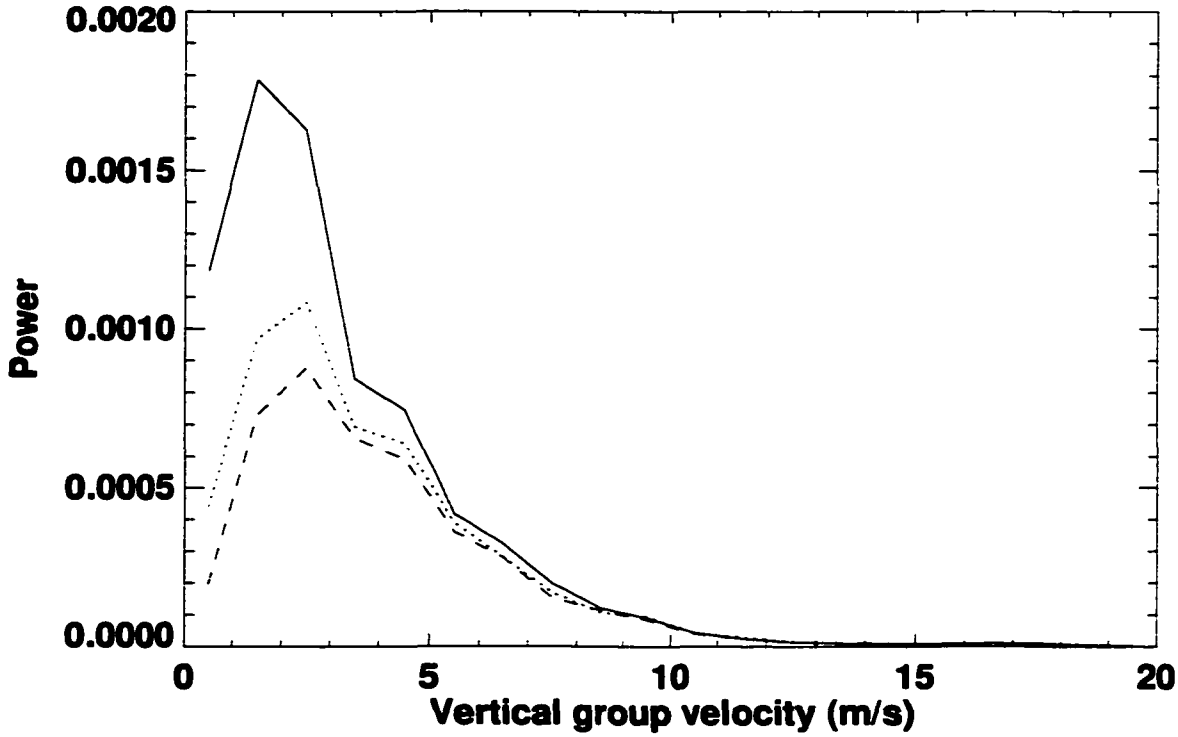

Fig. 13.17. Plot of the normalized spectra of vertical velocity at 19255 m (solid), 24927 m (dotted) and 29825 m (dashed) as a function of vertical group velocity for the TC control run.

implied mean flow forcing of the WK control run is that the waves from that simulation had a stronger momentum flux to begin with.

In addition to the TC control run, we also performed an experiment in which the wind above the jet maximum associated with the observed TC sounding was set to a constant value equal to the jet maximum (see Chapter 5). This created a "no jet" wind profile somewhat analogous to that of the WK control run. In this simulation, vigorous convection persisted for a little over three hours, as measured by the maximum vertical velocity, as we can see in Fig. 13.18. While it lasts, the vertical velocity maximum associated with the TC no jet run is somewhat similar to that of the WK control runs (see Fig. 5.9), with large-amplitude oscillations. Apparently, the reason for the death of the convection in the TC no jet run is that the storm is quite upright for much of its lifetime. Not much evaporative cooling can occur in an upright storm, in contrast to the westward-tilted anvil associated with the TC control run. Once the cold pool of the TC no jet run weakens, the environmental shear causes the storm to tilt forward, a situation analogous to Fig. 4.5c.

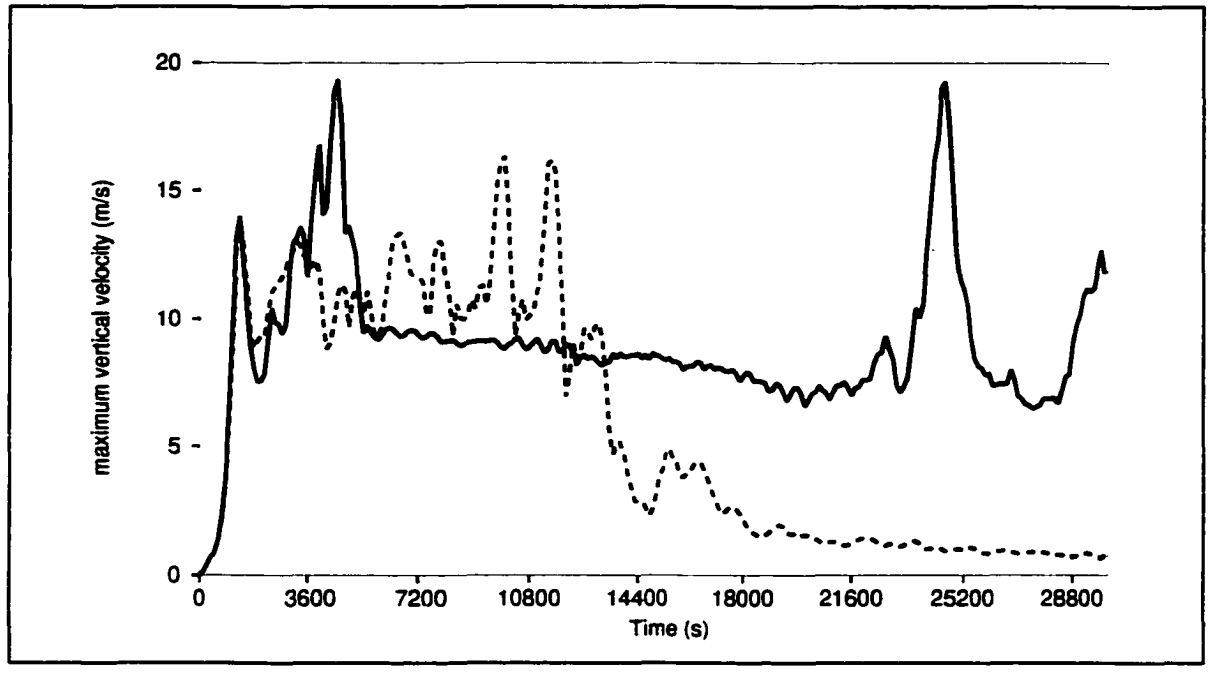

Fig. 13.18. Plot of the maximum vertical velocity as a function of time for the TC control (solid line) and TC no jet (dashed) runs.

The waves associated with the TC no jet run are actually quite a bit stronger than those of the TC control run. This is apparent in Fig. 13.19 and Fig. 13.20, where we see that the magnitudes of the easterly and westerly momentum fluxes produced by the TC no jet run are approximately twice as strong as those produced by the TC control run. Also evident in these figures is the fact that the easterlies are stronger than the westerlies in this simulation. This may be because of the forward tilt of the storm described above.

13.5. Impact of variations in tropospheric wind

In this section, we will examine how the momentum flux spectra produced by the model vary with different structures in the tropospheric wind. The first case that we will examine is one that initially has zero wind throughout the atmosphere, with the same thermodynamic structure as the WK control run. As mentioned in Chapter 5, a 2 K warm bubble was used to initiate convection in this case. The momentum flux spectrum for this simulation is shown in Fig. 13.21, and is quite symmetric, as one might expect with no environmental wind to alter the symmetry of the convection itself. This is particularly evident in the plot of easterly, westerly, and total momentum flux shown in Fig. 13.22. In this simulation, there was an initial central updraft, which produced a cold pool that spread to

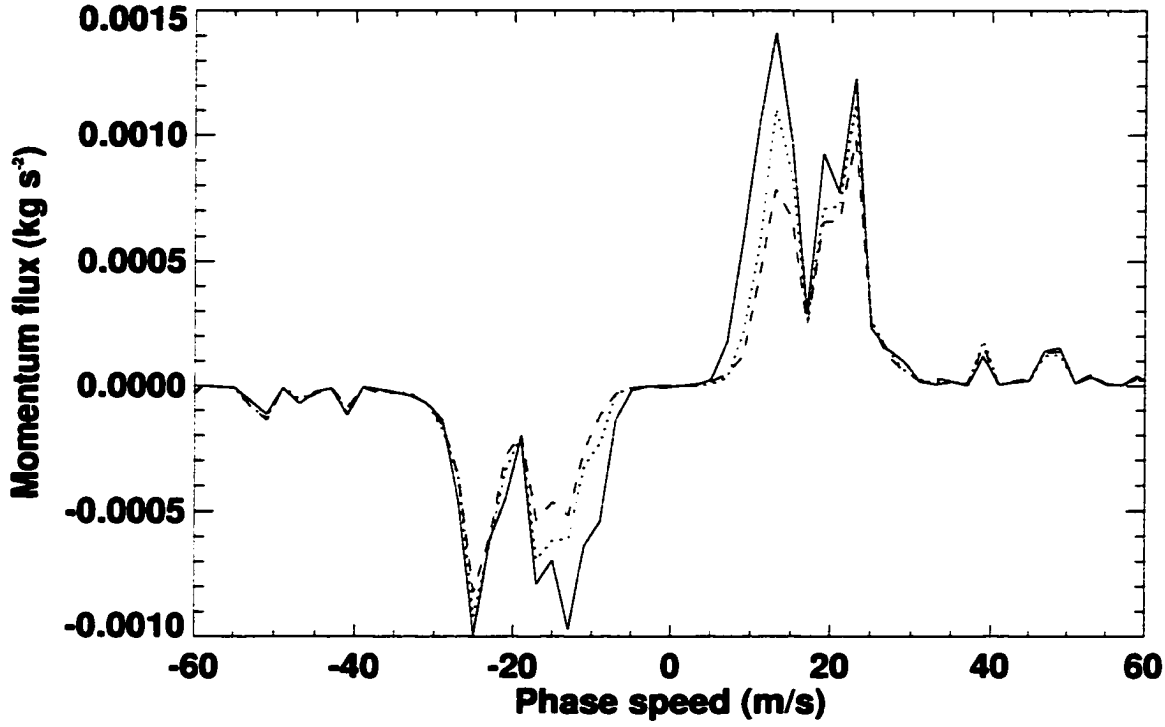

Fig. 13.19. Plot of the momentum flux $\rho_0 \overline{u'w'}$ at 19255 m (solid), 24927 m (dotted) and 29825 m (dashed) as a function of horizontal phase speed for the TC no jet run.

the east and west, forcing convection at its two edges. These arrangements are similar to those seen in Fig. 4.5a and Fig. 4.5b. The amplitude of the momentum flux is somewhat smaller than that of the WK control run (compare to Fig. 13.9 and Fig. 13.10), probably because the convection is less vigorous, as measured by the maximum vertical velocity.

Note that the parameterizations offered by Kershaw (1995), Chun and Baik (1998), and Roadnight (1999) would each predict the momentum flux to be zero in the WK calm experiment. While this is true in terms of the net momentum flux, the offsetting eastward and westward momentum fluxes produced by these runs could be associated with significant mean flow accelerations if the waves were allowed to propagate upward into an environment with shear.

The next simulations that we will examine are the WK low-shear and high-shear experiments. The momentum flux spectra for these runs and the WK control run are shown in Fig. 13.23. We see that the spectra have a similar shape and amplitude, but the WK low-shear and high-shear runs have lower and higher amounts of westerly momentum

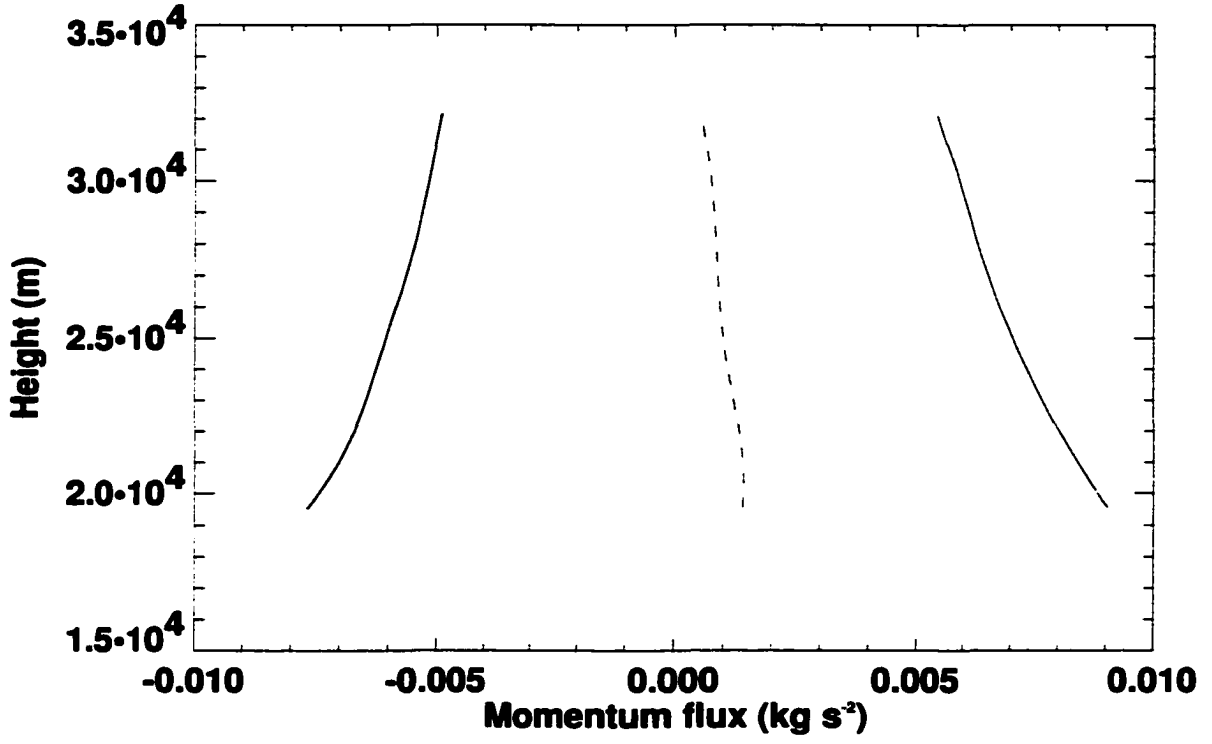

Fig. 13.20. Plot of the momentum flux $\rho_0 \overline{u'w'}$ as a function of height due to westward-propagating (thick solid line) and eastward-propagating (thin solid line) waves for the TC no jet run. Their sum is represented by the dashed line.

flux, respectively. Also, the peak that is near -25 m s^{-1} in the WK control run is shifted to lower and higher phase speeds for the WK low-shear and high-shear runs, respectively. The vertical profiles of the easterly, westerly, and total momentum fluxes are shown in Fig. 13.24. In this figure, we see that the westward momentum fluxes are fairly similar between the WK control and WK low-shear runs, while the WK low-shear run produces slightly more eastward momentum flux. One possible explanation for this behavior is that variations in shear that do not change the morphology of the storm itself will not have a significant contribution to the overall gravity wave source term, as we saw in Chapter 6. This is to be distinguished from the WK calm simulation, which produced a significantly different storm structure, or a simulation with shear that was so high that persistent convection was inhibited. The WK high-shear run produced slightly less westward momentum flux, but considerably more eastward momentum flux.

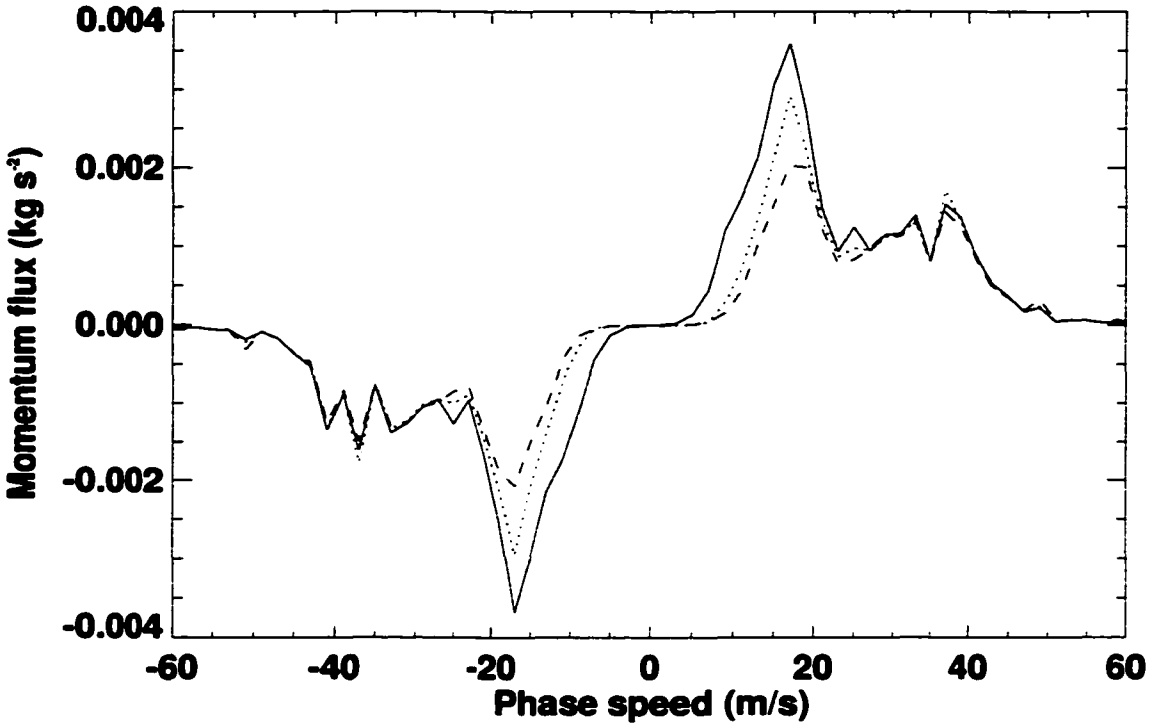

Fig. 13.21. Plot of the momentum flux $\rho_0 \overline{u'w'}$ at 14125 m (solid), 21125 m (dotted) and 28125 m (dashed) as a function of horizontal phase speed for the WK calm run.

13.6. Impact of ice microphysics

It is of interest to see what effects the deletion of ice microphysics has on the simulated convection and attendant gravity waves. Since the freezing of water in deep convective clouds is associated with latent heating in addition to that provided by the condensation of water vapor, we might expect simulated convection without ice microphysics to be weaker than that with ice microphysics. Also, as we saw in the gravity wave source analysis of Chapter 6, diabatic heating was a significant contributor to the production of gravity waves. The momentum flux spectrum of the WK no ice run is shown in Fig. 13.25, and is largely similar to that of the WK control run. There does seem to be more dissipation in the WK no ice run between the altitudes of 14 km and 28 km than for the WK control run. This is particularly evident in a comparison of Fig. 13.26 to Fig. 13.10. One explanation for this behavior is that the concentration of cloud ice in the upper troposphere is actually smaller in the WK control run than the WK no ice run, as shown in Fig.

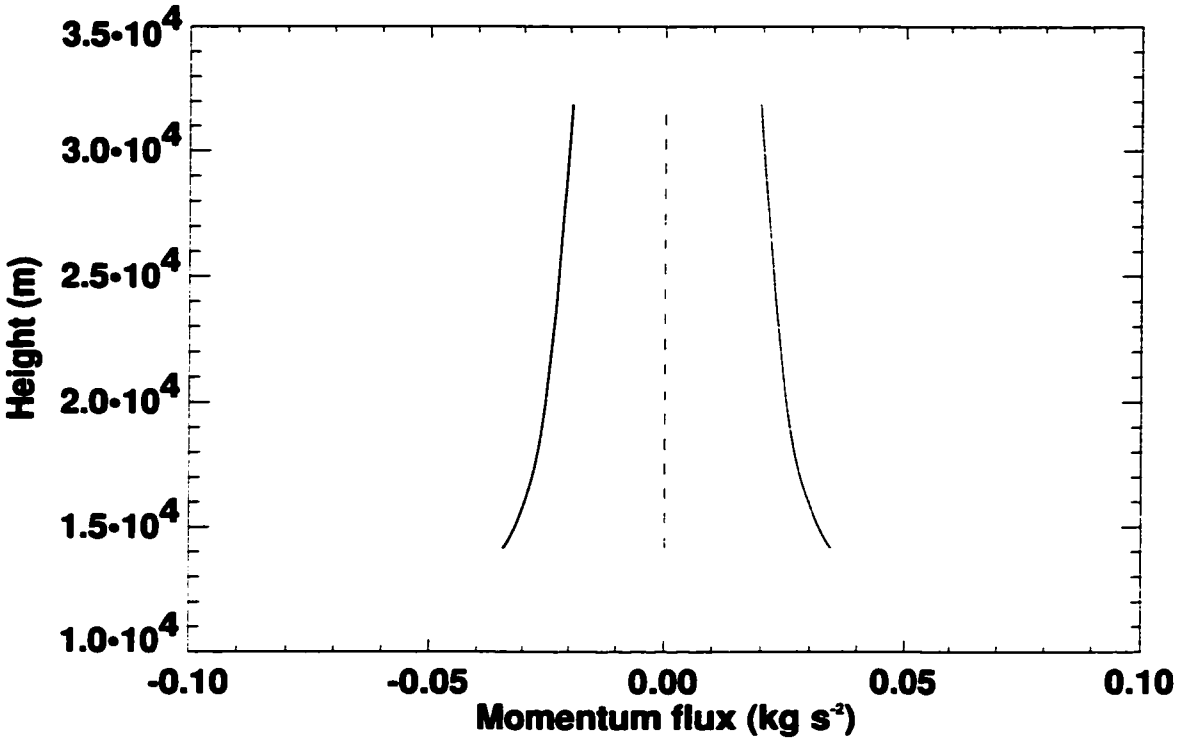

Fig. 13.22. Plot of the momentum flux $\rho_0\overline{u'w'}$ as a function of height due to westward-propagating (thick solid line) and eastward-propagating (thin solid line) waves in the WK calm run. Their sum is represented by the dashed line.

13.27. This phenomenon is somewhat surprising at first glance, but can be explained by examining how autoconversion is treated in ARPS (and many other models, M. Khairoutdinov, personal communication). The threshold for the conversion of cloud liquid water to rain is 2 g kg^{-1}, while the threshold for the conversion of cloud ice to snow is 0.6 g kg^{-1}. In the upper troposphere, the concentration of cloud condensate is generally below 2 g kg^{-1}, but snow is only allowed to remove this moisture in the simulation with ice. Pandya and Alexander (1999) have shown that short-wavelength waves can be reflected when encountering an area with a low effective Brunt-Väisälä frequency, such as a cloud anvil. Therefore, we would expect the waves in the WK no ice run to be damped more strongly than in the WK control run. Also evident in Fig. 13.27 is the fact that these simulations did have some overshooting convection, as seen by the nonzero cloud concentrations above z = 12 km.

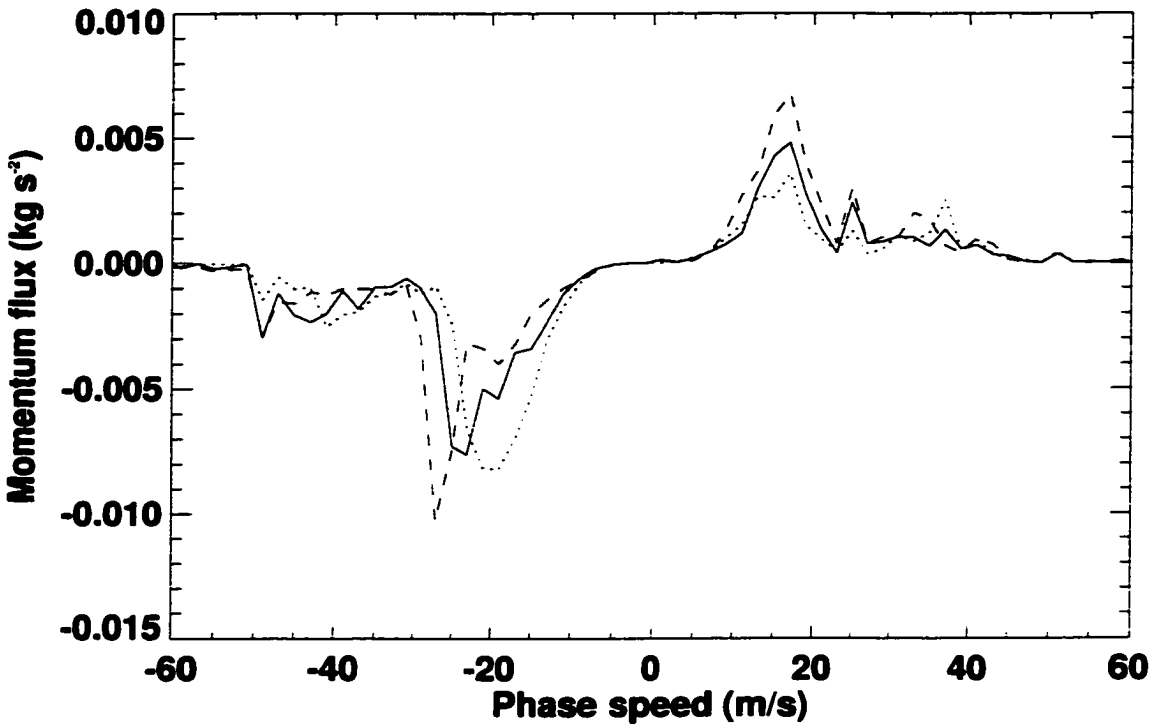

Fig. 13.23. Plot of the momentum flux $\rho_0\overline{u'w'}$ at 14125 m for the WK control run (solid), low-shear run (dotted), and high-shear run (dashed).

In this chapter, we have seen that simulated midlatitude and tropical squall lines produce a wide spectrum of gravity waves that propagate into the stratosphere, in terms of both frequency and wavenumber. The most prominent periods and wavelengths were in the range of 10-60 minutes, and 10-100 km, respectively. These values are comparable to those of similar modeling and observational studies. We have also seen that the wave modes identified by the EOF analysis were similar in character to those seen in the Fourier analysis. The partitioning of momentum flux by phase speed showed that the waves simulated by the WK control, low-CAPE and high-CAPE runs were quite similar in properties other than amplitude, which indicates that atmospheres with the same upper-level thermodynamic and shear profiles tend to support the generation of similar spectra of waves. When we examined the WK low-shear and high-shear runs, we found that the wave spectra produced were again broadly similar to those of the WK control run, but the position of the peak of the westward-propagating waves was found to shift to higher phase speeds for higher values of shear. The simulation without ice microphysics showed that the role of

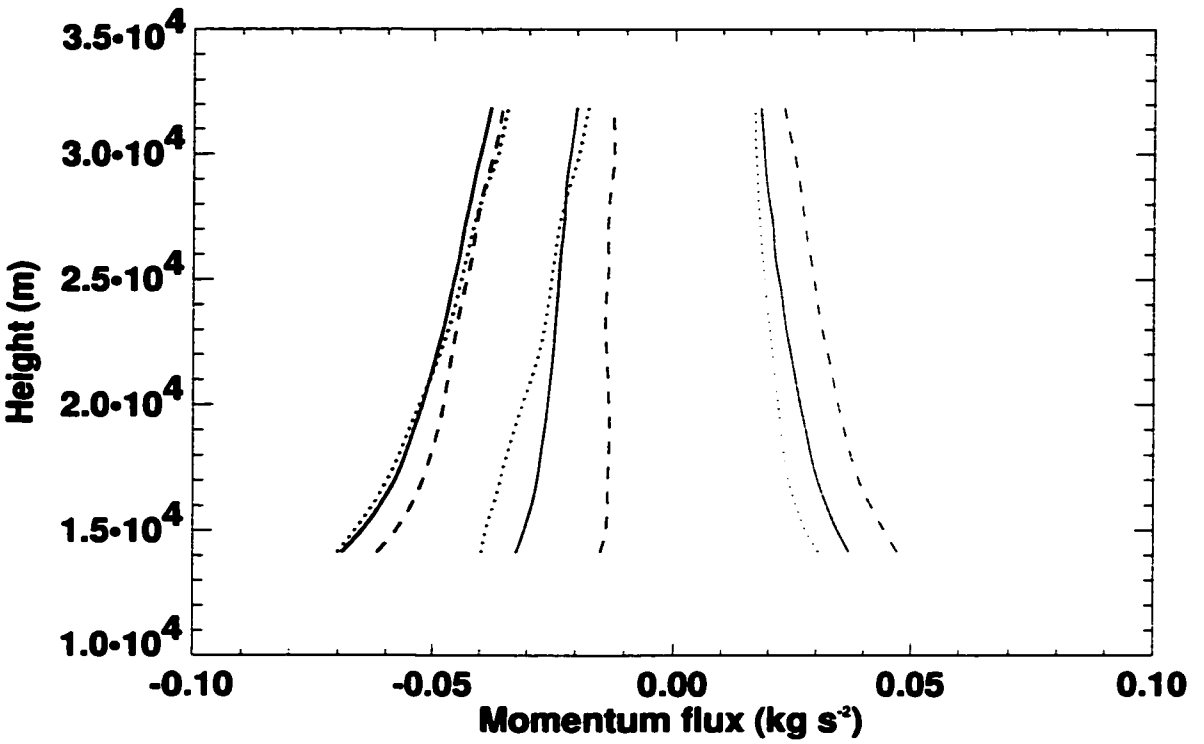

Fig. 13.24. Plot of the momentum flux $\rho_0 \overline{u'w'}$ as a function of height due to westward-propagating (thickest lines) and eastward-propagating (thinnest lines) waves. Their sum is represented by the lines of medium thickness. The WK control run, low shear run and high shear run are denoted by solid, dotted, and dashed lines, respectively.

ice microphysics in the generation of simulated gravity waves was relatively small, for the particular case tested. One could imagine the deletion of ice microphysics having a stronger role for other thermodynamic soundings.

The TC control run generated a spectrum of gravity waves that was quite different from that of the WK runs. The waves had a much smaller amplitude than the WK runs, and were also less biased towards westward-propagating waves. In the case of the TC no jet run, the eastward-propagating waves were actually stronger than the westward-propagating waves.

Many of the results in this chapter indicated that although the net momentum flux generated by a simulated squall line might be quite small (or even zero in the case of the WK calm run), the magnitudes of the positive and negative momentum fluxes could actually be fairly large. This is an important point, in that parameterizations that assign a single phase speed to the gravity waves generated by convection (Kershaw 1995; Boussuet et al. 1998;

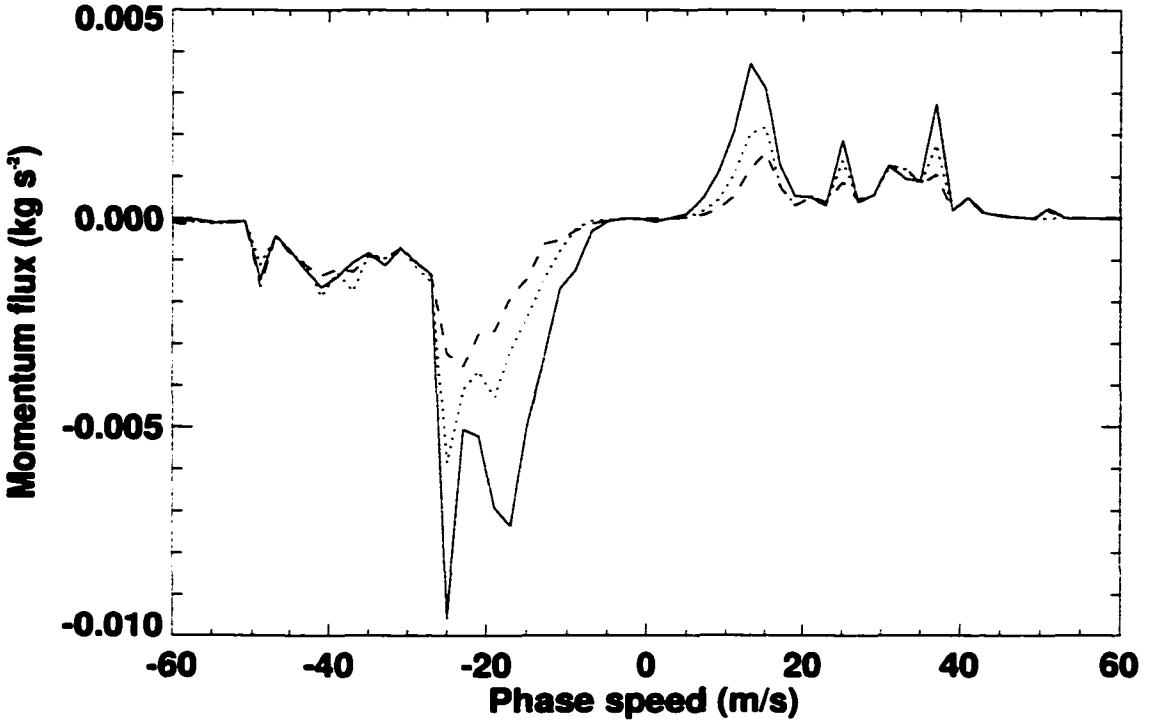

Fig. 13.25. Plot of the momentum flux $\rho_0\overline{u'w'}$ at 14125 m (solid), 21125 m (dotted) and 28125 m (dashed) as a function of horizontal phase speed for the WK no ice run.

Chun and Baik 1998; Roadnight 1999) cannot account for this. In the following chapter, we will study the effects of adding easterly and westerly shear layers in the stratosphere.

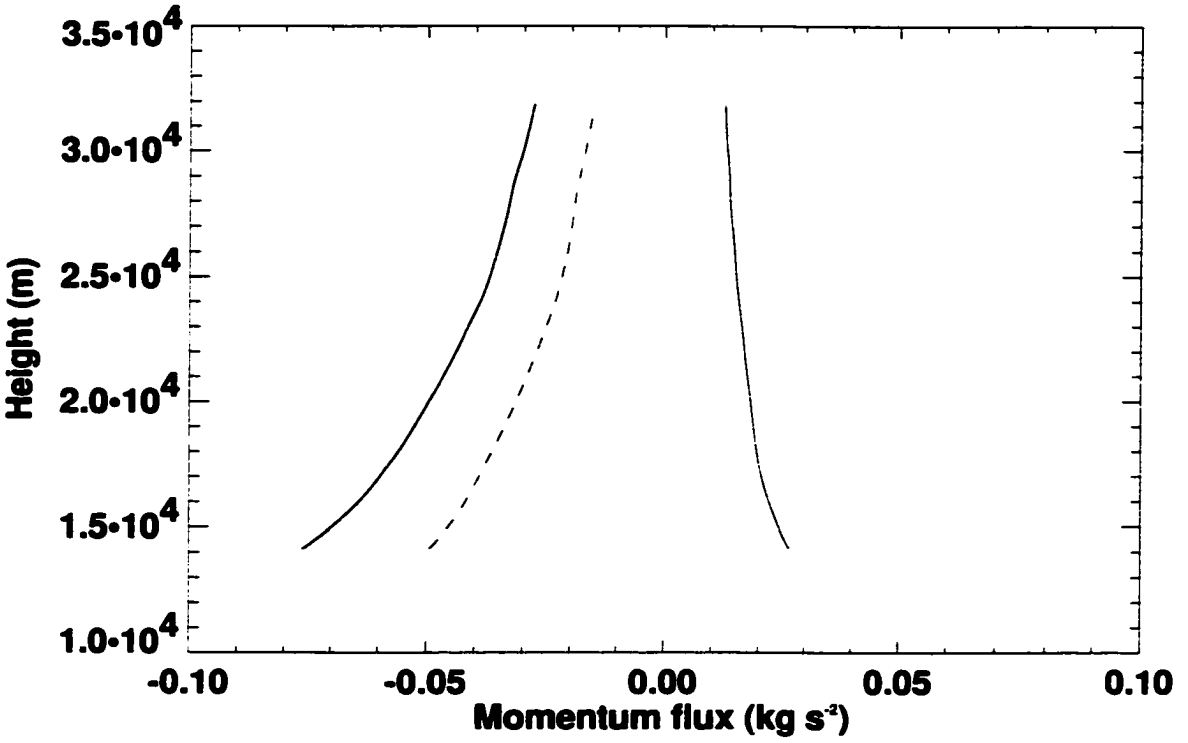

Fig. 13.26. Plot of the momentum flux $\rho_0\overline{u'w'}$ as a function of height due to westward-propagating (thick solid line) and eastward-propagating (thin solid line) waves in the WK calm run. Their sum is represented by the dashed line.

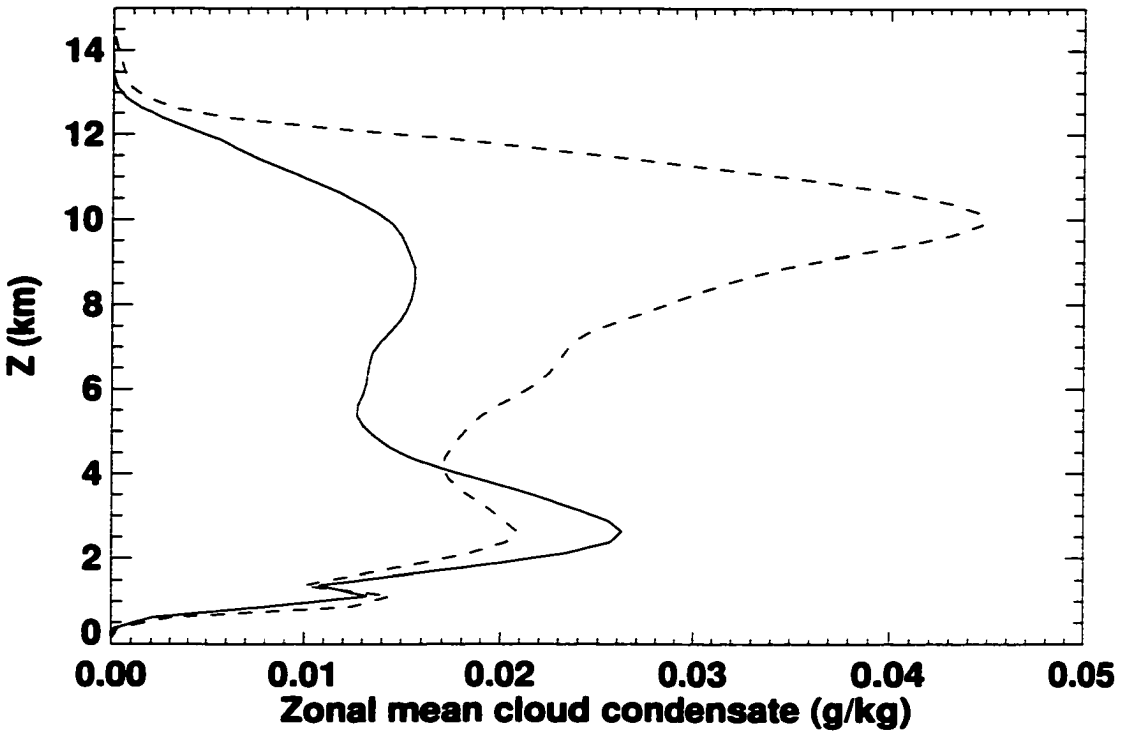

Fig. 13.27. Comparison of time-averaged, zonal mean cloud condensate (cloud liquid water plus cloud ice) for the WK control run (solid line) and WK no ice run (dashed line).

Chapter 14: Effects of varying stratospheric shear

As stated in Chapter 8, Eliassen and Palm (1960) and subsequent authors have noted that waves propagating vertically through the atmosphere will not change the mean flow unless the waves' momentum flux is deposited. This can occur due to critical level absorption or wave breaking. Critical level absorption occurs when the phase speed of a wave matches that of the mean flow, whereas wave breaking occurs when the amplitude of a wave is sufficient to cause low Richardson number instability (see Chapter 9; Lindzen 1981). The most important mechanism for momentum flux deposition in the simulations performed in this chapter is critical level absorption.

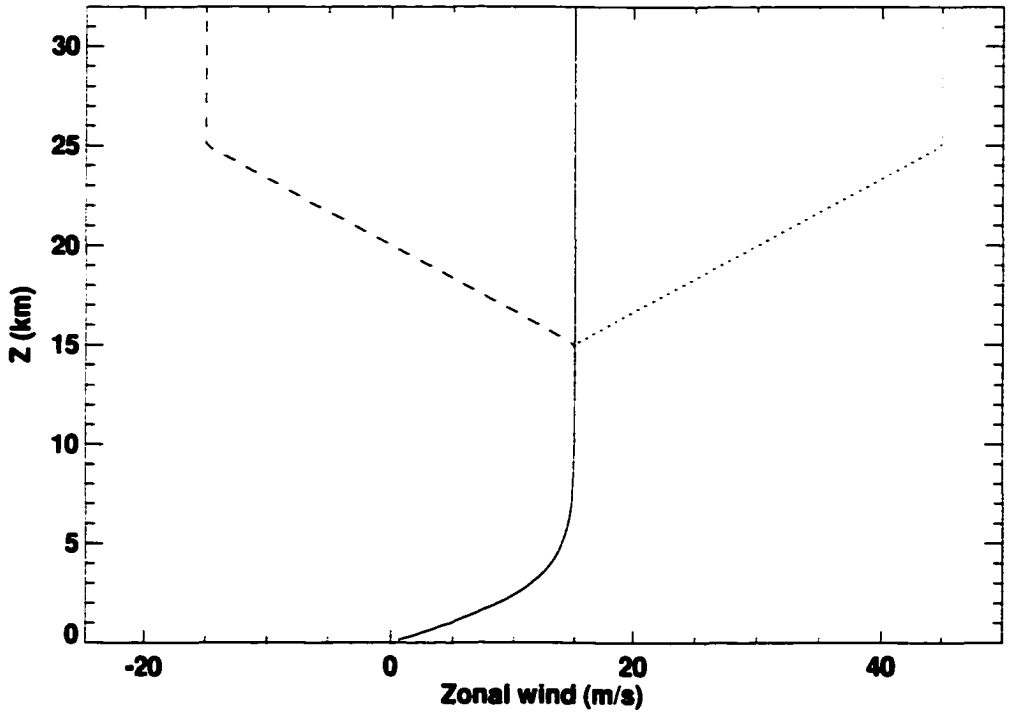

Fig. 14.1. Plot of wind profiles as a function of height for the three cases. The easterly shear case is dashed, the westerly shear case is dotted, and the no shear case is solid.

Three simulations were performed with identical tropospheric soundings. These correspond to the WK control, WK easterly stratospheric shear, and WK westerly stratospheric shear cases listed in Table 1 of Chapter 5. As shown in Fig. 14.1, the wind in each of the soundings asymptotically approaches 15 m s^{-1} from the surface to the tropopause at $z = 12$ km, with the majority of the tropospheric shear in the lowest 3 km. In the control case, the wind stays at 15 m s^{-1} through the stratosphere, while the westerly and easterly shear cases contain a linear shear layer between 15 and 25 km that has a magnitude of ±30 m s^{-1}, and then no shear above 25 km. The magnitude of the shear in the two shear profiles is comparable to that of QBO shear layers (Baldwin et al. 2001). The three wind profiles used are shown in Fig. 14.1.

The potential temperature surfaces and cloud outlines the no shear, westerly shear and easterly shear simulations are shown in Fig. 14.2, Fig. 14.3, and Fig. 14.4, respectively. The outline of 0.1 g kg^{-1} cloud condensate is indicated by a thick contour in all figures. The behavior of the simulated storms is very similar in the troposphere between the three simulations, as would be expected. After an initial upright orientation to the storms at 2 hours, the storms develop a cold pool which becomes stronger with time. This causes a rearward tilt to the main updraft, similar to what Fovell and Ogura (1988) observed in their two-dimensional simulation of midlatitude convection. It should be noted that in all of these simulations, the periodic boundary conditions allow low-frequency, westward-propagating waves to eventually appear in the eastern portion of the domain, and vice-versa.

In the stratosphere, we see a significant amount of both eastward- and westward-propagating waves in the no shear case at 2 hours, but the westward-propagating waves become dominant as time goes on. This has been observed in similar simulations (Fovell et al. 1992; Alexander et al. 1995), and is likely due to the rearward tilt of the mature squall line. An alternative explanation for this behavior (similar to that of Lane et al. 2001) is that the environment of the source region of the gravity waves experiences increasingly intense easterly winds, causing an initially isotropic spectrum of waves to become shifted towards the production of westward-propagating waves. After 8 hours have passed, the wave activity in the lower stratosphere has decreased, corresponding with the weakening of the storm.

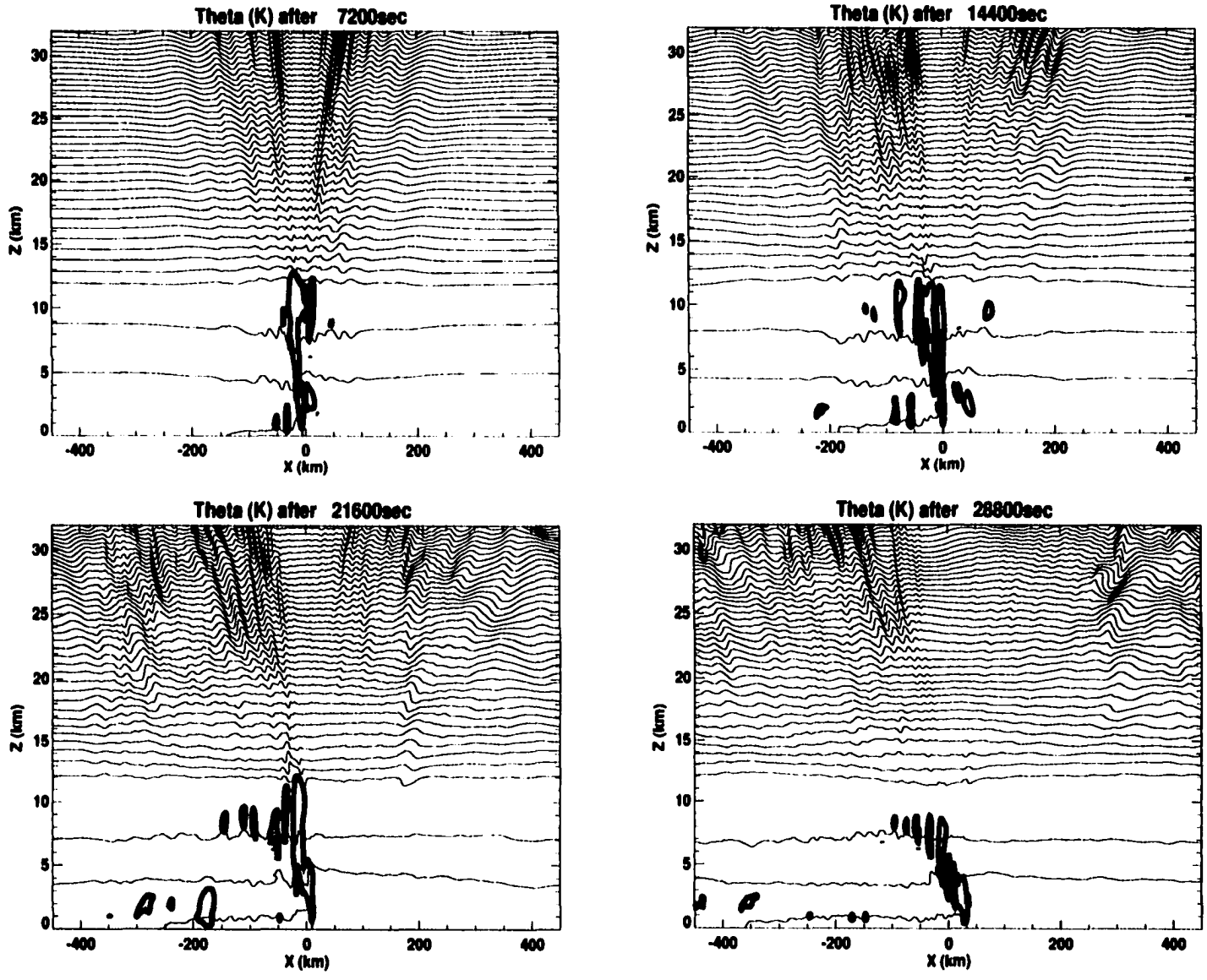

Fig. 14.2. Potential temperature contoured at 15 K intervals for the no shear case after a) 2 hours; b) 4 hours; c) 6 hours; d) 8 hours.

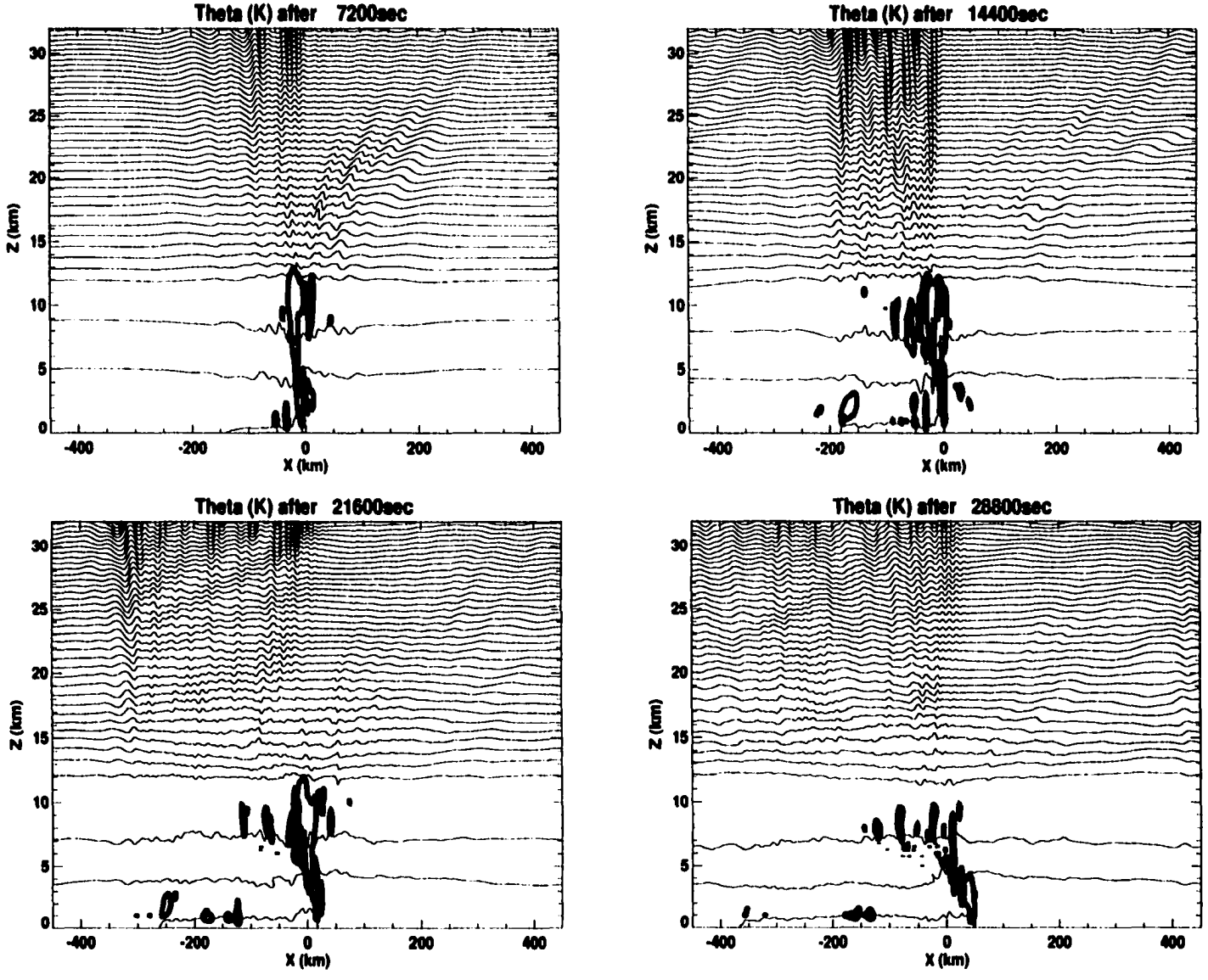

Fig. 14.3. Potential temperature contoured at 15 K intervals for the westerly shear case after a) 2 hours; b) 4 hours; c) 6 hours; d) 8 hours.

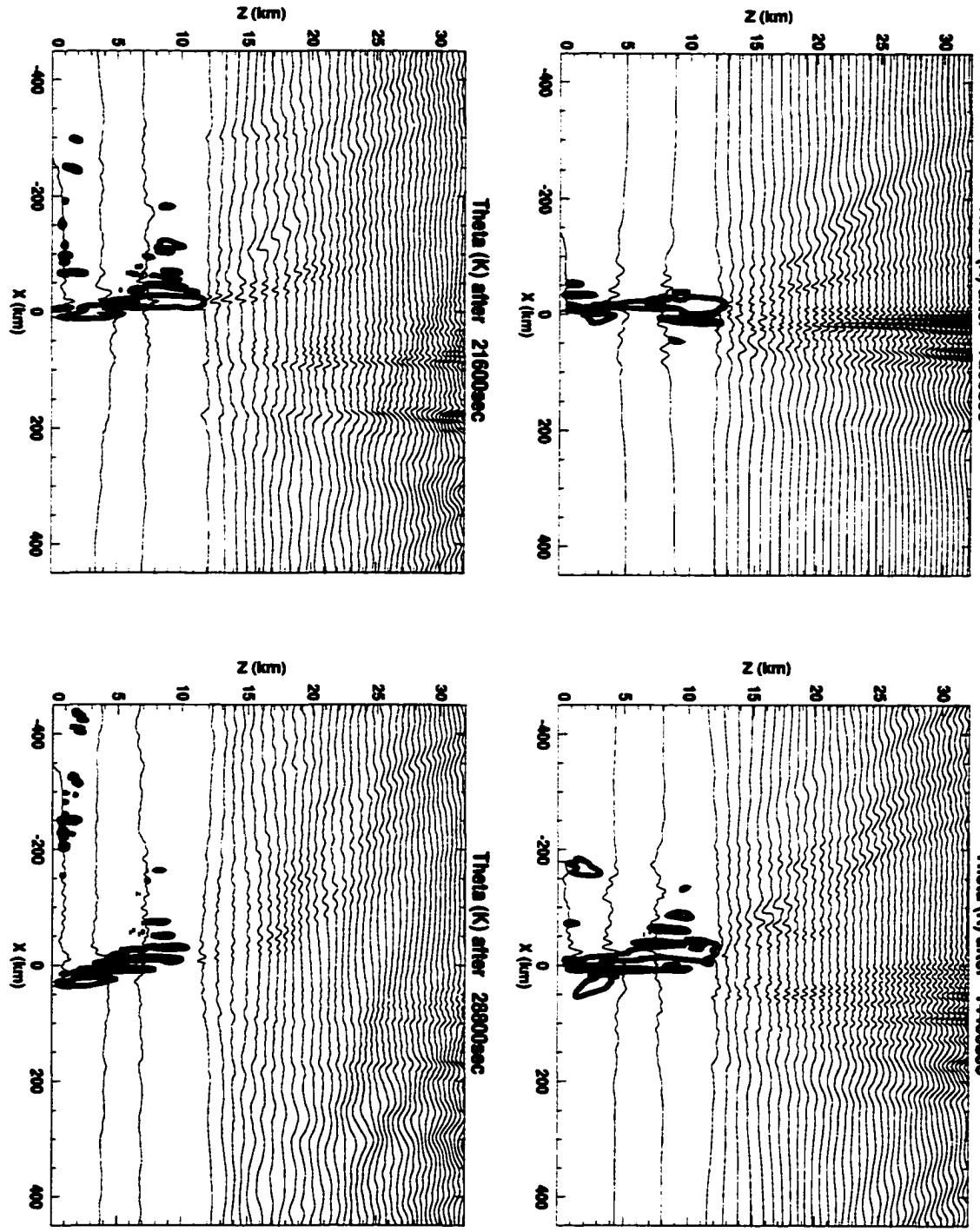

Fig. 14.4. Potential temperature contoured at 15 K intervals for the easterly shear case after a) 2 hours; b) 4 hours; c) 6 hours; d) 8 hours.

In the westerly shear case, we see waves propagating to the east and west in the lower-most stratosphere (between 12 and 15 km) after 2 hours, but the waves with positive phase

speeds relative to the storm become damped within the shear layer. The bias towards westward-propagating waves is even more pronounced in the westerly shear case than the no shear case at 4 and 6 hours, due to wave absorption. This wave absorption is shown here with potential temperature perturbations that decrease in amplitude with height. As we saw in section 8.2., this can also be interpreted as a decrease of height perturbations on isentropic surfaces. It is interesting to note that the eastward-propagating waves that do survive above the 25 km level amplify with height, as would be expected due to the density effect. These waves apparently have phase speeds that are faster than the 30 m s^{-1} of the shear layer. As these waves propagate to the east, they eventually interfere with the wave pattern of the westerlies (see Fig. 14.3c).

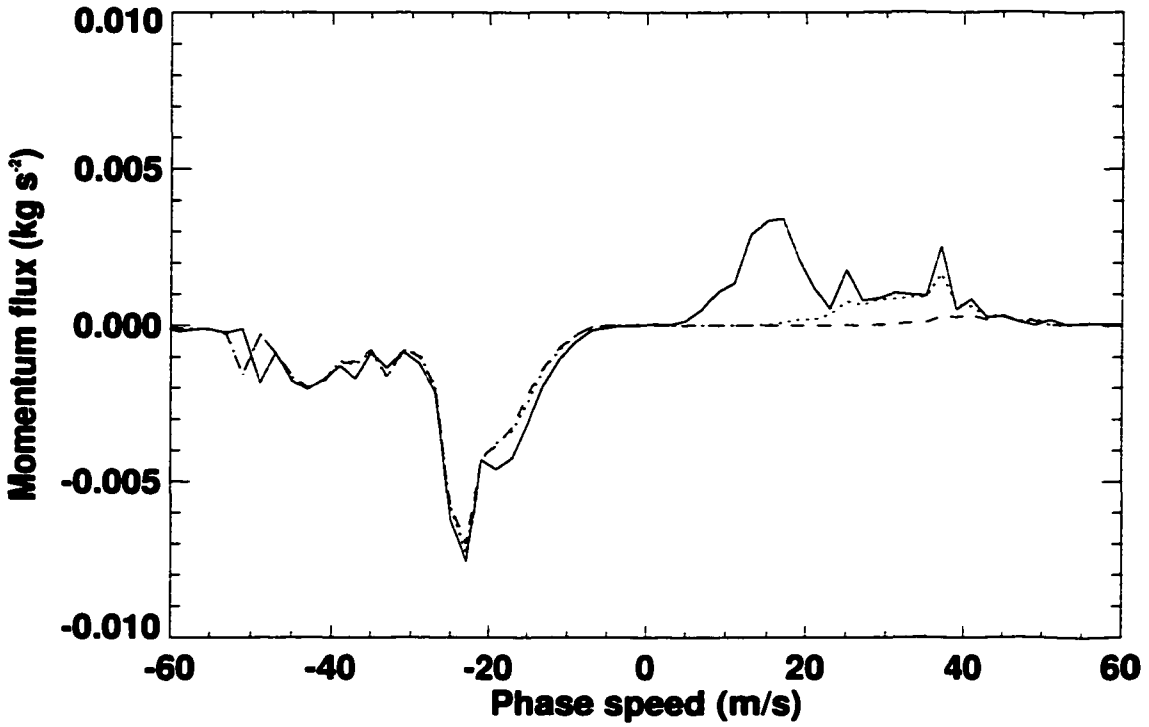

Fig. 14.5. Plot of the momentum flux $\rho_0\overline{u'w'}$ at 14125 m (solid), 20125 m (dotted), and 25125 m (dashed) for the WK westerly shear run as a function of intrinsic horizontal phase speed.

In the easterly shear case, there is a clear dominance of eastward-propagating waves after 2 hours, with the westward-propagating waves becoming absorbed by the mean flow. This bias is not as apparent after 4 hours, probably because the absorption of the west-

ward-propagating waves is offset by the lack of production of eastward-propagating waves that is due to the tropospheric storm structure.

The behavior of the momentum flux spectra with height for the westerly and easterly shear runs are shown in Fig. 14.5 and Fig. 14.6, respectively. We see that the momentum flux has a similar structure at z = 14.125 km for both runs, but the waves with positive phase speeds less than 30 m s^{-1} are absorbed within the shear layer of the westerly shear run, as would be expected from the results of Eliassen and Palm (1960) detailed in Chapter 8. Similarly, the waves with negative phase speeds are preferentially absorbed within the shear layer of the easterly shear run.

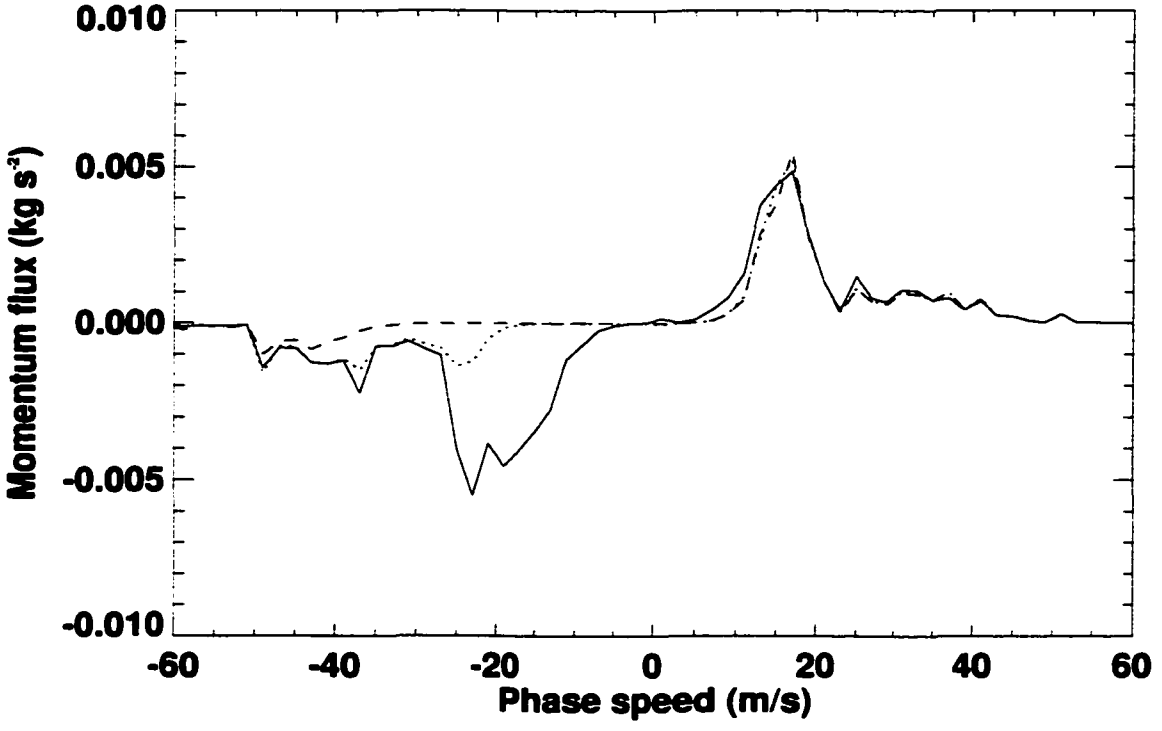

Fig. 14.6. Plot of the momentum flux $\rho_0 \overline{u'w'}$ at 14125 m (solid), 20125 m (dotted), and 25125 m (dashed) for the WK easterly shear run as a function of intrinsic horizontal phase speed.

The absorption of individual waves within a phase speed interval of ±1 m s^{-1} in the westerly and easterly shear runs are shown in Fig. 14.7 and Fig. 14.8, respectively. In these figures, the normalized momentum flux of the waves was calculated by dividing the momentum flux in the shear runs at each level by the momentum flux from the no shear run at the same levels. This allows the effects of any wave attenuation not associated with

the presence of shear to be removed from the analysis. In both the easterly and westerly shear runs, the momentum flux of individual waves remains relatively constant with height until the waves reach a level approximately 5 km below the critical level, with the exception of the -29 m s^{-1} case. Even for this wave, the attenuation is considerably faster in the 5 km below the critical level. Almost all of the waves' momentum flux is absent once the waves reach their critical level, as would be expected from the results of Eliassen and Palm (1960).

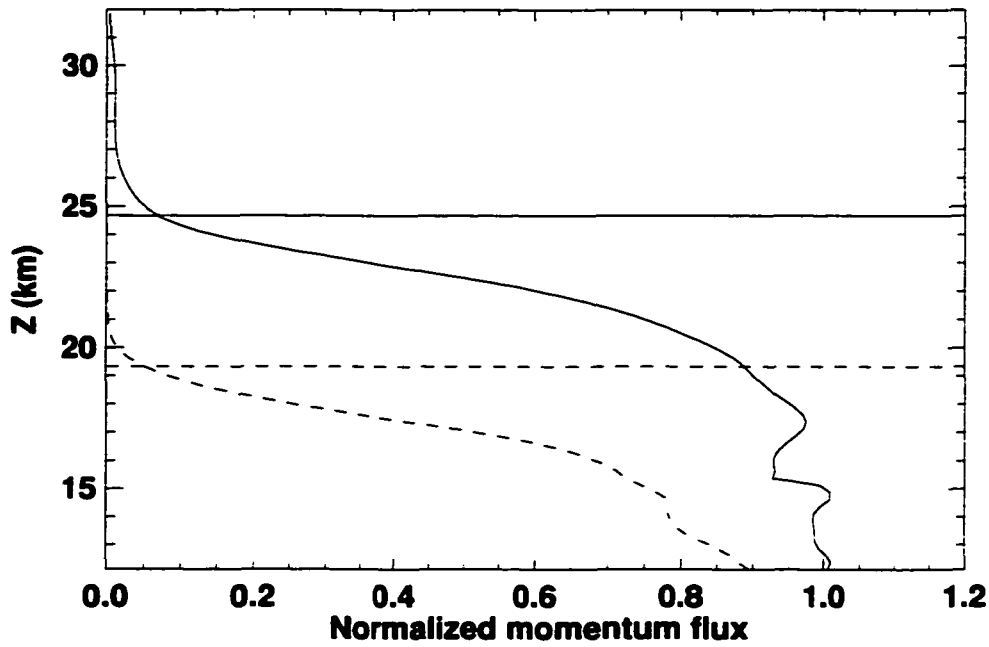

Fig. 14.7. Plot of the normalized momentum flux associated with waves with intrinsic phase speeds of 13 m s^{-1} (solid) and 29 m s^{-1} (dashed) for the WK westerly shear run. Critical levels for the waves are shown as horizontal lines with the same patterns.

The change of the mean zonal flow in the model atmosphere for the three cases after 10 hours is shown in Fig. 14.9. If we ignore the effects of the sponge layer at 32 km, the behavior of the mean flow in the stratosphere is as one would expect. Below the shear layer, all three cases experience a westerly acceleration of the flow, due to the upward extension of the momentum transport by the convection itself. The atmosphere of the easterly shear case experiences a negative acceleration in the shear layer, associated with the absorption of waves with negative phase speeds. Conversely, the westerly shear case is

associated with a positive acceleration in the shear layer, due to the absorption of waves with positive phase speeds. The no shear case is associated with relatively little wave absorption in the 15 - 25 km layer, although the dominance of waves with negative phase speeds does apparently lead to a slight deceleration of the flow.

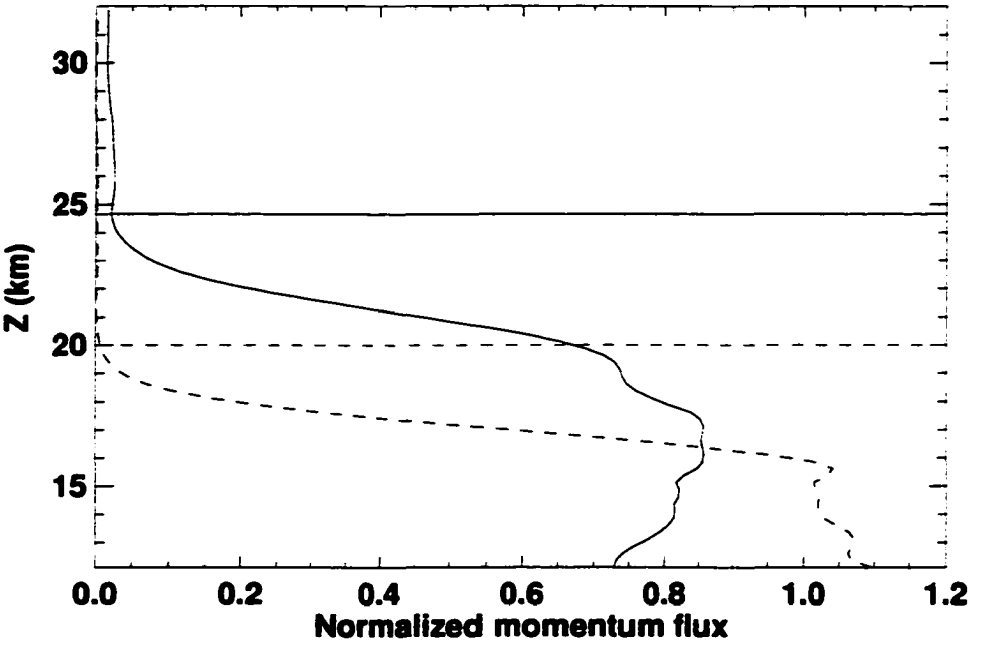

Fig. 14.8. Plot of the normalized momentum flux associated with waves with intrinsic phase speeds of -29 m s^{-1} (solid) and -15 m s^{-1} (dashed) for the WK easterly shear run. Critical levels for the waves are shown as horizontal lines with the same patterns.

We have seen that the simulated squall line convection produces a spectrum of gravity waves which cause the westerly and easterly winds in the stratosphere that match the phase speeds of the waves to become stronger as the waves are absorbed. The acceleration of the mean flow within the stratospheric shear zones by approximately 1 m s^{-1} after 10 hours (or 2.4 m s^{-1} day^{-1}) would certainly be large enough to argue for the significance of gravity wave forcing of the QBO, and indicates that such forcing may be important in middle latitudes when convection is active. However, caution should be exercised when extending the results of the above simulations of mid-latitude squall lines to the decidedly tropical QBO. If we assume that the amplitude of the wave momentum flux spectrum associated with the TC control run is more representative of tropical convection (about one tenth that of the WK control run, see Fig. 13.16 of Chapter 13), then an acceleration of the

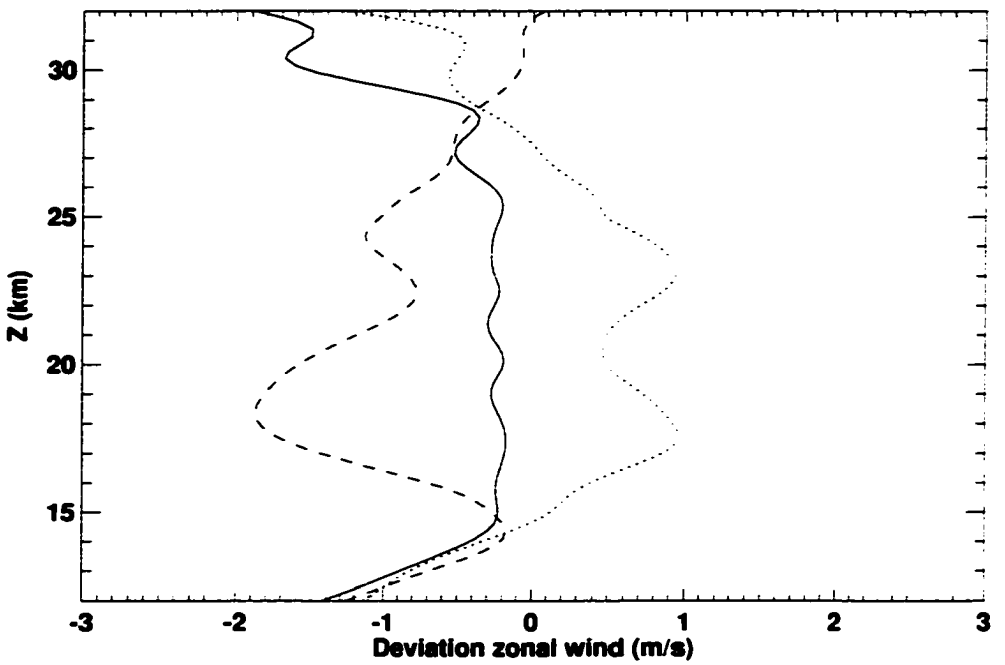

Fig. 14.9. Plot of the deviation of the zonal mean zonal wind as a function of height for the three cases after ten hours. The easterly shear case is dashed, the westerly shear case is dotted, and the no shear case is solid.

mean flow by 0.24 m s^{-1} day^{-1} within the stratospheric shear zones could still be important for the QBO, since the observed QBO zonal shear zone accelerations are approximately 0.2 m s^{-1} day^{-1} for the westerly phase and -0.13 m s^{-1} day^{-1} for the easterly phase (Piani et al. 2000; Dunkerton and Delisi 1985). The importance of gravity waves generated by MCS convection on the QBO largely depends upon the amount of MCSs that occur in the tropics (Piani et al. 2000). Following Piani et al. (2000) and Mohr and Zipser (1996), we assume that the density of MCSs in the tropics is approximately 1 per every 1350000 km^2. If the MCS simulated in the TC control run were constant in the meridional direction and contained in a hypothetical 600 x 600 km box, we have a simulated MCS density of 1 per every 360000 km^2, or 4.5 times more dense than observed. Accounting for this factor, and if the system in the TC control run is representative of actual convection, we would then expect the accelerations due to MCSs to be approximately 0.05 m s^{-1} day^{-1}. If we also take into account a reduction by a factor of two due to the effects of Brewer-Dobson upwelling (Dunkerton 1997), this acceleration is approximately 0.03 m s^{-1} day^{-1}.

In this chapter, we have examined the behavior of convectively generated gravity waves propagating in a stratospheric shear zone. The absorption of these waves has been shown to be an important means by which the mean flow in the middle atmosphere can be changed. In the following chapter, we will describe a parameterization for these waves.

Chapter 15: A parameterization of convectively generated gravity wave drag

For a parameterization of convectively generated gravity waves, we need to establish the following:

- What conditions will trigger the waves?
- How do we relate the amount of momentum flux (or wave energy flux) at the top of the convection to properties of the convection itself?
- What characteristics of the waves do we need to know (wavelength, phase speed), and how can we assign values to these quantities based on properties of the simulated convection?
- How is the momentum flux imparted to the mean flow (critical level, Kelvin-Helmholtz instability, etc.)?
- How should wave reflection be accounted for?

Note that the final two points in the above list also need to be accounted for in parameterizations of orographic gravity wave drag. In the discussion below, we will begin with a discussion of the relationship between the wave energy flux and wave momentum flux spectra. Then, we will review the Arakawa-Schubert (1974) parameterization, as implemented in the CSU GCM (Pan and Randall 1998). Following this, we will review the "transient topography" mechanism for the production of gravity waves by convection given by Pfister et al. (1993), and then propose a modified version for this work. Finally, conditions for the absorption and reflection of waves will be discussed.

If we want to relate the wave energy flux $\overline{p'w'}$ to the wave momentum flux $\overline{u'w'}$, we can use the following Eliassen-Palm (1960) relationship for discrete waves:

$$\overline{p'w'(\hat{c})} = -\rho_0 \hat{c} \overline{u'w'(\hat{c})}. \tag{15.1}$$

Here, $\hat{c}$ is the intrinsic phase speed $\bar{u} - c$. Here, the spectrum of wave momentum flux is treated as the input, and the wave energy flux is treated as the output. A test of the above relationship for the convectively generated waves is shown in Fig. 15.1. In this figure, we have taken the time-averaged Eulerian-mean $\overline{p'w'}$, and compared it to a summation of the RHS of (15.1). We see that the agreement is very good in the model stratosphere, but considerably worse in the model troposphere. Since we expect gravity waves to dominate the motion fields in the stratosphere but not the troposphere, this result makes sense. Apparently, the triple-moment and forcing terms in relationships such as (8.67) are not negligible in the troposphere. Note that this relationship holds up well in the model stratosphere of several other simulations, as shown in Fig. 15.2.

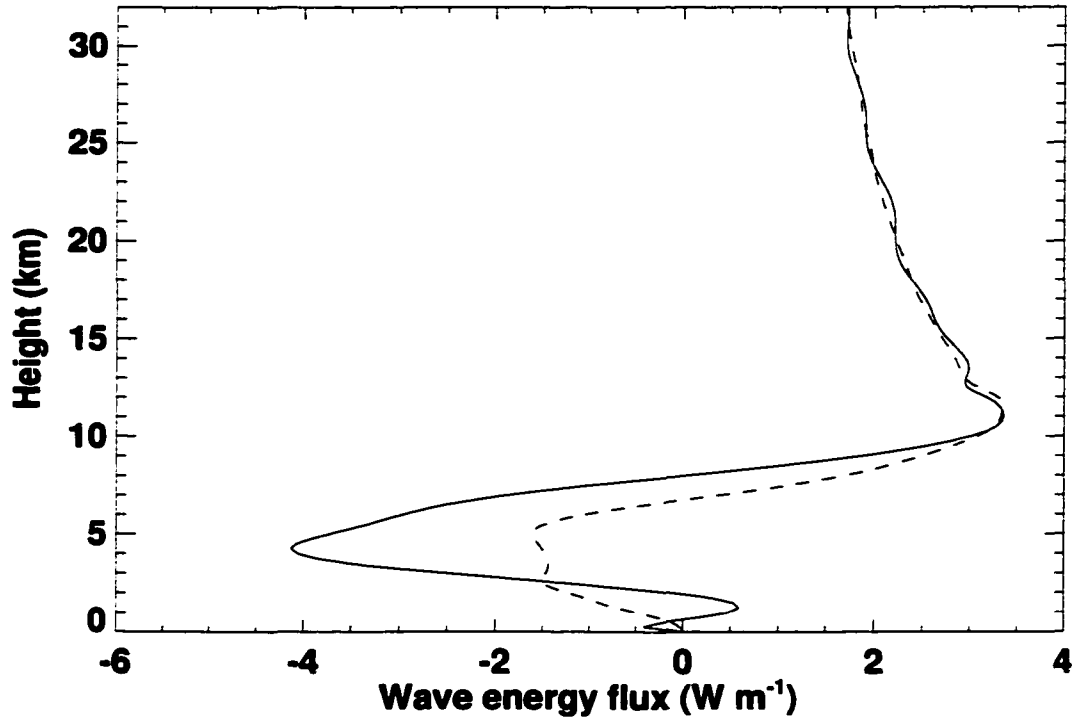

Fig. 15.1. Comparison of time-averaged Eulerian-mean wave energy flux (solid line) to a summation of the RHS of (15.1) (dashed line) for the WK control run.

When both the wave energy flux and wave momentum flux are accounted for, it is important to note that the total amount of wave energy flux implied by differentmomentum flux spectra can be quite different. In particular, a spectrum of $\overline{u'w'(\hat{c})}$ with too much

power at high intrinsic phase speeds will imply that too much perturbation kinetic energy is leaving the troposphere via vertically propagating gravity waves, as will be explained further below. In Fig. 15.3, we have a comparison between the AD99 spectrum of momentum flux, and a sinusoidal spectrum that is nonzero for $|\hat{c}| < 60$ m s^{-1}, each with the same total amount of easterly and westerly momentum flux (0.08 kg s^{-1}). The total wave energy flux is different by a factor of 1.6, however, with the AD99 spectrum yielding 7.7 W m^{-1} of wave energy flux, versus 4.8 W m^{-1} for the sinusoidal spectrum. In Fig. 15.4, the functional dependence of $\overline{p'w'}$ on $\hat{c}$ is shown. Note that the maximum in $\overline{p'w'}(\hat{c})$ is at a phase speed that is higher than the maximum in $\overline{u'w'}(\hat{c})$ for both spectra, but the shift is larger between the AD99 $\overline{u'w'}(\hat{c})$ and $\overline{p'w'}(\hat{c})$ spectra (from 25 m s^{-1} to 50 m s^{-1}) than the corresponding shift between the sinusoidal $\overline{u'w'}(\hat{c})$ and $\overline{p'w'}(\hat{c})$ spectra (from 30 m s^{-1} to 40 m s^{-1}). Also note that the AD99 spectrum is associated with significant amounts of wave energy flux at high ($|\hat{c}| > 100$ m s^{-1}) phase speeds.

Many middle atmosphere gravity wave parameterizations (Lindzen 1981, Fritts and Lu 1993; Hines 1997a,b) have focused on the issue of saturation. AD99 note that the simple parameterization of Lindzen and Holton (1968) (in which all of the momentum flux associated with a given phase speed is deposited at the critical level) works well within the lower stratosphere, but cannot account for the waves that amplify to the point of breaking (as is eventually required due to the decrease of density with height) without encountering their critical levels.

The existing multiwave parameterizations for convectively generated gravity waves (Rind et al. 1988, AD99) use a launch height near the tropopause for the waves. Since the results in Chapter 13 from the TC simulations indicate that momentum flux can be produced by clouds that do not extend through the depth of the troposphere, a launch height within the troposphere may be more appropriate. The bias of the momentum flux spectrum tends to be in the direction of the tilt of the convection. Since this tilt is generally the result of shear within the troposphere, this implies that the sign of the momentum flux due to the convection itself may be linked to the sign of the net momentum flux due to the waves. A complicating influence within the cloudy troposphere is the presence of moisture, which

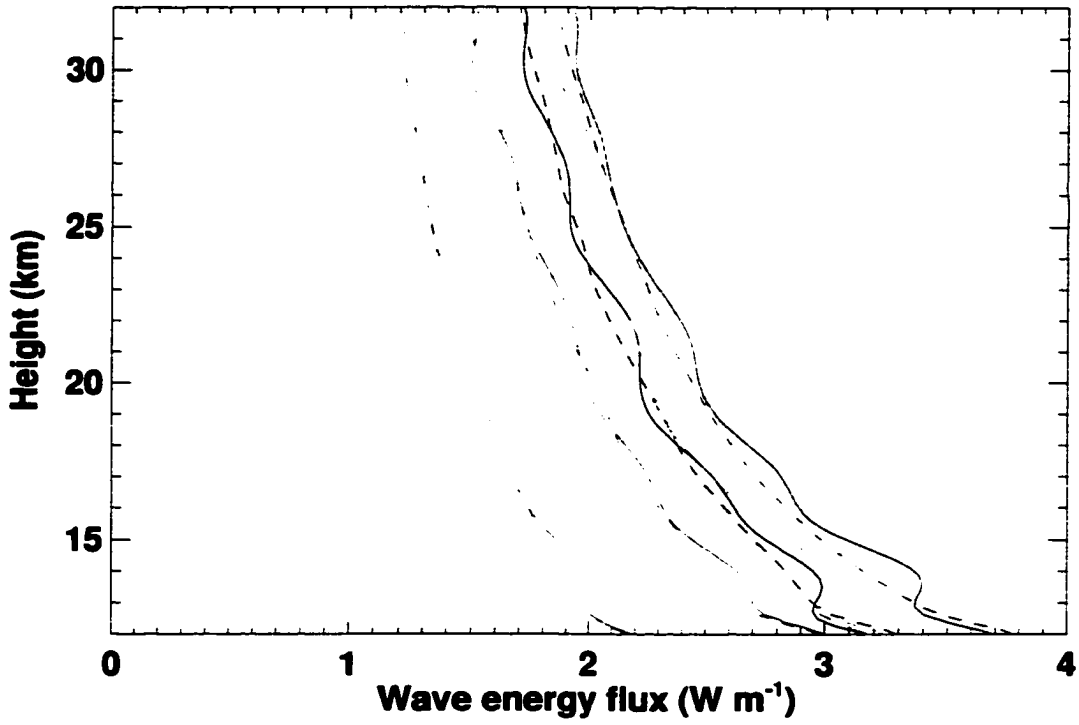

Fig. 15.2. Comparison of time-averaged Eulerian-mean wave energy flux (solid lines) to a summation of the RHS of (15.1) (dashed lines) in the model stratosphere for the WK control run (black), WK low-CAPE run (red), WK high-CAPE run (blue), WK low-shear run (green), and WK high-shear run (violet).

lowers the effective Brunt-Väisälä frequency (Durran and Klemp 1982), and filters out waves with short horizontal wavelengths (Pandya and Alexander 1999).

As noted in Chapter 7, the prognostic equation for perturbation kinetic energy can be written as

$$\frac{\partial}{\partial t}\left(\frac{\rho_0\overline{u_i'u_i'}}{2}\right)+\frac{\partial}{\partial x_j}\left(\frac{\rho_0\bar{u}_j\overline{u_i'u_i'}}{2}+\frac{\rho_0\overline{u_j'u_i'u_i'}}{2}+\overline{p'u_j'}\right)= \delta_{i3}\frac{\rho_0 g}{\bar{\theta}}\overline{u_i'\theta'}-\rho_0\overline{u_i'u_j'}\frac{\partial\bar{u}_i}{\partial x_j}+\varepsilon \quad , \tag{15.2}$$

where ε represents dissipation. If we associate the perturbations in (15.2) with the circulations caused by moist convection inside a grid cell of a large-scale model, we can define the cumulus kinetic energy (CKE) as the vertical integral of the perturbation kinetic energy, or

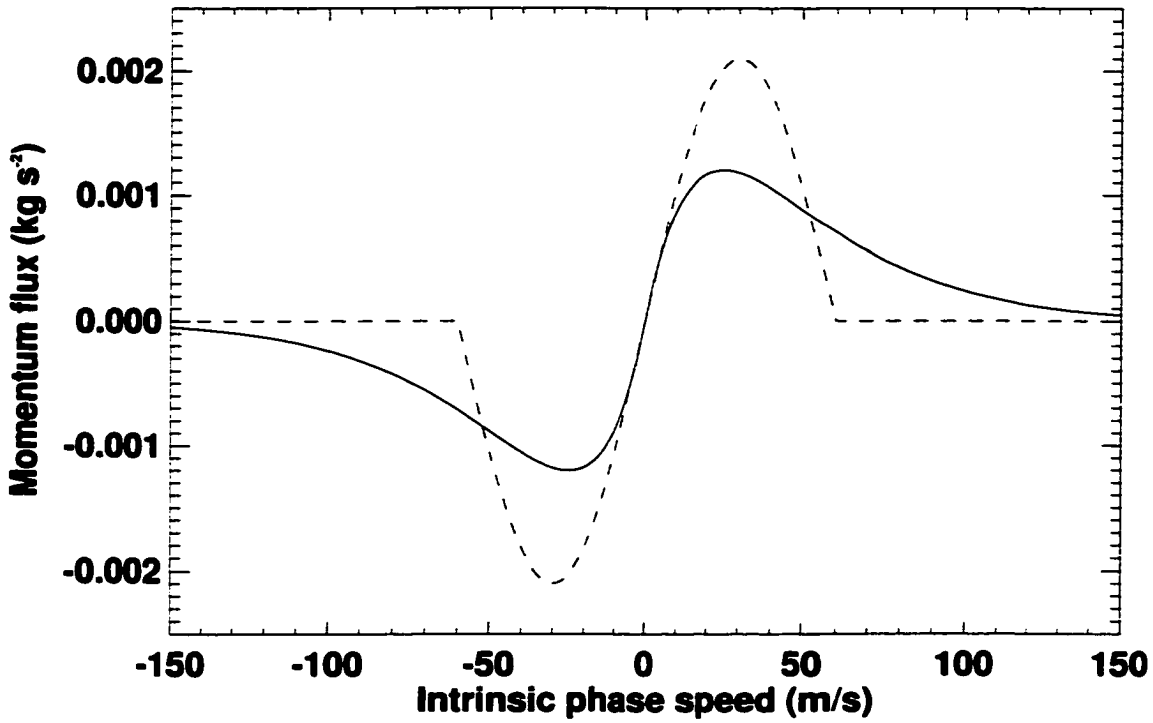

Fig. 15.3. Comparison of momentum flux within 1 m s^{-1} phase speed bins for the AD99 spectrum (solid) and a sinusoidal spectrum (dashed) that has an identical total amount of eastward and westward momentum flux.

$$K \equiv \int_{z_T}^{z_S} \frac{\rho_0 \overline{u_i' u_i'}}{2} dz, \tag{15.3}$$

following Pan and Randall (1998). Here, z_T and z_S stand for the heights of the cloud top, and the surface, respectively. If we neglect horizontal transports and the triple moment term, (15.2) has the form

$$\frac{\partial K}{\partial t} = B + S - D - R, \tag{15.4}$$

where B represents the production of CKE by buoyancy

$$B = \int_{z_T}^{z_S} \delta_{i3} \frac{\rho_0 g}{\bar{\theta}} \overline{u_i' \theta'} dz, \tag{15.5}$$

and S represents the production of CKE by shear

$$S = -\int_{z_T}^{z_S} \rho_0 \overline{u_i' u_j'} \frac{\partial \bar{u}_i}{\partial x_j} dz, \tag{15.6}$$

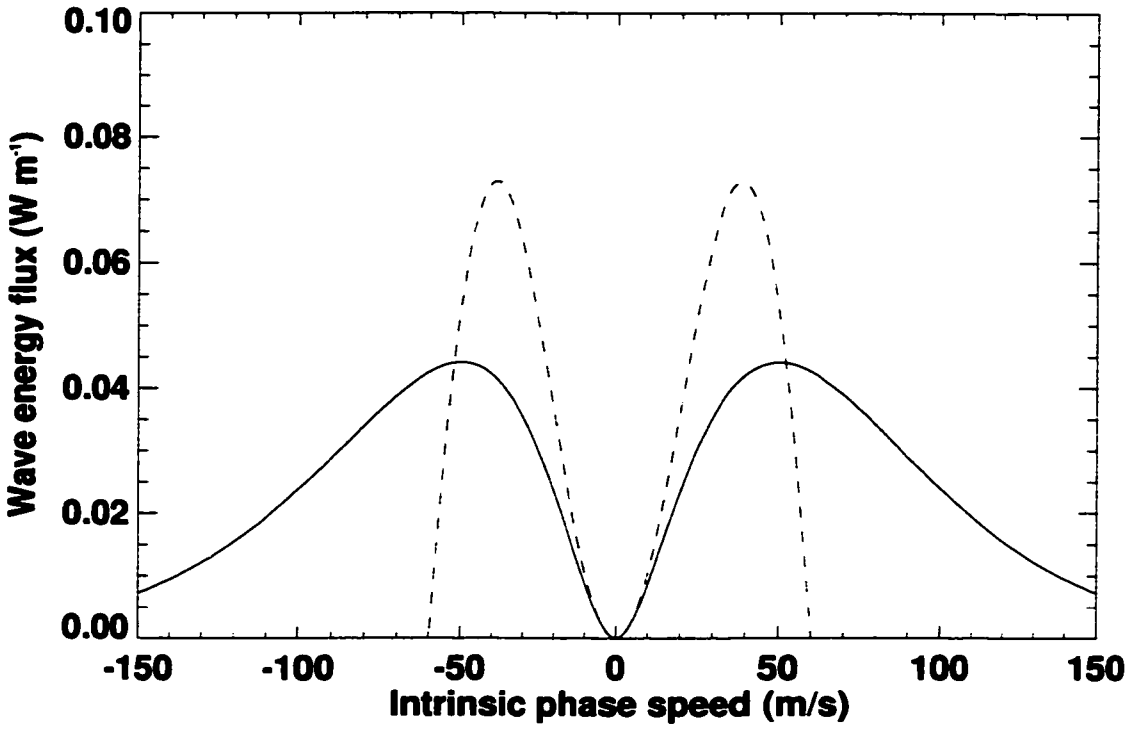

Fig. 15.4. Comparison of wave energy flux within 1 m s^{-1} phase speed bins for the AD99 spectrum (solid) and a sinusoidal spectrum (dashed) that has an identical total amount of eastward and westward

and D represents the viscous dissipation of CKE

$$D = \int_{z_T}^{z_S} \varepsilon dz . \tag{15.7}$$

The final term in (15.4) represents the energy loss due to the radiation of vertically propagating gravity waves (see Stull 1976), or

$$R = \overline{p'w'}(z_T) . \tag{15.8}$$

In Fig. 15.5, we compare the above term to the triple-moment terms in (15.2) for the WK control run at four separate times. We see from this figure that although the triple-moment terms are important in the troposphere, $\overline{p'w'}$ is dominant within the stratosphere. Similar results were obtained in the TC control run. This indicates that the only important flux of energy out of the model troposphere appears to be due to the wave energy flux. In addition, the distribution of $\overline{p'w'}$ is far more continuous across the tropopause than that of the net momentum flux $\rho_0 \overline{u'w'}$. This may be because as we saw in Chapter 13, there

exists a substantial amount of eastward- and westward-propagating waves in the lower troposphere of the WK control run (as well as most other simulations), each of which has a positive contribution to the total $\overline{p'w'}$, while these oppositely propagating waves partially cancel each other out in terms of the net momentum flux.

The Arakawa-Schubert (1974, also see Schubert 2000) cumulus parameterization is a way to account for the effects of subgrid-scale cumuli in large-scale models. Since there is typically an ensemble of shallow and deep cumuli coexisting within the area represented by a single grid cell, each cloud-top height is assigned a separate "type," or subensemble. Since the heating and drying effects of cumulus convection can be determined in terms of a mass flux into the cumuli, we need to determine this mass flux. The prognostic equation for the CKE of each subensemble in the Arakawa-Schubert cumulus parameterization as implemented by Pan and Randall (1998, also see Randall and Pan 1993) is a representation of (15.4) with only the B and D terms, and is given by

$$\frac{\partial K(s)}{\partial t} = M_B(s)A(s) - D(s), \tag{15.9}$$

where s takes on different values for each subensemble, K is the CKE, A is the work done by each cloud element due to buoyancy, M_B is the mass flux into the cloud at its base, and D is the dissipation rate of CKE. If we introduce a dissipation time scale τ_D for the CKE, (15.9) becomes

$$\frac{\partial K}{\partial t} = M_B A - \frac{K}{\tau_D}. \tag{15.10}$$

As Randall and Pan (1993) state, if A is defined to represent the effects that liquid water and ice have on buoyancy, the dissipation term of (15.10) represents only the effects of true kinetic energy dissipation. However, additional terms on the RHS of (15.10) can be introduced that include the effects of vertically and horizontally propagating wave generation by the cumuli. The sign of a term for the vertically propagating waves will be certainly be negative, as the waves represent energy produced by the convection that becomes lost to the middle and upper atmosphere, where new moist convection cannot be generated. In the case of horizontally propagating waves, it is likely that at least some new convection may be triggered by the waves (Mapes 1993).

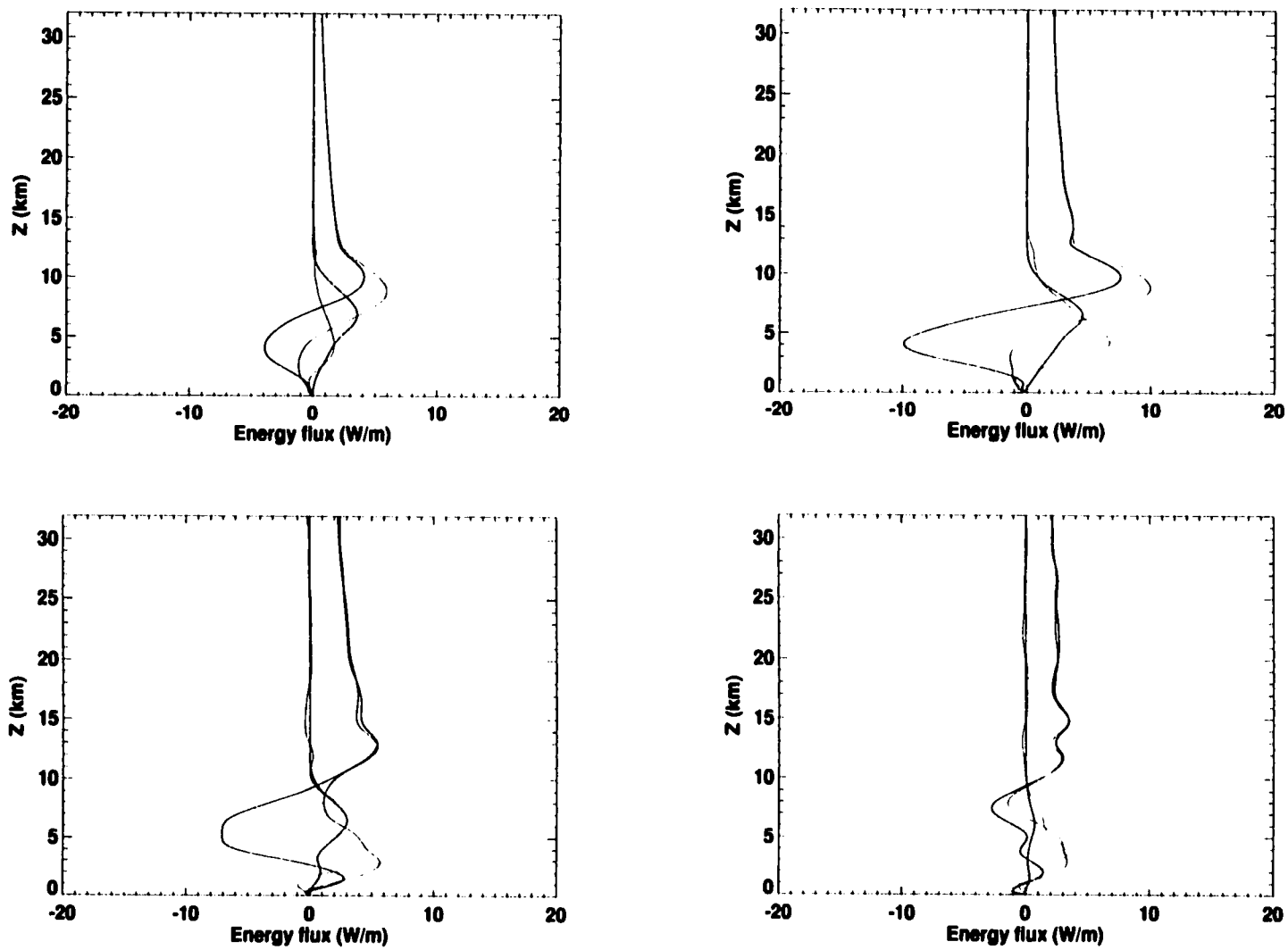

Fig. 15.5. Time-averaged energy fluxes due to $\overline{p'w'}$ (black lines), $\rho_0\overline{u'u'w'}/2$ (red lines), $\rho_0\overline{w'w'w'}/2$ (blue lines), and their sum (green lines) over a) 0-2 h, b) 2-4 h, c) 4-6 h, d) 6-8h for the WK control run.

If we focus on the effects of the vertically propagating waves denoted by W_V, we might be tempted to introduce another term in the same form as the dissipation in (15.10):

$$R = -\frac{K}{\tau_V}. \tag{15.11}$$

An estimate of the time scale τ_V can be obtained by measuring the turbulent kinetic energy of the troposphere in a mesoscale model that contains active convection, and then dividing this quantity by the wave energy flux $\overline{p'w'}$. A graph of this timescale for a variety of the squall-line simulations is shown below in Fig. 15.6. After the waves have had a

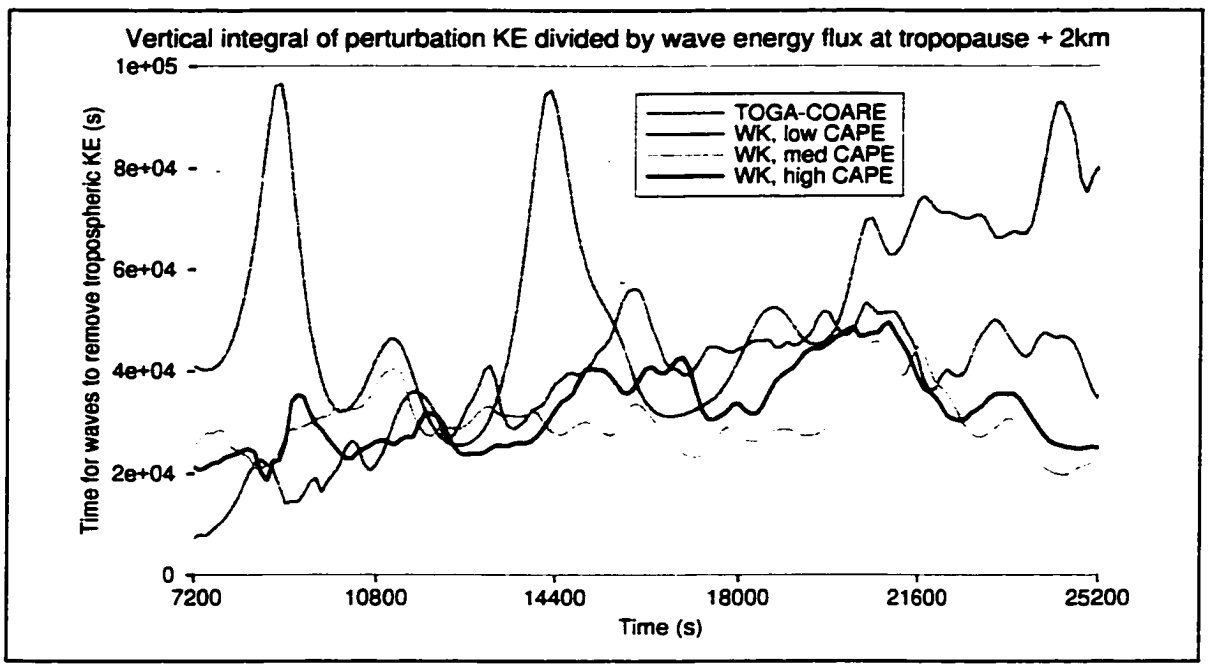

Fig. 15.6. Integrated perturbation kinetic energy of the troposphere divided by the wave energy flux at an altitude of 2 km above the model tropopause (14 km for the WK runs, 21 km for the TC run) versus

chance to propagate into the stratosphere, the timescale tends to oscillate around ten hours for the WK runs, but is highly variable for the TOGA-COARE run. These results indicate that using an equation with the form of (15.11) is likely not the best approach, unless the dependence of τ_V on other variables is derived.

If an equation such as (15.4) is to be used for the MCS, the sensitivity of the CKE to grid size should be considered. The horizontal domain of 900 km used in the simulations in this study is larger than a typical modern GCM grid cell size. We can calculate the CKE inside the central 700, 500 and 300 km of the mesoscale simulation. If large amounts of

the CKE associated with the simulated MCS are outside of a given horizontal scale, then we know that more than one GCM grid cell of that scale may be necessary to represent the CKE of a parameterized MCS.

In Fig. 15.7, we see that in the developing (first two hours) stage of the storm, the perturbation kinetic energy due to the central 300, 500 and 700 km are quite close to that of the entire domain. However, in the mature stage (3 - 7 hours) of the simulated storm, the perturbation kinetic energy is quite large outside of the central 300 and 500 km, although the CKE due to the central 700 km is still quite close to that of the entire domain.

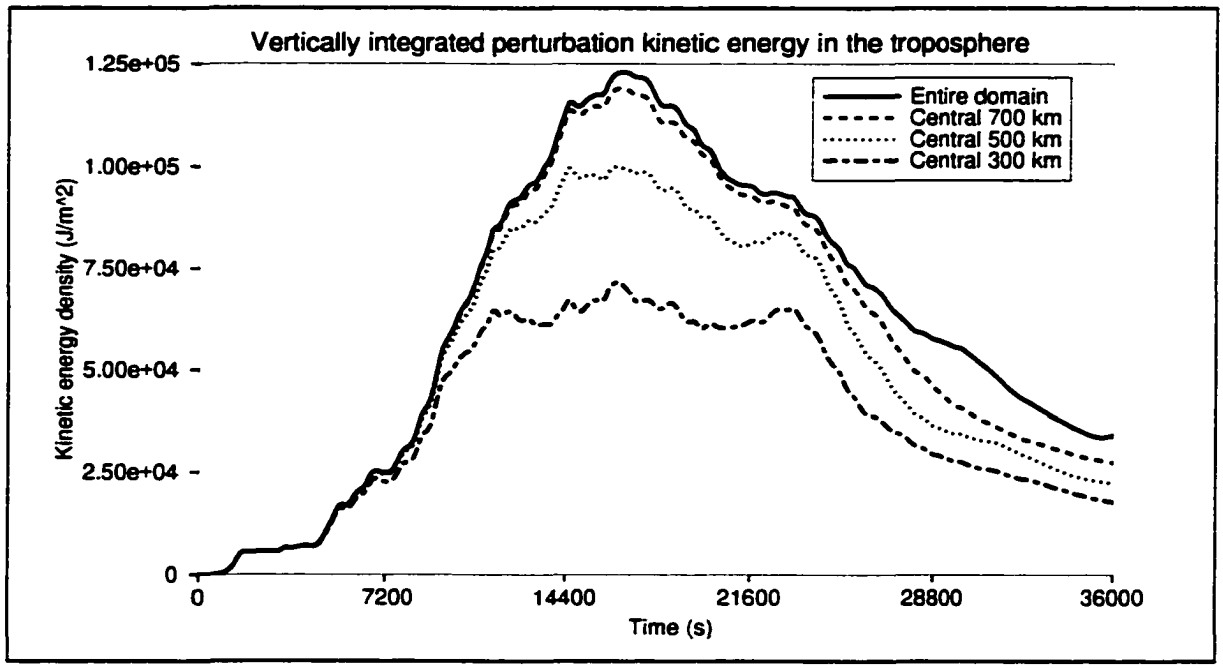

Fig. 15.7. Time series of vertically integrated perturbation kinetic energy density (J m^{-2}) of the model troposphere, over the entire domain, the central 700 km of the domain, the central 500 km, and the central 300 km for the WK low-CAPE run.

The perturbation kinetic energy with cloud masking applied (see Chapter 12) for the central 300, 500 and 700 km of the domain is shown in Fig. 15.8. This figure indicates that the portion of the CKE that is contained within cloudy air is practically insensitive to grid size, at least over this range of grid sizes.

In addition to the effects of the waves on the CKE, we need to address the transformation of symmetric spectra such as those shown in Fig. 15.3 to the asymmetric profiles that we saw in Chapter 13 and Chapter 14. Some insight into this may have been provided by a model of convectively generated gravity waves given by Pfister et al. (1993; hereafter

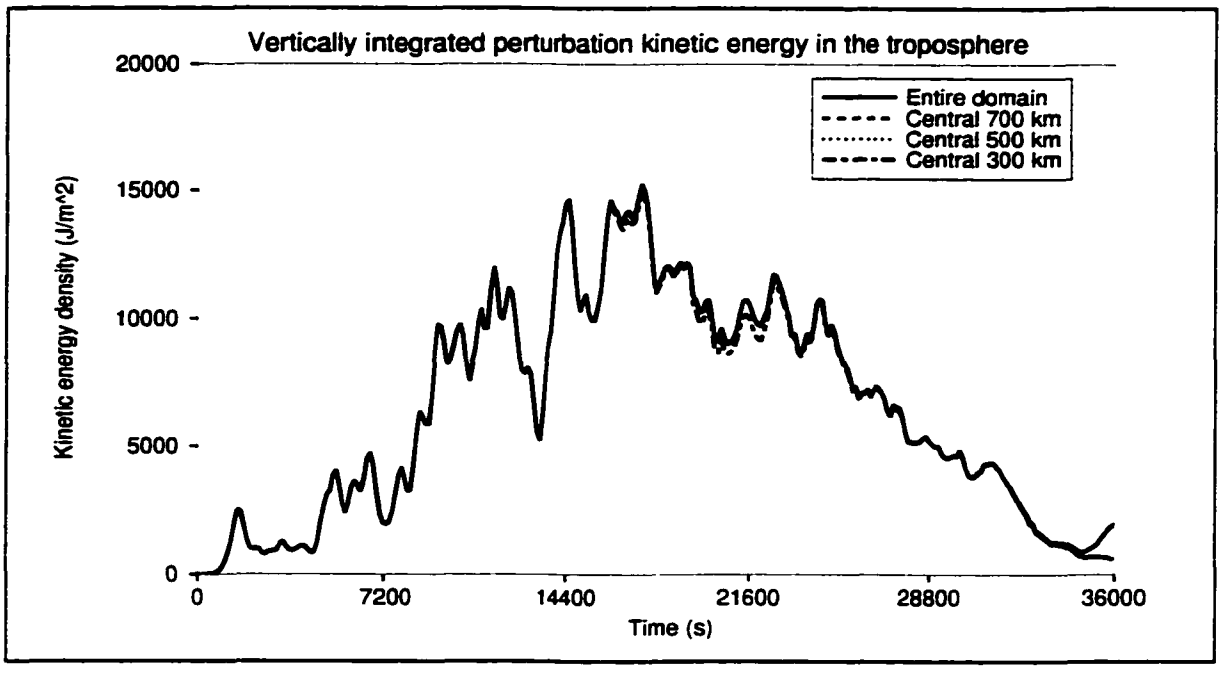

Fig. 15.8. As in Fig. 15.7, but only including points with cloud condensate concentrations > 0.1 g kg^{-1}.

P93). In their model, convection acted as transient topography, and shear between the troposphere and stratosphere was allowed to adjust the spectrum, as shown in Fig. 15.9. Note the qualitative similarity between the momentum flux spectrum associated with the $\bar{u}_0 = 0$ case in Fig. 15.9 and that of the WK calm run shown in Fig. 13.21, although the maximum and minimum values of $\rho_0 \overline{u'w'}$ are located at smaller (approximately ±8 m s^{-1}) phase speeds.

The spectra shown in Fig. 15.9 were calculated by P93 assuming that the transient topography had the form of

$$h(x, y, t) = f(x)f(y)g(t), \tag{15.12}$$

with the spatial and temporal functions given by

$$f(x) = \frac{L_2}{L_2 - L_1}\exp\left[-\left(\frac{x - x_0}{L_1}\right)^2\right] - \frac{L_1}{L_2 - L_1}\exp\left[-\left(\frac{x - x_0}{L_2}\right)^2\right], \tag{15.13}$$

and

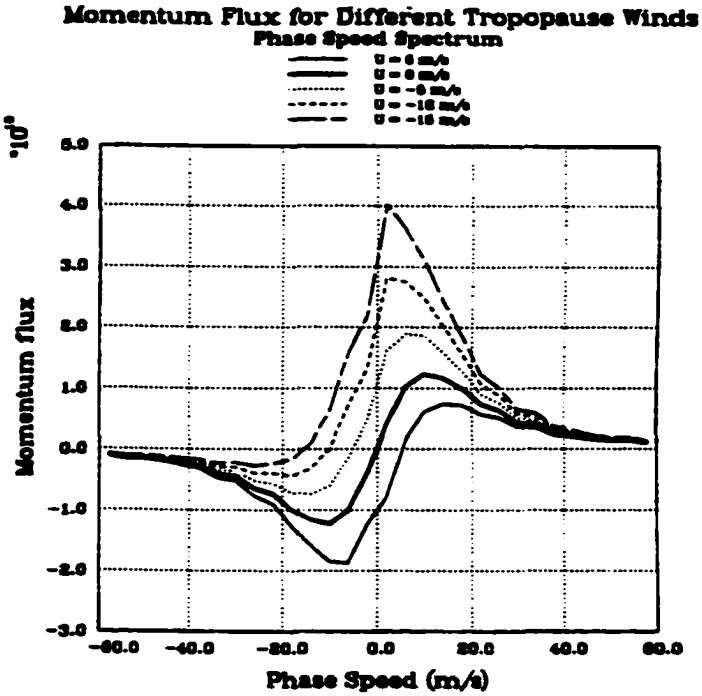

Fig. 15.9. Momentum flux spectra calculated by Pfister et al. (1993) for a "transient mountain" impinging upon the tropopause, which has various wind speeds relative to the mountain.

$$g(t) = \begin{cases} 0, & t \le t_0 + \tau \\ \dfrac{g_0}{2}\left[1 - \cos\left(\dfrac{2\pi(t - t_0)}{\tau}\right)\right]^{3/2}, & t_0 < t < t_0 + \tau \\ 0, & t \ge t_0 + \tau, \end{cases} \tag{15.14}$$

respectively, with an additional $f(y)$ defined in the same manner as $f(x)$. Here, P93 used parameter values of L_1 = 65.6 km, L_2 = 656 km, g_0 = 300 m, and τ = 5 h. These values were chosen to represent the "topographic" effect of the anvil of an MCS on the stratosphere. The amplitude g_0 was obtained from observed deviations in the height of potential temperature surfaces in the lower stratosphere. Representations of $f(x)$ and $g(t)$ are shown in Fig. 15.10. From these figures, the characteristic width and time of the convective topography can be estimated as 200 km and 5 hours, respectively. With the above forms of $f(x)$ and $g(t)$, P93 formed an expansion of $h(x, y, t)$ in Fourier coefficients:

a)

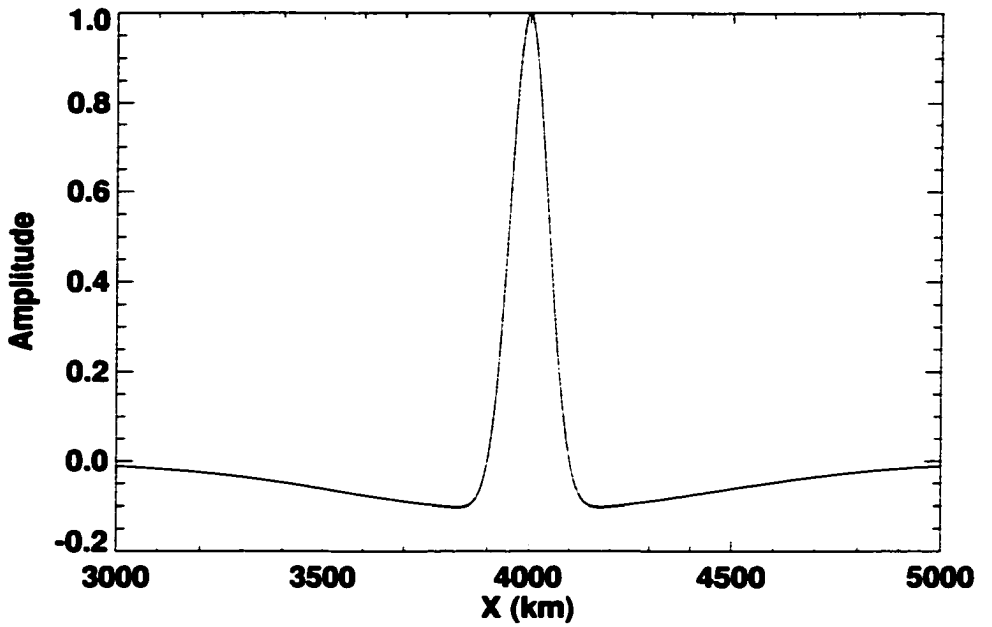

b)

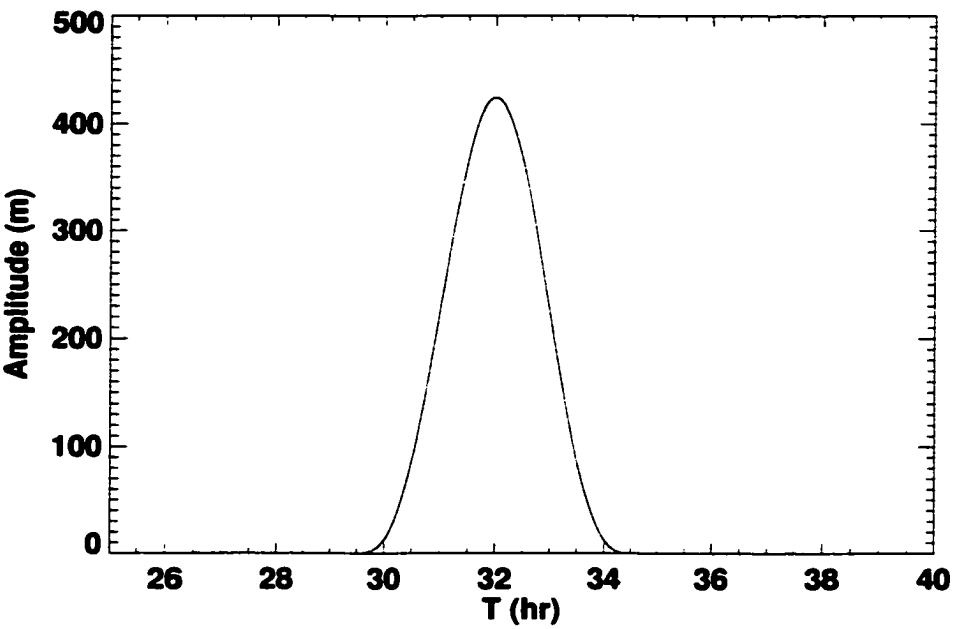

Fig. 15.10. Plots of a) $f(x)$ and b) $g(t)$ from (15.13) and (15.14), respectively, using the parameters assigned by P93.

$$h(x, y, t) = \sum_{j=-M}^{M} \sum_{m=-M}^{M} \sum_{n=-N}^{N} r_j r_m q_n \exp\left[2\pi i\left(\frac{jx}{L} + \frac{my}{L} - \frac{nt}{T}\right)\right] \qquad (15.15)$$

with

$$r_j = \frac{1}{L}\int_0^L f(x)\exp\left[-2\pi i\left(\frac{jx}{L}\right)\right]dx, \tag{15.16}$$

$$q_n = \frac{1}{T}\int_0^T g(t)\exp\left[2\pi i\left(\frac{nt}{T}\right)\right]dt. \tag{15.17}$$

The height field was then related to vertical velocity using the boundary condition

$$w'(x, y, t) = \frac{\partial h}{\partial t} + \bar{u}_0\frac{\partial h}{\partial x}, \tag{15.18}$$

where $\bar{u}_0$ represents a mean wind speed (see Holton 1992, p. 205 for the analogous application to orographic waves). In the P93 formulation, $\bar{u}_0$ is interpreted as the wind at the tropopause relative to the convective system. In our formulation, this quantity is interpreted as the difference between the zonal wind inside the convective updrafts and the large-scale wind, which we measured in Chapter 12 for several simulations. Using (15.15), P93 note that the expression for w' can be stated in terms of Fourier amplitudes as

$$W_{jmn} = -i\left(\frac{2\pi n}{T} - \frac{2\pi j}{L}\bar{u}_0\right)r_j r_m q_n. \tag{15.19}$$

Using the polarization relationships for gravity waves (see Chapter 1), a similar expression can be derived for the Fourier representation of the horizontal component of velocity,

$$U_{jmn} = W_{jmn}\left(\frac{2\pi j}{L}\right)\left(\frac{2\pi}{\lambda_z}\right)\left[\frac{L^2}{4\pi^2(j^2+m^2)}\right]. \tag{15.20}$$

Here, λ_z corresponds to the vertical wavelength,

$$\left(\frac{2\pi}{\lambda_z}\right)^2 = \frac{N^2\kappa^2}{\omega_0^2} - \kappa^2 - \frac{1}{4H^2}. \tag{15.21}$$

Here, we have used the definitions

$$\kappa^2 = \frac{4\pi^2(j^2+m^2)}{L^2}, \tag{15.22}$$

$$\omega_0 = \frac{2\pi n}{T} - \frac{2\pi j}{L}\bar{u}_0. \tag{15.23}$$

Combining (15.19) and (15.20), P93 obtained the following expression for the momentum flux associated with a given wavenumber and frequency:

$$(\rho_0 \overline{u'w'})_{jmn} = \frac{\rho_0}{4}(U_{jmn} W^*_{jmn} + U^*_{jmn} W_{jmn}). \tag{15.24}$$

Then, we can calculate the amount of area- and time-integrated momentum flux within a phase speed interval by performing the summation given by

$$(\rho_0 \overline{u'w'})_c = \frac{L^2 T}{\delta c} \sum_{j=1}^{M} \sum_{m=-M}^{M} \sum_{n=jTc/L}^{jT(c+\delta c)/L} (\rho_0 \overline{u'w'})_{jmn}. \tag{15.25}$$

The P93 formulation can also be restated to represent the effects of convective updrafts rather than a mesoscale anvil. To do this, we want to use parameter values in $f(x)$ and $g(t)$ that represent shorter length and time scales. In Chapter 12, we saw that typical widths of the updraft points are approximately 10-15 km in the upper troposphere. Typical timescales for the updrafts are approximately 15-30 minutes. The wind speed of the ambient air $\bar{u}_0$ relative to the convection can be interpreted as $-u_{up}'$. In Fig. 15.11, we have performed similar calculations to those of P93 shown in Fig. 15.9, except with no modes in the meridional direction, and with $L_1 = 6.56$ km, $L_2 = 65.6$ km, and $\tau = 20$ min. Note that these length scales combine to represent a height perturbation with a width of approximately 20 km. Other values of these parameters were tried, but this combination is consistent with the spatial and temporal scales illustrated in Chapter 12, and produce spectra similar to those shown in Chapter 13. When large values of τ are used, the spectra tend to become peaked at $\hat{c} = -\bar{u}_0$, or $c = 0$. This is apparent in Fig. 15.9 for large values of $\bar{u}_0$, and would also be present for sufficiently large values of $\bar{u}_0$ for the length and time scales that we have used.

We used 800 modes in the spatial and temporal domains, corresponding to a minimum horizontal wavelength of 10 km and a minimum period of 4.8 minutes. When additional modes were added, the shapes of the spectra did not change noticeably. The shapes of the spectra are also relatively insensitive to the use of meridional modes, at least when a symmetric structure such as those used in P93 are used. Note that in this figure, we have used the intrinsic phase speed, rather than the ground-relative phase speed to facilitate compari-

son with the figures in Chapter 13. Also, the amplitudes of the spectra in Fig. 15.11 are normalized so that the peaks of the $\bar{u}_0 = 0$ line are equal to ± 1.

We can see several similarities between these spectra and those calculated in Chapter 13. The peaks of the $\bar{u}_0 = 0$ spectrum are located at approximately $\hat{c} = \pm 17$ m s^{-1}. This is quite close to the value seen in the WK calm run in Fig. 13.21. We also see an asymmetry between the magnitudes of the momentum fluxes associated with the eastward- and westward- propagating waves that increases with $\bar{u}_0$. The increase in $\bar{u}_0$ is also associated with an increasing asymmetry in the position of the peaks, with the negative peak moving towards more strongly negative values of $\hat{c}$, and the positive peak moving to lower values of $\hat{c}$. Also, the momentum flux curves trail off towards zero at high phase speeds, in accordance with the spectra calculated from the model simulations, although the decrease is not as rapid. However, the decrease is much more rapid than that of the AD99 spectrum (see Fig. 15.3).

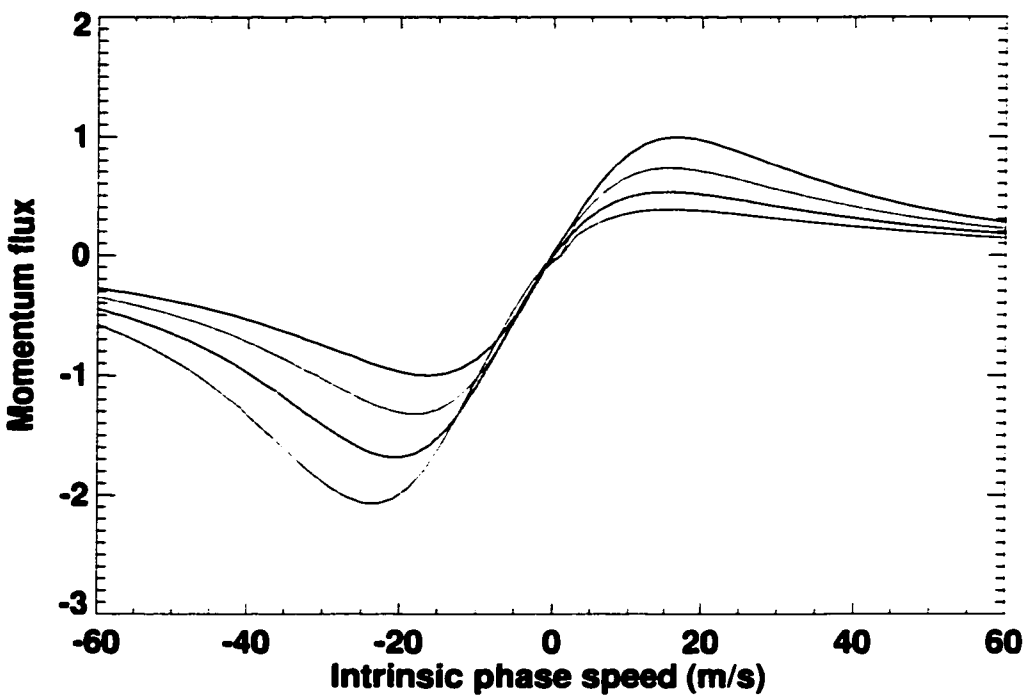

Fig. 15.11. Comparison of modified P93 profiles versus intrinsic phase speed for $\bar{u}_0 = 0$ m s^{-1} (black line), $\bar{u}_0 = 5$ m s^{-1} (red line), $\bar{u}_0 = 10$ m s^{-1} (blue line), and $\bar{u}_0 = 15$ m s^{-1} (green line).

There are also some differences between the curves plotted in Fig. 15.11 and those of Chapter 13. One difference is that the parameterized spectra are more smooth than those from the simulations. One explanation is that there are multiple temporal and spatial scales present in the updrafts produced by the simulations. In addition, when large values of L and T are used in (15.15) in comparison to the values of L_1, L_2, and τ, smoother spectra are produced. In addition, the spectra in Fig. 15.11 are not as flat near $\hat{c} = 0$. Since these waves are initially close to their critical levels, dissipation can affect them more readily than waves with higher intrinsic phase speeds.

P93 diagnosed the amplitude g_0 from observations of isentropic displacements. However, when similar values are used in our formulation, the amplitude of the momentum fluxes are far too small (by several orders of magnitude) in comparison to what we saw from the model results in Chapter 13. If we instead use the entire depth of the updraft as a proxy for g_0, we obtain values that are much more comparable to the model results. As we mentioned in Chapter 6, the gravity wave source terms were large over a fairly large depth. This was also found to be the case in Lane et al. (2001). To identify the depth of the updrafts from the model data, we calculate the depth over which there is an updraft with a width of at least 5 km. The top of this updraft is then taken to be the launch height for the waves. The instantaneous addition of a net momentum flux at the launch height (which will happen if $u'_{up} \neq 0$) will imply an acceleration below the launch height. However, since the GCM also predicts momentum transport due to the convection itself (Cheng 2001), and the amount of momentum flux due to waves is comparatively small in the convective layer (see Fig. 15.12), this effect should be relatively small.

Still another issue to be dealt with in a parameterization is that of wave reflection. AD99 showed that this could be an important issue for short-wavelength waves in the mesosphere. As mentioned in Chapter 1 and Chapter 9, wave reflection occurs when the frequency of the incident wave is higher than that of the ambient atmosphere. This is not generally a problem in the stable stratosphere, but becomes an issue in the mesosphere, where the stability can become quite weak, as shown by Clark and Morone (1981). As noted in section 13.6 and Pandya and Alexander (1999), this phenomena can also occur in connection with the propagation of waves through cloudy air. The problem of wave reflec-

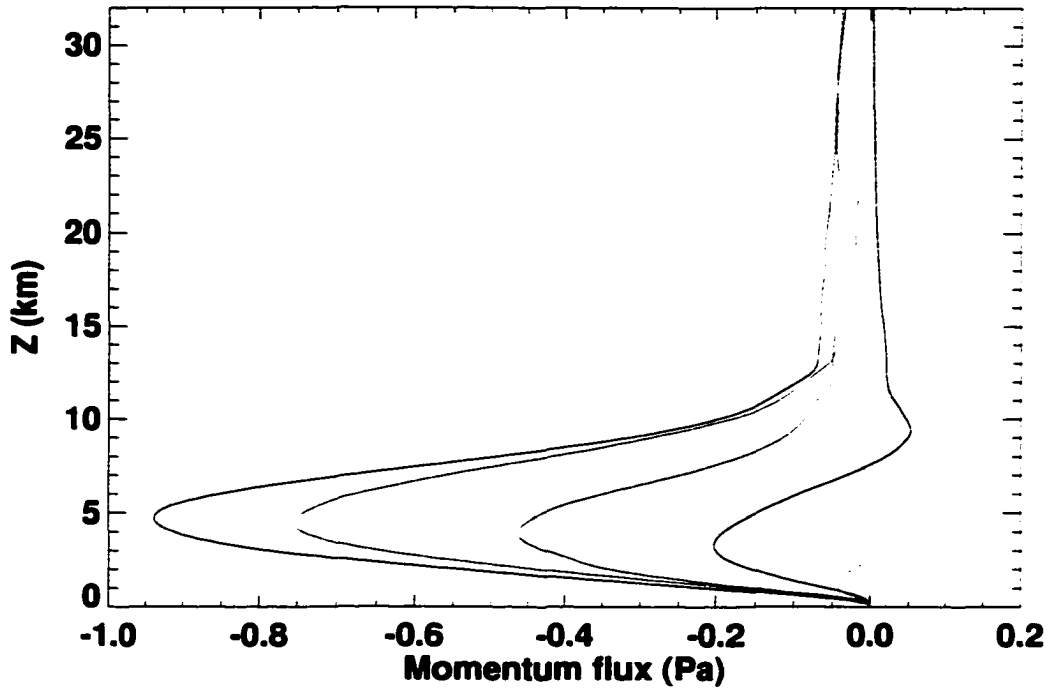

Fig. 15.12. Time-averaged momentum flux over different spans for the WK control run: 0-2 h (black line), 2-4 h (red line), 4-6 h (blue line), 6-8 h (green line), and 8-10 h (violet line).

tion necessarily brings about the additional issue of how many horizontal wavenumbers to allocate to the phase speed spectrum. One physically plausible solution is to pick an initial single vertical wavelength, corresponding to twice the depth of the convection. If we assume that this vertical wavenumber is located at the phase speed with the highest momentum flux denoted by $\hat{c} = \hat{c}_{max}$, then we can solve for a single horizontal wavenumber. If computational resources allow, additional horizontal wavenumbers should be used, since the waves are certainly not monochromatic (see Fig. 13.4). Then, a spectrum of vertical wavenumbers can be calculated from this horizontal wavenumber and the spectrum of phase speeds, using a modified form of (1.11),

$$m^2 = \frac{N_m^2}{\hat{c}^2} - \left(k^2 + \frac{1}{4H^2} + \frac{1}{\hat{c}}\frac{d^2\bar{u}}{dz^2}\right). \tag{15.26}$$

Note that there is an additional term in the parentheses that is related to the curvature of the flow. To the extent that the shear is linear, this term can be ignored. Those waves for

which $m^2 < 0$ can be eliminated, since these waves decay exponentially with height (Holton 1992, p. 205).

Here, we have used N_m to represent the moist Brunt-Väisälä frequency, which is approximated by Durran and Klemp (1982) as

$$N_m^2 = g\left[\frac{1+(L_v q_s/RT)}{1+(\varepsilon L_v^2 q_s/c_p RT^2)}\left(\frac{1}{\theta}\frac{d\theta}{dz}+\frac{L_v}{c_p T}\frac{dq_s}{dz}\right)-\frac{dq_w}{dz}\right] \tag{15.27}$$

for saturated air. Here, L_v represents the latent heat of vaporization, q_s is the saturation mixing ratio of water vapor, q_w is the total (liquid plus vapor) water mixing ratio, T is the temperature, R is the ideal gas constant for dry air, and ε is the ratio of the gas constants for dry air and water vapor, with $\varepsilon = R/R_v$. Note that the moist and dry Brunt-Väisälä frequencies will be quite close to one another in regions that are dry, such as the upper troposphere. Thus, using the dry Brunt-Väisälä frequency is probably a reasonable approximation for deep convection. The condition given in (15.26) can also be used for waves in the middle atmosphere. In GCMs that do not extend into the mesosphere, wave reflection above the tropopause is probably not an important effect.

Consistent with the ray-tracing results of Bretherton (1966), and Marks and Eckermann (1995) for a horizontally homogenous atmosphere, we assume that the (ground-based) frequency and horizontal wavenumber is constant for each wave. The vertical wavenumber of the waves can change, since the atmosphere within a grid box cannot be assumed to be homogeneous in the vertical. However, the vertical wavenumber is only used to calculate the initial horizontal wavenumber spectrum.

Vertically propagating waves that are not reflected must eventually be absorbed at a critical level or break. As Lindzen (1981) pointed out, wave breaking typically occurs at mesospheric heights. As we saw in Chapter 9, AD99 use a combination of the Lindzen (1981) and Lindzen and Holton (1968) approaches to diagnose wave breaking events. This method accounts for both wave breaking and As with wave reflection, this approach also depends upon the horizontal wavenumber, using the parameter

$$Q_n(\hat{c}) = \frac{\rho_l}{\rho(z_n)}\frac{2N(z_n)\overline{u'w'(\hat{c})}}{k\hat{c}^3}. \tag{15.28}$$

Here, ρ_l is the density at the launch height. As mentioned in Chapter 9, the AD99 approach is that when $Q_n(\hat{c}) \geq 1$ for a wave, all of that wave's momentum flux is absorbed between z_n and z_{n-1}, similar to Lindzen and Holton (1968). Note that this condition must be fulfilled at some height even for high values of $\hat{c}$ (e.g., easterly waves propagating through a deep layer of westerly winds), due to the decrease of density with height.

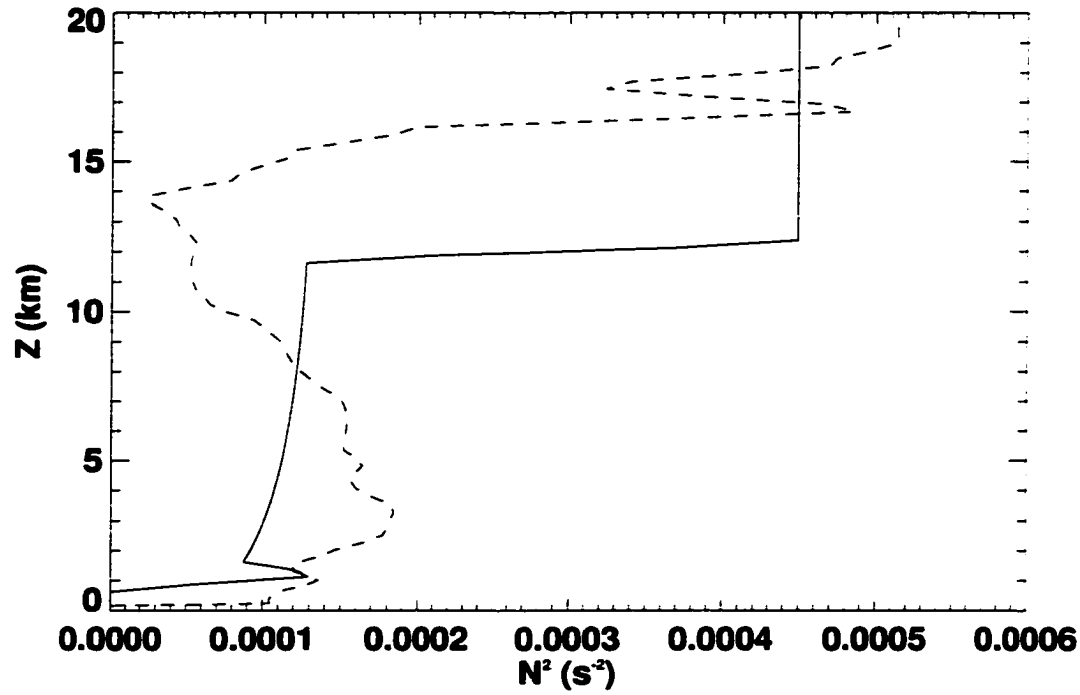

Fig. 15.13. The square of the Brunt-Väisälä frequency versus height for the WK control (solid line) and TC control (dashed line) runs.

The steps of the parameterization will be are as follows. We will use parameter values from the WK control run instead of a large scale model. First, generate a spectrum of momentum flux as a function of phase speed, using a value of u_{up}' diagnosed from the convective momentum transport parameterization of the large-scale model to obtain the shape of the spectrum. From Fig. 12.5, we estimate a value of -5 m s^{-1}. For the sake of computational efficiency, a family of spectral shapes for different values of u_{up}' can be generated and stored before the GCM simulation begins. To generate the spectrum, we also need values of L_1, L_2, τ, g_0, ρ_l, and N_m^2. For the first three parameters, we use the

same values that produced the spectra shown in Fig. 15.11, with L_1 = 6.56 km, L_2 = 65.6 km, and τ = 20 min. We diagnose g_0 from a calculation of the root mean square depth of the updraft, which is 8668 m for the WK control run. The depth of the updrafts in the WK control run is shown as a function of time in Fig. 15.14a. We calculate the root mean square rather than the arithmetic mean, since the momentum flux scales as g_0^2. Since the maximum height of the "mountain" is a factor of $\sqrt{2}$ higher than g_0 (see (15.14)), we use a value of 6129 m. The values of ρ_l and N_m^2 are diagnosed from near the top of the convection, and are taken to be 0.34 kg m^{-2} and 0.00012 s^{-2}, respectively. The diagnosis of N_m^2 is somewhat problematic, since the updrafts are sometimes quite close to the tropopause, where there is a jump in the Brunt-Väisälä frequency (see Fig. 15.13). The initial parameterized spectrum, without taking the effects of reflection and saturation into account, is shown as the dashed line in Fig. 15.15, and is compared to the spectrum calculated from the simulation itself. Note that both spectra are partitioned into bins of ± 1 m s^{-1}, so there are 60 bins represented in this figure. Also, we have multiplied the parameterized spectrum by a factor of 1707, which corresponds to the product of the ratio of the lengths of the spectral and simulation domains (8000 km/900 km), the ratio of the time scales of the two domains (64 h/10 h), and the number of 20-minute updraft cycles that occur in the 10-hour simulation (30). We see that the spectra are quite similar, although the parameterized spectrum does not fall off as quickly as the simulated spectrum. As we noted with the AD99 spectrum, this causes the wave energy fluxes to be unrealistically high, 5.8 W m^{-1} in this case, as compared to 3.2 W m^{-1} (see Fig. 15.2). Also, the integrated momentum fluxes from westward- and eastward-propagating waves are too large, at -0.12 Pa and 0.08 Pa, as compared to -0.07 Pa and 0.04 Pa (see Fig. 13.10).

As mentioned earlier, we need some information about the horizontal wavenumbers of the waves to take the effects of reflection and saturation into account. Using the depth of the updraft, a representative vertical wavenumber within the troposphere is diagnosed, corresponding to a wavelength that is twice the depth of the updraft. Using a figure of $\hat{c}_{max} = -18$ m s^{-1} and $m = 0.00036$ m^{-1}, we use (15.26), where we have neglected the

effects of curvature in $\bar{u}$, since there is relatively little shear in the WK control simulation near the tropopause throughout the simulation. We obtain a value of $k = 0.00048$ m^{-1}, or a wavelength of approximately 13 km. This is on the short side of what was directly calculated from the simulation (see Fig. 13.4), but is within the broad 10-100 km peak. This calculation is quite sensitive to the value of $\hat{c}_{max}$ that is used, introducing one possible source of error. To represent the effects of waves with higher and lower wavelengths, we assume that for each value of $\hat{c}$, the momentum flux is partitioned equally among wavenumbers of 0.00192 m^{-1}, 0.00096 m^{-1}, 0.00048 m^{-1}, 0.00024 m^{-1},and 0.00012 m^{-1}, corresponding to multiplications of 4, 2, 1, 0.5 and 0.25 times the original value. This quintuples the number of waves that must be kept track of to 300. This may be too computationally expensive for a GCM, so some compromise between the number of phase speeds and wavenumbers will likely need to be made for this scheme to be practical. Those waves that produce $m^2 < 0$ in (15.26) are eliminated from the spectrum. The spectrum with these waves removed is shown as the dotted line in Fig. 15.15. We see that wave reflection has had a large effect on waves at high phase speeds, attenuating them dramatically. The elimination of reflected waves causes the total momentum fluxes to become more realistic (-0.06 Pa for westward-propagating waves, 0.04 Pa for eastward-propagating waves). However, this spectrum is more biased towards waves with low values of $\hat{c}$ than the one produced by the simulation, causing the parameterized wave energy flux to drop to 2.1 W m^{-1}, which is about 35% below the total produced by the simulation. One possible explanation for this is that the exponentially decaying waves above the reflection point still carry some energy (see Gill 1982, p. 149).

To see whether waves break, our approach is similar to that of AD99, which itself is largely due to Lindzen (1981) and Lindzen and Holton (1968). The saturation criterion given in (15.28) is tested at each grid level above the launch height, and the mean flow is accelerated according to

$$\frac{\partial \bar{u}}{\partial t} = \frac{1}{\rho(z_{n-1/2})\Delta z_{n-1/2}} \sum_i \rho_l \overline{u'w'(\hat{c}_i)}, \qquad (15.29)$$

where $\rho(z_{n-1/2})$ is the density at $z_{n-1/2} = (z_n + z_{n-1})/2$, $\Delta z_{n-1/2} = z_n - z_{n-1}$, and the summation is over the waves that are absorbed. In the case of the WK control run, none of the waves fulfill the saturation criterion at the launch height. The depth over which the waves are absorbed could be increased to cover more than one grid level, which would be consistent with the results of Chapter 14 (see Fig. 14.7 and Fig. 14.8) for a GCM with fine vertical resolution. The removal of only that portion of each wave's momentum flux that is necessary to restore $Q_n(\hat{c}) = 1$ in (15.28) could also be implemented. This process is repeated, checking whether waves are absorbed or reflected, until the top grid level is reached, where all of the remaining waves can either be absorbed, or allowed to pass through. Although the former approach is sometimes used in orographic gravity wave parameterizations (Palmer et al. 1986), the latter is probably preferable, since the absorption of all waves at a single level could lead to spurious accelerations, particularly if the model has fine vertical resolution.

We repeated the exercise outlined above using the WK calm run. The temporal behavior of the updrafts in this simulation is shown in Fig. 15.14b. The root mean square updraft depth is 9420 m according to this diagnosis. When this is used with the $\bar{u}_0 = 0$ spectrum, we obtain the dashed line in Fig. 15.16. This parameterized spectrum is qualitatively similar to the spectrum from the simulation, but the magnitudes of the positive and negative momentum fluxes are far too high at 0.12 Pa each, versus approximately 0.035 Pa (see Fig. 13.22), and a wave energy flux of about 6.0 W m^{-1} (compared to about 2.1 W m^{-1} in the simulation). The effects of reflection produce a spectrum that is much closer to the simulated spectrum, as seen in the dotted line of Fig. 15.16. The parameterized spectrum with reflection produces positive and negative momentum fluxes with a magnitude of 0.05 Pa each, and a wave energy flux of 2.1 W m^{-1}. Another test using parameters from the TC control run was not as successful. This may be because the waves generated in this simulation propagate through an upper troposphere that has weak stability (see Fig. 15.13), causing partial reflection.

Once the spectrum of waves that escapes the troposphere is determined, the stratospheric sink on the CKE can be diagnosed using (15.1). Note that reflected waves are not a treated as a sink of CKE in the current parameterization, which is consistent with our

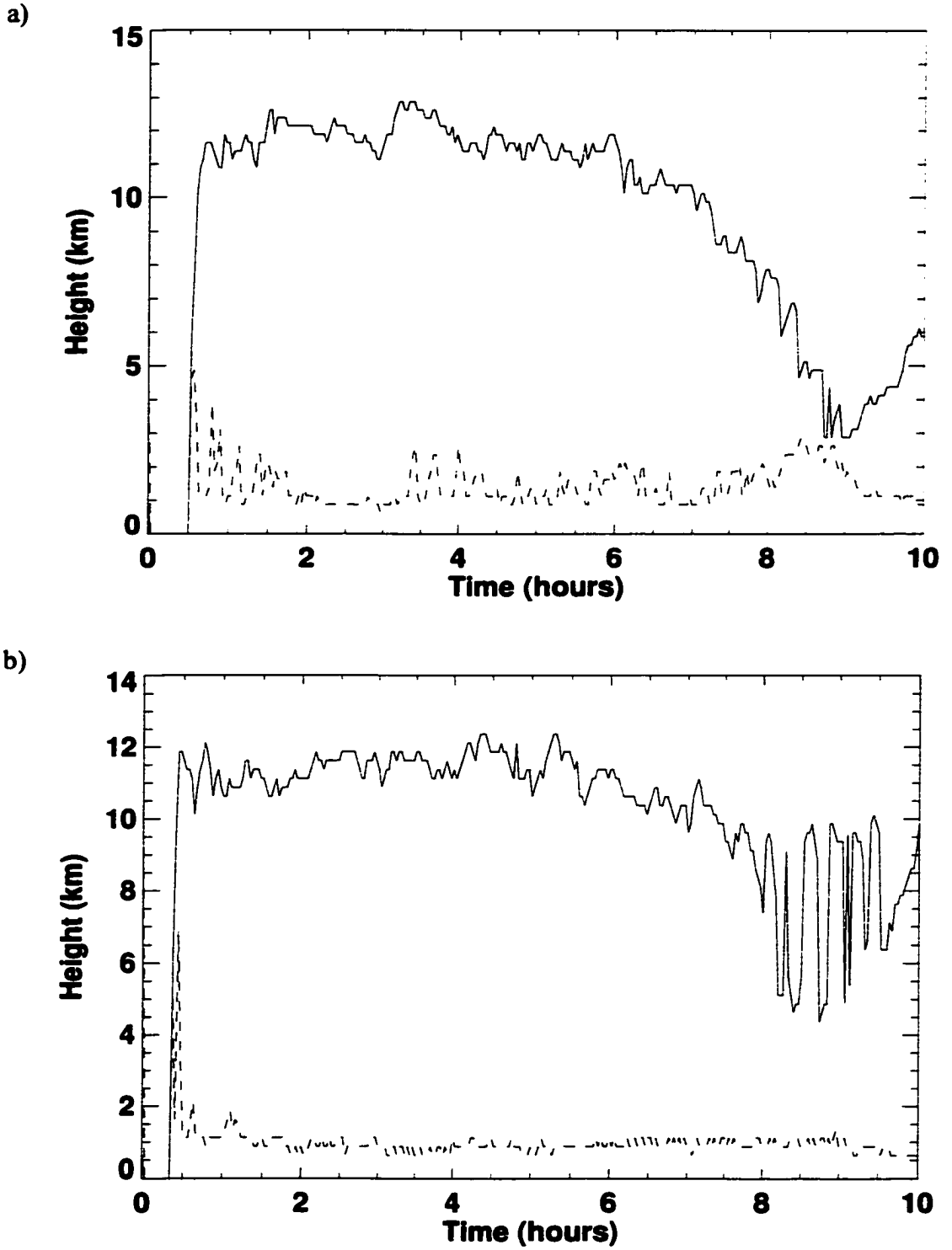

Fig. 15.14. Plots of the heights of the top and bottom of the updrafts (as defined in the text) for a) the WK control run b) the WK calm run.

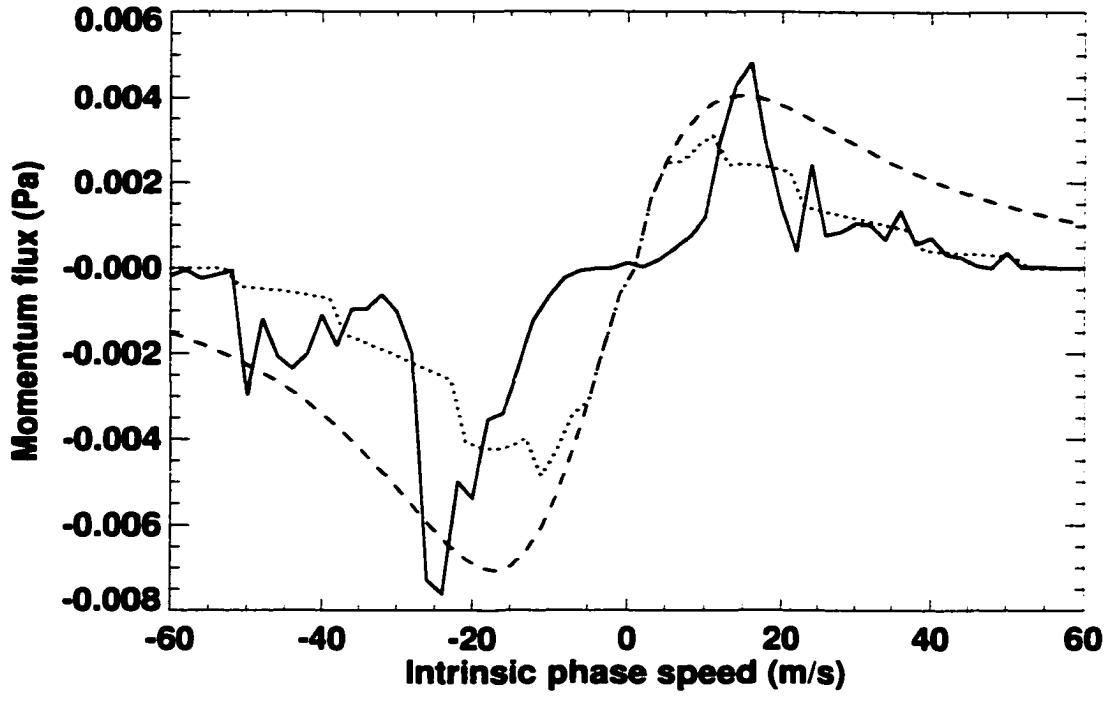

Fig. 15.15. Plot of momentum flux spectra from the WK control run (solid) and the parametrization (dashed), and the parameterization with wave reflection (dotted).

neglect of the effects of horizontally-propagating waves. Since the timescales in Fig. 15.6 are significantly longer than τ_D in (15.10), the effect on the CKE is likely to be small over the lifetime of individual clouds. However, the effects of the gravity wave sink may be more significant over longer time periods.

The Eliassen and Palm (1960) relationship between the momentum flux spectrum with the wave energy flux was demonstrated to be valid in Fig. 15.2 for waves produced by the convection in this study. This allows us to obtain a quantitative measure of the dissipative effect that the waves have on the convection. The parameterization presented in this chapter contains elements of many other theories of vertically propagating gravity waves. The modified P93 formulation presented here has some conceptual similarities to the formulation given by Kershaw (1995), but the Kershaw parameterization relies on a single phase speed. In conditions with very high values of u_{up}', these approaches may be similar, but for the simulations presented in this work, multiple phase speeds are necessary. The spectra generated by the modified P93 formulation are somewhat similar to that of AD99. However, the AD99 spectrum is much broader, and does not allow for shear to affect the

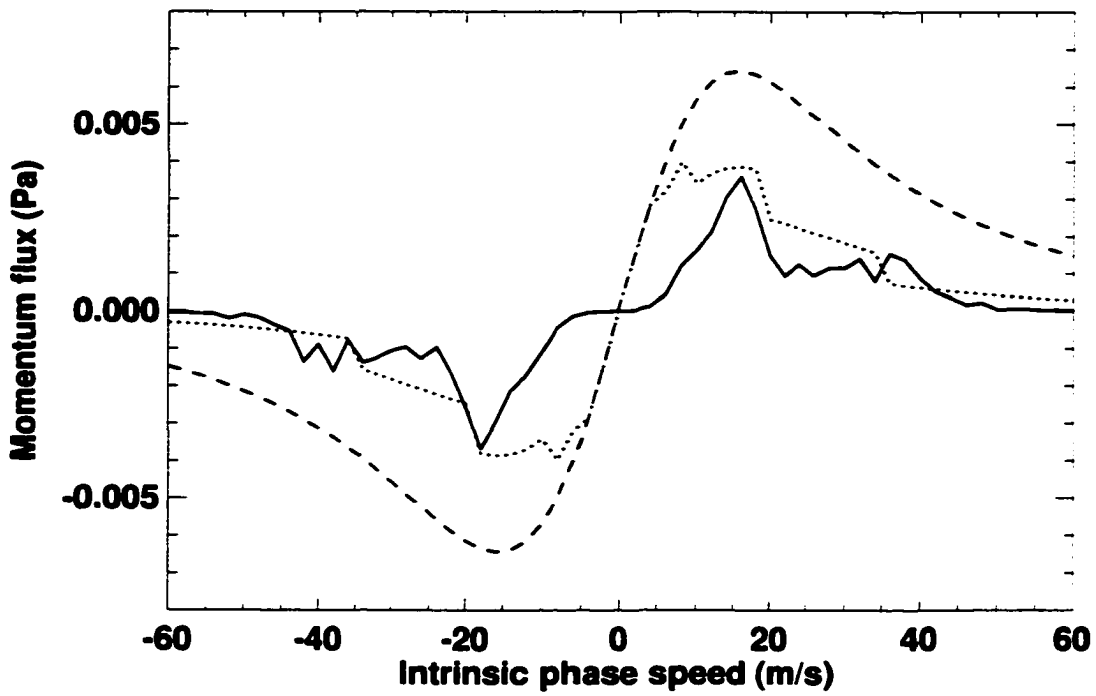

Fig. 15.16. Plot of momentum flux spectra from the WK calm run (solid) and the parametrization (dashed), and the parameterization with wave reflection (dotted).

shape of the spectrum. Also, the AD99 spectrum implies a stronger flux of wave energy for a given amount of momentum flux than the parameterization presented here. We have seen that the new parameterization produces a fairly realistic momentum flux spectrum for the example of the WK control run, showing that this scheme has promise for use in large-scale models, although more tests need to be performed to verify this.

Chapter 16: Conclusions

In this dissertation, we have studied the generation of vertically propagating gravity waves by convection, as simulated by a two-dimensional numerical model. We have applied several types of analysis to the simulated storms, the results of which are summarized below.

From the gravity wave source analysis, we found that the production of gravity waves can be understood as a linear response to a forcing composed of shear, heating and nonlinear advection. The shear was found to play a small role, while the heating and nonlinear advection terms were comparable to one another. This is somewhat different from the findings of Lane et al. (2001), who found that the nonlinear advection term was dominant. However, the simulated convection in their study (three dimensional multicell) is quite different from the convection in this study (two dimensional squall line), so the differences may relate to different convective regimes.

The analysis of the budgets of first and second moment quantities revealed that several of the budgets could be diagnosed well, particularly those of the zonal mean zonal wind, zonal mean potential temperature, and the variances of the horizontal wind and potential temperature. These revealed that changes the mean zonal wind were primarily due to a divergence of the momentum flux, and diabatic heating was the most important factor in changing the mean potential temperature in the troposphere, while the divergence of the vertical heat flux was dominant in the stratosphere. Also, we found that the budget of the horizontal component of kinetic energy was dominated by a balance between the turbulent transport and pressure terms, and that the budget of potential temperature variance is primarily affected by a combination of gradient production and diabatic heating in the troposphere, and gradient production in the stratosphere. In addition, we derived extended versions of the Eliassen-Palm relationships between wave momentum flux and wave energy flux, and illustrated that given certain assumptions, these extended relationships

reduce to the original results. A new relationship for the vertical structure of the variance of pressure was derived in Chapter 8, and it agrees with the numerical results for the behavior of this quantity in the presence of gravity waves.

In Chapter 10, we presented an EOF analysis, in which we were able to separate different modes of behavior according to the amount of variance that is explained by each mode. In doing so, we found that the first several modes were dominated by convective activity within the troposphere, while higher modes associated with travelling stratospheric gravity waves were also present. In view of the difficulty in interpreting the physical processes involved in some of the modes, the utility of EOFs as applied in Chapter 10 towards the diagnosis of convection is questionable. There may be combinations of fields other than u, w, and θ for which EOF analysis is more useful.

The trajectory analysis allowed us to determine qualitative behavior of particles within the model troposphere into physically relevant categories such as moist updrafts, waves and turbulence, and subsidence. The behavior of the particles in the model stratosphere was consistent with what would be expected in the presence of high-frequency gravity waves. The thresholds used in the identification of updraft particles proved useful in the determination of thresholds for updraft points in the conditional sampling analysis.

From the conditional sampling analysis, we found that the updrafts in the WK runs tended to be deeper, wider, and stronger than those of the TC runs, which might be expected, considering the higher values of CAPE in the WK simulations. The majority of the horizontal perturbation kinetic energy was found outside of the clouds, while a disproportionate amount of the vertical perturbation kinetic energy was confined within the points categorized as moist updrafts. We were also able to measure the difference between the horizontal velocity of the updrafts and the mean flow. This difference is a measure of the extent to which the updrafts act as an obstacle to the flow, and also relates to the convective momentum transport.

The Fourier analysis presented in Chapter 13 showed that convectively generated gravity waves cannot be accurately characterized by a single phase speed, since it is typical to see both eastward- and westward-propagating waves. This points to a problem with several existing parameterizations, as mentioned in Chapter 9. The vertical wavenumber spectrum for the WK control run indicates that the power peaks at a wavelength that is

twice the depth of the convection, consistent with both theoretical (Salby and Garcia 1987) and modeling (Pandya and Alexander 1999) results. The simulations with stronger convection tended to produce more wave momentum flux than those with weaker convection, as might be expected. Also, updrafts that propagate relative to the mean flow produces more waves that propagate in the same direction, which is consistent with the results of Fovell et al. (1992), Alexander et al. (1995), and Alexander and Holton (1997).

From the experiments in which we varied the stratospheric shear, we found that westward-propagating waves forced by the simulated convection were dissipated in regions of easterly shear, and vice versa. This is consistent with the theory of Eliassen and Palm (1960), and with the modeling results of Alexander and Holton (1997), among others. Further analysis of individual waves revealed that they were indeed dissipated at their critical levels, although the region of dissipation was distributed over a region of a few kilometers below the critical levels themselves. Since the vertical group velocity of a vertically propagating wave decreases to zero as it approaches its critical level (Bretherton 1966), it is not surprising that such waves experience dissipation below the level itself. The dissipation of the waves led to substantial changes in the mean flow, indicating that high-frequency, short-wavelength gravity waves forced by convection may play a significant role in the forcing of the QBO, consistent with the findings of Alexander and Holton (1997), Dunkerton (1997) and Piani et al. (2001).

The parameterization outlined in Chapter 15 invokes the transient topography mechanism of P93 to explain the momentum flux spectra seen in Chapter 13. The interpretation that the width, height and timescale of the updrafts define the convective "mountain" is quite different than that of P93, who used an anvil. When this parameterization is forced with temporal and spatial scales similar to those of the updrafts, it produces spectra with shapes that are peaked at approximately $\hat{c} = \pm 20$ m s^{-1}, and fall off quickly beyond, particularly when the effects of reflection are included. This is closer to the modeling results of the work presented here and in other sources (Alexander and Holton 1997; Piani et al. 2000) than the AD99 or original P93 spectra. This indicates that the new parameterization is more likely to produce waves whose momentum is deposited in the correct locations. As mentioned in Chapter 15, the amount of wave energy flux is dependent upon the shape of the momentum flux spectrum, so this quantity will also be represented more realistically

in the new parameterization. One of the advantages of the new convectively generated gravity wave parameterization is that in addition to being a source of mean flow forcing in the middle atmosphere, waves are allowed to act as a drain on the CKE.

In the future, much of the analysis in this work can be extended to fully three-dimensional studies. Also, more types of convection need to be analyzed. This includes different kinds of MCSs such as mesoscale convective complexes and leading-line stratiform squall lines. A parameterization has recently been developed (Cheng 2001) that can diagnose the type of MCS that is produced within a GCM grid cell, using information about the vertical wind shear and the moist Brunt-Väisälä frequency. The shape of the MCSs could be related to momentum flux spectra by using a transient mountain with an asymmetric shape. The waves produced by shallower cumuli, which are ubiquitous in the tropics, should also be studied. This would help justify the assumptions that the "mountain" is proportional to the updraft depth, and that the vertical wavelengths of the waves are equal to twice the depth of the convection, although the theoretical results of Salby and Garcia (1987) indicate that this latter assumption is a fairly robust feature. Another effect that may be important is the role of partial wave reflection, since our parameterization assumes that waves are either completely transmitted or completely reflected, while studies (Gill 1982, p. 146) have shown that waves are typically partially reflected at a level where the Brunt-Väisälä frequency changes.

In addition, the role of convective strength in producing gravity waves needs to be explored further. Also, the functional dependence of the spatial and temporal functions that comprise the transient "mountain" may need to be studied further. Another issue that may be important is that some of the waves produced by convection may propagate long horizontal distances, into what would be adjacent grid boxes in a GCM. Future parameterizations may need to take this effect into account, particularly as grid boxes become smaller. Also, the production of horizontally-propagating gravity waves needs to be studied further, as these waves may also act as a sink to the CKE of an individual cloud, but may act as a source of CKE to another cloud (Mapes 1993). In addition, this study has not addressed other non-orographic sources of gravity waves such as shear, which may also be important. Finally, and perhaps most importantly, more observational studies need to be made of convectively generated gravity waves.

References

Alexander, M. J., 1998: Interpretations of observed climatological patterns in stratospheric gravity wave variance. *J. Geophys. Res.*, **103,** 8627-8640.

Alexander, M. J., J. H. Beres, and L. Pfister, 2000: Tropical stratospheric wave activity and relationships to clouds. *J. Geophys. Res.*, **105,** 22,299-22,309.

Alexander, M. J., and T. J. Dunkerton, 1999: A spectral parameterization of mean-flow forcing due to breaking gravity waves. *J. Atmos. Sci.*, **56,** 4167-4182.

Alexander, M. J., and J. R. Holton, 1997: A model study of zonal forcing in the equatorial stratosphere by convectively induced gravity waves. *J. Atmos. Sci.*, **54,** 408-419.

Alexander, M. J., J. R. Holton, and D. R. Durran, 1995: The gravity wave response above deep convection in a squall line simulation. *J. Atmos. Sci.*, **52,** 2212-2226.

Alexander, M. J., and R. A. Vincent, 2000: Gravity waves in the tropical lower stratosphere: A model study of seasonal and interannual variability. *J. Geophys. Res.* **105,** 17,983-17,993.

Andrews, D. G., 1983: A finite-amplitude Eliassen-Palm theorem in isentropic coordinates. *J. Atmos. Sci.*, **40,** 1877-1883.

Andrews, D. G., J. R. Holton, and C. B. Leovy, 1987: *Middle Atmosphere Dynamics*. Academic Press. 489 pp.

Arakawa, A., and W. H. Schubert, 1974: Interaction of a cumulus cloud ensemble with the large-scale environment. Part I. *J. Atmos. Sci.*, **31,** 674-701.

Arakawa, A., and K.-M. Xu, 1990: The macroscopic behavior of simulated cumulus convection and semi-prognostic tests of the Arakawa-Schubert cumulus parameterization. *Physical Processes in Atmospheric Models*, D. R. Sikka and S. S. Singh, Eds., Wiley Eastern, 3-18.

Baldwin, M. P., L. J. Gray, T. J. Dunkerton, K. Hamilton, P. H. Haynes, W. J. Randel, J. R. Holton, M. J. Alexander, I. Hirota, T. Hironouchi, D. B. A. Jones, J. S. Kinnersley, C. Marquardt, K. Sato, and M. Takahashi, 2001: The quasi-biennial oscillation. *Rev. Geophys.*, **39,** 179-229.

Bannon, P. R., 1996: On the anelastic approximation for a compressible atmosphere. *J. Atmos. Sci.*, **53,** 3618-3628.

Barnett, T. P., 1983: Interaction of the monsoon and Pacific trade wind systems at interannual time scales. Part I: The equatorial zone. *Mon. Wea. Rev.*, **111,** 756-773.

Bossuet, C., M. Déqué, D. Cariolle, 1998: Impact of a simple parameterization of convective gravity-wave drag in a stratosphere-troposphere general circulation model and its sensitivity to vertical resolution. *Ann. Geophysicae*, **16,** 238-249.

Bluestein, H. B., 1993: Synoptic-dynamic meteorology in midlatitudes. Volume II: Observations and theory of weather systems. Oxford University Press, New York.

Bretherton, F. P., 1966: The propagation of groups of internal gravity waves in a shear flow. *Quart. J. Roy. Meteor. Soc.*, **92,** 466-480.

Bretherton, F. P., 1969: Momentum transport by gravity waves. *Quart. J. Roy. Meteor. Soc.*, **95,** 213-243.

Brewer, A. W., 1949: Evidence for a world circulation provided by the measurements of helium and water vapor distribution in the stratosphere. *Quart. J. Roy. Meteor. Soc.*, **75,** 351-363.

Chane-Ming, F., F. Molinaro, J. Leveau, P. Keckhut, A. Hauchecorne, and S. Godin, 2000: Vertical short-scale structures in the upper tropospheric and lower stratospheric temperature and ozone at la Réunion Island (20.8° S, 55.3° E). *J. Geophys. Res.*, **105,** 26,857-26,870.

Cheng, A., 2001: A theory of the mesoscale organization of moist convection and the associated vertical momentum transport. Ph. D. Dissertation, Colorado State University.

Chun, H.-Y., and J.-J. Baik, 1998: Momentum flux by thermally induced gravity waves and its approximation for large-scale models. *J. Atmos. Sci.*, **55,** 3299-3310.

Chun, H.-Y., M.-D. Song, J.-W. Kim, and J.-J. Baik, 2001: Effects of gravity wave drag induced by convections on the atmospheric general circulation. *J. Atmos. Sci.*, **58,** 302-319.

Clark, J. H. E., and L. T. Morone, 1981: Mesospheric heating due to convectively excited gravity waves - A case study. *Mon. Wea. Rev.*, **109,** 990-1001.

Clark, T. L., T. Hauf, and J. P. Kuettner, 1986: Convectively forced internal gravity waves: Results from two-dimensional numerical experiments. *Quart. J. Roy. Meteor. Soc.*, **112,** 899-925.

Danielson, E. F., 1959: The laminar structure of the atmosphere and its relation to the concept of a tropopause. *Arch. Meteor. Geophys. Biokl.*, Series A, **11,** 293-332.

Dewan, E. M., R. H. Picard, R. R. O'Neill, H. A. Gardiner, J. Gibson, J. D. Mill, E. Richards, M. Kendra, and W. O. Gallery, 1998: MSX satellite observations of thunderstorm-generated gravity waves in midwave infrared images of the upper stratosphere. *Geophys. Res. Lett.*, **25,** 939-942.

Dobson, G. M. B, 1956: Origin and distribution of the polyatomic molecules in the atmosphere. *Proc. Royal Soc., A*, **236,** 187-192.

Dunkerton, T. J., 1997: The role of gravity waves in the quasi-biennial oscillation. *J. Geophys. Res.*, **102,** 26,053-26,076.

Dunkerton, T. J., and D. P. Delisi, 1985: Climatology of the equatorial lower stratosphere. *J. Atmos. Sci.*, **42,** 376-396.

Durran, D. R., and J. B. Klemp, 1982: On the effects of moisture on the Brunt-Väisälä frequency. *J. Atmos. Sci.*, **39,** 2152-2158.

Eliassen, A., and E. Palm, 1960: On the transfer of energy in stationary mountain waves. *Geofys. Publikasjoner*, **22,** No. 3, 1-23.

Emanuel, K. A., 1994: *Atmospheric Convection*. Oxford University Press. 580 pp.

Ford, R., 1994: Gravity wave radiation from vortex trains in rotating shallow water. *J. Fluid Mech.*, **281,** 81-118.

Fovell, R. G., D. R. Durran, and J. R. Holton, 1992: Numerical simulations of convectively generated stratospheric gravity waves. *J. Atmos. Sci.*, **49,** 1427-1442.

Fovell, R. G., and Y. Ogura, 1988: Numerical simulation of a midlatitude squall line in two dimensions. *J. Atmos. Sci.*, **45,** 3846-3879.

Fritts, D. C., and W. Lu, 1993: Spectral estimates of gravity wave energy and momentum fluxes. Part II: Parameterization of wave forcing and variability. *J. Atmos. Sci.*, **50,** 3695-3713.

Fritts, D. C., and G. D. Nastrom, 1992: Sources of mesoscale variability of gravity waves. Part II: Frontal, convective, and jet stream excitation. *J. Atmos. Sci.*, **49,** 111-127.

Gallus, W. A., Jr., and R. H. Johnson, 1992: The momentum budget of an intense midlatitude squall line. *J. Atmos. Sci.*, **49,** 422-450.

Gao, K., D.-L. Zhang, M. W. Moncrieff, and H.-R. Cho, 1990: Mesoscale momentum budget in a midlatitude squall line: A numerical case study. *J. Atmos. Sci.*, **47,** 1011-1028.

Gill, A. E., 1982: *Atmosphere-Ocean Dynamics*. Academic Press. 662 pp.

Grant, W. B., R. B. Pierce, S. J. Oltmans, and E. V. Browell, 1998: Seasonal evolution of total and gravity wave induced laminae in ozonesonde data in the tropics and subtropics. *Geophys. Res. Lett.*, **25,** 1863-1866.

Haertel, P. T., and R. H. Johnson, 2000: The linear dynamics of squall line mesohighs and wake lows. *J. Atmos. Sci.*, **57,** 93-107.

Haertel, P. T., R. H. Johnson, and S. N. Tulich, 2001: Some simple simulations of thunderstorm outflows. *J. Atmos. Sci.*, **58,** 504-516.

Hamming, R. W., 1998: *Digital Filters*. Dover, 296 pp.

Hartmann, D. L., 1999: ATM 552 Notes. [Available online at http://www.atmos.washington.edu/~dennis/.]

Hines, C. O., 1997a: Doppler-spread parameterization of gravity-wave momentum deposition in the middle atmosphere. Part 1: Basic formulation. *J. Atmos. Sol.-Terr. Phys.*, **59,** 371-386.

Hines, C. O., 1997b: Doppler-spread parameterization of gravity-wave momentum deposition in the middle atmosphere. Part 2: Broad and quasi monochromatic spectra, and implementation. *J. Atmos. Sol.-Terr. Phys.*, **59,** 387-400.

Holton, J. R., 1992: *An introduction to dynamic meteorology*. Academic Press. 511 pp.

Holton, J. R., and M. J. Alexander, 1999: Gravity waves in the mesosphere generated by tropospheric convection. *Tellus*, **51A-B,** 45-58.

Houze, R. A., Jr., 1982: Cloud clusters and large-scale vertical motions in the tropics. *J. Meteor. Soc. Japan*, **60,** 396-410.

Houze, R. A., Jr., 1989: Observed structure of mesoscale convective systems and implications for large-scale heating. *Quart. J. Roy. Meteor. Soc.*, **115,** 425-461.

Houze, R. A., Jr., 1993: *Cloud dynamics*. Academic Press. 570 pp.

Houze, R. A., Jr., S. A. Rutledge, M. I. Biggerstaff, and B. F. Smull, 1989: Interpretation of Doppler weather-radar displays in midlatitude mesoscale convective systems. *Bull. Amer. Meteor. Soc.*, **70,** 608-619.

Jorgensen, D. P., M. A. LeMone, and S. B. Trier, 1997: Structure and evolution of the 22 February 1993 TOGA COARE squall line: Aircraft observations of precipitation, circulation, and surface energy fluxes. *J. Atmos. Sci.*, **54,** 1961-1985.

Karoly, D. J., G. L. Roff, and M. J. Reeder, 1996: Gravity wave activity associated with tropical convection detected in TOGA COARE sounding data. *Geophys. Res. Lett.*, **23,** 261-264.

Kershaw, R., 1995: Parameterization of momentum transport by convectively generated gravity waves. *Quart. J. Roy. Meteor. Soc.*, **121,** 1023-1040.

Kessler, E., 1969: On the distribution and continuity of water substance in atmospheric circulations. *Meteor. Monogr.*, **10,** No. 32, 84 pp.

Klemp, J. B., and D. K. Lilly, 1978: Numerical simulation of hydrostatic mountain waves. *J. Atmos. Sci.*, **35,** 78-107.

Klemp, J. B., and R. B. Wilhelmson, 1978: The simulation of three-dimensional convective storm dynamics. *J. Atmos. Sci.*, **35,** 1070-1096.

Krueger, S. K., G. T. McLean, and Q. Fu, 1995: Numerical simulation of the stratus-to-cumulus transition in the subtropical marine boundary layer. Part II: Boundary-layer circulation. *J. Atmos. Sci.*, **52,** 2851-2868.

Kutzbach, J. E., 1967: Empirical eigenvectors of sea-level pressure, surface temperature and precipitation complexes over North America. *J. Appl. Meteor.*, **6,** 791-802.

Lane, T. P., M. J. Reeder, and T. L. Clark, 2001: Numerical modeling of gravity wave generation by deep tropical convection. *J. Atmos. Sci.*, **58,** 1249-1274.

Lighthill, M. J., 1952: On sound generated aerodynamically. Part I: General theory. *Proc. Royal Soc., A,* **211,** 564-587.

Lighthill, M. J., 1978: *Waves in Fluids*. Cambridge University Press, 504 pp.

Lilly, D. K., 1978: A severe downslope windstorm and aircraft turbulence event induced by a mountain wave. *J. Atmos. Sci.*, **35,** 59-77.

Lin, Y.-L., and H.-Y. Chun, 1991: Effects of diabatic cooling in a shear flow with a critical level. *J. Atmos. Sci.*, **48,** 2476-2491.

Lin, Y.-L., R. D. Farley, and H. D. Orville, 1983: Bulk parameterization of the snow field in a cloud model. *J. Clim. Appl. Meteor.*, **22,** 1065-1092.

Lindzen, R. S., 1981: Turbulence and stress owing to gravity wave and tidal breakdown. *J. Geophys. Res.*, **86,** 9707-9714.

Lindzen, R. S., 1984: Gravity waves in the middle atmosphere. *Dynamics of the Middle Atmosphere*, J. R. Holton and T. Matsuno, Eds., Terra, 3-18.

Lindzen, R. S., and J. R. Holton, 1968: A theory of the quasi-biennial oscillation. *J. Atmos. Sci*, **25,** 1095-1107.

Lorenz, E. N., 1956: Empirical orthogonal functions and statistical weather prediction. M. I. T. Dept. of Meteorology, Sci. Rept. No. 1, Contract AF19(604)-1566, 49 pp.

Lucas, C., E. J. Zipser, and B. S. Ferrier, 2000: Sensitivity of tropical west Pacific oceanic squall lines to tropospheric wind and moisture profiles. *J. Atmos. Sci*, **57,** 2351-2373.

Mapes, B. E., 1993: Gregarious tropical convection. *J. Atmos. Sci*, **50,** 2026-2037.

Marcus, S. L., M. Ghil, and J. O. Dickey, 1996: The extratropical 40-day oscillation in the UCLA general circulation model. Part II: Spatial structure. *J. Atmos. Sci*, **53,** 1993-2014.

Marks, C. J., and S. D. Eckermann, 1995: A three-dimensional nonhydrostatic ray-tracing model for gravity waves: Formulation and preliminary results for the middle atmosphere. *J. Atmos. Sci*, **52,** 1959-1984.

Matsuno, T., 1971: A dynamical model of the stratospheric sudden warming. *J. Atmos. Sci.*, **28,** 1479-1494.

McFarlane, N. A., 1987: The effect of orographically excited gravity wave drag on the general circulation of the lower stratosphere and troposphere. *J. Atmos. Sci.*, **44,** 1775-1800.

McLandress, C., M. J. Alexander, and D. L. Wu, 2000: Microwave Limb Sounder observations of gravity waves in the stratosphere: A climatology and interpretation. *J. Geophys. Res.*, **105,** 11,947-11,967.

Mohr, K. I., and E. J. Zipser, 1996: Mesoscale convective systems defined by their 85-GHz ice scattering signature: Size and intensity comparison over tropical oceans and continents. *Mon. Wea. Rev.*, **124,** 2417-2437.

Montgomery, M. T., and R. J. Kallenbach, 1997: A theory for vortex-Rossby waves and its application to spiral bands and intensity changes in hurricanes. *Quart. J. Roy. Meteor. Soc.*, **123,** 435-465.

Newell, R. E., V. Thouret, J. Y. N. Cho, P. Stoller, A. Marenco, and H. G. Smit, 1999: Ubiquity of quasi-horizontal layers in the troposphere. *Nature*, **398,** 316-319.

Newell, R. E., Z.-X. Wu, Y. Zhu, W. Hu, E. V. Browell, G. L. Gregory, G. W. Sachse, J. E. Collins Jr., K. K. Kelly, and S. C. Liu, 1996: Vertical fine-scale atmospheric structure measures from NASA DC-8 during PEM-West A. *J. Geophys. Res.*, **104,** 1943-1960.

Nicholls, M. E., 1987: A comparison of the results of a two-dimensional numerical simulation of a tropical squall line with observations. *Mon. Wea. Rev.*, **115,** 3055-3077.

Nicholls, M. E., R. H. Johnson, and W. R. Cotton, 1988: The sensitivity of two-dimensional simulations of tropical squall lines to environmental profiles. *J. Atmos. Sci*, **45,** 3625-3649.

Nicholls, M. E., R. A. Pielke, and W. R. Cotton, 1991: Thermally forced gravity waves in an atmosphere at rest. *J. Atmos. Sci*, **48,** 1869-1884.

Nilsson, E. D., L. Pirjola, and M. Kulmala, 2000: The effect of atmospheric waves on aerosol nucleation and size distribution. *J. Geophys. Res.*, **105,** 19,917-19,926.

North, G. R., T. L. Bell, R. F. Calahan, and F. J. Moeng, 1982: Sampling errors in the estimation of empirical orthogonal functions. *Mon. Wea. Rev.*, **110,** 699-706.

Palmer, T. N., G. J. Shutts, and R. Swinbank, 1986: Alleviation of a systematic westerly bias in general circulation and numerical weather prediction models through an orographic gravity wave drag parameterization. *Quart. J. Roy. Meteor. Soc.*, **112,** 1001-1039.

Pan, D.-M., and D. A. Randall, 1998: A cumulus parameterization with a prognostic closure. *Quart. J. Roy. Meteor. Soc.*, **124,** 949-981.

Pandya, R. E., and M. J. Alexander, 1999: Linear stratospheric gravity waves above convective thermal forcing. *J. Atmos. Sci*, **56,** 2434-2446.

Pandya, R., D. Durran, and C. Bretherton, 1993: Comments on "Thermally forced gravity waves in an atmosphere at rest." *J. Atmos. Sci*, **50,** 4097-4101.

Parker, M. D. B., 1999: May 1996 and May 1997 linear mesoscale convective systems of the central plains: Synoptic meteorology and a reflectivity-based taxonomy. M. S. Thesis, Colorado State University.

Parker, M. D., and R. H. Johnson, 2000: Organizational modes of midlatitude mesoscale convective systems. *Mon. Wea. Rev.*, **128,** 3413-3436.

Pauluis, O., V. Balaji, and I. M. Held, 2000: Frictional dissipation in a precipitating atmosphere. *J. Atmos. Sci*, **57,** 989-994.

Percival, D. B., and A. T. Walden, 1993: *Spectral Analysis for Physical Applications: Multitaper and Conventional Univariate Techniques*. Cambridge University Press. 569 pp.

Piani, C., D. Durran, M. J. Alexander, and J. R. Holton, 2000: A numerical study of three-dimensional gravity waves triggered by deep tropical convection and their role in the dynamics of the QBO. *J. Atmos. Sci*, **57,** 3689-3702.

Pierce, R. B., and W. B. Grant, 1998: Seasonal evolution of Rossby and gravity wave induced laminae in ozonesonde data obtained from Wallops Island, Virginia. *Geophys. Res. Lett.*, **25,** 1859-1862.

Pfister, L., S. Scott, M. Loewenstein, S. Bowen, and M. Legg, 1993: Mesoscale disturbances in the tropical stratosphere excited by convection: Observations and effects on the stratospheric momentum budget. *J. Atmos. Sci*, **50,** 1058-1075.

Pfister L., W. Starr, R. Craig, M. Loewenstein, and M. Legg, 1986: Small scale motions observed by aircraft in the tropical lower stratosphere: Evidence for mixing and its relationship to large scale flows. *J. Atmos. Sci*, **43,** 3210-3225.

Plumb, R. A., 1977: The interaction of two internal waves with the mean flow: Implications for the theory of the quasi-biennial oscillation. *J. Atmos. Sci*, **34,** 1847-1858.

Potter, B. E., and J. R. Holton, 1995: The role of monsoon convection in the dehydration of the lower tropical stratosphere. *J. Atmos. Sci*, **52,** 1034-1050.

Randall, D. A., and D.-M. Pan, 1993: Implementation of the Arakawa-Schubert parameterization with a prognostic closure. *The Representation of Cumulus Convection in Numerical Models*, K. Emanuel and D. Raymond, Eds. Meteor Monogr. Vol. 24, No. 46., p. 137-144.

Redelsperger, J.-L., P. R. A. Brown, F. Guichard, C. Hoff, M. Kawasima, S. Lang, T. Montemerle, K. Nakamura, K. Saito, C. Seman, W. K. Tao, and L. J. Donner, 2000: A GCSS model intercomparison for a tropical squall line observed during TOGA-COARE. I: Cloud-resolving models. *Quart. J. Roy. Meteor. Soc.*, **126,** 823-863.

Rind, D., R. Suozzo, N. K. Balachandran, A. Lascis, and G. Russell, 1988: The GISS global climate-middle atmosphere model. Part I: Model structure and climatology. *J. Atmos. Sci.*, **45,** 329-370.

Roadnight, C. E., 1999: Momentum transport by convection. Ph.D. dissertation, The University of Leeds.

Rotunno, R., J. B. Klemp, and M. L. Weisman, 1988: A theory for strong, long-lived squall lines. *J. Atmos. Sci.*, **45,** 463-485.

Salby, M. R., and R. R. Garcia, 1987: Transient response to localized episodic heating in the tropics. Part I: Excitation and short-time near-field behavior. *J. Atmos. Sci.*, **44,** 458-498.

Saravanan, R., 1990: A multiwave model of the quasi-biennial oscillation. *J. Atmos. Sci.*, **47,** 2465-2474.

Sato, K., 1992: Vertical wind disturbances in the afternoon of midsummer revealed by the MU radar. *Geophys. Res. Lett.*, **19,** 1943-1946.

Sato, K., 1993: Small-scale wind disturbances observed by the MU radar during the passage of typhoon Kelly. *J. Atmos. Sci*, **50,** 518-537.

Sato, K., H. Hashiguchi, and S. Fukao, 1995: Gravity waves and turbulence associated with cumulus convection observed with the UHF/VHF clear-air Doppler radars. *J. Geophys. Res.*, **100,** 7111-7119.

Schmidt, J. M., and W. R. Cotton, 1990: Interactions between upper and lower tropospheric gravity-waves on squall line structure and maintenance. *J. Atmos. Sci*, **47,** 1205-1222.

Schubert, W. H., 2000: A retrospective view of Arakawa's ideas on cumulus parameterization. *General Circulation Model Development*, D. A. Randall, Ed., p. 181-224.

Soong, S.-T., and Y. Ogura, 1973: A comparison between axisymmetric and slabsymmetric cumulus cloud models. *J. Atmos. Sci*, **30,** 879-893.

Stull, R. B., 1976: Internal gravity waves generated by penetrative convection. *J. Atmos. Sci*, **33,** 1279-1286.

Stull, R. B., 1988: *An introduction to boundary-layer meteorology*. Kluwer Academic Publishers. 670 pp.

Tao, W.-K., and J. Simpson, 1993: Goddard cumulus ensemble model. Part I: Model description. *Terres. Atmos. Ocean. Sci.*, **4,** 35-72.

Tao, W.-K., J. Simpson, and M. McCumber, 1989: An ice-water saturation adjustment. *Mon. Wea. Rev.*, **117,** 231-235.

Trier, S. B., W. C. Skamarock, M. A. Lemone, D. B. Parsons, and D. P. Jorgensen, 1996: Structure and evolution of the 22 February 1993 TOGA COARE squall line: Numerical simulation. *J. Atmos. Sci.*, **53,** 2861-2886.

Vincent, R. A., and M. J. Alexander, 2000: Gravity waves in the tropical lower stratosphere: An observational study of seasonal and interannual variability. *J. Geophys. Res.* **105,** 17,971-17,982.

Warner, C. D., and M. E. McIntyre, 1999: Toward an ultra-simple spectral gravity wave parameterization for general circulation models. *Earth Planets Space*, **51,** 475-484.

Warner, C. D., and M. E. McIntyre, 2001: An ultrasimple spectral parameterization for nonorographic gravity waves. *J. Atmos. Sci.*, **58,** 1837-1857.

Weisman, M. L., 1992: The role of convectively-generated rear-inflow jets in the evolution of long-lived mesoconvective systems. *J. Atmos. Sci.*, **49,** 1826-1847.

Weisman, M. L., and J. B. Klemp, 1982: The dependence of numerically simulated convective storms on vertical wind shear and buoyancy. *Mon. Wea. Rev.*, **110,** 504-520.

Weisman, M. L., J. B. Klemp, and R. Rotunno, 1988: The structure and evolution of numerically simulated squall lines. *J. Atmos. Sci.*, **45,** 801-823.

Weisman, M. L., W. C. Skamarock, and J. B. Klemp, 1997: The resolution dependence of explicitly modeled convective systems. *Mon. Wea. Rev.*, **125,** 527-548.

Wilson, D. K., 1996: Empirical orthogonal function analysis of the weakly convective atmospheric boundary layer. Part I: Eddy structures. *J. Atmos. Sci.*, **53,** 1990-2013.

Wilson, D. K., and J. C. Wyngaard, 1996: Empirical orthogonal function analysis of the weakly convective atmospheric boundary layer. Part I: Eddy energetics. *J. Atmos. Sci.*, **53,** 801-823.

Wu, D. L., and J. W. Waters, 1996a: Gravity-wave-scale temperature fluctuations seen by the UARS MLS. *Geophys. Res. Lett.*, **23,** 3289-3292.

Wu, D. L., and J. W. Waters, 1996b: Satellite observations of atmospheric variances: A possible indication of gravity waves. *Geophys. Res. Lett.*, **23,** 3631-3634.

Xu, K.-M., A. Arakawa, and S. K. Kreuger, 1992: The macroscopic behavior of cumulus ensembles simulated by a cumulus ensemble model. *J. Atmos. Sci.*, **49,** 2402-2420.

Xue, M., K. K. Droegemeier, V. Wong, 2000: The Advanced Regional Prediction System (ARPS) - A multi-scale nonhydrostatic atmospheric simulation and prediction model. Part I: Model dynamics and verification. *Meteorol. Atmos. Phys.*, **75,** 161-193.

Xue, M., K. K. Droegemeier, V. Wong, A. Shapiro, K. Brewster, F. Carr, D. Weber, Y. Liu, and D.-H. Wang, 2001: The Advanced Regional Prediction System (ARPS) - A multi-scale nonhydrostatic atmospheric simulation and prediction tool. Part II: Model physics and applications. *Meteor. Atmos. Physics*, **76,** 143-165.

Xue, M., K. K. Droegemeier, V. Wong, A. Shapiro, and K. Brewster, 1995: ARPS version 4.0 user's guide. EC #1110, Center for Analysis and Prediction of Storms, University of Oklahoma, Norman, OK 73109, 380 pp.

Xue, M., and S.-J. Lin, 2001: Numerical equivalence of advection in flux and advective forms and quadratically conservative high-order advection schemes. *Mon. Wea. Rev.*, **129,** 561-565.